Universidad Pública de Navarra
Nafarroako Unibertsitate Publikoa

Doctoral thesis submitted for the degree of Doctor of Philosophy in Telecommunication Engineering

Postgraduate programme: Communication Technology

Advanced metamaterials for high resolution focusing and invisibility cloaks

Presented by: Bakhtiyar Orazbayev

Director: Dr. Miguel Beruete Díaz

Pamplona, November 2016

Abstract

Metamaterials, the descendants of the artificial dielectrics, have unusual electromagnetic parameters and provide more abilities than naturally available dielectrics for the control of light propagation. Being able to control both permittivity and permeability, metamaterials have opened a way to obtain a double negative medium. The first experimental realization of such medium gave an enormous impulse for research in the field of electromagnetism. As result, many fascinating electromagnetic devices have been developed since then, including metamaterial lenses, beam steerers and even invisibility cloaks. The possible applications of metamaterials are not limited to these devices and can be applied in many fields, such as telecommunications, security systems, biological and chemical sensing, spectroscopy, integrated nano-optics, nanotechnology, medical imaging systems, etc.

The aim of this doctoral thesis, performed at the Public University of Navarre in collaboration with the University of Texas at Austin, the Valencia Nanophotonics Technology Center in the UPV and King's College London, is to contribute to the development of metamaterial based devices, including their fabrication and, when possible, experimental verification. The thesis is not focused on a single application or device, but instead tries to provide an extensive exploration of the different metamaterial devices. These results include the following:

Three different lens designs based on a fishnet metamaterial are presented: a broadband zoned fishnet metamaterial lens, a Soret fishnet metamaterial lens and a Wood zone plate fishnet metamaterial. All lenses have been experimentally realized, demonstrating a good agreement with numerical analysis. Moreover, a metasurface, a 2D case of metamaterial, built with closed ring resonators has been used to design an ultrathin carpet cloak. Numerical as well as experimental analysis is done, confirming the cloaking performance of the designed cloak in relatively wide frequency range and angle span. Also, a design of a transformation based cloak for diffusive light is presented. It is demonstrated, that by restricting the cloak to work in one direction it is possible to obtain an ideal cloaking performance under transient illumination, which is normally beyond reach in typical cloak designs. Finally, the theoretical demonstration of three different beam steering devices based on graphene metamaterial is presented. The used graphene metamaterial allows to dynamically control the output angle of the radiation with ultrahigh speed.

Resumen

Los metamateriales, descendientes de los dieléctricos artificiales, tienen parámetros electromagnéticos inusuales y proporcionan más posibilidades que los dieléctricos naturales para el control de la propagación de la luz. Los metamateriales han posibilitado la obtención de medios doblemente negativos, gracias a la capacidad que ofrecen para controlar tanto la permitividad y la permeabilidad. La primera realización experimental de un medio de ese tipo dio un enorme impulso a la investigación en el campo del electromagnetismo. Como resultado, se han desarrollado desde entonces muchos dispositivos electromagnéticos fascinantes, incluyendo lentes de metamateriales, dispositivos de control de dirección de haz e incluso capas de invisibilidad. Las posibles aplicaciones de los metamateriales no se limitan a estos dispositivos y se pueden aplicar en muchas áreas como las telecomunicaciones, sistemas de seguridad, detección biológica y química, la espectroscopía, nanoóptica integrada, la nanotecnología, los sistemas de imágenes médicas, etc.

El objetivo de esta tesis doctoral, realizada en la Universidad Pública de Navarra en colaboración con la Universidad de Texas en Austin, el Centro de Tecnología Nanofotónica de Valencia de la UPV y el King's College London, es contribuir al desarrollo de dispositivos basados en metamateriales, incluyendo su fabricación y, cuando sea posible, la verificación experimental. La tesis no se centra en una sola aplicación o dispositivo, sino que trata de proporcionar una extensa exploración de diferentes dispositivos de metamateriales. Los resultados de la misma son los siguientes:

Se presentan tres lentes de diferentes diseños basados en un metamaterial fishnet: una lente zonada de ancha banda, una lente Soret y una lente de Wood. Todas las lentes han sido experimentalmente realizadas, demostrando un buen acuerdo con el análisis numérico. Por otra parte, se ha demostrado una capa de invisibilidad ultrafina basada en una metasuperficie, un caso 2D de metamaterial, construida con resonadores de anillo. Se ha realizado un análisis numérico, y experimental confirmando el comportamiento de invisibilidad dentro de un rango de frecuencias y de ángulos relativamente amplios. Además, se presenta un diseño de una capa de invisibilidad basada en la óptica de transformación para la luz difusa. Se demuestra, que mediante la restricción de la capa para trabajar en una sola dirección es posible obtener un rendimiento de camuflaje ideal bajo las condiciones de iluminación transitoria, que normalmente está fuera de alcance en los diseños típicos de capas de invisibilidad. Por último, se presenta la demostración teórica de tres diferentes dispositivos de control del haz basados en metamateriales de grafeno. El metamaterial de grafeno utilizado permite controlar dinámicamente el ángulo de salida de la radiación con velocidad ultra alta.

Acknowledgments

I would like to take this chance to extend my gratitude to all people who helped me during my study. The thesis would not be accomplished without their help. However, it is not possible to include all of them in this short acknowledgement. Hope those people I missed out in the following can accept my sincere appreciation at this moment.

At first, I would like to express my gratitude to my supervisor Dr. Miguel Beruete for his excellent guidance (not just scientific). His advices and encouragement have been of vital importance during my research work. I also would like to thank and Dr. Francisco Falcone for his constant support during my study. Thanks then goes to Dr. Miguel Navarro-Cía and Dr. Irina Khromova. The valuable discussions with them, their advices, and experienced instruction helped greatly with my research work. I want to give my special thanks to Prof. Mario Sorolla, who unfortunately passed away. Without him it would have been impossible to make this work. In the Department of Electronic and Electrical Engineering, there are still more people I want to thank.

I would like to thank to Prof. Andrea Alù from University of Texas, Prof. Alejandro Martínez and Dr. Carlos García-Meca from Universitat Politècnica de València, Prof. Anatoly Zayats from King's College London for giving me the opportunity of being part of their research groups and so improving my quality as a researcher. Thanks to all people that I met in Austin and Valencia, particularly to Jason, Eun, Romain, Alba, Luis and Álvaro, for making me feel like if I never would have left home.

During my study in Spain, I am lucky to have the company of my friends and colleagues: Laura, Unai, Aitziber, Daniel, Víctor, Pablo, Alicia, Amagoia, Jose, Adur and Dr. Torres. Without them, my years in Pamplona would not have been as pleasant.

I acknowledge Spanish Ministerio de Economía y Competitividad for the financial support (under grant FPI BES-2012-054909) of my study at UPNA.

Last, but of course not least, I thank my parents for their love and support all the time.

Agradecimientos

Me gustaría aprovechar esta oportunidad para expresar mis agradecimientos a todas las personas que me ayudaron durante mi estudio. La tesis no se llevaría a cabo sin su ayuda. Sin embargo, no es posible incluir todos ellos en estos breves agradecimientos. Espero que las personas que se me pasó mencionar aquí puedan aceptar mi agradecimiento sincero en este momento.

En primer lugar, me gustaría expresar mi agradecimiento a mi supervisor el Dr. Miguel Beruete por su excelente orientación (no sólo científica). Sus consejos y ánimo han sido de vital importancia durante mi trabajo de investigación. También me gustaría dar las gracias y el Dr. Francisco Falcone por su constante apoyo durante mi estudio. Gracias a continuación al Dr. Miguel Navarro-Cía y el Dr. Irina Khromova. Las valiosas discusiones con ellos, sus consejos, y la instrucción con experiencia ayudaron mucho con mi trabajo de investigación. Quiero dar las gracias especialmente al Prof. Mario Sorolla, que lamentablemente falleció. Sin él habría sido imposible realizar este trabajo. En el Departamento de Ingeniería Eléctrica y Electrónica, todavía hay más gente que quiero agradecer.

Me gustaría dar las gracias al Prof. Andrea Alù de la Universidad de Texas, el Prof. Alejandro Martínez y el Dr. Carlos García-Meca desde Universidad Politécnica de Valencia, el Prof. Anatoly Zayats del King College de Londres por darme la oportunidad de ser parte de sus grupos de investigación y así mejorar la calidad de mi como investigador. Gracias a todas las personas que conocí en Austin y Valencia, sobre todo a Jason, Eun, Romain, Alba, Luis y Álvaro, por hacerme sentir como si nunca hubiera salido de casa.

Durante mis estudios en España, tengo la suerte de tener la compañía de mis amigos y colegas: Laura, Unai, Aitziber, Daniel, Víctor, Pablo, Alicia, Amagoia, Jose, Adur y el Dr. Torres. Sin ellos, mis años en Pamplona no habrían sido tan agradable.

Reconozco el apoyo financiero de Ministerio español de Economía y Competitividad (en virtud de concesión FPI BES-2012-054909) para mis estudios en la UPNA.

Por último, pero por supuesto no menos importante, gracias a mis padres por su amor y apoyo todo el tiempo.

List of Figures

upna Universidad Pública de Navarra Nafarroako Unibertsitate Publikoa

upna Universidad Pública de Navarra Nafarroako Unibertsitate Publikoa

List of Tables

Contents

upna Universidad Pública de Navarra Nafarroako Unibertsitate Publikoa

Chapter 1. Overview of Metamaterials

Since the dawn of the civilization, the control of light has been one of the most important topics of the scientific community, long before the uprising of the electromagnetism and Maxwell's equations were introduced. And even the absence of the general expressions, revealing the nature of the light and explaining its behavior, could not prevent the humankind from inventing the devices, capable of controlling and molding the light. Such devices, like mirrors and lenses, which have been known for centuries, were invented by observing and repeating the phenomena occurring in the nature. Currently, the focusing of light still remains one of most important quests in the field of electromagnetism. In the past centuries the electromagnetic (EM) waves were manipulated by means of the conventional dielectrics, whose constitutive EM parameters, permittivity and permeability, are defined by the nature. However, this changed when the electromagnetism received the big boost – the ability to tailor at will the constitutive parameters (CP) of an artificial medium, including the possibility to obtain values of permittivity and permeability less than unity and even negative, overcoming conventional dielectrics commonly used in microwaves and optics. This opened fascinating possibility to get full control over the EM waves propagation and, as result, many interesting concepts and real applications have been proposed, such as perfect lens [1], chiral lens [2], super lens [3], hyperlens [4], invisibility cloaks [5], beam steerers [6], etc. More recently, with the appearance of metasurfaces, which consist of a monolayer of photonic artificial atoms, many attractive functionalities have been proposed for shaping wave fronts of light by introducing an abrupt interfacial phase [7–9], cloaking devices [10], etc.

The main purpose of this chapter is to put in context and highlight the main features of metamaterials and metasurfaces. The attention is centered on a fishnet and graphene based metamaterials as well as a metasurface based on closed ring resonators (CRR), which will be used in subsequent chapters. Finally, the organization of this thesis is described.

1.1. History of metamaterials and metasurfaces

The term metamaterial originates from the Greek word "*meta*" (which means beyond) and refers to artificially made materials with CP that are not available in the conventional materials, i.e. materials that cannot be found in the nature [11,12]. Artificial dielectrics [13,14] can be considered as first precursors of metamaterials, since they allowed to tune the dielectric properties of artificial media using conductors and even obtain negative values of permittivity. These man-made materials trace back to 1898, when the first experiment was conducted in microwave range by Bose [15]. In his experiment Bose demonstrated a rotation of polarization of EM wave in twisted structures – geometries that now are called as artificial chiral elements. The work on artificial dielectrics continued and in 1940s they found their use in antenna systems. In his seminal paper [16] Kock demonstrated for the first time a lightweight metal-lens antenna with the ability to focus EM waves, using conducting plates to tailor the refractive index. This work

drew the attention of the research community, promoting the appearance of new concepts and novel fabrication techniques for the synthesis of composite materials with new unusual CP.

In conventional materials the EM response of waves with wavelength much bigger than the periodicity of material's atomic structure is defined by the macroscopic Maxwell's equations [17]:

$$\begin{aligned} \nabla \times \boldsymbol{E} &= -\frac{\partial \boldsymbol{B}}{\partial t} \\ \nabla \times \boldsymbol{H} &= \frac{\partial \boldsymbol{D}}{\partial t} + \boldsymbol{J} \\ \nabla \cdot \boldsymbol{D} &= \rho \\ \nabla \cdot \boldsymbol{B} &= 0 \end{aligned} \quad , \tag{1.1}$$

where bold letters are vectors, $\boldsymbol{E}$ is the electric field, $\boldsymbol{B}$ is the magnetic flux density, $\boldsymbol{H}$ is the magnetic field, $\boldsymbol{D}$ is the electric displacement, and ρ and $\boldsymbol{J}$ are the external free charge density and current, respectively. When medium is linear[1], the following constitutive relations can be written:

$$\begin{aligned} \boldsymbol{D} &= \varepsilon\varepsilon_0 \boldsymbol{E} \\ \boldsymbol{B} &= \mu\mu_0 \boldsymbol{H} \end{aligned} \quad , \tag{1.2}$$

where ε_0 and μ_0 are the electric permittivity and magnetic permeability of vacuum, $\varepsilon = \varepsilon' + i\varepsilon''$ is the relative electric permittivity and $\mu = \mu' + i\mu''$ is the relative magnetic permeability. Thus from these equations it can be observed that all EM properties of the linear media can be characterized by permittivity and permeability [17]. And in turn, these EM properties are the result of the macroscopic response of the microscopic structure of media, molecules and atoms, to EM wave (Fig. 1.1).

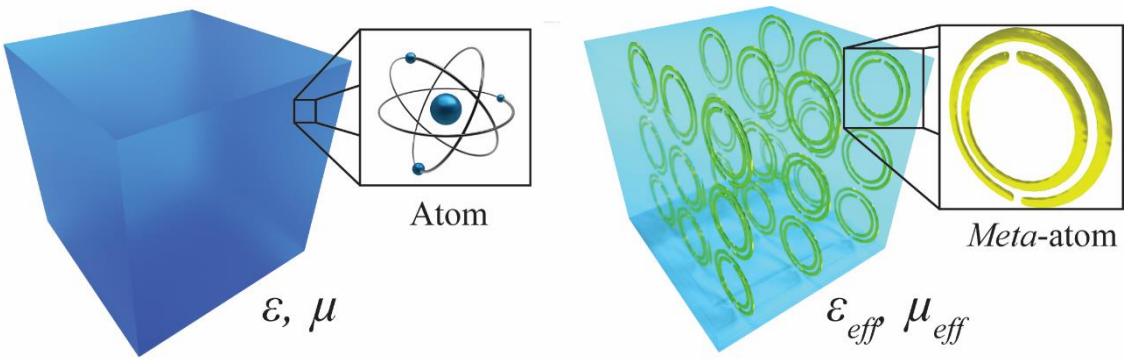

Fig. 1.1. Analogy between the atoms in natural materials and the meta-atoms in metamaterials, which in both cases define the constitutive parameters of the whole structure.

Therefore, the idea behind metamaterials is to exploit the same homogenization principle, which consist in achieving the effective CP by introducing a periodic structure of so-called *meta*-atoms (analogs of natural molecules and atoms) and obtaining the macroscopic response of the metamaterial to EM wave (Fig. 1.1). These artificially engineered subwavelength particles –

[1] Most of media demonstrate a linear response for small (i.e. low intensity) EM fields.

electric and magnetic dipoles, have a specific geometry and are made of natural materials. Since the size of *meta*-atoms is smaller than wavelength, the EM wave sees a continuous medium and its response is defined by the periodic structure of the *meta*-atoms. Therefore, by changing the geometry and arrangement of the *meta*-atoms it is possible to manipulate the effective CP, obtaining, for instance, negative values of permeability [11].

The propagation of the plane wave in the linear homogeneous medium can be described as:

$$\begin{aligned} &\boldsymbol{E}(\boldsymbol{r},t) = \boldsymbol{E}_0 e^{i\boldsymbol{k}\boldsymbol{r}-i\omega t}, \boldsymbol{B}(\boldsymbol{r},t) = \boldsymbol{B}_0 e^{i\boldsymbol{k}\boldsymbol{r}-i\omega t} \\ &\boldsymbol{k} = k\hat{\boldsymbol{k}}, k = \omega\sqrt{\varepsilon\varepsilon_0\mu\mu_0} = n\frac{\omega}{c}, \\ &n = \sqrt{\varepsilon\mu} \end{aligned} \tag{1.3}$$

where $\boldsymbol{E}_0$ and $\boldsymbol{B}_0$ are the constant vectors of the field, ω is the angular frequency, t expresses the temporal dependence, $\boldsymbol{k}$ is the wavevector (whose magnitude is the wavenumber k and unit vector $\hat{\boldsymbol{k}}$), n is the refractive index and c is the speed of light. The energy flux density is described by the Poynting vector:

$$\boldsymbol{S} = \boldsymbol{E} \times \boldsymbol{H} \tag{1.4}$$

For sake of simplicity, here and below we consider the media with low losses, i.e. $\varepsilon'', \mu'' \approx 0$. With this approximation, depending on their EM properties materials can be divided into four different classes [18,19]: a) double positive (DPS) or right-handed media (RHM), b) double negative (DNG) or left-handed media (LHM), c) negative permeability (MNG) media and d) negative permittivity (ENG) media. A general classification of materials is presented in Fig. 1.2, where μ and ε used as y and x axis respectively [19].

***Double-positive media* (DPS)**

In DPS media ε > 0 and μ > 0 and thus the index of refraction is positive, $n > 0$. The electric and magnetic vectors $\boldsymbol{E}$, $\boldsymbol{H}$ and wave vector $\boldsymbol{k}$ in such media form a right-handed triplet, and therefore the Poynting vector and $\boldsymbol{k}$ have the same direction. In this media the energy flows in the same direction as the phase propagation, which is usually called right-handed propagation, named after the triplet that EM vectors form. And the media with right-handed propagation is usually called the right-handed media. Most of the dielectrics available in nature can be grouped in this category.

***Epsilon-negative media* (ENG)**

In ENG media ε < 0 and μ > 0. Therefore, the wave vector is imaginary and the waves are evanescent. A negative permittivity can be found in a plasma medium, metals below their plasma frequency [17]. One of the example of metamaterial with negative permittivity is a wire medium [13], shown in top left inset of Fig. 1.2.

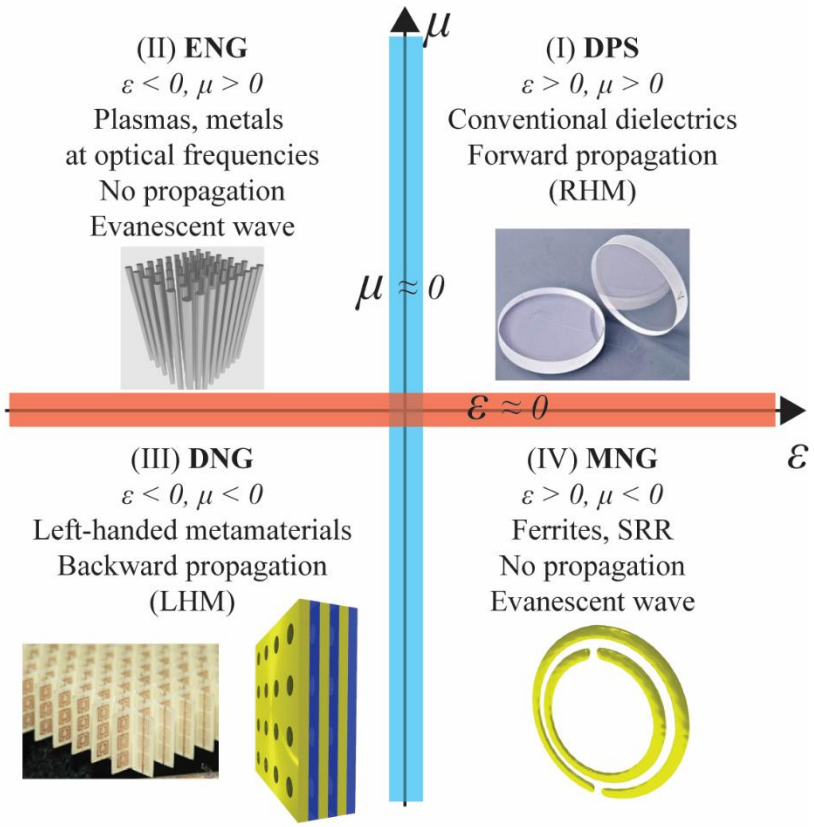

Fig. 1.2. Classification of materials in the ε, μ plane.

Double-Negative Media **(DNG)**

In these media ε < 0 and μ < 0 and ***E***, ***H*** and *k* form a left-handed triplet and ***S*** and *k* point in opposite directions. Therefore, the energy flows in the opposite direction to the phase propagation. These media are also called left-handed media [20], negative-index materials (NIM), backward wave media or negative refractive index media (NRI). They were first proposed in 1968 by Veselago, when he studied theoretically the properties of media with ε < 0 and μ < 0 [20]. He predicted that such media would have negative index of refraction $n = -\sqrt{\varepsilon\mu} < 0$ and multiple reverse effects, such as reverse Snell's law, reverse Cerenkov radiation and reverse Doppler Effect [20]. The reverse Snell's law results in the curious phenomenon of negative refraction, which occurs between a RHM and a LHM and is shown in Fig. 1.3(a). In this figure one can observe that the Snell's law:

$$n_1 \sin(\theta_1) = n_2 \sin(\theta_2) \tag{1.5}$$

is still valid, however the negative refractive index of the medium leads to the reversed refraction angle. Moreover, the wavevector inside the LHM is reversed and antiparallel to the Poynting vector. This fascinating property enables the possibility to build a NIM planar lens, which was later found by Pendry to act as a perfect lens [1], when both ε = μ = −1. In Fig. 1.3(b) is shown an ideal case of the NIM planar lens without losses ($\varepsilon'' = 0, \mu'' = 0$). The term "perfect lens" refers to an ability of NIM planar lens to restore the image with unlimited resolution, which is not

possible with conventional lenses. The explanation of such fascinating performance lies in the fine details of source contained in the evanescent components of wave, which are lost in conventional lenses but amplified in NIM slab. Therefore, in such lens the point source has the point image inside lens and then is restored on the image plane on other side of the slab.

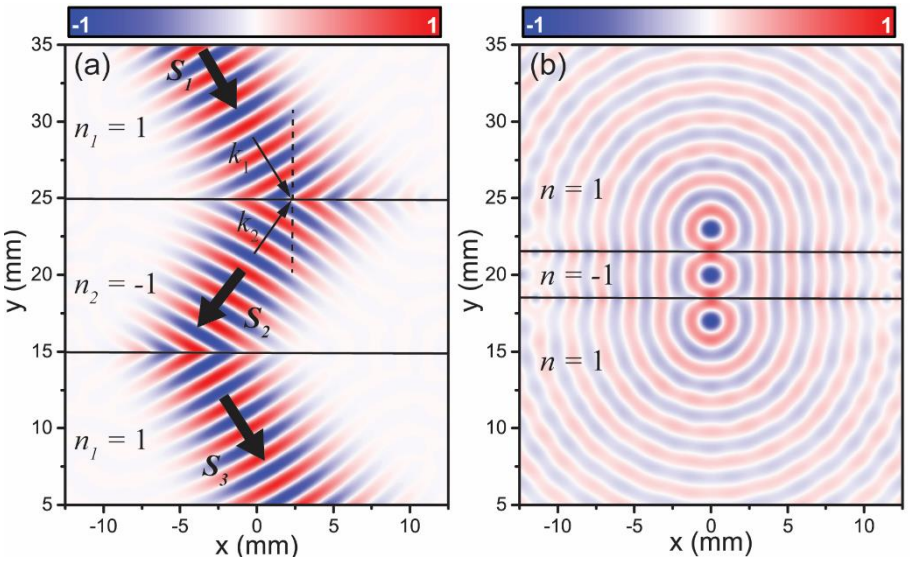

Fig. 1.3. (a) Normalized numerical electric field distribution for the negative refraction at the interface between RHM (n = 1) and LHM ($\varepsilon = \mu = n$ = -1). (b) Normalized numerical electric field distribution for the focusing of line source by the NIM (n = -1) planar lens. Both colormaps were obtained using COMSOL™ at frequency f = 150 GHz.

Despite the interesting properties and appealing potential applications of these media, Veselago's study did not attract much attention since it was considered unrealizable due to the absence of a medium with an effective negative permeability. It took nearly three decades to conceive the idea of a material with the negative permeability, bringing closer the realization of negative index media as proposed by Veselago. It was Pendry, who in 1999 in his pioneering work proposed a nonmagnetic particle with a strong magnetic response [21], opening the Pandora's box of metamaterials. The particle was a split-ring resonator (SRR) and had dimensions smaller than the wavelength, see bottom right inset in Fig. 1.2. Thanks to its strong magnetic response, the particle exhibits a negative effective permeability value, i.e., it can be considered as a negative permeability material (MNG). Based on this work, Smith in 2000 demonstrated a DNG [22], which consisted of SRRs mixed with a wire medium with effective negative electric permittivity achieving simultaneously negative values of permeability and permittivity. Such medium was experimentally demonstrated in 2000 by Smith [23] and used to observe the negative refraction in 2001 by Shelby [24], which gave a great impulse for the investigators of the metamaterials.

As it was mentioned above no natural materials are known to have these characteristics. However, there are several artificial structures, which exhibit a left-handed propagation. Most known and commonly spread are the combination of SRRs embedded in a wire medium [23] and stacked subwavelength hole arrays [25,26], both shown in inset of Fig. 1.2.

***Mu-negative media* (MNG)**

This media has $\varepsilon > 0$ and $\mu < 0$. Analogously to ENG the wave vector k is imaginary and, therefore, fields decay exponentially, forbidding propagation of EM waves. In nature, certain ferrites and some gyrotropic materials can exhibit negative permeability. In the field of metamaterials, the most widely-used elementary particle for $\mu < 0$ is SRR (see inset of Fig. 1.2).

Near zero index media

Another subcategory, which can be made in this classification, includes the metamaterials with permittivity and/or permeability near zero. They are also called near zero-index metamaterials (NZIM) because the index of refraction is, in absolute value, much smaller than unity when $\varepsilon \approx 0$ and/or $\mu \approx 0$. Such media demonstrate exciting properties, for instance, in a NZIM the fields are quasi-static and zero phase variation is seen across the medium. Moreover, a wave radiated from such medium has uniform phase front, which repeats the shape of the output surface [27]. This is illustrated in Fig. 1.4. where the focusing of a plane wave by a NZIM planoconcave lens is shown.

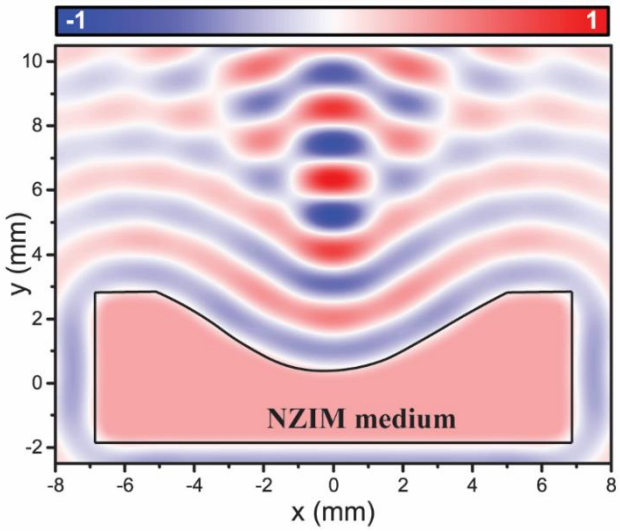

Fig. 1.4. Normalized numerical electric field density for the focusing of plane wave with NZIM ($n \approx 0$) planoconcave lens. The colormap was obtained using COMSOL™ at frequency f = 150 GHz.

In this figure it can be seen that the electric field distribution is uniform inside the NZIM slab. The so-called epsilon-near-zero (ENZ) metamaterials are a particular case of NZIM with only $\varepsilon \approx 0$ and demonstrating a great potentials for lenses, compact resonators and highly directive sources [28–30].

1.2. Extraordinary transmission metamaterials

Metamaterials based on SRR and wires usually suffer from increased losses and magnetic response saturation at higher frequencies and therefore their use is limited. From this point of view, one of the most promising metamaterials with effective negative refractive index (NRI) from microwave to visible range is the extraordinary transmission (ET) metamaterial [25,26,31].

The term *extraordinary transmission* refers to the phenomenon of a high transmittance in one single subwavelength hole array (SHA) [see Fig. 1.5(a)], which is supposed to act as opaque screen [32]. This can be seen in Fig. 1.5(b) where a high peak of transmittance appears in the cut-off region, just before the minimum that corresponds to the Wood-Rayleigh anomaly (at $f_{wr} = c/d$ where c is the speed of light and d is the period of the hole array) [33,34]. The ET phenomenon was reported for the first time by Ebbesen in his seminal work [32]. Since then, numerous experimental works have also been performed, demonstrating the ET from microwaves to the optical range [35–39]. Moreover, a tremendous amount of works has been done in an attempt to reveal the underlying physics of this phenomenon [32,40–45]. Several theories have been proposed, which include the explanations based on surface plasmons [32,46], a model based on waveguides and impedance matching concepts [47,48] and, finally, a model which explains ET by the scattering in each hole and subsequent excitation of surface waves [49]. The latter explanation describes the ET by the scattering of the wave in each hole to multiple diffraction modes, which are coupled to a surface wave and tunneled through the hole.

The stacked subwavelength hole arrays (SSHA), where metallic layers of SHA are alternated with dielectric layers [see Fig. 1.6(a)], is also known as a fishnet metamaterial and provides NRI and considerably low losses at millimeter waves and terahertz range [25,26,31,50,51]. Another interesting feature of the fishnet metamaterial and metamaterials in general is that they allow to control independently the permittivity ε and permeability μ at will and by neglecting the losses can be ideally matched with free space when the normalized characteristic impedance is:

$$\eta = \sqrt{\mu/\varepsilon} = 1 \tag{1.6}$$

Thanks to these properties the fishnet metamaterial has become rapidly one of the most popular metamaterials for designing metallic lenses in microwave and millimeter wave range, demonstrating low losses and NRI behavior [52–54].

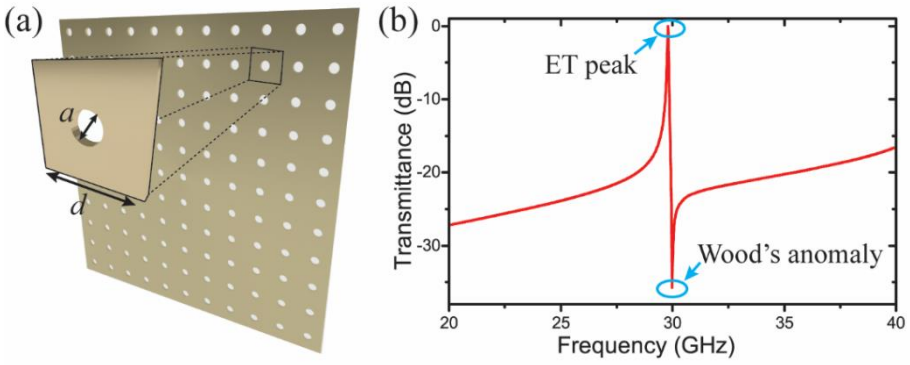

Fig. 1.5. (a) Sketch of the SHA with period d and hole diameter a. (b) Numerical transmission of SHA for period d = 10 mm, hole diameter $a = 0.3d$ and infinitesimal thickness.

For the design and performance analysis it is important to determine the effective EM parameters of the metamaterial. The effective CP of metamaterials, and fishnet metamaterial in particular, are usually retrieved using the scattering parameters [55–57]. However, this method does not provide reliable results since the fishnet metamaterial has usually a unit cell's transversal period comparable to the wavelength and cannot be treated as a truly homogeneous medium [58]. Another technique based on equivalent circuit and transmission line theory has been found more robust and accurate for modelling fishnet structures [26,47,48,59–62]. Moreover, this technique explicitly demonstrates the importance of the separation between the SHAs. As it was demonstrated in [48], for a separation less than half of the transversal periodicity d_y the fishnet metamaterial demonstrates left-handed propagation. This can be seen in Fig. 1.6(b), where the dispersion diagrams for different separations between plates (d_z) are shown. In this figure the curves with negative slope correspond to the propagation with antiparallel phase and group velocities, i.e. *LH* propagation. On the contrary, the dispersion diagrams with a positive slope correspond to the propagation with phase and group velocities parallel to each other, or *RH* propagation. It was shown in [48] that by increasing the separation, the electric coupling between the layers becomes weaker and the structure becomes right-handed. This can be observed in Fig. 1.6(b), where for the separation $> \approx 0.5d$ curves have a positive slope. Another interesting propagation regime can be observed in the transition between the *RH* and *LH* propagation, where the dispersion curve has a zero slope, or zero group velocity, see Fig. 1.6(b). This regime has been theoretically explained by the frozen modes [63] and a practical application has been proposed [64].

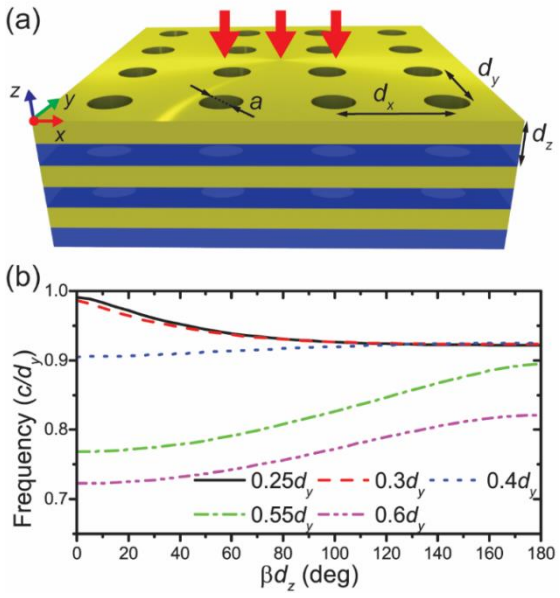

Fig. 1.6. (a) Sketch of the SSHA with periods d_x, d_y, d_z and hole diameter a. (b) Dispersion diagram of SSHA for different longitudinal periods d_z and hole diameter $a = 0.5d_y$.

The ability of the fishnet metamaterial to tune the effective EM response by changing its dimensions became one of the reasons of its wide use in the design of the metamaterial lenses, as well as its ability to provide NRI and NZIM, along with a good impedance matching and low losses. In the chapter II of this thesis, the fishnet metamaterial is extensively used for different designs of metallic metamaterial lenses, exploiting these unique properties to enhance the focusing performance.

1.3. Ultrathin metasurfaces to control the light

In metamaterials, like in the natural dielectrics, the control of the wave is realized by manipulating the amplitude and/or phase, as it propagates through the medium. This principle of accumulating the amplitude or phase change during the wave propagation is used in most optical devices, such as lenses, beam steerers, modulators, waveplates, etc. Moreover, a combination of the ability of metamaterials to tailor at will their CP and principles of the transformation optics[2] (TO) [65–67] results in a powerful tool, which allows to bend the light in unusual ways and achieve exciting effects, for instance, expanding and squeezing light [68], subwavelength focusing and even cloaking [5,69], as it will be discussed in Chapter III. However, in order to accumulate the sufficient change, distances more than a few wavelengths are usually required, resulting in bulky devices. The dimensions can be reduced by using extremely high values of the CP ($n >> 1$), which will allow to gain the required phase change in smaller distances[3]. In the case of conventional dielectrics this technique requires additional layers for impedance matching, since in most cases the device is designed to work in free space and an extremely high permittivity provokes impedance mismatch ($\eta = \sqrt{\mu/\varepsilon} \neq 1$). On other hand, the metamaterials with extreme values of CP can have the impedance matched to free space, however, they usually have higher losses and more complicated fabrication. This makes their use in practical applications almost impossible.

Recently, metasurfaces have shown great potential for achieving full control of the wave front of light with low fabrication cost given that they consist of only a monolayer of planar ultrathin structures and hence they do not require complicated three-dimensional (3D) nanofabrication techniques. As a result, a plenty of applications based on metasurfaces have been proposed and demonstrated, such as wave plates [70], ultrathin metalenses [7], quarter-wave plates [71] and many others. Metasurfaces are able to generate an abrupt interfacial phase change Φ, giving the possibility of controlling the local wave front on the subwavelength scale. By using the Fermat's principle of the least optical path, the generalized laws of reflection and refraction can be derived [72]. Therefore, the revised reflection and Snell's laws can be written respectively as:

[2] Transformation optics originates from two papers [65,66] and is based on twisting the Cartesian mesh by means of coordinate transformation. The invariance of the Maxwell's equations plays an essential role in transformation optics.
[3] The phase change $\Delta\varphi$ can be calculated using the method of Optical path difference: $\Delta\varphi = k_0 n d$, where d is the distance between two points in space.

$$\sin(\theta_r) - \sin(\theta_i) = \frac{\lambda_0}{2\pi n_i}\frac{d\Phi}{dx}$$
$$n_t \sin(\theta_t) - n_t \sin(\theta_t) = \frac{\lambda_0}{2\pi}\frac{d\Phi}{dx} \quad (1.7)$$

where θ_r, θ_i and θ_t, are the angles of reflection, incidence and refraction respectively, λ_0 is the wavelength in free space, n_i and n_t are the refractive indices of the incident and refraction media respectively and $d\Phi/dx$ is the gradient of phase discontinuity along the interface between two media. From these equations it can be seen that by providing a suitable gradient of phase discontinuity along the interface ($d\Phi/dx$) the reflected and refracted beams can have arbitrary directions.

Analogously to the metamaterials, in order to achieve a high efficiency of the metasurface, the separation between *meta*-atoms has to be subwavelength. The role of a particle, which introduces an abrupt phase change between the incident and scattered wave, can be entrusted to a wide range of the optical scatterers/antennas, including nanoparticles, nanocavities and dielectric resonators. Depending on the design, the metasurface can be used in reflection mode as a metamirror [73], or in transmission mode as a metascreen [74]. In the transmission mode the wavefront of the incident wave is manipulated by re-radiating the wave to the output side with the introduced abrupt phase change [72]. In the case of metamirrors, a ground plane is usually required to reflect the incident wave to the opposite direction with phase and amplitude distribution tailored by the metasurface. However, recently another approach has been introduced, which does not require a ground plane [75]. In this approach the proposed metamirror based on Huygens's elements [76,77] can control both reflected and transmitted waves and is practically transparent outside the operational band. This allows more flexible use in a variety of applications, such as optically transparent focusing antennas for satellites, low-profile conformal antennas for telecommunications, and nanoreflectarray antennas for integrated optics.

In this thesis we use a metasurface, which consists of an array of closed ring resonators (CRR) placed on ultrathin ($\lambda_0/23$) Silicon substrate and works in the reflection mode. The unit cell is shown in the inset of Fig. 1.7(a). The control of local phase response is realized by changing the radii of each element, which leads to the change of the phase of the reflected wave in almost 2π range, see Fig. 1.7(a) where as an example the response of the unit cell designed to work at frequency f_0 = 0.8 THz (λ_0 = 375 μm) is shown.

The advantage of such geometry is an insensitivity to the incident polarization, which makes it appealing for the devices where the polarization of the incident wave may not be defined. Moreover, since the proposed structure is non-resonant at operating frequencies it demonstrates low losses as it can be seen in Fig. 1.7(a) (dashed blue curve). By properly rearranging the CRR of the metasurface on the ground plane it is possible to manipulate the direction of the reflected wave. Analogously to reflectarrays, the metasurface can be used for focusing the light at one point, for example at the aperture of a detector [78]. As an example, the design and simulation results of a reflecting metasurface lens are shown in Fig. 1.7. The required lens profile calculated using the ray tracing method [79] is shown in Fig. 1.7(b). Since the chosen unit cell does not cover whole 2π range the real lens profile made of CRRs is slightly different (dashed red line). Anyway,

such deviation does not affect the final performance of the lens, see Fig. 1.7(c-d) where the spatial distributions of normalized electric field and power, respectively, are shown.

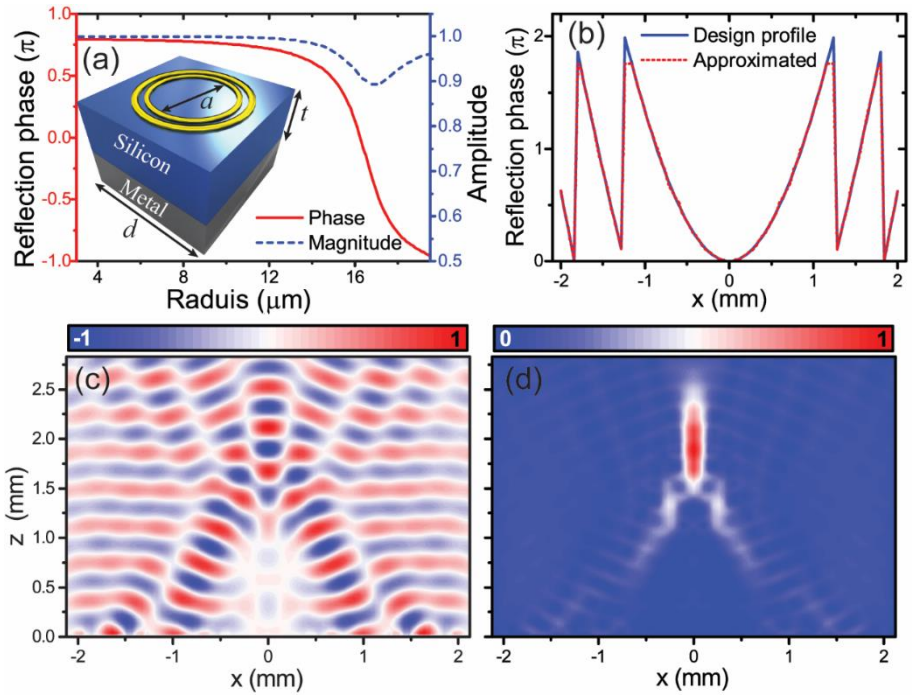

Fig. 1.7. (a) Reflection magnitude and phase response of CRR as a function of ring diameter *a*. In inset a schematic view of the unit cell of CRR. In this example the period d = 40 μm ($\lambda_0/9.4$), thickness of Silicon substrate t = 16.5 μm ($\lambda_0/23$). Rings are separated with gap of 1 μm. (b) Calculated lens profile obtained using ray tracing method and approximated using available unit cell phase responses. Normalized electric field (c) and power (d) distribution of the reflected wave for the metasurface lens. All simulations were performed using the transient solver of the commercial software CST Microwave Studio™.

From this example it can be seen that the metasurface can successfully mold the reflected wave, focusing the wave at desired point. However, the control of the local field amplitude and phase can be used not only to redirect and focus the incident wave. As it will be shown below, this metasurface can also be used to conceal an object on the ground plane, by manipulating the phase distribution on the edges of this cloaked object.

1.4. From metamaterials and metasurfaces to invisibility cloaks

With appearance of the metamaterials a huge leap has been made in the field of electromagnetism since the times when the artificial dielectrics were discovered. The metamaterials with a gradient refractive index [80], which can be adjusted at will by reconfiguring the *meta*-atoms and not always with negative permittivity and permeability, allow a total control of the propagation and can bend a EM wave in any desired direction. However, the biggest breakthrough yet had come after the principles of transformation optics were introduced [65,66] and the subsequent first experimental verification of the metamaterial invisibility cloak in the

microwave range was presented [5]. It was demonstrated then that the metamaterials can play a much bigger role, not only as homogeneous media with left handed propagation. The combination of the transformation optics with metamaterials gave an unprecedented freedom of the wave manipulation, which brought the attention of researchers around the world and resulted in many interesting effects and concepts, including the EM wormholes [81], hidden gateways [82,83], "optical black holes" [84–87], lenses [88–93], field concentrators [94], field rotators [95,96], field shifters [97], bending waveguides [98–100] and other advanced devices [101,102]. A squeezing device [68] is shown in Fig. 1.8(a) as one of the examples of transformation based applications. In this example the incident Gaussian beam with transverse electric (*TE*) polarization is compressed by the squeezer into a narrow beam, which can then be coupled, for instance, to a waveguide aperture.

Nevertheless, despite the vast variety of appealing concepts of TO based metadevices, the invisibility cloak still remains to be the most exciting application. The essence of TO for cloaking devices is to guide the light around a region of space as if nothing is there. This is achieved by compressing the hidden region to a point or a line. As an example, the most studied case of cylindrical cloak is shown in Fig. 1.8(b), where a cylinder is compressed to an out-of-plane line. In such cloak the CP are highly anisotropic and inhomogeneous, and take a very extreme range of values at the inner boundaries (at small radius). Moreover, since EM waves propagate longer paths around the inner volumes, in order to keep the phase, the same as that outside the cloaks, CP smaller than one are necessary to provide phase velocity faster than light speed. Therefore, the high complexity and singularity in CP, make the realization of perfect cloaks almost impossible. As a compromise, reduced models (especially for 2D cloaks) were proposed [69,103], which have pretty good performance and moderate constitutive parameters achievable with metamaterials. This is discussed in more detail in Chapter III.

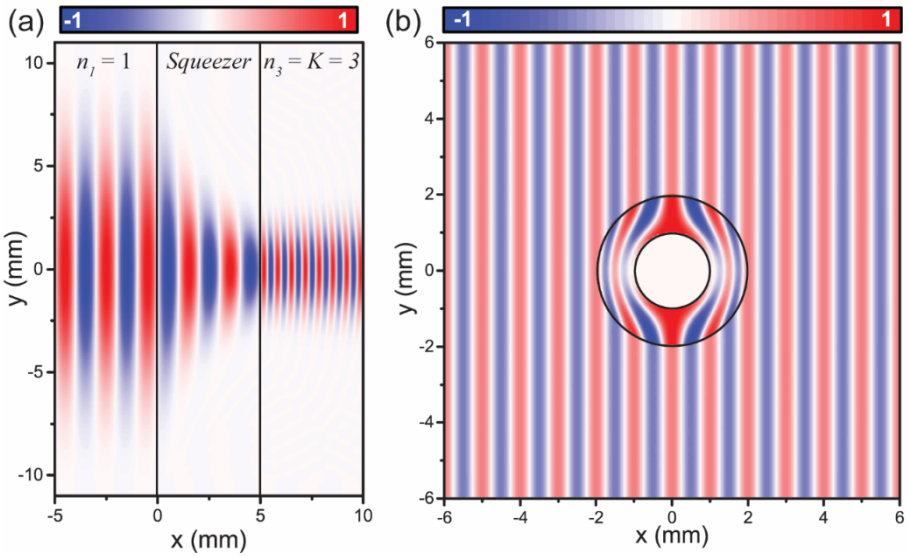

Fig. 1.8. Metamaterial devices based on transformation optics. (a) Normalized electric field distribution in the squeezer obtained at f = 150 GHz. The squeezing ratio is fixed to K = 3 and non-magnetic (μ = 1) media are used. The refractive index of medium at the output is n_3 = 3. (b) Normalized electric field distribution for a cylindrical cloak operating at f = 300 GHz.

Since the reduced models of the cloaks try to exclude the use of extreme values of CP, they usually have a bulky design, where the ratio of cloak to the cloaked object area is big [104,105]. And despite the simpler design, they are still complex for a practical realization. Thus they remain mostly as interesting concepts and are far away from use in real applications.

The alternative cloaking technique based on scattering cancellation [106–108] has a much simpler design, better performance and, in the case of mantle cloaking with metasurface [109], an ultrathin cloaking layer. However, the size of the hidden objects is limited to be smaller than a wavelength [110], and an attempt to extend the concealed region results in more complex design with several layers.

Recently, another approach based on ultrathin metasurface has been proposed [111–113]. These metasurface cloaks are ultrathin (usually $<< \lambda$) and less complicated in the fabrication, since they have only one layer of subwavelength particles. This is discussed in detail in the Chapter III, where an ultrathin metasurface based on CRR is used to conceal a triangular object on a ground plane.

1.5. Graphene based tunable metamaterials

Another metamaterial, which recently has gained the attention of the scientific community, is the multilayer graphene-dielectric metamaterial [114,115]. Such interest is provoked by the unconventional electronic and optical properties of its key ingredient – graphene, which is an ultrathin ($\approx$ 30 nm) monolayer of carbon atoms densely packed into a honey-comb lattice, see Fig. 1.9.

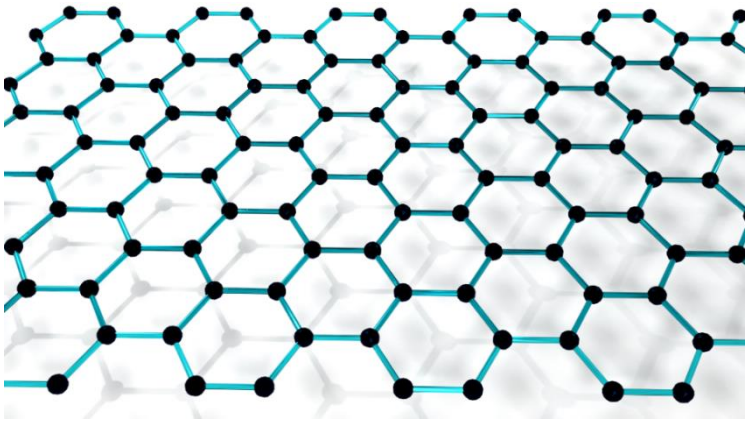

Fig. 1.9. Illustration of graphene layer.

Graphene was first isolated by Andre Geim and Konstantin Novoselov in 2004, what led them to be awarded with the Nobel Prize in Physics in 2010. Since 2004, there has been an explosion of interest in this unconventional material, resulting in fast growing number of published articles each year. The most intriguing properties of graphene, which make it an excellent choice for many applications at mid-infrared range are the tunability of the surface

conductivity and low losses. Moreover, with a recent rapid growth of the fabrication capabilities [116,117] the practical realization of graphene based devices now is more feasible, promising ultra-compact and low cost applications, such as ultrafast modulators and beam steering devices [118], polarizers, lenses [119], photo-detectors [120], integrated optoelectronic elements [121,122] and even cloaking devices [123].

The ultrathin geometry, low losses and, most importantly, tunability make the graphene also a very promising material for plasmonic applications [124]. Recently it was theoretically [125] and later experimentally [126,127] demonstrated, that the graphene layer supports the propagation of surface plasmons polariton (SPP) or graphene surface plasmon (GSP). The propagation of GSPs on graphene surface is shown in Fig. 1.10, where GSPs are excited by means of a horizontal electric dipole.

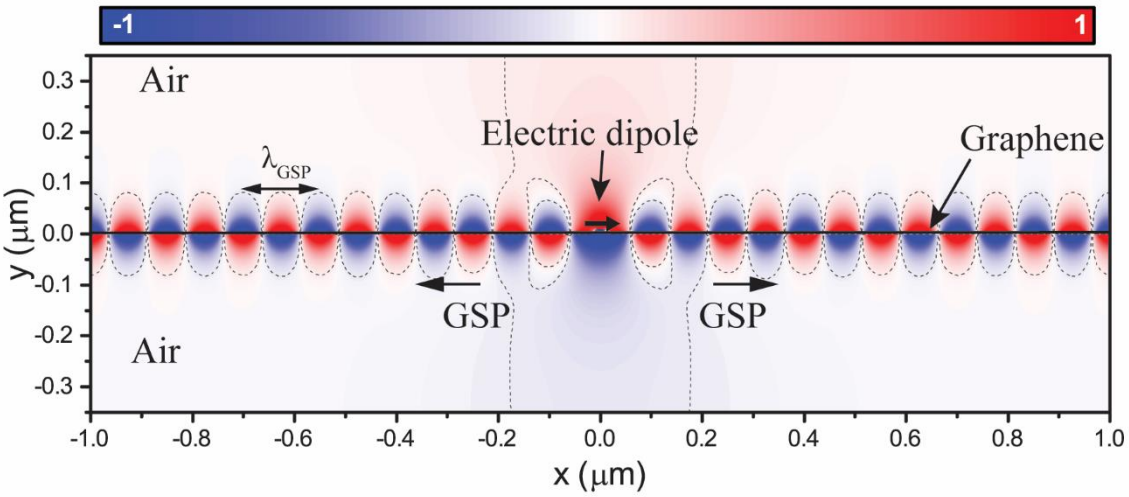

Fig. 1.10. Normalized numerical magnetic field H_z of a surface plasmon polariton propagating on a graphene layer. A horizontal electric point dipole, placed at a distance 10 nm from a graphene, is used to excite GSPs. In this example, the graphene layer has a conductivity of $\sigma_g = 5\times10^{-7} + 8\times10^{-5}$ S, which corresponds to chemical potential $\mu_c = 150$ meV, temperature $T = 3$ K and scattering rate $\gamma = 10^{12}$ s^{-1} at frequency $f = 30$ THz. The simulation was performed using COMSOL™.

Depending on the level of chemical potential μ_c, the imaginary part of graphene's conductivity σ_g can attain a different sign, defining the inductive [$\mathrm{Im}(\sigma_g) > 0$] or capacitive [$\mathrm{Im}(\sigma_g) < 0$] electromagnetic character. From point of view of plasmonic applications the inductive character is more interesting, since it supports the transversal magnetic (TM) mode, where the electromagnetic field is highly confined to the graphene layer. Using an approach of the graphene's equivalent permittivity [128] and the standard dispersion equation of electromagnetic guided mode [129] we can obtain the dispersion equation of TM GSP:

$$\beta_{spp} = \omega\sqrt{\mu_0\epsilon_0}\sqrt{1-\left(\frac{2}{\sqrt{\mu_0\varepsilon_0}\sigma_g}\right)^2} \tag{1.8}$$

where, ω is the angle frequency and β_{spp} is the wave number of SPP. From this equation the wave number of SPP is much bigger than the one of free space, which means that the guided wavelength is much smaller than in free space ($\lambda_{spp} << \lambda$). This allows more compact designs of plasmonic devices, however it complicates the excitation of GSP.

The ability of the controlling dynamically the local conductivity of graphene (as well as low losses) is the biggest advantage over the noble metals and allows to apply the principles of TO, resulting in very powerful tool for designing the one-atom-thick devices, such as beam splitters, lenses, optical waveguides [128] etc. In Fig. 1.11 are shown the examples of such optical transformation devices: a) a graphene waveguide with excited symmetrical mode and b) the graphene-based Luneberg lens.

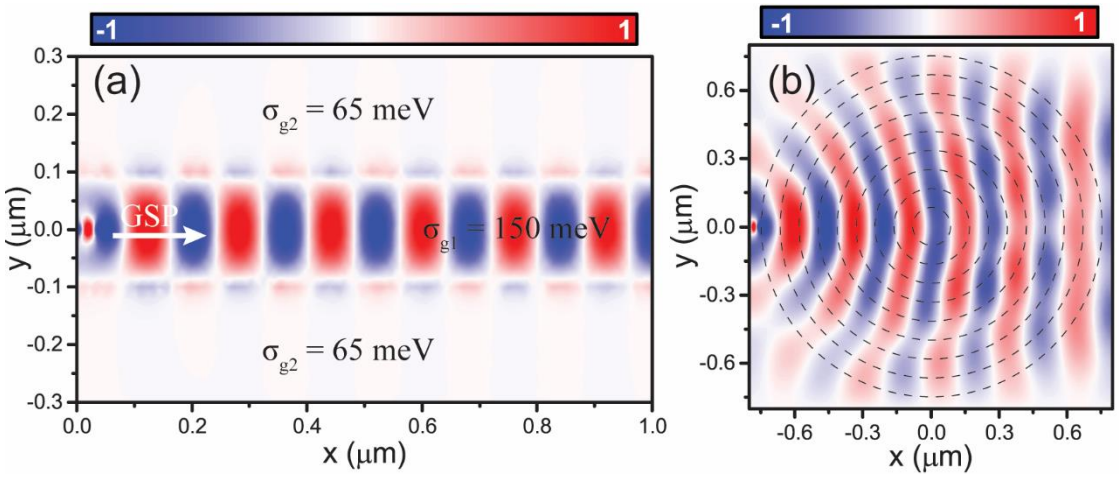

Fig. 1.11. (a) Normalized numerical magnetic field H_y of GSP symmetrical mode propagating in a graphene waveguide. A horizontal electric point dipole, placed at a distance 10 nm from a graphene, is used to excite GSPs. In this example, the graphene layer has two different conductivities $\sigma_{g1} = 5\times10^{-7} + 8\times10^{-5}$ S (150 meV) and $\sigma_{g2} = 2.15\times10^{-7} - 2.9\times10^{-5}$ S (65 meV), at temperature $T = 30$ K, scattering rate $\gamma = 10^{12}$ s^{-1}. (b) One-atom-thick Luneburg lens: normalized numerical electric field E_x of the SPP along the graphene (each zone has a width of 75 nm). All simulations were performed using CST Microwave Studio™ at frequency f = 30 THz.

In first example, the guided SPP wave is confined in the region with $\text{Im}(\sigma_g) > 0$, placed between two regions with $\text{Im}(\sigma_g) < 0$. The principal difference of such waveguide from a nanoribbon graphene waveguide is the lack of need to cut the graphene into small nanoribbons. The required distribution of chemical potential, which provides such distribution of the conductivity, can be created with a special configuration of bias voltage arrangement. In the second example, the SPP generated from a "point-like" source is transformed into an approximately one-atom-thick "collimated beam" of SPP on the graphene. The one-atom-thick

upna Universidad Pública de Navarra Nafarroako Unibertsitate Publikoa

Luneberg lens consists of effective SPP-graded index, which are also created using the special bias configuration [128].

However, in this thesis we focus on the use of the graphene to build an effective tunable medium, where the layers of graphene alternated with layers of dielectric yield a multilayer graphene-dielectric metamaterial [115,130–133]. The graphene's conductivity, modelling of graphene-dielectric metamaterial and its properties are discussed in detail in Chapter IV. Here we just want to emphasize the interesting possible applications of the graphene-based metamaterial. The effective permittivity ε_{eff} of such medium can be manipulated by changing the surface conductivity of the graphene [134,135]. The ε_{eff} can be seen only by the components of the electric field parallel to the graphene layers, whereas the perpendicular component of electric field can only see the permittivity of the host medium. Therefore the resulting effective permittivity of this metamaterial is anisotropic [115,136]. Moreover, with an appropriate combination of the design parameters some components of the effective permittivity can become negative. Metamaterials with such anisotropic dispersion are also termed as hyperbolic metamaterials. They demonstrate peculiar phenomena not only inside the medium, but also at the interface with conventional dielectrics, for instance a negative refraction of energy [137]. These phenomena enable a wide variety of compelling applications, such as super-resolution focusing (hyperlenses) [138], nanolithography [139], spontaneous emission engineering [140] to name a few. The recent experimental demonstration of the use of graphene in hyperbolic metamaterial [133] brought us a step closer to the tunability and lower losses of metamaterials, overcoming the limitations of other hyperbolic structures. However, despite all promising applications of the graphene based hyperbolic metamaterial, this is out of scope of present work and here we only discuss the graphene-dielectric metamaterial with all positive components of permittivity tensor. Using such metamaterial, we design and numerically analyze three designs for tunable beam steering.

1.6. Outline

The purpose of this thesis is to provide a systematic overview of the research work on metamaterials and their applications performed during the study under the doctorate program "Communication Technology" from Universidad Pública de Navarra (UPNA), for the degree of Doctor of Philosophy (PhD) in Telecommunications Engineering. The present thesis consists of three main parts. In the first part, the design, fabrication and experimental analysis of fishnet metamaterial lenses, as well numerical and analytical studies, are discussed. In the second part, the author's research works on invisibility cloaks are described in detail. Finally, in the third part the schemes of a tunable beam control based on the graphene metamaterials are introduced.

In Chapter II, the basic aspects and the parameters of the design of the metallic lenses based on the fishnet metamaterial are presented. The use of a zoning technique for slimming the metallic lenses is discussed. Furthermore, the general optimization procedure of the zoning technique followed in the design of a broadband zoned fishnet metalens is depicted. The second part of this chapter is devoted to the Fresnel zones theory and possibility of its combination with the fishnet metamaterial in order to improve focusing and radiation performance.

In Chapter III, a background on the invisibility cloaks is provided and the main cloaking techniques are discussed. The design, numerical and experimental results of the fabricated metasurface based carpet cloak are presented. Moreover, the limitations of the transformation optics for the diffusive light are discussed. The simplified unidirectional cloak for diffusive light is presented. Finally, the possible methods of the practical realization are shown.

In Chapter IV, the multilayer graphene-dielectric metamaterial is introduced and their properties are characterized. Three different solutions for ultrafast beam steering based on the graphene metamaterial are demonstrated and the numerical analysis of their performance is presented. Furthermore, the advantages and limitations of each design are discussed.

Finally, the conclusions of the thesis and future work in this field are given in chapter V. The theoretical principles used (Fermat´s principle) in the characterization of the metalenses' performance can be found in Appendix A. The materials and methods used in the design and simulation as well as the equipment used for experimental verification of the performance of the fabricated devices, are given in Appendix B. At the end of the thesis, a summary of the author's merits can be found in Appendix C.

Chapter 2. Metamaterial Lenses

Lenses are devices intended to focus the light in a single or various spots and have been employed all along the electromagnetic spectrum, from microwaves to optics. This chapter is dedicated to study three different types of lenses based on the fishnet metamaterial. The first device is a broadband zoned fishnet metamaterial lens (metalens) designed using a combination of the time-honored zoning technique and a best fitting procedure. This combination allows one to reduce the profile of a fishnet metamaterial lens maintaining at the same time a relatively broadband regime. The second part of this chapter is dedicated to a Soret fishnet metalens, which is designed using the principles of Fresnel zones and corresponds to the family of Fresnel zone plates (FZPs). It is shown that by combining the FZP with a fishnet metamaterial the reflection losses can be reduced and therefore the overall performance improved. Finally, the third lens – the Wood zone plate (WZP) fishnet metalens, which is an improved Fresnel zone plate lens (FZPL) based on the phase correcting technique, exploits the ability of the fishnet metamaterial to tailor the index refraction, with the aim to slim the metalens and improve the efficiency of the FZPL.

2.1. Background on metallic metamaterial lenses

The history of the metallic lenses starts in 1940's when Kock in his pioneering work demonstrated the use of artificial dielectrics for lens antenna applications [16]. The metallic lens devised by Kock consisted of an array of parallel metallic plates and was designed to work in two different regimes: with the electric field parallel (TE lens) and perpendicular to the plates (TEM lens). In the TEM lens the phase front shaping was achieved by creating different physical lengths, while in the TE lens, alike the metamaterial lenses, the difference in the optical path was achieved by manipulating the phase velocity of the propagating wave. This is equivalent to tuning the effective refractive index n_{lens} of the propagating TE_{10} mode, which is smaller than unity inside the parallel plates:

$$n_{lens} = \sqrt{1-\left(\lambda/2d\right)^2} \tag{2.1}$$

where λ is the free-space wavelength and d the distance between the plates. The most interesting feature of this type of metallic lenses is that they have a refractive index smaller than unity ($n_{lens} < 1$) and hence their profile is inverse to conventional dielectric lenses, where $n_{lens} > 1$. This can be easily demonstrated using the Fermat's principle, as it will be shown below. For instance, the convex profile used in common dielectric lenses changes to a concave profile in metallic lenses and vice versa. This profile inversion is also true for the metamaterial lenses with NRI ($n_{lens} < 0$). Since artificial dielectrics manipulate only the effective permittivity of the medium keeping the effective permeability constant and equal to free-space (μ = 1), according to (1.6) for all permittivities not equal to unity the metallic lens suffers from impedance mismatch, and when the permittivity approaches zero the mismatch becomes stronger ($\sqrt{\mu/\varepsilon} \to \infty$). On other hand, a

refractive index close to unity would result in lower reflection losses, but it would require a thicker lens in order to accumulate the sufficient phase difference inside the lens. As result, there is a trade-off between the thickness and reflection losses. This limitation can be surpassed by metamaterial lenses, where the effective medium can be matched to free-space (by tuning CP to get $\sqrt{\mu/\varepsilon}=1$) providing simultaneously the required refractive index.

As it was mentioned in Chapter I, among all practical realizations of metamaterials, the fishnet metamaterial, i.e., stacked subwavelength hole arrays, has become the strongest candidate for frequencies beyond microwaves because of its lower losses compared to other metamaterial structures and its frequency-robust magnetic response [141]. These advantageous properties of the fishnet metamaterial called the attention of the research community and, as result, multiple designs based on the fishnet metamaterial were proposed, including all metallic plano- and bi-concave fishnet lenses, operating at millimeter-wave range [52,53,142,143]. In 2008 Beruete *et al.* experimentally measured for the first time a planoconcave fishnet metalens at millimeter wave range [52] [see Fig. 2.1(a)], demonstrating a good performance and great potential at millimeter-waves and terahertz frequencies. After that, other designs also based on fishnet metamaterial were experimentally demonstrated the, such as bi-concave lens shown in Fig. 2.1(b).

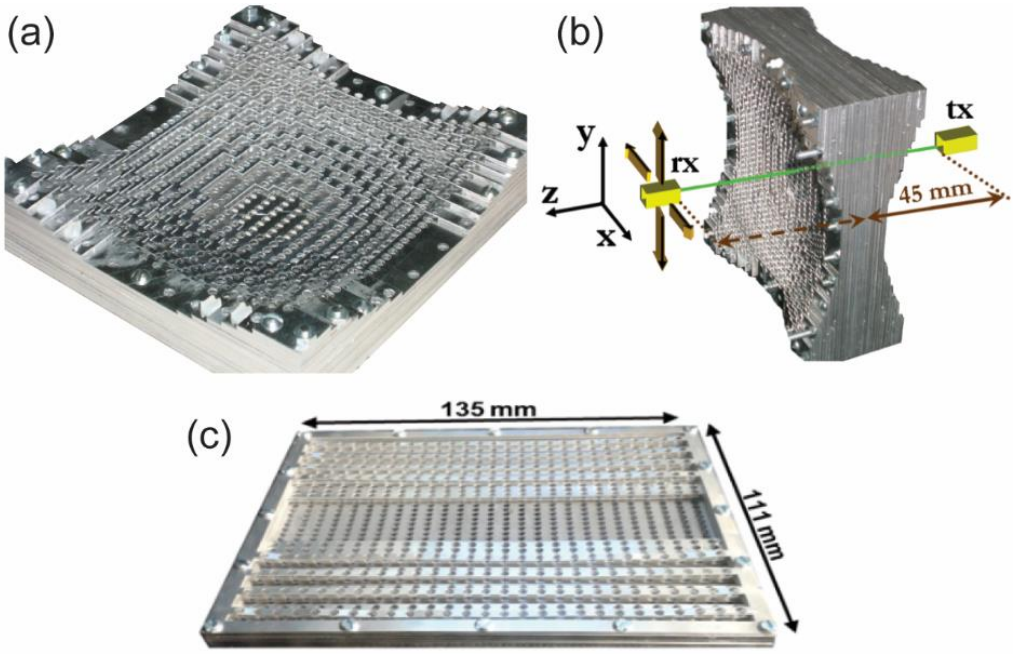

Fig. 2.1. Picture of the real prototype of (a) planoconcave, (b) bi-concave and (c) zoned fishnet metamaterial lenses designed to work at millimeter waves.

The low-loss and enhanced impedance matching properties inherited from the fishnet metamaterial made these metalenses good candidates for imaging and antenna applications. However, they were still relatively voluminous and heavy for practical implementations. In the next stage, in order to overcome these drawbacks, the time-honored zoning technique was applied, so that redundant material was removed [16,79,144]. Alike zoned metallic [16] and optical

dielectric lenses, also known as Fresnel lenses [79,145], this modification results in the fishnet metalens shown in Fig. 2.1(c), with low thickness and, therefore, reduced weight and absorption losses [54,146]. The outcome is then a diffractive optical element akin to Fresnel zoned metallic plate lenses [79,145] but with an enhanced impedance matching.

2.2. Broadband zoned fishnet metamaterial lens

The application of the zoning technique can provide a compact low-weight design of the zoned fishnet metalens, which, however, comes at the price of a narrow bandwidth. Due to the nature of the fishnet metamaterial, the operating frequency range is already narrow and the application of the zoning technique further reduces the bandwidth of the zoned lens. We propose to deal with this limitation by exploiting the high dispersion of the fishnet metamaterial to optimize the lens profile for a broadband performance. The optimization procedure consists of finding the optimal zoned lens profile, which provides a high focusing efficiency at two separate frequencies. Moreover, the fishnet metamaterial's finite size period is also taken into account in the design procedure.

2.2.1. Design and fabrication

Fishnet metamaterial

The unit cell of the fishnet metamaterial used for the lens has the following dimensions: d_x = 2.5 mm, d_y = 5 mm, d_z = 1.5 mm and thickness of the metallic plate w = 0.5 mm (see inset of Fig. 2.2). The index of refraction n_z for an infinite number of plates (i.e. the bulk refractive index) is calculated using the Eigenmode solver of the commercial software CST Microwave Studio™, applying periodic boundary conditions in all planes. In this analysis the metal is modeled as a perfect electric conductor (PEC).

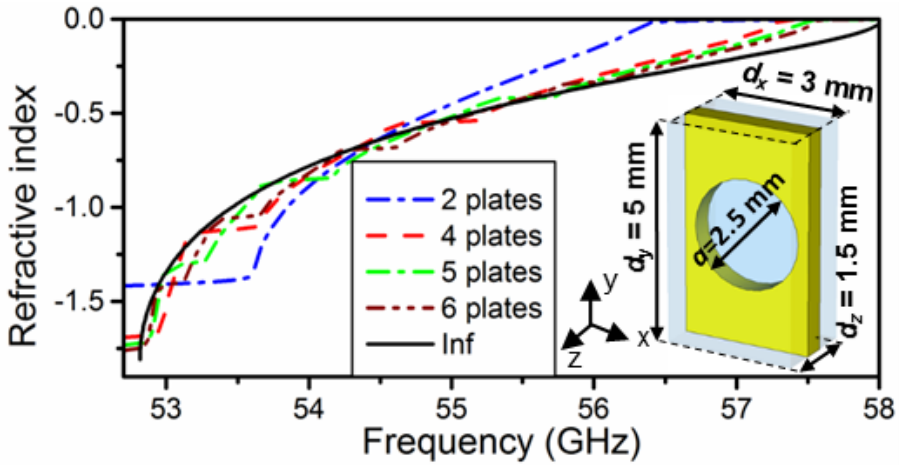

Fig. 2.2. Effective refractive index, n_z, for a fishnet metamaterial made of 2 (blue dashed-dot curve), 4 (red dashed curve), 5 (green dashed-dot curve), 6 (brown dashed-dot-dot curve) and an infinite number of plates (black solid curve). Fishnet metamaterial unit cell with dimensions (Inset).

As shown in Fig. 2.2 (black curve) the bulk refractive index is negative between 53 and 58 GHz and strongly dispersive. In addition, the effective refractive index of structures with a finite number of plates can be obtained from the *S*-parameters using a standard retrieval method [56]. These curves are obtained using the frequency domain solver of CST Microwave Studio™, with unit cell boundary conditions and modelling the metal as aluminum (σ_{Al} = 3.56×10^7 S/m). The effective refractive index for several plates is shown in Fig. 2.2. Since the fishnet metamaterial with only a few plates cannot be treated as a homogeneous medium, the effective index deviates from the infinite structure calculation. This can be clearly observed in Fig. 2.2, where the effective index for two plates (dash-dot blue curve) does not converge to the calculated bulk index. Obviously, as the number of plates increases the disagreement reduces rapidly. Hereby, it can be concluded that a relatively large number of plates is preferable to minimize the deviations of the effective refractive index with the number of stacked plates. However, this would result in undesirable increased thickness and losses. From previous experience (also it can be seen in Fig. 2.2) beyond four stacked plates (dashed red line) there is a good convergence with the bulk index, especially within the range 54-56 GHz. So an initial stack of 4 plates is a good trade-off [52–54,142,147] to maintain both thickness and losses low while the effective refractive index is not significantly altered with the addition of some additional stacked plates to reach the zoned profile.

Design procedure

Before applying the zoning technique, we first describe the profile of a non-zoned lens (Fig. 2.3), which follows an analytical curve, derived from the Fermat's principle [147]:

$$\sqrt{(FL-a)^2+b^2}\cdot n_0 + a\cdot n_{lens} = FL\cdot n_0 \tag{2.2}$$

where *FL* is the focal length, n_0 is refractive index of free-space and n_{lens} is the index of refraction of the lens medium.

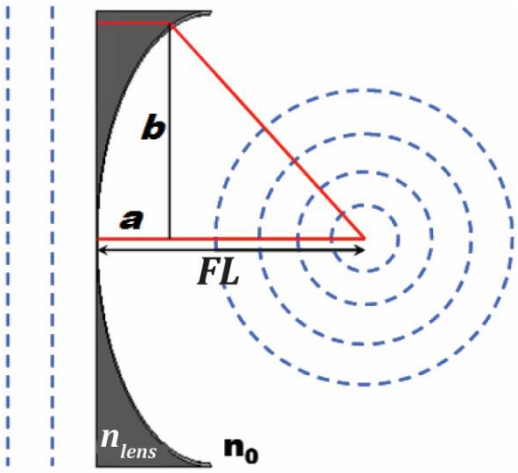

Fig. 2.3. Illustration of Fermat's principle for a non-zoned lens profile [147].

From this equation it can be noticed that the profile of the lens takes different forms, depending on the value of n_{lens}. As it was mentioned in the Section 2.1, for the values of $n_{lens} < 1$ the resulting profile of the lens is concave instead of the usual convex profile of traditional dielectric lenses. Particularizing to negative index values, it is easily demonstrated that for $n_{lens} < -1$ the lens profile is a hyperbola, for $n_{lens} = -1$ is a parabola and for $-1 < n_{lens} < 0$ it takes the form of an ellipse. In our case, the effective index of the fishnet metamaterial lays between −1 and 0, and thus the profile of the non-zoned lens must be an ellipse.

In the next step, in order to find the smooth zoned lens profile, we apply the well-known zoning technique, which implies the removal of material each time a 2π phase shift is reached. The thickness of this layer t can be calculated as [16]:

$$t = \frac{\lambda_0}{1 - n_{lens}}, \tag{2.3}$$

where λ_0 is the free-space wavelength and n_{lens} is the index of refraction of the medium. By combining (2.3) with (2.2), the design equation is as follows [54]:

$$\left(1 - n_{lens}^2\right)(z + mt)^2 - 2(FL + mt)(1 - n_{lens})(z + mt) + x^2 = 0, \tag{2.4}$$

where n_{lens} is the effective refractive index of the structure, FL is the focal length, and m is an integer (m = 0, 1, 2, 3, …) that represents the successive steps for the zoned lens profile. These steps and thickness limits for two demonstrative frequencies f_1 = 54 GHz and f_2 = 55.5 GHz are shown in Fig. 2.4. It is obvious that equation (2.3) contains two frequency-dependent components: the thickness of the zoned lens t and, since the fishnet metamaterial is highly dispersive, the refractive index n_{lens}.

The simultaneous dependence of the design equation on two parameters (frequency and focal length FL) makes it possible to find profiles for two different frequencies whose curves coincide, by simply selecting the appropriate focal lengths. As a result, we obtain one zoned lens profile for two different frequencies and focal lengths, as is demonstrated in Fig. 2.4 (solid black line).

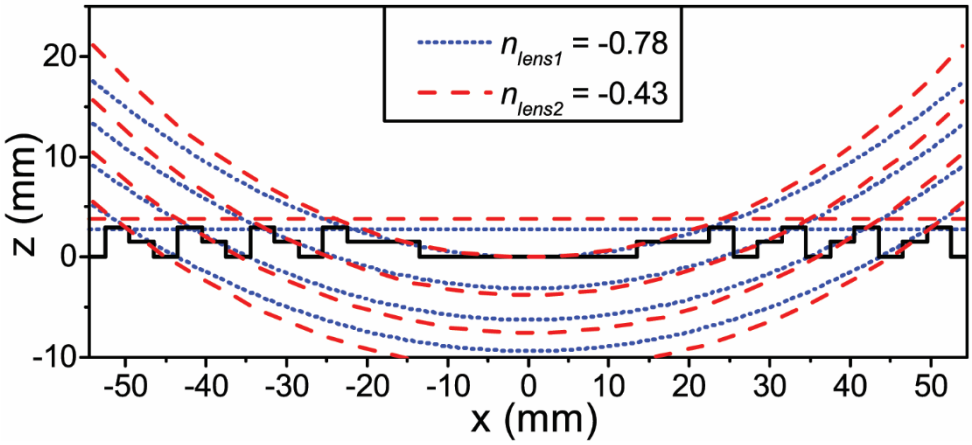

Fig. 2.4. Lens profiles and curves of the successive steps for: n_{lens1} = -0.78 (dotted blue curve) and for n_{lens2} = -0.43 (dashed pink curve) along with the values of the thickness limits, t_1 and t_2 (blue and pink horizontal curves, respectively).

Due to the discretization imposed by periods of the fishnet metamaterial d_x and d_z, the zoned yet smooth profile must be approximated by a staircase profile (see Fig. 2.4). As a criterion of good fitting we use the root-mean-square-error (RMSE) between the smooth profile and the staircase approximation:

$$RMSE(f, FL) = \sqrt{\frac{1}{N}\sum_{i=1}^{N}\left[z_c(f, FL, x_i) - z_a(d_z, x_i)\right]^2} \tag{2.5}$$

where N is the number of fishnet metamaterial periods along the x-axis, z_c and z_a are the coordinates along z-axis of non-zoned and zoned profile respectively. In order to obtain the optimal lens profile, which provides the broadband performance, a best fitting procedure to minimize the *RMSE* is done for the whole operation band. Notice that the effective refractive index of an infinite fishnet metamaterial is used for this analysis (black curve in Fig. 2.2). Due to the intrinsic dispersion of the fishnet structure, each frequency has only a unique optimal profile. So, for broadband operation a trade-off solution must be found. Therefore, as a result of this engineering procedure – combination of zoning technique and dispersion – the optimal zoned lens profile is obtained, see Fig. 2.4 (solid black curve). Notice that since there are many combinations of frequency and focal lengths it is possible to find several zoned lens profiles, whose *RMSE* is low.

The resulting *RMSE* for our optimal profile is plotted in Fig. 2.5(a) as a function of frequency/effective bulk refractive index and focal length. From Fig. 2.5(a) it can be seen that the RMSE has low values for the whole spectral window of interest demonstrating broadband regime. It should be noticed that the resulting lens profile is completely different from that used in previous works [54,146], where it was obtained by applying the zoning technique only for a single frequency, without applying best fitting procedure. As a result, the *RMSE* for a single frequency (f = 56.7 GHz) lens [see Fig. 2.5(b)] has low values for a narrower band.

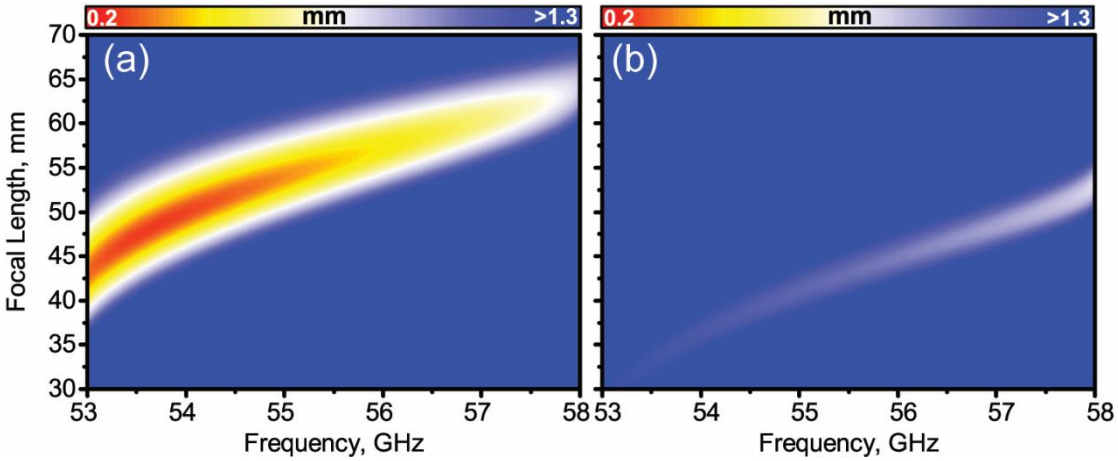

Fig. 2.5. Color maps of RMSE of the zoned lens profile as a function of frequency and focal length for (a) broadband zoned fishnet metamaterial lens and (b) single band zoned fishnet metamaterial lens.

From Fig. 2.5(a) it can be seen that the relative minimum of the *RMSE* follows a parabolic-like trend starting from *FL* = 41 mm at 53 GHz and reaching the top end of the color map *FL* = 65 mm around 58 GHz. This trend is a direct consequence of the strong dispersion of the fishnet metamaterial (see Fig. 2.2) that causes chromatic aberration for the fishnet lens [52,142,147]. According to Fig. 2.5(a), the absolute minimum *RMSE* is obtained for f = 53.5 GHz and *FL* = 45 mm. However, from Fig. 2.2 we know that the convergence of the effective bulk refractive index for infinite and finite numbers of plates is poor at that frequency. Therefore, poor performance at this frequency is expected. Observing Fig. 2.2, it is noticed that the best convergence happens in the interval 54-56 GHz. For this reason, for illustrative purposes we choose the frequencies at approximately both ends: f_1 = 54 GHz and f_2 = 55.5 GHz. At these frequencies, the effective bulk refractive index is n_{lens1} = -0.78 and n_{lens2} = -0.43, respectively.

At f_1 = 54 GHz and focal length FL_1 = 48.7 mm (8.8λ_1) the $RMSE_1$ = 0.22 mm. Such error can lead to a shift of the focus δFL_1 = –0.7 mm (0.23λ_1 ≈ 2%) because of the staircase approximation imposed by the fishnet metamaterial. This shift δFL is estimated by substituting in (2.4) the new focal length $FL_e = FL + \delta FL$ and profile height $z + \Delta z$, which lays within the margin of *RMSE* ($|\Delta z| \leq RMSE$). By solving the resulting equation, we obtain the estimated δFL. At the second frequency f_2 = 55.5 GHz and focal length FL_2 = 55 mm (10.2λ_2) the $RMSE_2$ = 0.44 mm and may result in a slightly larger focus shift δFL_2 = –2.3 mm (0.4λ_2 ≈ 4%). The curves defined by (2.4) for four successive steps (m = 0, 1, 2, 3) at the two considered frequencies are shown in Fig. 2.4: f_1, dotted blue lines; f_2, dashed pink lines. Also, the maximum thickness [16,54,146] for each frequency, t_1 = 2.8 mm (0.5λ_1 ≈ 2 d_z) and t_2 = 3.8 mm (0.7λ_2), are represented by horizontal dashed blue and pink lines, respectively.

From (2.3) the thickness limits are t_1 = 3.12 mm and t_2 = 3.78 mm. Taking into account that the fishnet longitudinal period is d_z = 1.5 mm, this means that the zoned profile can be built with one or two plates, i.e. contain three levels, see Fig. 2.4. And since four plates are the minimum for the central part (due to inhomogeneity of fishnet metamaterial), the total thickness of the lens results in $5d_z+w$ = 8 mm (1.4λ_1). Along x and y directions the structure consists of 37 d_x and 27 d_y periods, respectively. Therefore, the final design has total dimensions of 111 mm × 135 mm × 8 mm (19.8λ_1 × 24.1λ_1 × 1.4λ_1) without the frame used to facilitate the assembly. The fabricated zoned fishnet metamaterial lens is shown in Fig. 2.6.

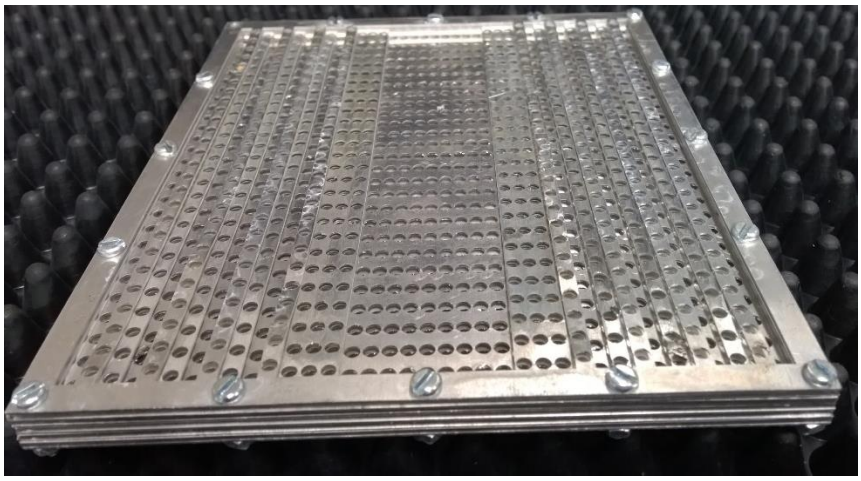

Fig. 2.6. Photograph of the fabricated broadband zoned fishnet metamaterial lens.

2.2.2. Analytical and Simulation Results

First, using the Huygens-Fresnel method described in Appendix A, the analytical power distribution is calculated as a function of frequency and position along the optical axis of the lens [Fig. 2.7(a)].

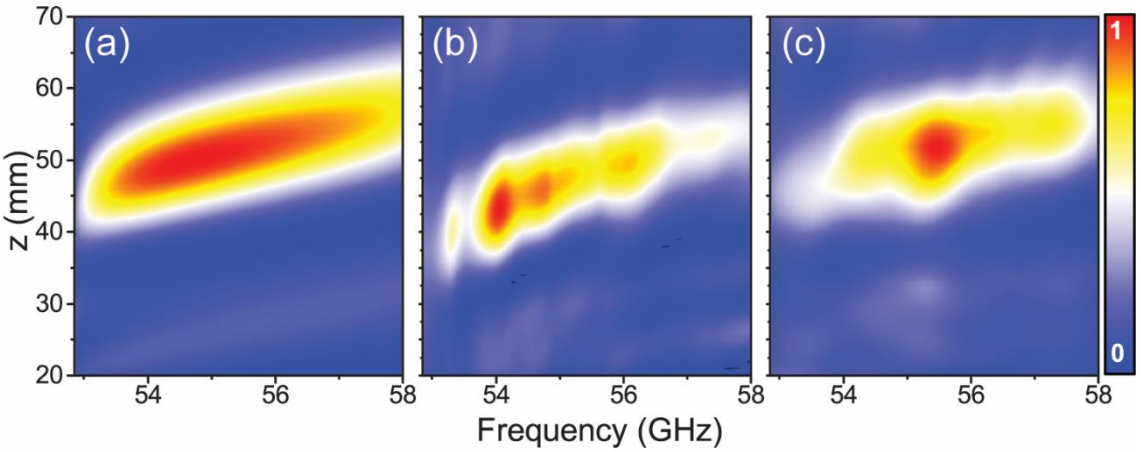

Fig. 2.7. Normalized to local maximum power distribution along *z* axis for the frequency range 52–58 GHz: (a) analytical, (b) simulation and (c) experimental results.

A broadband operation is observed, with a band extending from 53.5 GHz (*FL* = 45 mm) to 58 GHz (*FL* = 56 mm) with the absolute maximum power located between 54 and 56 GHz, in good agreement with the RMSE calculation. In Fig. 2.7(a) one can notice that, alike other diffractive optical elements [79,145], there are secondary foci. For the frequency span shown, a secondary focus within the z-range 20-35 mm is visible. This secondary focus is however significantly lower in amplitude than the main focus. As next step, the spatial power distribution on the *xz*-plane for the two design frequencies is presented in Fig. 2.8(a): f_1 = 54 GHz (top) and f_2 = 55.5 GHz (bottom). For both frequencies, clear foci can be observed with half-wavelength resolution, i.e. full width at half maximum (*FWHM*) $FWHM_1$ = 3 mm ($0.5\lambda_1$) and $FWHM_2$ = 3

mm ($0.6\lambda_2$). Also, prominent side lobes are noticeable off-axis surrounding the focus. Nevertheless, they emerge at significant different distance than the focal plane.

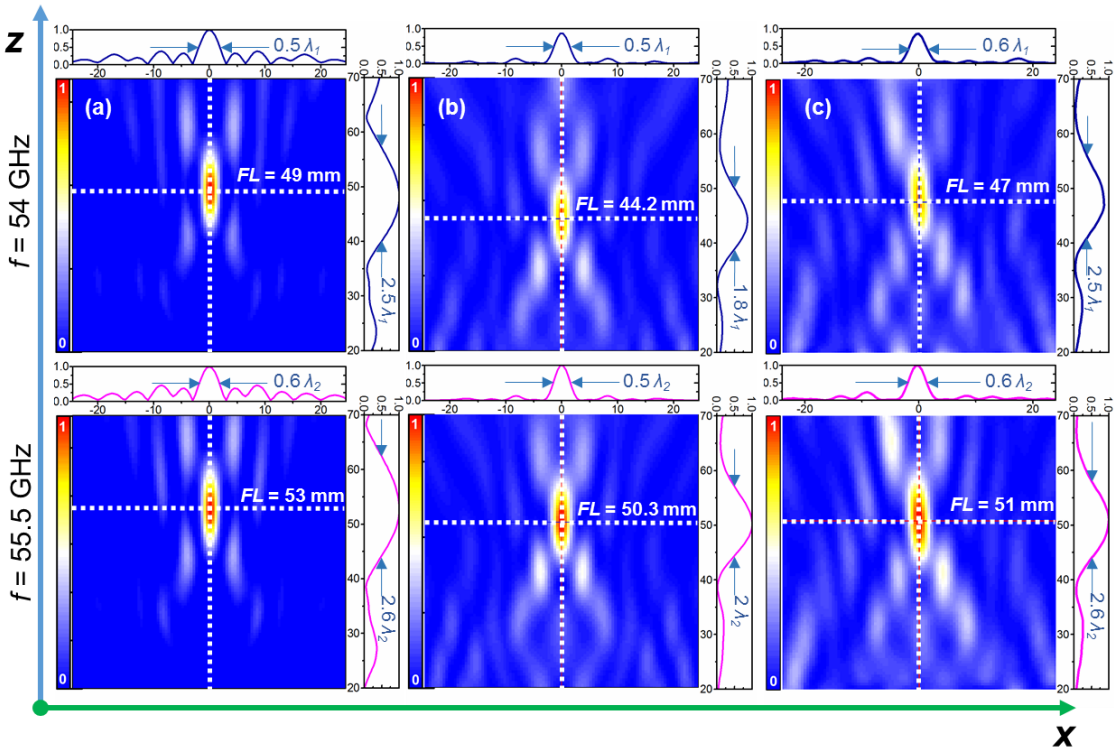

Fig. 2.8. Analytical (a), experimental (b) and simulation results (c) for of the spatial power distribution on the *xz*-plane for: (top) f_1=54 GHz and (bottom) f_2=55.5 GHz. The normalized power distributions along *x*-axis (at each focal length) and along the optical axis are represented in each panel on the top- and right-side plots, respectively.

Next, a full-wave numerical analysis of the realistic 3D model of the zoned lens is done using the transient solver of the commercial software CST Microwave Studio™. The bulk conductivity of aluminum (σ_{Al} = 3.56×10^7 S/m) is considered for the modeling of the fabricated fishnet metamaterial lens. A fine hexahedral mesh is used with minimum and maximum mesh cell sizes of 0.125 mm ($0.02\lambda_1$) and 0.28 mm ($0.05\lambda_1$), respectively. A vertically polarized (E_y) plane wave is used to excite the lens, impinging normally on its planar face. Perfectly matched layers ("open add space") are used in the boundaries of the simulation box to emulate a lens in free space. Given the two-fold symmetry of the problem, electric and magnetic mirror planes are placed in the *xz*- and *yz*-planes, respectively, with the aim to reduce computation time. The simulation is run for a sufficiently long time to ensure that the continuous-wave information computed by Fourier transformation is valid. Although time consuming, and thus, undesirable for a fast prototyping (unlike the Huygens-Fresnel principle), the results derived from this approach should obviously have a better agreement with the experimental ones.

Initially, the power distribution as a function of *z* position and frequency is obtained by placing *E*-field and *H*-field probes, along the optical axis (*z*-axis) with a step of 0.5 mm. These probes record the waveform at their positions and by Fourier transformation, the *E*- and *H*-field

spectra are obtained. The resulting power distribution is shown in Fig. 2.7(b). The focal spot is located in the frequency range 53.5-56.5 GHz and moves from 42 up to 51.5 mm along *z*-axis. This result resembles the analytical distribution. The dark red spot accounting for the maximum power is concentrated within a narrower frequency band.

Then, the *xz*-maps of power distribution generated from the simulation for f_1 = 54 GHz and f_2 = 55.5 GHz are plotted on the top and bottom color maps in Fig. 2.8(b), respectively. The foci with $FWHM_1$ = 2.8 mm (0.5λ_1) and $FWHM_2$ = 2.8 mm (0.5λ_2) are clearly observed. These color maps bear a resemblance to analytical results. In particular, they model more accurately than the analytical calculation the relative amplitude between the main focus and the side lobes, although, with a minor disagreement in focal length (see Table I).

Focusing performance bandwidth

In the next step, in order to confirm the broadband performance of the zoned lens, the power enhancement (i.e., the ratio between the intensity with and without lens for each *xz* position) as a function of frequency is compared to the enhancement of a zoned fishnet metamaterial lens optimized for single-band operation, already reported in previous works [54,146]. The numerical results are obtained using the same full-wave numerical analysis of the realistic 3D model and are shown in Fig. 2.9. The zoned lens discussed here exhibits an enhancement above 9 dB for the whole negative refractive index band (53.5-58 GHz) and has a maximum at the frequency f_1= 54 GHz, which is in good agreement with Fig. 2.5(a), where RMSE is minimal at this frequency. Therefore, the fractional bandwidth (FBW) for the proposed lens is FBW_{br}= 8.07%. The zoned lens optimized for single-band operation, in turn, achieves enhancement values above 9 dB only at the design frequency range, 55-56.5 GHz, also in agreement with Fig. 2.5(b), with FBW_s = 2.69%.

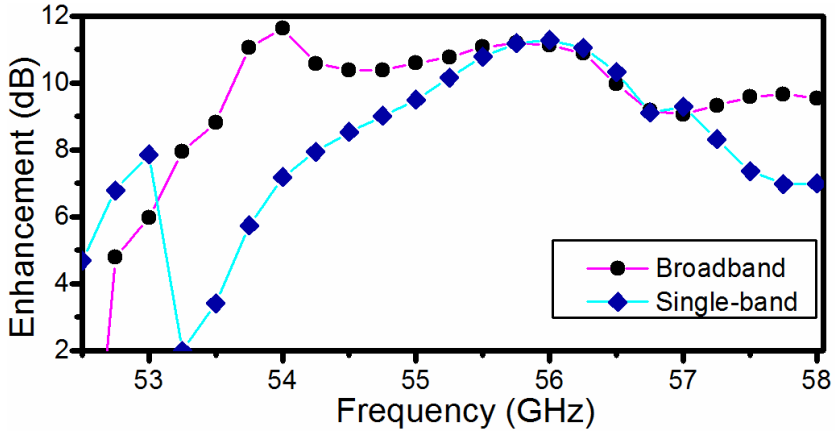

Fig. 2.9. Numerical results for the enhancement as a function of frequency for the single-mode zoned lens (red curve) and for the broadband zoned lens (blue curve).

Finally, the free-space matching is estimated by obtaining the reflectance for the full structure. The reflectance *R* is defined as the ratio of the reflected power P_{refl} and the incident power P_{inc}, $R = P_{refl}/P_{inc}$. The incident flux P_{inc} is calculated without the lens, in order to avoid any

contribution of reflected power. The reflected power P_{refl} is calculated from the instantaneous power flux P_{inst} located before the lens $P_{inst} = P_{inc} - P_{refl}$. Given the z normal planes at which we compute P_{inst} and P_{inc}, and that the lens is illuminated with a linearly polarized plane wave, we consider only the z-component of the power flux. The obtained reflectance R for the frequencies 52.5-58 GHz is shown in Fig. 2.10.

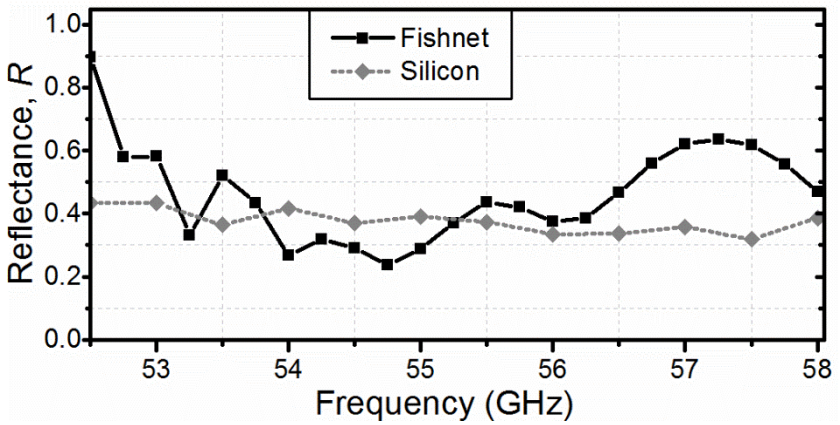

Fig. 2.10. Reflectance for the zoned fishnet metamaterial lens (solid black line) and the Silicon zoned lens (dashed grey line).

As it is expected from the dispersion diagram (Fig. 2.2), below 53 GHz the reflectance R is significantly high. At the chosen illustrative frequencies, R is 0.26 and 0.43 for the lower and higher frequency, respectively. One can notice the agreement with Fig. 2.7(b), where the maxima are at 54 GHz and 54.75 GHz. When comparing the reflectance of the zoned fishnet metamaterial lens with a zoned lens made of Silicon (dashed grey line), a material widely used for lenses at millimeter-waves and terahertz [148,149], it is evident that the lens analyzed here outperforms the Silicon counterpart in terms of Fresnel reflection losses for ~54-55. 5 GHz. This frequency range coincides with the band where good convergence of effective refractive index among different number of stacked layers was observed, see Fig. 2.2.

2.2.3. Experimental verification.

The experimental characterization is done using an AB Millimetre™ quasi-optical vector network analyzer with the setup illustrated in Fig. 2.11. To illuminate the lens, a V-band corrugated horn antenna is placed at a distance L = 3300 mm from the lens. At this distance the radius beam waist of the Gaussian beam is ~400 mm for both working frequencies, which ensures a uniform illumination of the lens. An open-ended rectangular waveguide (WR-15) is used as a detector, for the xz raster scanning. Millimeter-wave absorbers are used throughout the setup to mimic anechoic chamber conditions. The calibration is done by recording the transmitted power without the lens. For the power distribution as a function of frequency and z position, the lens is placed in the setup and the detector is moved from 20 to 70 mm away from the lens along z-axis (with 0.5 mm steps) while recording the spectrum is in the range 50-60 GHz. Similarly, z-frequency- and xz-maps are generated experimentally using the prototype described previously (Fig. 2.11).

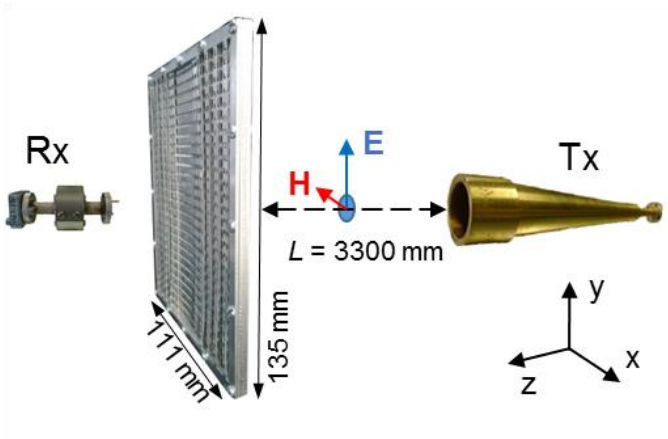

Fig. 2.11. Sketch of the experimental setup. Tx and Rx stand for transmitter and receiver, respectively.

First, analogously to the previous methods, the power distribution is obtained as a function of frequency and *z* position. The color map is shown in Fig. 2.7(c), with good agreement with both the analytical and numerical results (Fig. 2.7(a-b)). This color map is obtained after applying a Butterworth low pass filter, in order to minimize the ripples in the experimental data caused by the excitation of standing waves between the lens and the detector (demonstrated in the simulation results of next section but not shown here). In this figure, the broadband performance of the zoned lens from 54 GHz to 58 GHz (FBW_{exp} = 7.14%) can be observed, with some penalty in performance for extreme frequencies, which is in good agreement with the results obtained by the Huygens-Fresnel principle and numerical results. The maximum power enhancement is 10.5 dB at 54 GHz and 13.1 dB at 55.5 GHz. These maxima occur at z = 47 mm and 51 mm, respectively. It is also noticeable a secondary focus at around 30 mm for 55 GHz. Further, the power is scanned on *xz*-plane at frequencies f_1 = 54 GHz and f_2 = 55.5 GHz. The results of the spatial power distribution are shown in Fig. 2.8(c), for f_1 (top) and f_2 (bottom), respectively. Analogously to analytical and simulation results, clear foci with $FWHM_1$ = 3.3 mm ($0.6\lambda_1$) and $FWHM_2$ = 3.4 mm ($0.6\lambda_2$) are observed. Therefore, a good qualitative and quantitative agreement with the analytical as well as simulation results is evident.

2.2.4. Lens antenna configuration

Finally, after fully characterizing the zoned lens, we investigate its performance in a lens antenna configuration. To this end we use again the AB Millimetre™ quasi-optical vector network analyzer using a similar setup, but an open-ended WR-15 is used now as a feeder placed at the experimentally-computed focal length of each frequency. In order to measure the angular distribution of the radiated power, the feeder and the zoned lens stand on a rotating platform that rotates from -90 deg to +90 deg with step of 1 deg. A high gain standard horn antenna is placed 3650 mm away from the flat face of the zoned lens to detect the radiated power. Notice that, strictly speaking, the detection is not done in far-field according to the convention $z_{ff} = 2D^2/\lambda$, where D is the diameter of the lens: for f_1 = 54 GHz, z_{ff1} = 4435 mm and for f_2 = 55.5 GHz, z_{ff2} = 4560 mm. Nevertheless, it should give us a good approximation. Absorbing material is also used

throughout the setup for reflection suppression. The obtained co- and cross-polar angular measurements for f_1 = 54 GHz and f_2 = 55.5 GHz are displayed in Fig. 2.12. For f_1 [Fig. 2.12(a)], the main lobe has a half-power beamwidth (HPBW) and a first null beamwidth (FNBW) of 3.5 deg and 40 deg, respectively, with a side lobe level (SLL) of 5.7 dB at around ±8 deg. It can be demonstrated that this side lobe corresponds to the (0,−1) grating lobe of the periodic holey pattern [146]. From analytical calculations this grating lobe should appear at ±5 deg for f_1 and ±6.3 deg for f_2. An additional minor lobe caused by the spillover [146] can be seen at ±65 deg. In this case, the analytical value of the spillover angle for f_1 is ±56 deg. It can potentially be eliminated by increasing the lateral size of the lens. The results for f_2 [Fig. 2.12(b)] are similar. The main lobe has HPBW= 4.3 deg and FNBW = 39 deg, respectively, with SLL = 6.7 dB at around ±7 deg. The spillover lobe occurs at ±65 deg, while the analytical value is ±48 deg. The maximum directivity estimated using the method for fan-beam antennas (assuming a beam wide in the vertical plane and narrow in the horizontal) described in Ref. [150] is 16.6 dBi and 15.6 dBi for f_1 and f_2, respectively. The cross-polar level is ~25 dB and ~40 dB for f_1 and f_2 respectively, indicating the good performance of the zoned lens antenna. Arguably, the measured cross-polar level might be originated from experimental misalignment, since the on-axis cross-polarization should vanish for a perfectly symmetric configuration about the *yz*-plane, as the simulations described below confirm. The non-negligible cross-polar measured at ±65 deg arises evidently from the spillover.

The radiation parameters have also been modeled numerically. An open-ended WR-15 feeder is placed at the numerical focal length of each frequency and the radiation pattern is calculated at the same distance as in the experiment z_{ff}=3650 mm. The co-polar results are plotted also in Fig. 2.12 to facilitate the comparison with the experiment.

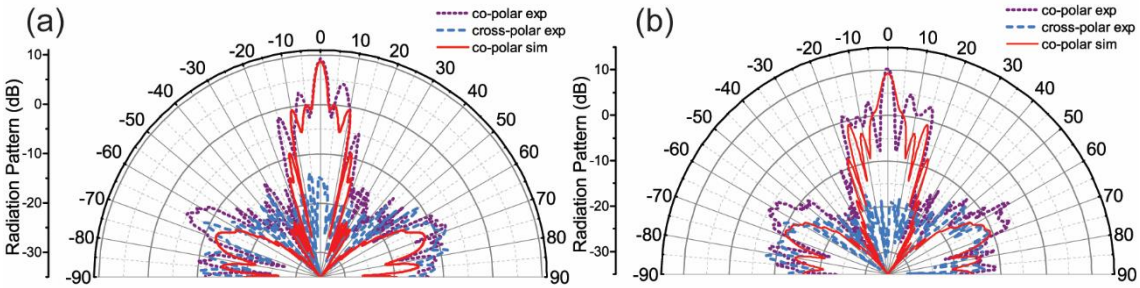

Fig. 2.12. *H*-plane (*xz*-plane) radiation pattern for: (a) f_1 =54 GHz and (b) f_2 =55.5 GHz. Dashed and solid lines represent experimental and numerical results, respectively. Purple and blue colors stand for co- and cross-polar data, respectively.

The numerical cross-polar, however, is not plotted given its negligible value. One can see that the radiation patterns for the numerical calculations are similar to the experimental results. The main lobe has HPBW = 3.2 deg and FNBW = 40 deg for f_1, and HPBW = 4.1 deg and FNBW = 56 deg for f_2. The first side lobes and the spillover lobe appear at similar angles, but with lower levels than in the experiment. The maximum directivity, which can be computed readily from the

simulation, is 15.4 dBi for f_1 and 15.2 dBi for f_2, which is in good agreement with values estimated from experimental results.

To facilitate the comparison, all main focal properties for the three methods investigated are gathered in Table I. It is shown that the results are also in good agreement quantitatively with each other and with the designed values based on ray tracing approximation. Only, the FWHM shows minor disagreement between measurements and both analytical and numerical calculations. This can be arguably ascribed to the non-subwavelength nature of the detector used in the experiment (an open-ended waveguide, WR-15), which averages the field strength.

Table I. Focal properties and radiation pattern parameters of broadband zoned fishnet metalens.

	FL_1[1] mm	FL_2 mm	$FWHM_1$[2] mm	$FWHM_2$ mm	DF_1[3] mm	DF_2 mm	FBW %	$HPBW_1$[4] deg	$HPBW_2$ deg	$FNBW_1$[5] deg	$FNBW_2$ deg	D_1[6] dB	D_2 dB
Analytical	49 $8.8\lambda_1$	53 $9.8\lambda_2$	3 $0.5\lambda_1$	3 $0.6\lambda_2$	14 $2.5\lambda_1$	13.8 $2.6\lambda_2$	-	-	-	-	-	-	-
Experimental	47 $8.4\lambda_1$	51 $9.4\lambda_2$	3.3 $0.6\lambda_1$	3.4 $0.6\lambda_2$	13.7 $2.5\lambda_1$	14.2 $2.6\lambda_2$	7.14	3.2	4.1	40	56	15.4	15.2
Simulation	44.2 $7.9\lambda_1$	50.3 $9.3\lambda_2$	2.8 $0.5\lambda_1$	2.8 $0.5\lambda_2$	10 $1.8\lambda_1$	10.7 $2\lambda_2$	8.07	3.5	4.3	40	39	16.6	15.6

[1] *FL* is the focal length.
[2] *FWHM* is the full width at half maximum.
[3] *DF* is the depth of focus.
[4] *HPBW* is the half power beamwidth.
[5] *FNBW* is the first null beamwidth.
[6] *D* is the directivity.

For the analytical results, the deviations of the focal positions from the designed values are less than 2%, which falls within the error of the zoned lens profile. The experimental results show deviations of focal length below 6%. These discrepancies fall perfectly within the experimental error caused by misalignments and defects of the fabricated zoned lens. As for simulations, the deviations are less than 9.5%. It is worth noting that for the initial design based on ray tracing, the lens is assumed to be isotropic with refractive index extracted from the infinite-layered fishnet structure. Hence, it is reasonable to expect a good agreement between the experimental and numerical results, where the anisotropic nature of the fishnet is fully considered. The Huygens-Fresnel principle is more similar to the ray tracing design, where the lens is assumed isotropic, therefore, the analytical results obtained with this method should deviate more from experimental and numerical results. However, the simulation results deviate from experimental results slightly more than analytical. This discrepancy could be due to the fabrication imperfections, which could lead to the different unit cell parameters, and, therefore different effective refractive index. This, in turn, would affect the focal lengths.

Thereby, the good agreement observed between all approaches validates the good performance of the lens for frequencies from 54 GHz to 58 GHz. Also, these results demonstrate

that, despite all the assumptions used for the Huygens-Fresnel principle, it can be well used initially for a fast prototyping.

2.3. Soret fishnet metalens

In this section another metalens is presented – a Soret lens, member of the Fresnel-zone plate lens (FZPL) family. These binary amplitude-only diffractive optical elements emulate refractive lenses without the need of large profiles, at the expense of frequency narrowing. Unfortunately, they also present larger Fresnel reflection loss than conventional lenses. This is usually tackled by implementing unattractive cumbersome designs. Here we propose and alternative solution, which is the application of metamaterials to improve the radiation pattern of a Soret lens. The building block of this advanced Soret lens is the fishnet metamaterial operating in the near-zero refractive index regime with one of the edge layers designed with alternating opaque and transparent concentric rings made of subwavelength holes. The hybrid Soret fishnet metalens retains all the merits of classical Soret lenses such as low profile, low cost and ease of manufacturing with improved radiation features.

2.3.1. Fresnel zones plate (FZP) for focusing light

The FZPL consists of alternating transparent and opaque concentric rings, where the radii of the rings are calculated using the Fresnel zones formulation [151]:

$$r_i = \sqrt{\frac{2FL \cdot \lambda_0 \cdot i}{p} + \left(\frac{i \cdot \lambda_0}{p}\right)^2} \tag{2.6}$$

where FL is the focal length of the FZPL, λ_0 is the operation wavelength, i is an integer denoting zone number and $p = 2, 4, 6\ldots$ is the number of phase quantization levels.

At the beginning, this lens was considered as a purely optical device. Ultimately, the same concept has been successfully applied throughout the whole electromagnetic spectrum and in particular in the microwave range for lens antennas [79,144,145]. At microwaves these lenses present interesting characteristics such as low profile, low cost and ease of fabrication. However, FZPLs in microwave regime have a low efficiency in transmission compared to conventional lenses, due to the fact that half of the incident energy is reflected from opaque zones. This low focusing efficiency also deprecates the radiation efficiency of antenna applications, such as Fresnel-zone plate antennas (FZPA), making them less competitive than other conventional antennas. Another drawback is that the best performance of a FZPA is normally obtained for a large focal distance/diameter ratio ($F/D \sim 3\text{-}15\lambda$) [145]. Thus, the volume enclosing the Soret lens along with the feeder is very large, making FZPAs not suitable for compact systems. This leaves original FZPLs and FZPAs attractive only for a few niches such as broadcast satellite reception [145].

The performance of FZPLs and FZPAs can be improved by an advanced design, which reduces the amount of reflected power, i.e. improves the efficiency, by introducing selective phase shifts instead of blocking negative (odd) or positive (even) Fresnel zones [79,145]. This smart

approach leads to high gain, aperture efficiency and low side lobe level [152]. Below in this chapter it is demonstrated that the fishnet metamaterial can be also combined with such advanced phase reversing technique in order to reduce the thickness and improve the focusing efficiency.

2.3.2. Fishnet metamaterial for FZP lens design

In order to improve the performance of the FZPA we propose to replace the transparent rings of the Soret lens by subwavelength hole arrays, which allows the excitation of surface currents (leaky-waves) and could improve coupling-in and -out of the spatial wave as it happens in the extraordinary transmission phenomenon [153]. Moreover, as it was mentioned in Chapter I, by introducing at the input of the FZPA a metamaterial slab with near zero index (NZIM) it is possible to increase the directivity of the antenna and reduce the sidelobe level, since the phase front at the output surface of the NZIM follows its shape and therefore the electromagnetic field becomes locally closer to a plane-wave distribution [27,154,155]. The fishnet metamaterial is a good candidate for this role, since it can provide NZIM with low losses. Moreover, alike the single holey plate exhibiting extraordinary transmission, the leaky-wave mechanism present in the fishnet metamaterial may facilitate the coupling-in and -out, guaranteeing then a low insertion loss [25], and may improve the effective illumination and extend the radiating area [38], increasing the total efficiency of the lens antenna. This increased illumination efficiency allows a comparatively smaller F/D ratio, which means that the volume of FZPA can be reduced, by placing the transmitter closer to the FZPL. And as it was also mentioned in Chapter I, the effective impedance of fishnet metamaterial can be matched with free space, in the desirable NZIM regime.

The unit cell of the fishnet metamaterial used for this lens (inset of Fig. 2.13) is designed using the commercial substrate Rogers RO5880™ and has the following dimensions: d_x = 1.26 mm, d_y = 2.1 mm, d_z = 0.398 mm (metal thickness w = 0.017 mm and thickness of dielectric substrate t_d = 0.381 mm), hole diameter $a = d_y/4$ = 0.525 mm and spacer dielectric permittivity ε_r = 2.2, with loss tangent $\tan\delta = 9\times10^{-4}$. For these parameters, the cut-off frequency of the hole fundamental TE_{11} mode is 112 GHz. The dispersion diagram of the infinite structure is numerically calculated using the commercial software CST Microwave Studio™, using the same procedure described in Section 2.2.1 of this chapter. The first band appears at 87-96 GHz, as shown by the black dash-dotted line in Fig. 2.13, and corresponds to the fishnet extraordinary transmission band. However, the calculation for a finite number of plates deviates from the infinite structure curve due to the inhomogeneity of the fishnet metamaterial. In Section 2.2.1 of this chapter we found that four plates are a good trade-off between total thickness and electromagnetic performance in terms of insertion loss.

In order to obtain the effective refractive index of the fishnet metamaterial, consisting of 4 periods with periodicity d_z, we use now the phase of the electric field inside the structure (assuming that the transmittance is high), by exploiting the frequency domain solver in the range 90-110 GHz. Unit cell boundary conditions were used and the metal was modelled as aluminium ($\sigma_{Al} = 3.56\times10^7$ S/m). A fine tetrahedral mesh is used, with minimum and maximum edge lengths of 0.007 mm (~$0.003\lambda_0$) and 0.64 mm (~$0.2\lambda_0$), respectively.

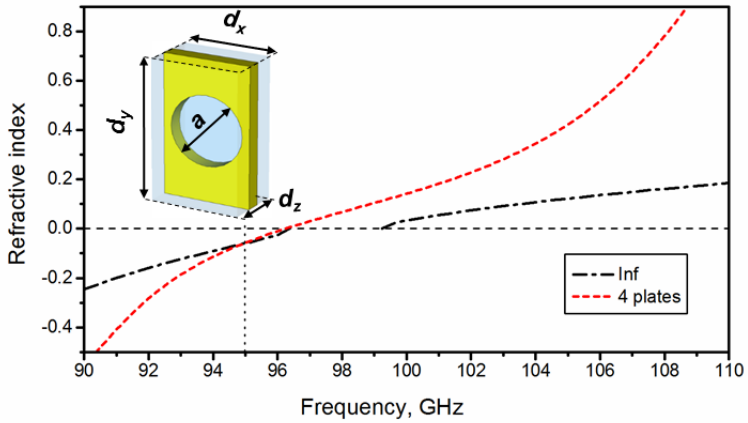

Fig. 2.13. Effective refractive index of fishnet metamaterial for infinite number of plates (black dash-dotted line) and four plates (red dashed line). Dimensions of unit cell (Inset).

The resulting effective index of refraction can be calculated as:

$$n_z = \frac{\Delta\varphi}{k_0 \Delta d}, \tag{2.7}$$

where Δφ is the phase variation in the thickness Δd and k_0 is wave number in free-space. The resulting effective index of refraction for 4 cascaded plates is shown in Fig. 2.13 (red dashed line). As it can be noticed, the bandgap between 97 and 99 GHz due to Wood's anomaly disappears in this case. This is more evident in the transmission coefficient S_{21} for 4 cascaded plates, shown in Fig. 2.14. This feature has been observed before and is due to the tunneling of energy when the number of plates is small. Finally, since we want the fishnet metamaterial to behave as NZIM, we choose 95 GHz ($\lambda_0 \sim 3.16$ mm) as design frequency where the index of refraction is $n_z = -0.06$.

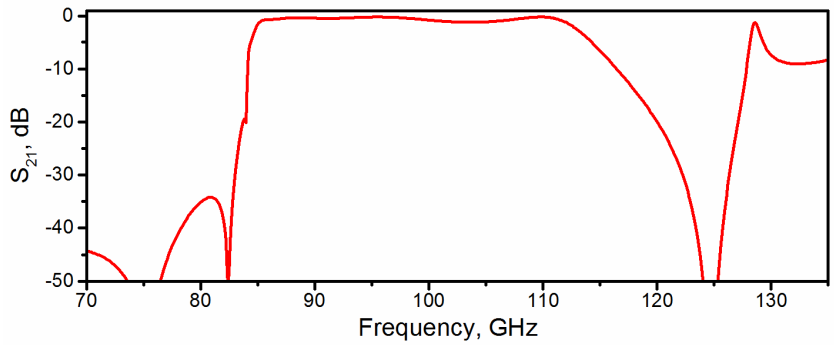

Fig. 2.14. Transmission coefficient for a four-plate fishnet metamaterial.

Soret lens design

Once we have defined our fishnet metamaterial we design a Soret lens. The radii of the Fresnel zones r_i of the Soret lens can be found using the classical design equation (2.6). The positive (odd) zones are made of holes of the same dimension as the fishnet, while the negative (even) zones remain without holes. Since the fishnet metamaterial unit cell size (with in-plane periods d_x and d_y) is comparable to the free space wavelength, it is also comparable to the radii of the Fresnel zones. This restricts the possible combinations of the parameters. For example, the

number of phase quantization levels p can be only equal to 2, since with p higher than 2 the transparent zones will become too narrow compared to one unit cell. Therefore, the performance of the Soret fishnet metalens depends on the filling ratio of the Fresnel zones. This, in turn, depends on many parameters of the design, such as FL, λ, i, p.

In order to quickly and easily estimate the performance of the designed FZPL, we use a three-dimensional analytical calculation using the Huygens-Fresnel principle, which is described in Appendix A. Here it should be noticed that, unlike traditional designs, a subwavelength focal length $FL = 0.5\lambda_0 = 1.58$ mm is chosen to demonstrate the possibility of designing very compact systems. In order to improve the aperture efficiency, or equivalently the illumination efficiency, which is low due to the small focal length, an optimization routine is run, which included the numerical calculations of the directivity for the whole structure. A small number of Fresnel zones $i = 7$ is found to be optimal. The calculated radius of the last zone is $r_7 = 12.5$ mm. The final lens has a total thickness of $5t_d + 4w = 1.973$ mm ($\sim 0.62\lambda_0$). Thus, the whole structure has dimensions of 32 mm × 32 mm × 1.973 mm. The final lens profile and fabricated Soret fishnet metalens are shown in Fig. 2.15(a,b).

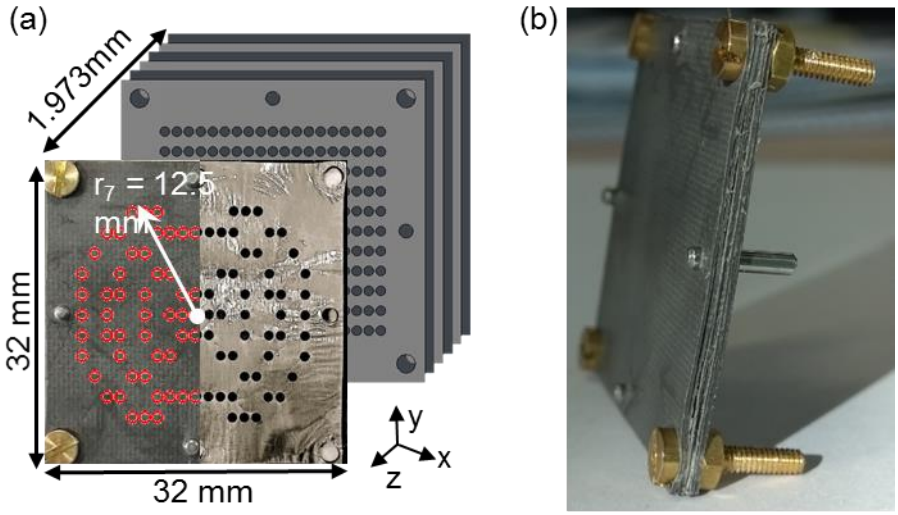

Fig. 2.15. Fabricated Soret fishnet metamaterial lens (a) front-view and its design with seven Fresnel zones. Light grey slabs account for perforated plates and dark grey for RO5880™ slabs; (b) side-view with alignment pins and fastening screws.

Fabrication

The Soret fishnet lens is fabricated using aluminum foil with thickness 0.021±0.003 mm perforated and cut by laser (see Fig. 2.15). The substrate Rogers RO5880™ with permittivity $\varepsilon_r = 2.2$ and thickness 0.381 mm is used as dielectric spacer between successive aluminum foils and as additional protective outer layers. The pins are used to align the layers and screws to fasten all layers.

2.3.3. Analytical and numerical analysis

First, the power distribution is calculated as a function of frequency and position along the optical axis of the lens [Fig. 2.16(a)] using the Huygens-Fresnel principle. In this calculation, we model the holes as point sources located at the output plate. Also for simplicity we neglect reflection and absorption. Furthermore, all sources have the same amplitude and radiate vertically polarized (E_y) cylindrical waves. The absolute maximum in this case occurs at 95.5 GHz, with focal length $FL_1 = 1.87$ mm ($\sim 0.60\lambda_0$). The secondary focus is located at $FL_2 = 7.01$ mm ($\sim 2.22\lambda_0$) and has a significantly lower magnitude. As shown in Fig. 2.16(a), the Soret lens suffers from chromatic aberration, i.e. the focal point is shifted in frequency. Next, the power distribution colour-maps calculated at the design frequency are presented in Fig. 2.17(a, b) for the *xz*- and *yz*-plane respectively. In both cut-planes, clear foci can be observed with transverse dimensions $0.36\lambda_0$ and $0.5\lambda_0$ for *xz*- and *yz*-plane respectively.

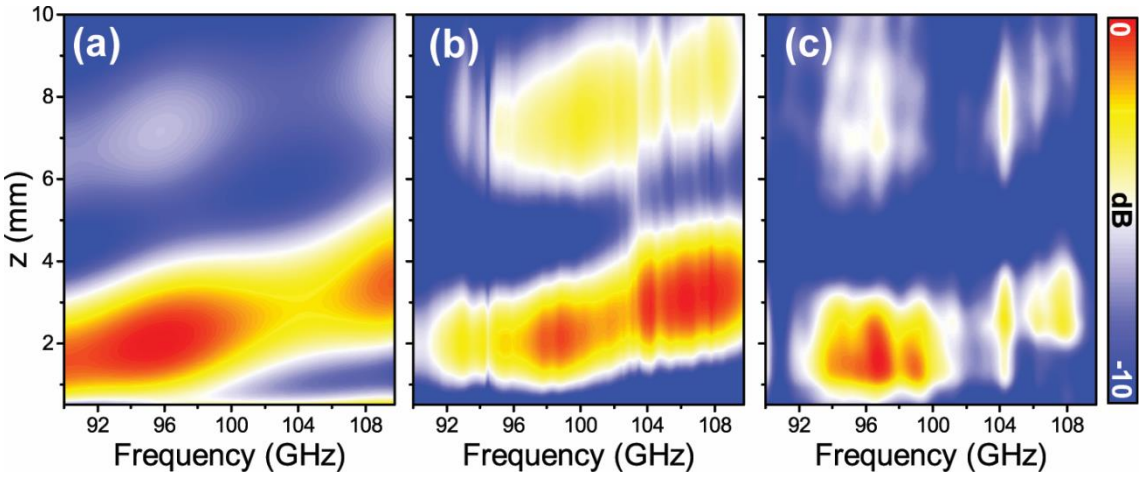

Fig. 2.16. Power spectra along the optical axis. Power distribution along *z* axis for the frequency range 90–110GHz: (a) analytical results, (b) simulation and (c) experimental results.

A full-wave numerical analysis of the realistic 3D model of the Soret fishnet metalens is done using the transient solver of the commercial software CST Microwave Studio™. The metal aluminum layer is modelled as a lossy metal with the bulk conductivity of aluminum ($\sigma_{Al} = 3.56\times10^7$ S/m). A fine hexahedral mesh is used with minimum and maximum mesh cell sizes of 0.088 mm ($\sim 0.03\lambda_0$) and 0.25 mm ($\sim 0.08\lambda_0$), respectively. The metalens is illuminated by a vertically polarized (E_y) plane wave impinging normally on the fishnet side. Perfectly matched layers (i.e., the solver-defined *open add space* boundaries) are used at the boundaries of the simulation box to emulate a lens in free space. Given the two-fold symmetry of the problem, electric and magnetic symmetries are imposed in the *xz*-plane ($y = 0$) and *yz*-plane ($x = 0$), respectively, to reduce computation time. The simulation is run for a sufficiently long time to ensure steady-state regime so that the continuous-wave information computed by Fourier transformations was valid. The colour-map of the power spectrum as a function of *z* position is obtained by placing *E*-field and *H*-field probes along the optical axis (*z*-axis) with a step of 0.05 mm. These probes record the waveform at their positions and by Fourier transformation, the *E*- and *H*-field spectra are obtained. These full-wave numerical results should provide a better modelling of the lens than the analytical results, where some simplifications were made.

The power distribution as a function of frequency and position along the optical axis (*z*-axis) is obtained and shown in Fig. 2.16(b). A focal spot appears within the frequency range 97-110 GHz, moving from 1.9 mm ($0.57\lambda_0$) up to 3 mm ($0.95\lambda_0$) along the *z*-axis. One can see that these results resemble closely the analytical results previously shown, but here the secondary focal spot is more prominent. The power enhancement corresponding to the first maximum is 10.28 dB at 98.75 GHz ($\lambda_0 \sim 3.04$ mm) with a focal distance $FL = 1.94$ mm ($\sim 0.64\lambda_0$). The blueshift of the focal spot can be simply explained by taking into account that in the analytical calculations we neglect the dielectric substrate covering the first layer which changes the effective permittivity at the output surface. Finally, the colour-map of power distribution is generated for *xz*- and *yz*-planes at 98.75 GHz [Fig. 2.17(c,d)]. These colour-maps resemble the analytical results but again show minor dissimilarities because of the different accuracy of each method.

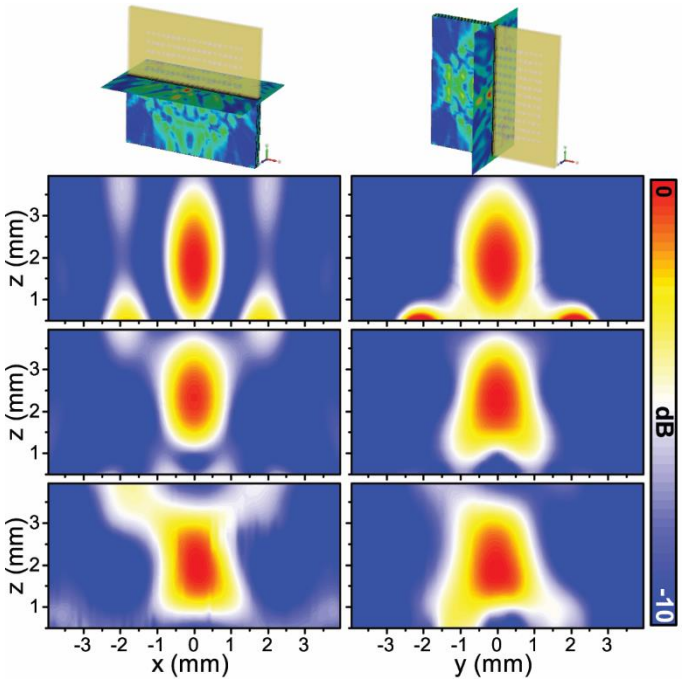

Fig. 2.17. Normalized spatial power distribution on the *xz*-plane (left column) and *yz*-plane (right column) for: (a-b) analytical results at 95.5 GHz; (c-d) simulation results at 96.45 GHz; (e-f) experimental results at 98.75 GHz. (Inset) Representation of the cutting plane in each case: *xz*-plane (left column) and *yz*-plane (right column).

2.3.4. Measuring focusing properties

The experimental verification is done using an AB Millimetre™ quasi-optical vector network analyzer with the setup illustrated in Fig. 2.18. To illuminate the lens, a W-band corrugated horn antenna is placed at a distance $L = 4000$ mm from the lens. At this distance the radius beam waist of the Gaussian beam is ~400 mm, which ensures a uniform illumination of the lens. A waveguide probe WR-8.0 is used as a detector, for the *xz* raster scanning. Millimeter-wave absorbers are used throughout the setup to mimic anechoic chamber conditions.

The calibration is done by recording the transmitted power without the lens. To obtain the power distribution as a function of frequency and *z* position, the lens is placed in the setup and

the detector was moved from 0.5 to 10 mm away from the lens along *z*-axis (with 0.05 mm steps) while recording the spectrum in the range 90-110 GHz. The results are shown in Fig. 2.16(c) and confirm our preliminary analytical and numerical results. The maximum power enhancement is 11.04 dB at 96.45 GHz ($\lambda_0 \sim 3.11$ mm) with a focal distance $FL_1 = 1.9$ mm ($\sim 0.61\lambda_0$). A secondary focus appears at $FL_2 = 7$ mm ($2.25\lambda_0$) similarly to the analytical and numerical results. One can notice that for the experimental results the power enhancement is significantly lower within the frequency range 100-104 GHz. This can be due to the presence of thin air gaps between metallic and dielectric plates arising from imperfections of the fabrication. Additional simulations for the unit cell of the fishnet metamaterial were run and showed that indeed the air gaps inside the fishnet metamaterial deprecate its electromagnetic performance, reducing the transmitted power in this frequency range.

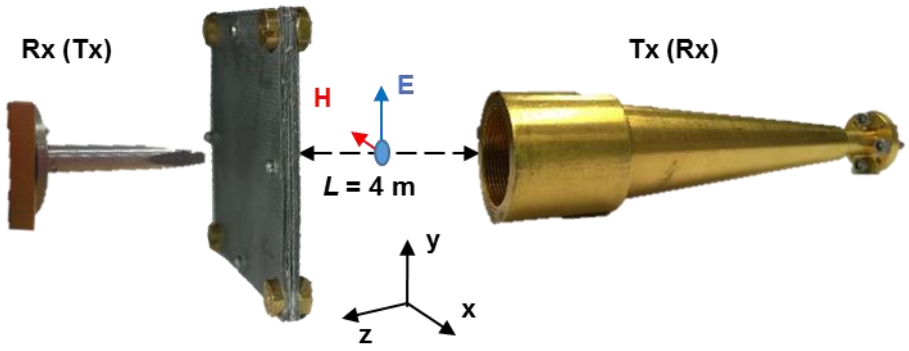

Fig. 2.18. Experimental setup. Scheme of experimental setup for the focus measurements (radiation measurements) with a waveguide probe as a receiver (transmitter) and a standard high gain horn antenna as a transmitter (receiver).

Next, the power is scanned on *xz*- and *yz*- planes at 96.45 GHz. The results of the spatial power distribution are shown in Fig. 2.17(e,f). The qualitative agreement with the numerical results is evident. To facilitate the comparison, all the results are gathered in Table II.

2.3.5. Radiation properties of metalens antenna

After a characterization of the focal properties of the Soret fishnet metalens, next we investigate its performance as FZPA. To this end, the waveguide probe WR-8.0 is used as a feeder placed at the experimental focal length $FL = 1.9$ mm ($0.63\lambda_0$). A schematic of the experimental setup along with the fabricated Soret fishnet metamaterial lens is shown in Fig. 2.18. Notice that now the input part of the hybrid lens is the Soret lens and the output is composed of the fishnet metamaterial. Meanwhile, a high gain standard horn antenna is placed 4000 mm away from the output face (NZIM slab) of the Soret lens to detect the radiated power. To measure the angular distribution of the radiated power, the feeder and the zoned lens stand on a rotating platform that can rotate from -90 deg to +90 deg with step of 0.5 deg. Absorbing material is also used throughout the setup for reflection suppression. The normalized experimental results for co- and cross-polar components as a function of frequency and angle are shown in Fig. 2.19(e-f) *E*-plane and Fig. 2.19(g-h) *H*-plane.

In the numerical simulations the realized gain is directly calculated by the built-in far-field monitors of CST Microwave Studio™. The realistic waveguide probe WR-8.0 is used as a feeder and placed at the previously numerically-found position z = 1.9 mm, which corresponds to the maximum radiation of the FZPA. The rest of the simulation parameters were described previously. Far-field monitors are used to record the radiation pattern of the lens within the frequency range 90-110 GHz with a step of 0.25 GHz. Numerical results of co- and cross-polar angular power distributions for *E*- and *H*-plane are displayed in Fig. 2.19(a-d). The maximum is located at 98.75 GHz, in agreement with the previous numerical study. It is evident from these figures that the angular beamwidth for *H*-plane is wider than for *E*-plane. This can be explained by the excitation of leaky waves on the surface of the Soret lens, where the current density is higher and runs parallel to the *E*-plane [156,157].

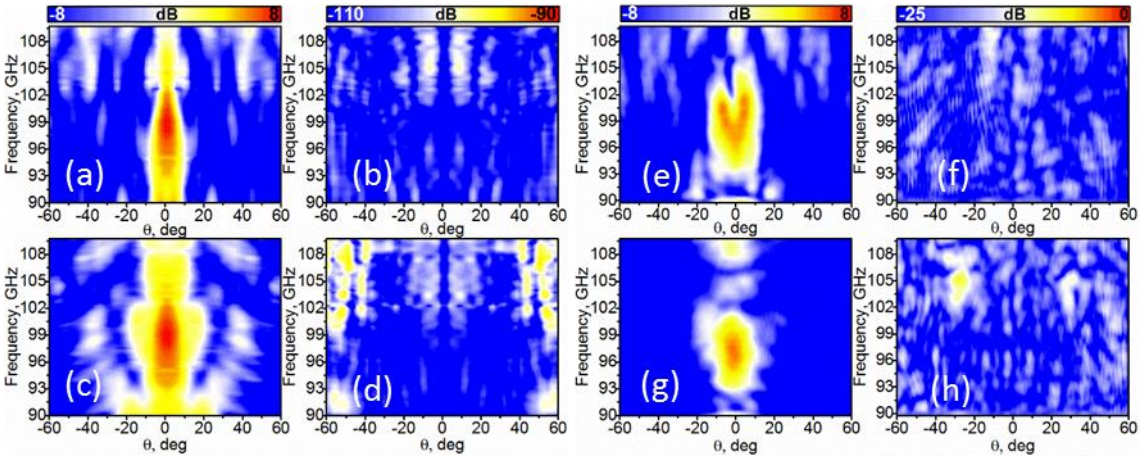

Fig. 2.19. Radiation pattern vs. frequency. Numerical (a-d) experimental (e-h) radiation pattern of the Soret fishnet metamaterial lens antenna in the frequency range 90-110 GHz: *co*- (a, c, e, g) and *cross*-polarization (b, d, f, h). (a, b, e, f) *E*-plane and (c, d, g, h) *H*-plane.

One can notice the small disagreement between experimental and numerical results for the co-polar component for *E*-plane, in particular the division of the main beam for frequencies 99 – 103 GHz. Even though the experiment is done with the greatest possible care and precision, this could be well explained by an undesired tilt of the lens in the experimental setup since additional simulations for a tilted lens (with a tilt angle θ = 7 deg in *H*-plane) were run and demonstrated a similar pattern. Consistently with the previous experiment (investigating the focal properties of the Soret lens) the experimental maximum is located at 96.45 GHz, i.e. slightly shifted from the frequency obtained by simulation. In Fig. 2.20(a, b), we plot together the numerical and experimental results of the maximum at each respective frequency. In this figure, to facilitate the comparison, the normalized simulation and experimental radiation patterns for the *E*- and *H*-plane are presented. Logically, the performance is different, and most notably the beamwidth is wider in the experiment. Additional simulations prove that the frequency shift of 2 GHz provokes broadening of the beamwidth from 8.7 deg up to 13 deg. Another factor for the wider beamwidth in the experimental *E*-plane is a displacement of the waveguide probe. For example, in our case the focal displacement of 0.3 mm in the simulations increases the beamwidth

from 8.7 deg up to 11 deg. The combination of these two factors widens the beam more than two times: from 8.7 deg up to 18.5 deg.

Additional measurements were performed for the radiation patterns in order to confirm the performance of the metalens-antenna. To this end the waveguide probe at the focal position is replaced by a high gain horn antenna. Due to the changes in the setup the focal position with maximum power shifts slightly from FL_{probe} = 1.9 mm (0.64λ_0) to FL_{horn} = 2.3 mm (0.64λ_0) with the frequency f_{horn} = 98.6 GHz, which is closer to the f_{sim}. The normalized numerical and experimental radiation patterns for this setup are shown in Fig. 2.21(a,b) for *E*- (a) and *H*-plane (b) respectively. The results (measurement vs. simulation) are in better agreement than for the case when the waveguide probe is used. We believe that this is because the configuration is significantly more robust to misalignment, due to the integration of field by the horn antenna.

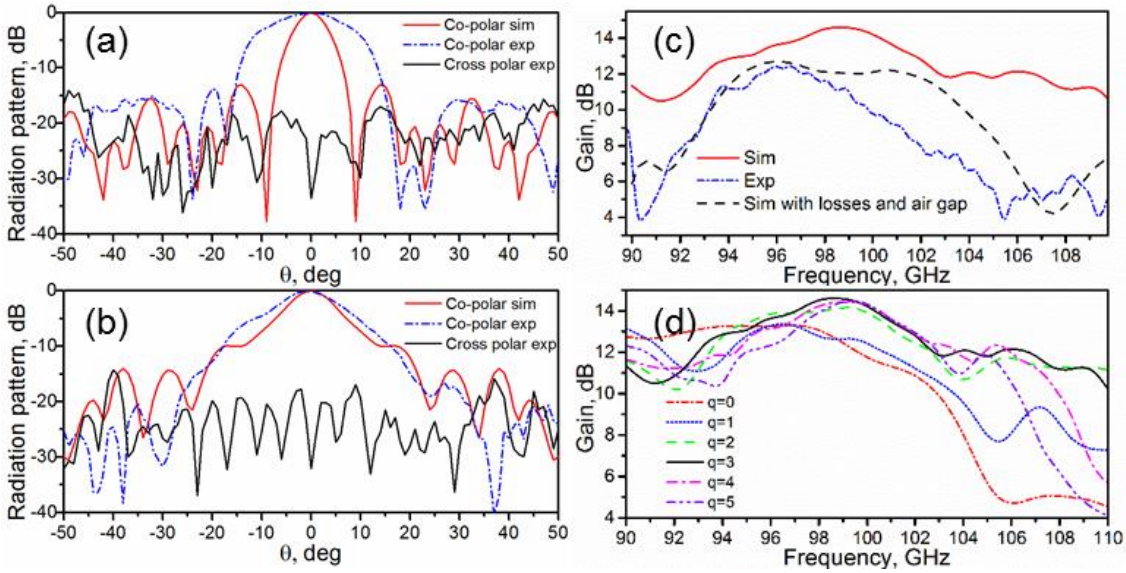

Fig. 2.20. Normalized radiation pattern and gain. Normalized radiation patterns for: (a) *E*-plane and (b) *H*-plane at frequencies 98.75 GHz and 96.45 GHz (simulation and experimental respectively). (c) Simulation gain (solid red line), experimental gain (dash dotted blue line) and simulation gain considering air gaps and losses (dashed black line). (d) Simulation results for the gain of the Soret lens antenna with a different number of stacked plates *q*.

To complete the study, the numerical and experimental gain of the Soret fishnet metamaterial lens antenna is presented in Fig. 2.20(c). In the experiment, the gain is obtained by comparing our lens antenna with a standard horn antenna following the gain comparison method [158]. For this aim, the received power was measured using a standard gain horn antenna with the lens and waveguide probe as a transmitter. Then the lens was removed and a standard high gain horn antenna replaced the transmitter. As a result, a high gain of 10.64 dB is found experimentally at 96.45 GHz (solid blue line). The numerical value of 14.6 dB is found at frequency 98.75 GHz by using the software-implemented far-field monitors (dashed red line). The difference in the results, the lower values of gain and shift in frequency, can be explained as a sum of all previously described factors, such as experimental errors (misalignment, accuracy of distance

measurement) and by defects in the fabrication (non-perfect contact between dielectric and metallic plates) and effective substrate losses higher than nominal values.

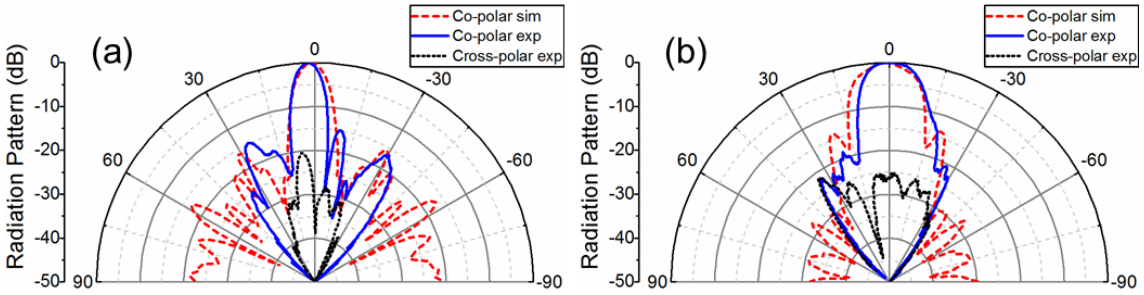

Fig. 2.21. Normalized radiation pattern for *E*-plane (a) and *H*-plane (b), measured with horn antenna.

To confirm these factors, additional simulations for the complete 3D model of the FZPA are run with an air gap of 50 μm and higher dielectric loss tangent tanδ = 0.015. The resulting gain is shown in Fig. 2.20(c) (dashed dotted black line). Here an air gap of 50 μm between metallic and dielectric plates results in a frequency shift of the maximum from 98.75 GHz to 96.25 GHz and the higher losses result in a lower gain. Consequently, the numerical gain of the lens with higher losses and spurious air gap is closer to the experimental gain. The maximum directivity, computed readily from the simulation, is 15.1 dBi at 98.75 GHz, and a directivity 15.4 dBi is estimated from experimental results at 96.45 GHz [150]. To facilitate the comparison, all the results are gathered in Table II. Analogously to the radiation patterns, a high gain of 18.2 dB was measured at frequency f_{horn} = 98.6 GHz by means of a high gain standard horn antenna. The higher gain in this case can be explained by closer to f_{sim} frequency and the higher illumination efficiency when the horn antenna is used as source.

Table II. Focal properties and radiation pattern parameters of Soret fishnet metalens.

	Frequency, GHz	***FL***[1], mm	***FWHM***[2], mm		***DF***[3], mm	**HPBW**[4], **deg**		**FNBW**[5], **deg**		**FSLL**[6], **deg**		**Directivity, dBi**
		E-plane *H*-plane	*E*-plane	*H*-plane	*E*-plane *H*-plane	*E*-plane	*H*-plane	*E*-plane	*H*-plane	*E*-plane	*H*-plane	
Analytical	95 λ_0 = 3.15 mm	1.87 0.59λ_0	1.13 0.36λ_0	1.58 0.5λ_0	1.45 0.46λ_0	-	-	-	-	-	-	-
Simulation	98.75 λ_0 = 3.04 mm	1.94 0.64λ_0	1.39 0.46λ_0	1.58 0.52λ_0	1.97 0.65λ_0	8.1	12.7	48	50	-13.1	-9.9	15.1
Experimental	96.45 λ_0 = 3.15 mm	1.9 0.61λ_0	1.44 0.46λ_0	1.73 0.56λ_0	2 0.64λ_0	18.1	13.7	42	67	-13.5	-20.7	15.4

[1]FL is the focal length.
[2]FWHM is the full width at half maximum.
[3]DF is the depth of focus.
[4]HPBW is the half-power beam width
[5]FNBW is the first null beam width
[6]FSLL is the first side-lobe level

In order to demonstrate the advantages and improvements of the hybrid Soret fishnet metamaterial lens antenna, we compare its performance in terms of gain for an increasing number of cascaded fishnet plates. As it was mentioned in Chapter I, NZIM can improve the radiation parameters due to the redistribution of the energy on its boundaries. Since the phase advance

inside NZIM is close to zero, at the output of the fishnet metamaterial the phase distribution is conformal to the exit surface, which is planar in our case. Therefore, the curved phase front, propagating from the Soret lens, is transformed into quasi-planar at the interface between the fishnet metamaterial and free space. Due to the inhomogeneity of the fishnet metamaterial, the NZIM regime depends on the number of the plates and tends to deviate significantly when this number is small. This can be clearly seen in Fig. 2.22, where the E_y component on *yz*-plane at 98.75 GHz is plotted for a different number q of cascaded plates. With the increase of q, the field distribution at the output of the hybrid Soret fishnet metamaterial lens tends to become planar. As a result, the radiation is more directive, i.e. higher directivity and smaller side lobe level. In Fig. 2.20(d) the numerical results for the gain are shown for an increasing number of plates q = 0, 1, 2, 3, 4, 5 (q = 0 refers to the case when only the first layer of the lens sandwiched between substrate layers (RO5880^{TM}) is present).

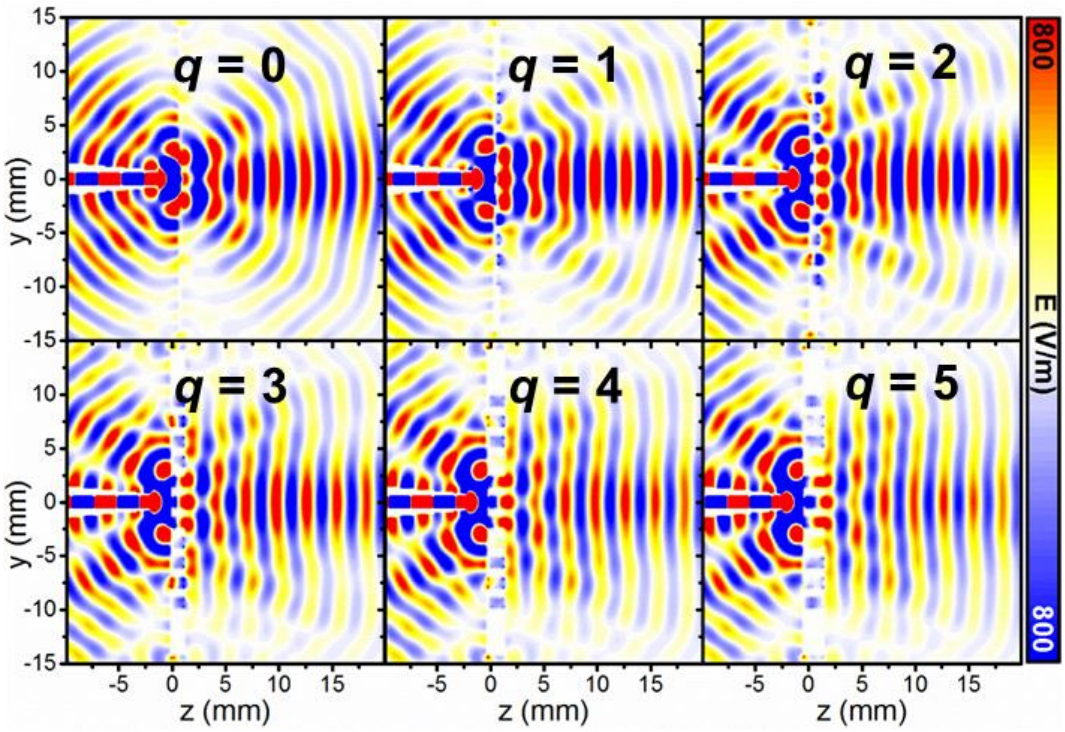

Fig. 2.22. Electric field distribution on the *yz*-plane. The colour-maps for the distribution of E_y component on the *yz*-plane for different number of stacked plates q.

From these figures, it is evident that increasing the number of plates improves the directivity of the hybrid Soret fishnet metamaterial lens. However, a large number results in an increased thickness and therefore higher losses. Hence, for $q > 3$, the gain decreases. As a compromise solution, we thus designed our lens with the first Soret layer plus 3 fishnet plates. Such design ensures lower losses and a maximum gain of metalens antenna.

2.4. Wood zone plate fishnet metalens.

In this section we demonstrate the next fishnet metalens – a low-profile WZP fishnet metalens, which is based on the fishnet metamaterial working in a near-zero regime with an

equivalent refractive index less than unity (n_f = 0.51). The Wood-type or phase corrected zone plate is also a member of the FZPL family and is free from the main drawback of the Soret-type lenses – high reflections from the even (odd) zones, which are made of opaque rings [79,145]. The metalens is made of alternating dielectric and fishnet metamaterial concentric rings. The use of fishnet metamaterial allows reducing the reflections from the lens, while maintaining low profile, low cost and ease of manufacturing. The lens is designed to work at the W-band of the millimeter-waves range aiming at antenna or radar system applications. The focusing performance of the lens along with its radiation characteristics in a lens antenna configuration have been studied numerically and confirmed experimentally.

2.4.1. Phased-corrected zone plates

In the phase corrected zone plate, the reflections from opaque zones are avoided by reversing the phase of the wave in these zones instead of blocking them, see Fig. 2.23. This idea was first suggested by Rayleigh [159] and implemented by Wood [160]. Therefore, the zone plate with different phase retardation for odd (even) and even (odd) zones is also known as Rayleigh-Wood lens or Wood zone plate lens (WZPL) and outperforms the Soret lens in diffraction efficiency.

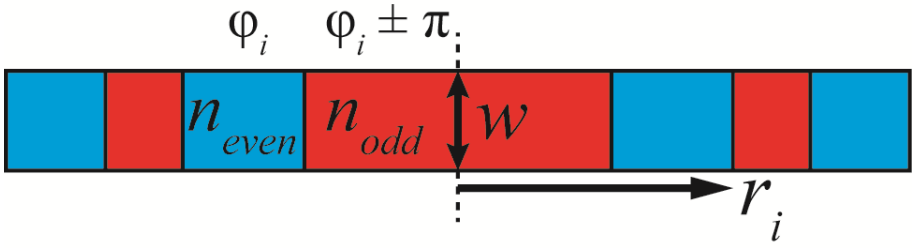

Fig. 2.23. Illustration of the WZPL (cut view). n_{odd}, n_{even} are the refractive indices of odd and even zones respectively, w is the thickness of the WZPL and r_i, φ_i are the radius and output phase of i Fresnel zone.

In general the thickness of the WZPL with two dielectric blocks can be calculated by [145]:

$$w = \frac{\lambda_0}{2\left(\sqrt{\varepsilon_{r2}} - \sqrt{\varepsilon_{r1}}\right)} \tag{2.8}$$

where ε_{r1}, ε_{r2} are the effective permittivities of the dielectrics, w is the thickness of the lens, λ_0 is the wavelength in free space. As it can be seen, the thickness of the WZPL depends on the difference between the refractive indices of the materials used for even and odd zones, and for materials with close values of refractive index the lens becomes too thick and heavy. Conversely, for high values of the refractive index the transmission coefficient decreases rapidly, reducing the focusing efficiency of the lens [79,145].

2.4.2. Exploiting fishnet metamaterial for Wood-type zone plate

One possible way to improve the focusing efficiency while maintaining the low profile and light weight is to apply a metamaterial for even or odd zones. As it was said in Chapter I

metamaterials enable the engineering of extreme values of refractive index, unattainable with natural materials, while tailoring simultaneously the effective impedance [11]. The latter avoid insertion losses due to reflection, which results in increasing overall efficiency in the case of lenses. Moreover, in case of a negative index of refraction the thickness of the WZPL can be reduced significantly, since the phase difference of π between odd and even zones can be obtained with small thickness ($<\lambda_0/4$). Here, we propose to use the fishnet metamaterial, which is the strongest candidate for microwave and millimeter wave range [25,32,153]. Due to the leaky-wave mechanism present in the fishnet metamaterial, it has the potential to lower insertion loss [25,161]. And as it has been demonstrated in this chapter, such metamaterial can be used for advanced lens design and its good performance is confirmed experimentally [52–54,146,147,161–163].

To create different optical paths in even and odd zones we use two materials: a standard dielectric (from a commercial substrate) and a fishnet metamaterial, which has dispersive nature and its index of refraction can be adjusted by varying, for instance, the separation between the plates d_z and the diameter a of the subwavelength holes. In this thesis we use the commercial substrate Rogers RO5880™, with thickness t_d = 0.381 mm, dielectric permittivity ε_r = 2.2 and loss tangent $\tan\delta = 9\times10^{-4}$. The unit cell of the fishnet metamaterial [inset of Fig. 2.13] has the following dimensions: d_x = 1.26 mm, d_y = 2.1 mm, d_z = 0.398 mm (metal thickness t_m = 0.017 mm and thickness of dielectric t_d = 0.381 mm) and variable a. And since the effective refractive index for a finite number of plates varies with the number of periods (due to the inhomogeneity of the fishnet metamaterial [164,165]), we use four plates (plus one dielectric plate as protection cover), since it is a good trade-off between total thickness and electromagnetic performance in terms of insertion loss [52–54,146,147,161,162]. Therefore, the total thickness of the structure is $w = 4t_m+5t_d$ = 1.97 mm ($\sim0.62\lambda_0$). It should be noted, that despite the theoretical minimal thickness can be $< \lambda_0/4$ (for negative refractive indices), the finite period d_z of the fishnet limits the minimal thickness of the metalens. In order to further reduce the total thickness, one can decrease the longitudinal period d_z by selecting different unit cell parameters (for instance by increasing the permittivity of the dielectric). From the equation (2.8) of the thickness of the WZPL we find the required refractive index n_f = 0.51 of the fishnet metamaterial for the given thickness of the metalens. Here we should note that the effective refractive index $n_f < 1$ allows to decrease the total thickness of metalens w. The effective refractive index of the finite fishnet metamaterial was obtained using the transient solver of CST Microwave Studio™ in the range 85-110 GHz. Periodic boundary conditions were used and the metal was modelled as copper ($\sigma_{Al} = 5.96\times10^7$ S/m). A fine hexahedral mesh was used, with minimum and maximum edge lengths of 0.007 mm ($\sim0.003\lambda_0$) and 0.64 mm ($\sim0.2\lambda_0$), respectively. The effective index of refraction n_m was calculated as:

$$n_m = \Delta\varphi \big/ (k_0 \Delta d) \tag{2.9}$$

where $\Delta\varphi$ is the phase variation along the total thickness Δd and k_0 is the wave number in free-space. The resulting color-map for effective index of refraction for 4 cascaded plates as a function

of frequency and radius of the hole is shown in Fig. 2.24(a). Also it is important to ensure a high transmission coefficient at the design frequency. To this end the transmission coefficient S_{21} was obtained as a function of frequency and radius of the holes and is plotted in Fig. 2.24(b). From these color-maps we chose 99 GHz ($\lambda_0 \sim 3.03$ mm) as the operation frequency and $a = 1.08$ mm as the diameter of the holes where the index of refraction is $n_f = 0.51$.

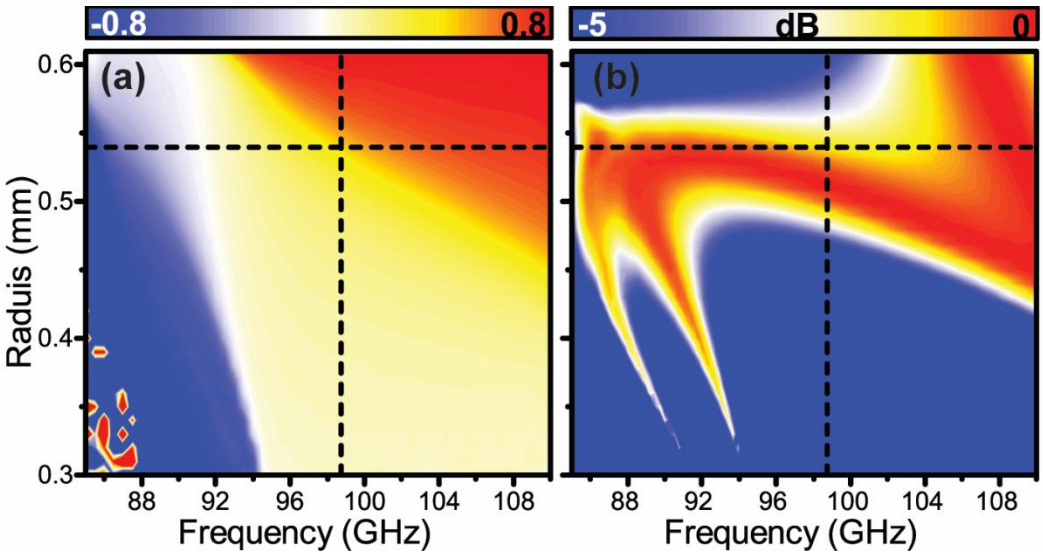

Fig. 2.24. (a) Equivalent refractive index, n_f, for a fishnet metamaterial made of four plates. Vertical and horizontal black dashed lines correspond to the working frequency $f_0 = 99$ GHz and hole diameter a = 0.54 respectively. (b) Transmission coefficient S_{21} for a four-plate fishnet metamaterial.

Fresnel zones

The radii of the Fresnel zones r_i of the WZPL can be calculated using the equation (2.6). It should be noted that the performance of the WZPL can be improved by increasing the number of quantization levels, i.e. going from half-wavelength to multilevel zone plates [158]. However, given the comparable size of the fishnet in-plane periods d_x and d_y with the radii of the Fresnel zones, the maximum number of quantization levels is $p = 2$. The total performance of the WZP fishnet metalens also depends on the filling ratio of the Fresnel zones, i.e. how well the zones are filled with holes. This, in turn, depends on multiple design parameters, such as FL, λ_0, i. For this reason, a three-dimensional analytical calculation was done initially by means of the Huygens-Fresnel principle for a fast prototyping. After the optimization procedure the following parameters were chosen: $FL = 22.8$ mm ($\sim 7.5\lambda_0$), $i = 7$, $p = 2$. The final lens profile and fabricated WZP fishnet metalens is shown in Fig. 2.25(a,b). The radius of the last zone was $r_7 = 24.5$ mm. The positive (odd) zones were made of holes of the same dimension as the fishnet (see Fig. 2.13). Thus, the whole structure has dimensions of 50 mm × 50 mm × 1.973 mm along the x-, y- and z-axis, respectively. The WZP fishnet metalens was fabricated using the commercial substrate Rogers RO5880™ with thickness $t_d = 0.381$ mm coated with a copper layer of thickness $t_m = 0.017$, by milling the holes and rings in the metal, keeping the dielectric substrate untouched. Then all layers and an additional protective outer layer were fastened with screws.

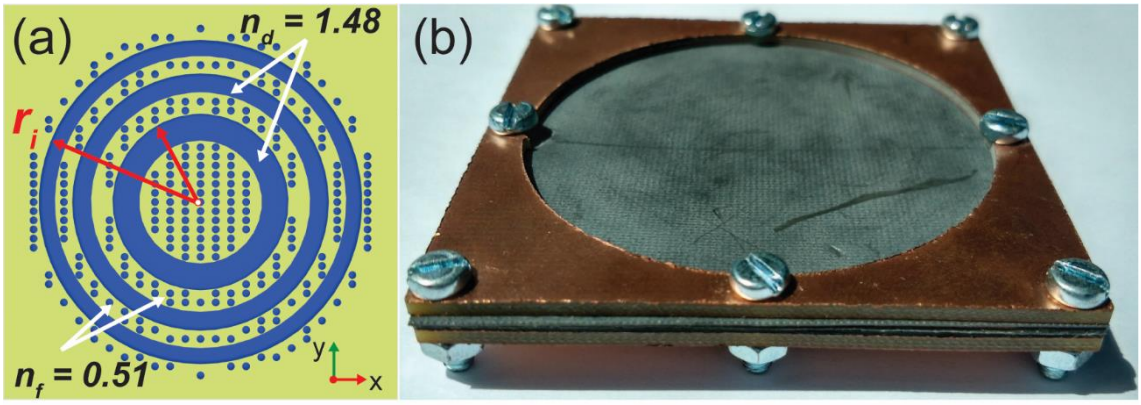

Fig. 2.25. (a) The final lens profile with seven zones. (b) Fabricated WZP fishnet metalens and its seven Fresnel zones.

2.4.3. Analytical and numerical analysis of focusing performance

Analytical results

The designed lens was analyzed using the Huygens-Fresnel principle. From this method the power distribution was calculated as a function of frequency and position along the optical axis of the lens [Fig. 2.26(a)].

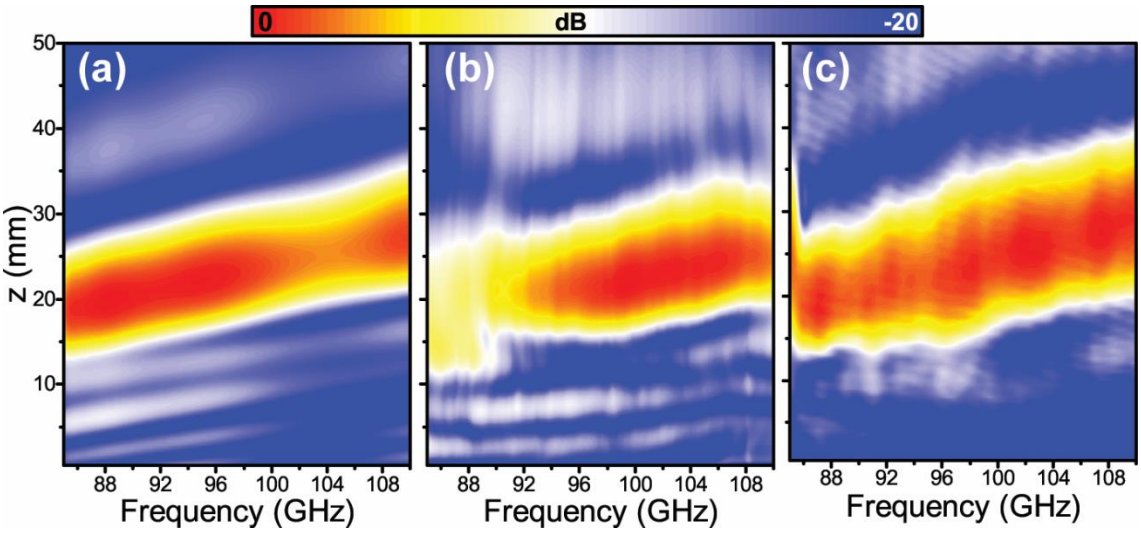

Fig. 2.26. Normalized power distribution along *z* axis for the frequency range 85–110 GHz: (a) analytical results, (b) simulation and (c) experimental results.

The absolute maximum in this case occurs at 96 GHz, with focal length FL_1 = 22.3 mm (~7.4λ_0). A secondary focus is observed at FL_2 = 41 mm (~13.5λ_0). Like any diffractive optical element, the WZPL suffers from chromatic aberration which results in a shift of the focal point with frequency. Finally, the power distribution color-maps were calculated at the design frequency for the *xz*- and *yz*-plane and presented in Fig. 2.27(a, b) respectively. In this figure clear foci can be observed with transverse dimension 0.66λ_0 for *xz*- and *yz*-plane.

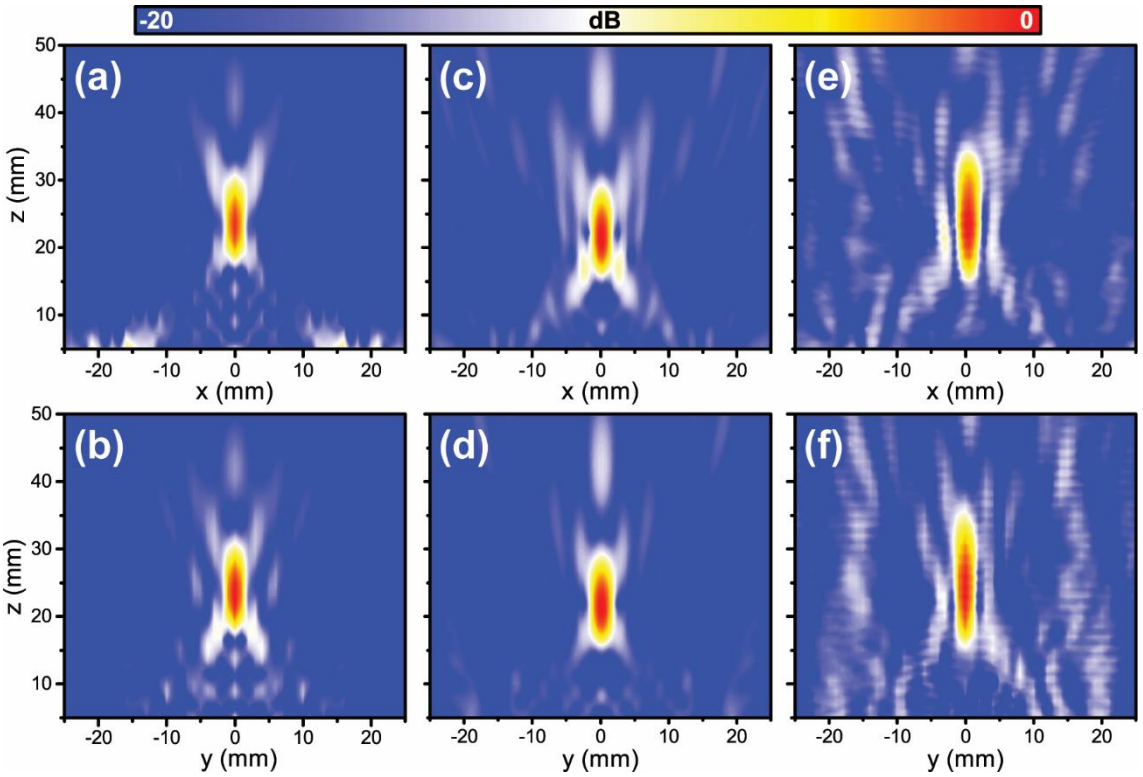

Fig. 2.27. Normalized spatial power distribution on the *xz*-plane (top row) and *yz*-plane (bottom row) for: (a, b) analytical results, (c, d) simulation results and (e, f) experimental results at f_0 = 99 GHz.

Simulation results

Next, a full-wave numerical analysis of the realistic 3D model of the fishnet WZPL was done using the transient solver of the CST Microwave Studio™. In the simulations, the metal copper layer was modelled using a lossy metal with the bulk conductivity of copper ($\sigma_{Al} = 5.96\times10^7$ S/m). A fine hexahedral mesh was used with minimum and maximum mesh cell sizes of 0.12 mm (~$0.04\lambda_0$) and 0.43 mm (~$0.14\lambda_0$), respectively. A vertically polarized (E_y) plane wave with normal incidence was used to illuminate the lens. To emulate a lens in free space, perfectly matched layers were used at the boundaries of the simulation box. Given the two-fold symmetry of the problem, electric and magnetic symmetries were imposed in the *xz*-plane (y = 0) and *yz*-plane (x = 0), respectively, to reduce the computation time. The simulation was run for a sufficiently long time to ensure steady-state regime so that the continuous-wave information computed by Fourier transformations was valid. The color-map of the power spectrum as a function of *z* position was obtained by placing *E*-field and *H*-field probes along the optical axis (*z*-axis) with a 0.5 mm step. These probes record the waveform at their positions and by Fourier transformation the *E*- and *H*-field spectra are obtained.

The obtained power spectrum is shown in Fig. 2.26(b). The focal point shifts within the frequency range 92-108 GHz, from 20 mm ($6.6\lambda_0$) up to 25 mm ($8.2\lambda_0$) along the *z*-axis. These results resemble the analytical results, with some differences. Firstly, a blueshift is noticeable. This arises from the fact that in the analytical model the dispersion of the fishnet metamaterial was not taken into account for the sake of simplicity. Secondly, since in the numerical simulations

the amplitude of each hole is obtained more accurately, the secondary focal spot in simulations is more pronounced. The power enhancement (i.e., the ratio between the intensity with and without lens for each *z* position) corresponding to the first maximum is 19 dB at 99.3 GHz ($\lambda_0 \sim 3.04$ mm) with a focal distance $FL = 22.5$ mm ($\sim 7.4\lambda_0$). Finally, in Fig. 2.27(c,d) the power distribution at 99.3 GHz is shown for *xz*- and *yz*-planes respectively, with *FWHM* of the foci $0.66\lambda_0$ for *xz*- and *yz*-plane. These color-maps also match the analytical results with some minor, yet expected, differences.

2.4.4. Experimental measurements of focusing properties

The experimental characterization is done using an AB Millimetre™ quasi-optical vector network analyzer with the setup illustrated in Fig. 2.28. The metalens is illuminated with a *W*-band corrugated horn antenna, placed at distance $L = 3000$ mm from the lens. At this distance the radius beam waist of the Gaussian beam is ~310 mm, which ensures a uniform illumination of the lens. The *xz* raster scanning is done using a waveguide probe WR-8.0 as a detector. Millimeter-wave absorbers are used throughout the setup to mimic anechoic chamber conditions.

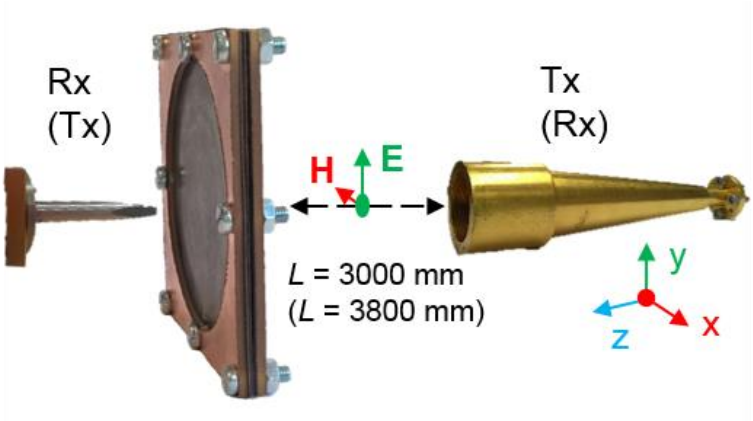

Fig. 2.28. Scheme of experimental setup for the focal measurements (radiation measurements) with a waveguide probe as a receiver (transmitter) and a standard high gain horn antenna as a transmitter (receiver).

First, the calibration was done by recording the transmitted power without the lens. Next, the power distribution as a function of frequency and *z* position was measured by moving the detector from 5 to 50 mm away from the metalens along the *z*-axis (with 0.5 mm step) while recording the spectrum in the range 85-110 GHz. The experimentally measured color-map for the power spectrum along the optical *z*-axis is shown in Fig. 2.25(c). The experimental results match our previous analytical and numerical results [Fig. 2.26(a,b)]. The maximum power enhancement 12.44 dB occurs at 97.75 GHz with a focal distance $FL = 23$ mm ($7.57\lambda_0$). Next, the spatial power distribution at this frequency was obtained experimentally for the *xz*-, *yz*-planes, see Fig. 2.27(e,f). The qualitative good agreement with the numerical results is evident. The transverse dimension of the foci is $0.69\ \lambda_0$ for *xz*- *yz*-plane. To facilitate the comparison, all the results are gathered in Table III. Since in the analytical analysis we do not estimate the radiation performance of the metalens in antenna configuration, in Table III the corresponding fields are left blank.

Table III. Focal properties and radiation pattern parameters of WZP fishnet metalens.

	FL[1], mm	***FWHM***[2], mm		***DF***[3], *mm*	**HPBW**[4]**, deg**		**FNBW**[5]**, deg**		**FSLL**[6]**, deg**	
	E-plane *H*-plane	*E*-plane	*H*-plane	*E*-plane *H*-plane	*E*-plane	*H*-plane	*E*-plane	*H*-plane	*E*-plane	*H*-plane
Analytical	22.3 $7.4\lambda_0$	2 $0.66\lambda_0$	2 $0.66\lambda_0$	7.8 $2.6\lambda_0$	-	-	-	-	-	-
Simulation	22.5 $7.4\lambda_0$	2 $0.66\lambda_0$	2 $0.66\lambda_0$	7.8 $2.6\lambda_0$	4	3.6	14	10	-25	-19
Experimental	23 $7.6\lambda_0$	2.1 $0.69\lambda_0$	2.1 $0.69\lambda_0$	9.64 $3.2\lambda_0$	4	3.6	9.5	9.5	-14	-12

[1]FL is the focal length.
[2]FWHM is the full width at half maximum.
[3]DF is the depth of focus.
[4]HPBW is the half-power beam width
[5]FNBW is the first null beam width
[6]FSLL is the first side-lobe level

2.4.5. Wood zone plate fishnet metalens antenna

Next we investigate the performance of WZP fishnet metalens in a lens-antenna configuration. For the numerical characterization, the simulations included the realistic waveguide probe WR-8.0 as a feeder and placed at the previously numerically-found focal position z = 22.5 mm. The rest of the simulation parameters were those described previously. Far-field monitors were used to record the radiation pattern of the lens within the frequency range 85-110 GHz with a step of 0.25 GHz

For the experimental verification, a waveguide probe WR-8.0 was used as a feeder placed at the experimental focal length *FL* = 23 mm ($7.6\lambda_0$). A schematic of the experimental setup is shown in Fig. 2.28. A high gain standard horn antenna was placed 3800 mm away from the flat face of the zoned lens to detect the radiated power. The radiation diagram was measured by rotating the feeder and metalens from -90 deg to +90 deg with 1 deg step. Absorbing material was also used throughout the setup for reflection suppression.

Numerical results of co- and cross-polar angular power distributions for *E*- and *H*-plane are displayed in Fig. 2.29(a-d). The maximum is located at 99.5 GHz, in agreement with the previous numerical study. The normalized experimental results for co- and cross-polar components as a function of frequency and angle are shown in Fig. 2.29(e-f) *E*-plane and Fig. 2.29(g-h) *H*-plane. The experimental maximum is located at 99 GHz, i.e. slightly shifted from the frequency obtained by simulation. In Fig. 2.29(a,b) to facilitate the comparison, the normalized simulation and experimental radiation patterns for the *E*- and *H*-plane are presented. One can see that the radiation patterns are in very good agreement.

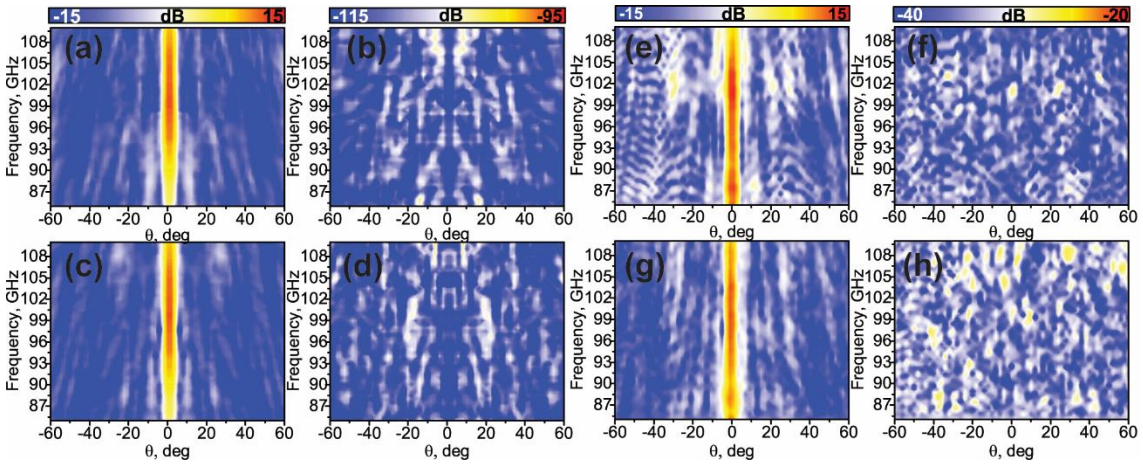

Fig. 2.29. Numerical (a–d) experimental (e–h) radiation pattern of the WZP fishnet metalens antenna in the frequency range 85–110 GHz: co- (a, c, e, g) and cross-polarization (b, d, f, h). (a, b, e, f) *E*-plane and (c, d, g, h) *H*-plane.

To complete the study, the numerical and experimental gain for the WZP fishnet metalens antenna is presented in Fig. 2.30(c). In the experiment, the gain was obtained by comparing our lens antenna with a standard horn antenna following the gain comparison method [158]. A high gain of 16.6 dB is found experimentally at 99 GHz (solid red line). The numerical value of 24.3 dB is found at 99.5 GHz by using the software-implemented far-field monitors (dashed blue line). The lower values of gain in the experiment can be explained as a result of different factors, such as experimental errors (misalignment, accuracy of distance measurement) and by defects in the fabrication (non-perfect contact between dielectric and metallic plates, errors in the radius of the holes) and effective substrate losses higher than nominal values. In order to confirm these factors, additional simulations for the complete 3D model of the metalens-antenna were run with diameter of holes a = 1.2 mm, an air gap of 80 μm and higher dielectric loss tangent tanδ = 0.015. The resulting gain is shown in Fig. 2.30(c) (dashed dotted black line). An error in the diameter of the holes along with an air gap of 80 μm between metallic and dielectric plates changes the effective permittivity of the fishnet metamaterial and therefore the phase at the output of each hole. This leads to a non-optimal phase difference (which is π in the ideal case) between the odd and even rings, and therefore to lower gain and frequency shift of the maximum. Consequently, the numerical gain of the lens with higher losses, error in the radius of the holes and air gap is closer to the experimental gain. To facilitate the comparison, all the results are gathered in Table III.

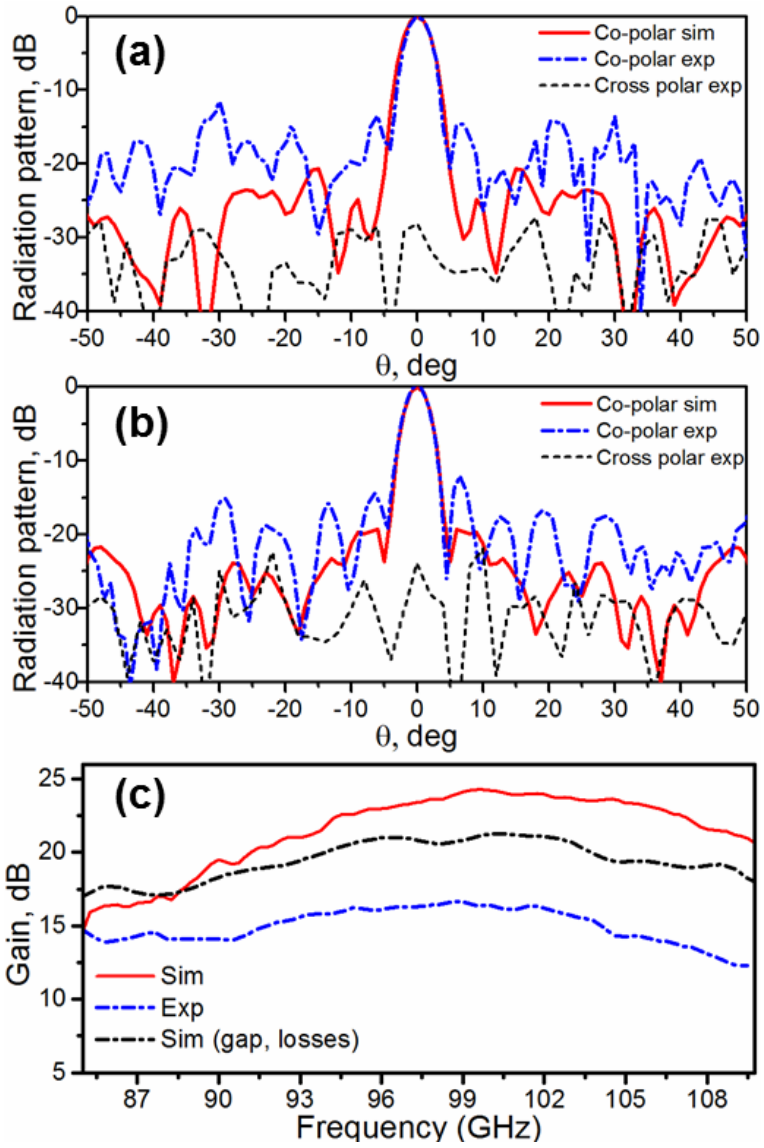

Fig. 2.30. Normalized radiation patterns for: (a) *E*-plane and (b) *H*-plane at frequency 99 GHz (simulation and experimental). (c) Simulation gain (solid red line), experimental gain (dash dotted blue line) and simulation gain, considering air gaps, larger diameter of subwavelength holes and losses (dash dotted black line).

Chapter 3. Metamaterials and metasurfaces for invisibility cloaks

The ability to become invisible was primarily a subject of different tales and science fiction novels, in which heroes could hide from others by wearing a special cloak. However, recently thanks to the rapid progress of metamaterials, the path towards invisibility is gradually becoming possible. The topic is evolving fast and now is one of the most thrilling applications based on metamaterials. In this chapter we discuss the basics of invisibility cloaks and introduce two different cloaks: a metasurface based carpet cloak, which is able to conceal an object on a ground plane from the incident wave, and a transformation based cloak for diffusive light.

3.1. Introduction to cloaking devices

The principle of invisibility is depicted in Fig. 3.1. In this figure it can be seen that the main phenomena why an object can be detected by external observer are the scattering and absorption from the object. Ideally, if we manage to completely eliminate these factors for all angles, independently of the environment, of the position of the observer or the polarization of the incoming wave, and over a wide frequency range, we could achieve the invisibility.

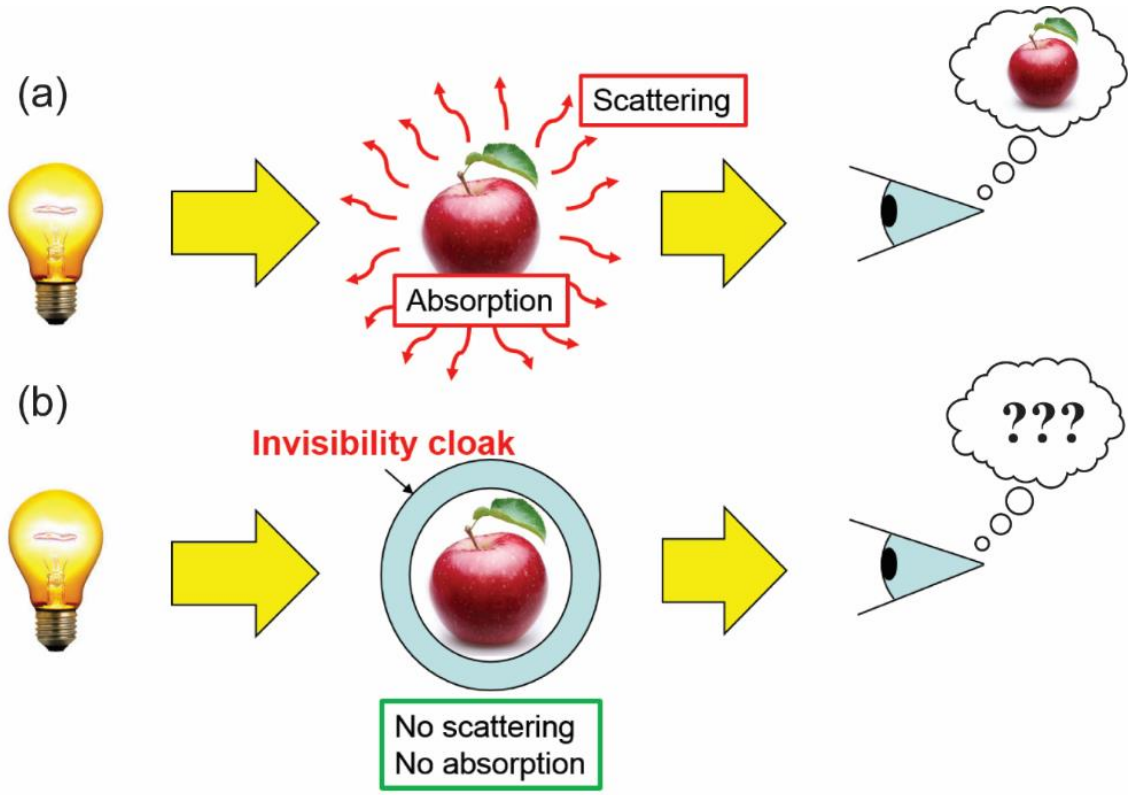

Fig. 3.1. Principle of invisibility cloak. (a) Scattering and absorption from the object make it visible to an external observer. (b) The invisibility cloak eliminates any scattering or absorption from the object making it invisible.

Historically, several approaches have been used for this purpose, the most popular are:

- **Radar absorbing materials.** In this method most of the incident wave is absorbed and the reflections are minimized. This approach can work for monostatic radar systems (the transmitter and receiver are at the same location), which detect objects by detecting the reflected waves. However, this method in general does not work for bistatic radar systems (the transmitter and receiver are not at the same location).
- **Plasmonic and mantle cloaking (scattering cancellation technique).** In 2005, a new method was proposed to cloak nanoparticles by coating them with homogeneous and isotropic materials, whose permittivity is less than unity within the optical frequency region [106]. In mantle cloak [166], instead of using isotropic homogenous material, a frequency selective surface is used [167], which gives an ultrathin and light weight prototype. Such techniques provide a robust performance and simplified design. However, the scattering cancellation technique is limited by size of particle. If the size of the particle is not small, the design becomes more complicated for a practical realization.
- **Transformation optics (TO) based cloaking.** In 2006, Pendry *et al*. [65] and Leonhardt [66] proposed a new cloaking method based on coordinate transformation, which is able to cloak a large object in all directions regardless of the object to be concealed. However, the cloaks based on this approach are usually quite thick, suffer from losses, and are challenging to build.

In Chapter I we already discussed metamaterials, which allow to tailor at will the intrinsic electromagnetic parameters of a composite, providing interesting solutions for one of the most intriguing quests of electromagnetism – invisibility cloaking [65,66]. In this chapter we discuss two leading categories of cloaking mechanisms listed above: transformation optics [65,66] and scattering cancelation [106,108,168]. We present the design of metasurface based carpet cloak, which have been recently proposed as an alternative cloaking technique [111,112]. The performance of the carpet cloak is numerically analyzed and experimentally verified. Moreover, we design a transformation based cloak for diffusive light, which works in the static as well as in the transient regimes.

3.1.1. Transformation optics for hiding objects

The technique based on transformation optics represents an idea to manipulate the electromagnetic flow using a transformation that stretches the coordinate grid of space, as showed in Fig. 3.2.

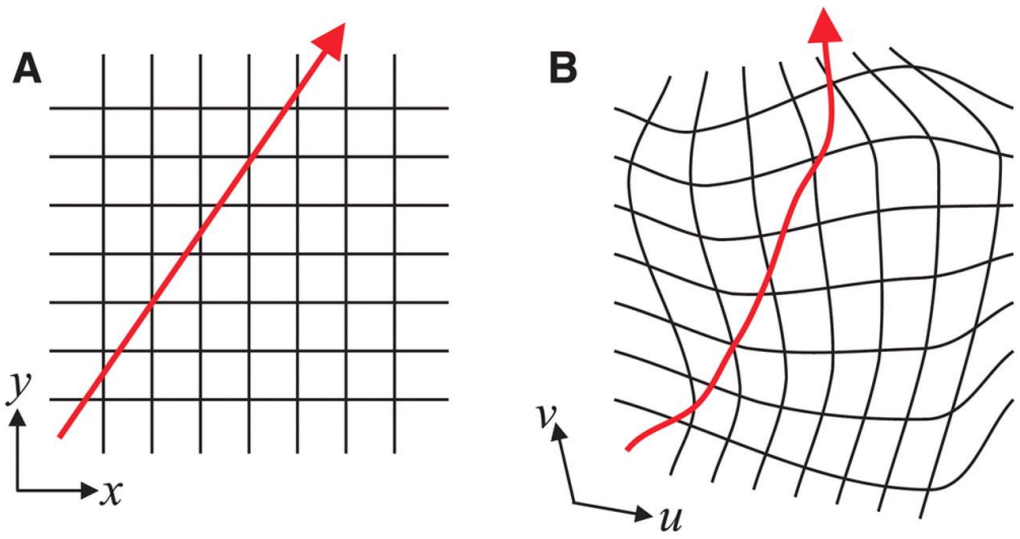

Fig. 3.2. Illustration of the ray distortion offered by transformation optics. ©2006 AAAS. Reprinted with permission, [65].

In Fig. 3.2(a), the red arrow represents a ray of light going through a homogeneous material. As it is shown in Fig. 3.2(b), by stretching and compressing the Cartesian space, it is possible to bend the ray at will and control its propagation. The form-invariance of Maxwell's equations under a coordinate transformation allows to treat the electromagnetic propagation in the transformed system as a propagation in the untransformed coordinate system with a specific functional distribution of the permeability (μ) and permittivity (ε) tensors. Metamaterials, which allow to control the inhomogeneity and anisotropy of CP and therefore to mimic any coordinate transformation in the physical space, can be used to force light to follow curved coordinates.

By substituting (1.2) into (1.1) we can write Maxwell's equations as:

$$\begin{aligned} \nabla \times \boldsymbol{E} &= -i\omega\mu\mu_0 \boldsymbol{H} \\ \nabla \times \boldsymbol{H} &= i\omega\varepsilon\varepsilon_0 \boldsymbol{E} \end{aligned} \tag{3.1}$$

After a coordinate transformation $x' = x'(\boldsymbol{x})$ is applied, the equations maintain the same form in the transformed coordinate system:

$$\begin{aligned} \nabla \times \boldsymbol{E}' &= -i\omega\mu'\mu_0 \boldsymbol{H}' \\ \nabla \times \boldsymbol{H}' &= i\omega\varepsilon'\varepsilon_0 \boldsymbol{E}' \end{aligned} \tag{3.2}$$

where the permittivity tensor (ε′) and permeability tensor (μ′) in the transformed coordinate system are related to the original ε and μ and by the relationships:

$$\begin{aligned} \varepsilon'^{i'j'} &= \left|\det\left(\Lambda_i^{i'}\right)\right|^{-1} \Lambda_i^{i'} \Lambda_j^{j'} \varepsilon^{ij} \\ \mu'^{i'j'} &= \left|\det\left(\Lambda_i^{i'}\right)\right|^{-1} \Lambda_i^{i'} \Lambda_j^{j'} \mu^{ij} \end{aligned} \tag{3.3}$$

where $\Lambda_\alpha^{\alpha'} = \partial x^{\alpha'} / \partial x^{\alpha}$ denotes the Jacobian transformation matrix between the virtual space and the original space.

The first TO based spherical cloak was proposed simultaneously and independently by Pendry [65] and Leonhardt [66] in 2006. They theoretically proposed to squeeze the space from an original volume of free space with radius R_2 into a shell with radius R_1 surrounding the object to be concealed. In this way, the external waves, which would have fallen on the object, are effectively guided around the object by the curved coordinates (constructed with anisotropic and inhomogeneous metamaterials), as shown in Fig. 3.3. Inside this region an arbitrary object can be hidden because it remains untouched from external radiation.

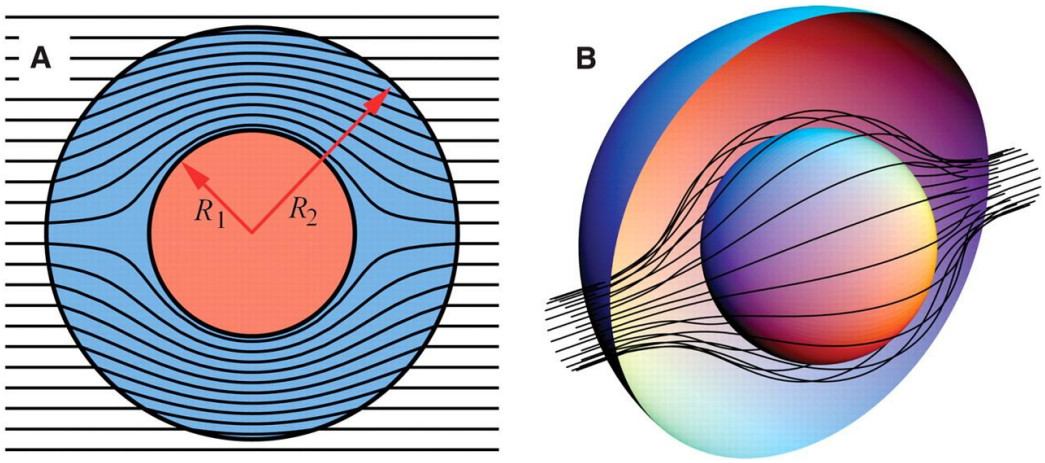

Fig. 3.3. Principle of operation of transformation-based spherical cloaks. ©2006 AAAS. Reprinted with permission, [65].

The corresponding radial transformation can be written as:

$$\begin{aligned} r' &= R_1 + \frac{r(R_2 - R_1)}{R_1} \\ \theta' &= \theta \\ \phi' &= \phi \end{aligned} \tag{3.4}$$

Using (3.3) one obtains the required CP tensors for the cloak [65]:

$$\begin{aligned} \varepsilon_{rr} &= \mu_{rr} = \frac{R_2}{R_2 - R_1}\frac{(r - R_1)^2}{r^2} \\ \varepsilon_{\theta\theta} &= \mu_{\theta\theta} = \frac{R_2}{R_2 - R_1} \\ \varepsilon_{\phi\phi} &= \mu_{\phi\phi} = \frac{R_2}{R_2 - R_1} \end{aligned} \tag{3.5}$$

Note, that for $r < R_1$ the CP can take any values and do not contribute to electromagnetic scattering, since the power flow is successfully rerouted around this region. For the 2D case of such cloak, i.e. cylindrical cloak, similar equations can be obtained. As an example, the performance of the cylindrical cloak is demonstrated in Fig. 1.8(b).

However, despite its elegant form on paper, it is impossible to fabricate the ideal cloak. This is due to the strong demands on bulk metamaterial designs, such as a specific profile of

inhomogeneity and anisotropy of the material parameters. Moreover, since most of the cloaks are designed to work in free space, the permittivity and permeability tensors of the cloak material must be identical, in order to guarantee impedance matching and therefore no reflection from the interfaces. Also, a ray of light that normally does not need time to cross the center of untransformed coordinate system ($r = 0$), now is required to propagate in zero time along the finite-length circle with $r = R_1$. This implies a superluminal (faster than light) phase propagation (phase velocity $v_p > c_0$), which requires extreme values of CP. Although such extreme values are attainable with metamaterials, they result in inevitable material losses due to the material resonances. And, as it was depicted in Fig. 3.1, the absorption losses result in unwanted scattering, making the object visible.

In general, some approximations have to be made in order to simplify the design. Nevertheless, even after the simplification, such cloaking devices are difficult to realize in practice, due to their high complexity. Schurig et al. experimentally verified the concept of the first transformation cloak, using a simplified 2D model [5][4]. Fig. 3.4 shows a photograph of the first experimental cloak at microwaves frequencies and the experimental results are shown in Fig. 3.5.

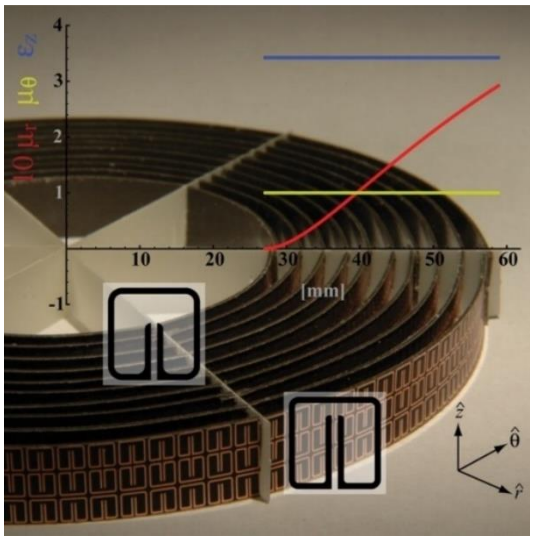

Fig. 3.4. Photograph of first ex perimental transformation based cloak at microwave frequencies. ©2006 AAAS. Reprinted with permission, [5].

The simulated field for the ideal and simplified cloak are shown in Fig. 3.5(a-b) respectively. The measured fields for a bare cylinder and cloak are shown in Fig. 3.5(c-d), where the wave fronts are less disturbed when cloak is applied, demonstrating the cloaking performance. It is obvious that the simplified design even in numerical analysis cannot give the ideal cloaking performance and the experimental results remarkably resemble the simulations.

[4] In their experiment they studied a cylindrical cloak (r, θ, z), where components of CP tensors have only radial dependence. Moreover, they forced constant values for all components of, except for μ_{rr}. A disadvantage of such simplification is that it leads inevitably to reflections due to the impedance mismatch, making the cloak detectable.

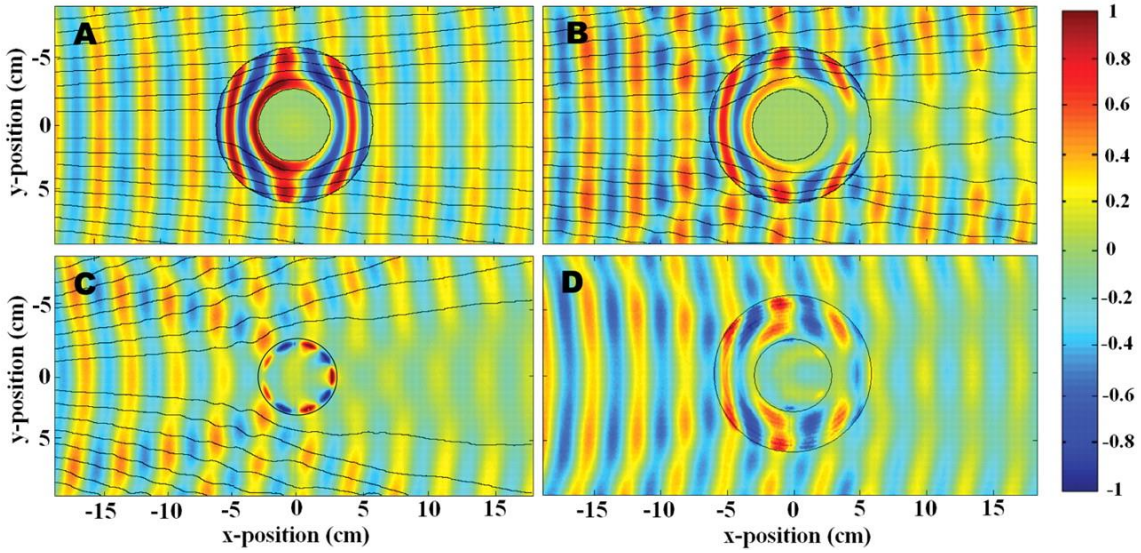

Fig. 3.5. Numerical and experimental electric field for the cylindrical transformation cloak. a) Simulation, ideal cloak. b) Simulation, eikonal cloak. c) Measurements, bare cylinder. d) Measurements, covered cylinder. ©2006 AAAS. Reprinted with permission, [5].

3.1.2. Scattering cancellation technique

The next approach is radically different from the TO based cloaking as it consists in cancelling the dominant scattering terms of scattered field. In contrast to the very complicated material properties of the transformation cloaks, the scattering cancellation cloak only requires homogeneous and isotropic materials and provides a more robust performance. However, this technique is limited by the size of the cloaked objects [110] and in its simplest form can be only applied to objects with size comparable to the wavelength. For large objects the design becomes cumbersome due to the fact that the number of the scattering harmonics and therefore the number of cloaking layers increases with the size of the object, leading to similar complexities as the TO approach. Although this is not necessarily a strong drawback, since there are several applications which do not require a cloaking of large objects, such as non-invasive sensing [169].

The scattering problem can be approached using the Mie expansion in spherical harmonics[5]. Therefore, the scattered field from a plane wave can be described as the discrete sum of spherical harmonics with complex amplitudes c_m^{TE} and c_m^{TM} ($m \geq 1$), respectively for the *TE* and *TM* spherical waves [170,171]. In this problem we consider a monochromatic wave $\hat{x}E_0e^{ik_0z}$ propagating in vacuum, which is scattered by an arbitrary object placed at the origin of a spherical coordinate system (r,θ,ϕ). The scattered wave then can be expanded in spherical harmonics as [17,172]:

[5] In this example we use a spherical symmetry for sake of simplicity, but it can be done for arbitrarily shaped objects as well.

$$\vec{E}_{scat} = E_0\left(\sum_{m=1}^{+\infty} c_m^{TM}\nabla\times\nabla\times\left(\vec{r}\psi_m^1\right) + i\omega\mu_0\sum_{m=1}^{+\infty} c_m^{TE}\nabla\times\left(\vec{r}\psi_m^1\right)\right) \tag{3.6}$$

where μ_0 is the free-space permeability, ψ_m^n are scalar spherical harmonics, solutions of the Helmholtz equation (n = 1 due to spherical symmetry) in the spherical coordinate system (r,θ,ϕ). Then, the total scattering cross-section σ_{scat} can be expressed as a function of the Mie scattering coefficients c_m^{TE} and c_m^{TM} [173]:

$$\sigma_{scat} = \frac{2\pi}{|k_0|^2}\sum_{m=1}^{\infty}(2m+1)\left(\left|c_m^{TE}\right|^2 + \left|c_m^{TM}\right|^2\right) \tag{3.7}$$

In this equation after a given order m =N_{max} the successive scattering coefficients have negligible impact on σ_{scat} [172]. The value of N_{max} usually depends on the physical or electrical size of the scatterer and increases for larger objects. Therefore, by canceling the dominant ($m \leq N_{max}$) scattering coefficients in (3.7), it is possible to achieve the invisibility of a given object, which is the main principle of the scattering cancellation technique.

As it was mentioned above there are two main categories of the scattering cancellation cloaking: plasmonic cloak and mantle cloak. The plasmonic cloak is made of homogeneous isotropic materials, which in the ideal case should be less than unity[6]. This is the reason of the plasmonic label, since these permittivity values are available in plasmonic materials with plasma-like dispersion. As an example we take a small dielectric sphere with radius a and electromagnetic parameters ε, μ that scatters an incident plane wave. The sphere is coated with a shell of radius a_c and material with parameters ε_c, μ_c [see Fig. 3.6(a)]. For the sake of simplicity, the radius of the shell is assumed to be small $k_0 a_c << 1$, so the scattered wave is dominated by first-term order of scattering harmonics (m = 1)[7]. By imposing the boundary conditions, the scattering coefficients c_m^{TE} and c_m^{TM} can be calculated as [174]:

$$\begin{aligned} c_1^{TE} &\approx 0 \\ c_1^{TM} &= -j\left(k_0 a_c\right)^3 q\left(\varepsilon_c,\gamma\right) \end{aligned} \tag{3.8}$$

where q is a function of ε_c and $\gamma = a/a_c$. This parameter can reach zero when the following equation holds [106]:

$$\left(\frac{a}{a_c}\right)^3 = \frac{\left(\varepsilon_c-\varepsilon_0\right)\left(2\varepsilon_c+\varepsilon\right)}{\left(\varepsilon_c-\varepsilon\right)\left(2\varepsilon_c+\varepsilon_0\right)} \tag{3.9}$$

In case the core is PEC ($\varepsilon \rightarrow i\infty$) and assuming a 2D cylindrical geometry the invisibility condition becomes [106]:

[6] The principle of plasmonic cloaking can be interpreted as the cancellation of the induced dipole moment in the cloak and object by using media with opposite polarizabilities [106,174]

[7] For big objects or for multi-frequency operation several layers will be required, since one layer can cancel only one order and the rest of the orders are not non-zero anymore.

upna Universidad Pública de Navarra Nafarroako Unibertsitate Publikoa

$$\left(\frac{a}{a_c}\right)^2 = \frac{(\varepsilon_c - \varepsilon_0)}{(\varepsilon_c + \varepsilon_0)} \tag{3.10}$$

which can be satisfied for $0 < \varepsilon_c < \varepsilon_0$. The full-wave numerical simulations of this example are shown in Fig. 3.6(b,c). The impinging TM plane wave is scattered by PEC cylinder, as can be seen in Fig. 3.6(b). When the cloak is applied the object becomes invisible for an incoming wave, resulting in an almost undisturbed EM field distribution, see Fig. 3.6(c).

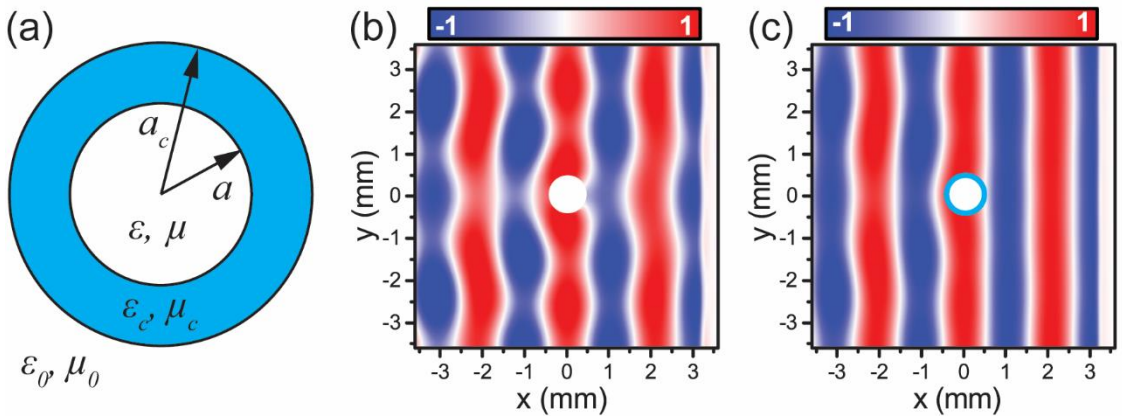

Fig. 3.6. (a) Cross section of a spherical scatterer composed of two concentric layers of different isotropic materials. Numerical magnetic H_z field for the plasmonic cloak. (b) Bare PEC scatterer with $a = \lambda_0/5$. (c) Covered with plasmonic shell with radius $a_c = 1.106a$ and $\varepsilon_c = 0.1$, $\mu_c = 5.1$. The numerical simulations were performed at $f = 150$ GHz using COMSOL™.

The second category of scattering cancellation technique includes the mantle cloaks, where the isotropic homogeneous materials are replaced with an ultrathin isotropic metascreen in order to tune the surface impedance and cancel the scattering from the object. The advantage of this approach is that it leads to ultrathin and light weight designs with a robust performance. Moreover, since the invisibility can be achieved by controlling the surface impedance, for this purpose one can use a graphene patches [175], which allow changing dynamically the surface conductivity as it was discussed in Chapter I. However, at visible frequencies, plasmonic cloaks may be more advantageous, since they use natural materials and patterned surfaces with subwavelength resolution are more difficult to fabricate. The scattering cancellation technique has been extensively studied [176–178] and confirmed experimentally [108,179], demonstrating a good performance in a broader frequency range than transformation cloaks.

3.1.3. Carpet cloaks

The challenging requirements on the electromagnetic parameters imposed by TO can be relaxed using a different cloaking approach that loosens up the causality limitations in size and bandwidth. An alternative approach is that known as carpet cloaking or ground cloaking. The main idea is to make a bump appear as a flat ground plane. The principle of this type of cloak is shown in Fig. 3.7 [103].

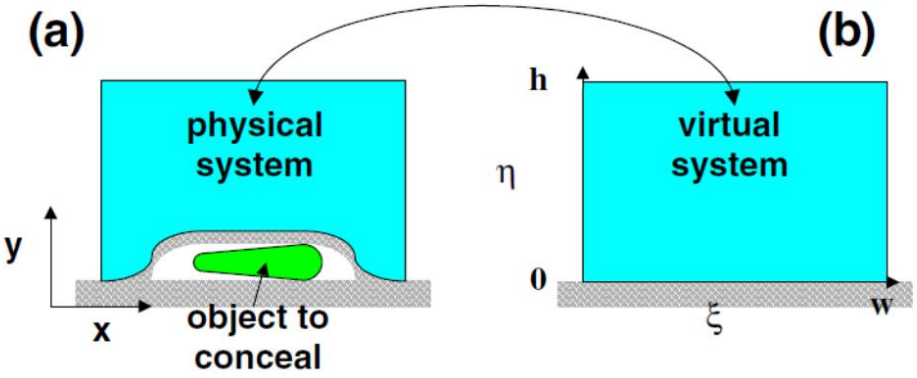

Fig. 3.7. Principle of operation of a carpet cloak. ©2008 APS. Reprinted with permission, [103].

In this figure the transformation is applied to the medium represented as a blue region. The grey regions correspond to PEC. In this case cloaking is achieved by tailoring the cloak material properties to effectively compress the volume of an object (PEC bump) to an infinitesimally thin sheet over a ground plane. This problem has gained the interest of many researchers, due to its inherently relaxed constraints, its simplified design, and wide range of applications. Transformation-based carpet cloaks exploit a quasi-conformal mapping [103,180], which allows minimizing the anisotropy of the required materials and can be implemented using non-magnetic materials with an inhomogeneous permittivity [181], simplifying the design and reducing absorption losses. Low refractive index gradient materials have been explored to improve the impedance matching with free-space [182].

In Fig. 3.8 are shown the numerical results of full wave simulations obtained for the carpet cloak [103]. From this figure it is obvious that without the cloak [Fig. 3.8(a)] the bump scatters the incident beam in different directions. Conversely, when the cloak is applied to the bump [Fig. 3.8(b)], the reflected Gaussian beam is recovered as if the mirror were flat. The main drawback of this method is that it works only in a 2D geometry and requires a flat mirror, which obviously narrows the range of possible applications. Moreover, the proposed cloak is still volumetric and non-trivial to realize.

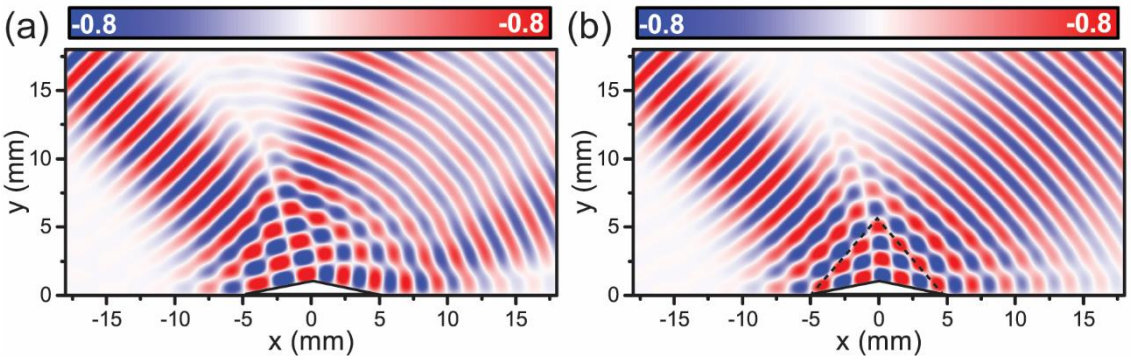

Fig. 3.8. (a) Electric field distribution for the reflection by PEC mirror with a bump without the cloak and (b) covered by the carpet cloak (contained within the dashed triangular). The numerical simulations were performed at f = 150 GHz using COMSOL™.

Another important hurdle for practical applications of carpet cloaks is the lateral shift they introduce under the isotropic approximation. Unfortunately, the introduced lateral shift is comparable to the case when a ground plane is placed above the cloaked object to suppress its scattering. Since the cloaking medium is typically denser than free-space, the beam inside the cloak is refracted into a smaller angle. However, if we require that a finite-size beam emerges from the cloak at the same location as it would be reflected by a flat ground plane, it should be refracted into a larger angle, which is only possible with anisotropic materials. This lateral shift presents a serious problem, since an external observer still can notice that the beam emerges from a different point [183], and it also begs the question of whether another flat reflector on top of the bump would not provide a simpler solution to the problem. This problem is illustrated in Fig. 3.9 [183].

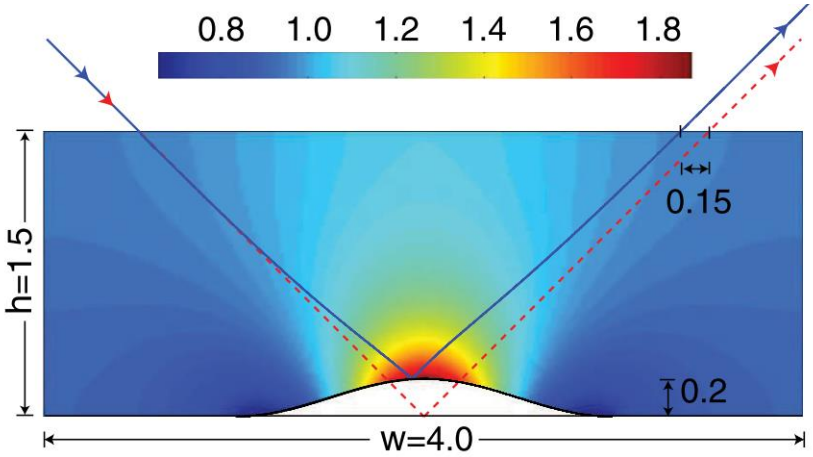

Fig. 3.9. A ray (blue solid line) incident at 45 deg with respect to the normal onto an isotropic ground-plane cloak. The red dotted line represents the trajectory of a ray reflecting on a flat ground plane. Notice the distorted ray has been shifted on top of the cloak toward the incident point. ©2010 APS. Reprinted with permission, [183].

Despite the difficulties in the practical realization due to the complexity of the design, the transformation based cloaks have been experimentally demonstrated from microwave to optical range [69,104,105,181,182], demonstrating the cloaking performance.

3.2. Metasurface based carpet cloak

To overcome the issues associated with conventional ground cloaking approaches, recently it has been proposed that covering a bump with a specially designed surface can reduce unwanted scattering from an arbitrary bump, creating an effective ultrathin *cloaking surface* [111,112]. The metasurface is used to build a phase distribution on the bump edge equal to the phase response created upon reflection from a conducting ground plane, i.e. when no bump is present. In this case, for the external observer the reflected wave will have the same phase distribution as if it were reflected from the ground plane, creating an ultrathin, and relatively simple cloaking configuration for practical implementation. Moreover, due to surface phase compensation, the metasurface cloak does not create a lateral shift [111]. Obviously this approach is dependent on

the object to hide and the illumination, but, given its robustness, it may provide a viable solution for several practical applications. Here, we propose a design of such ultrathin metasurface carpet cloak and perform numerical and experimental analysis of its cloaking performance.

3.2.1. Carpet cloak design

Fig. 3.10 shows the general scheme of the cloak and the object. An oblique incident wave, with angle of incidence θ (with respect to the horizontal ground plane), illuminates a PEC bump with a tilt angle ψ. Any arbitrary object we aim to conceal can be placed inside the bump, as long as it fits in its volume. The goal is to create a field distribution on the external boundary of the object (dashed line), identical to the case when no bump is presented, in view of the field equivalence principle. This technique is different from carpet cloaks based on quasi-conformal mapping, where the object is concealed by controlling the propagation of the incident waves and effectively isolating the hidden region from the incident wave. Here, reconstruction of the field can be done by introducing an abrupt phase variation on the boundary, which can be calculated at each point of the bump's edge as:

$$\delta = \pi - 2k_0 h\cos\theta\,, \tag{3.11}$$

where k_0 is the free space wave vector at the operation frequency, h is the height of the unit cell center from the ground plane, and θ is the angle of incidence of the incoming wave with respect to the back-plane normal.

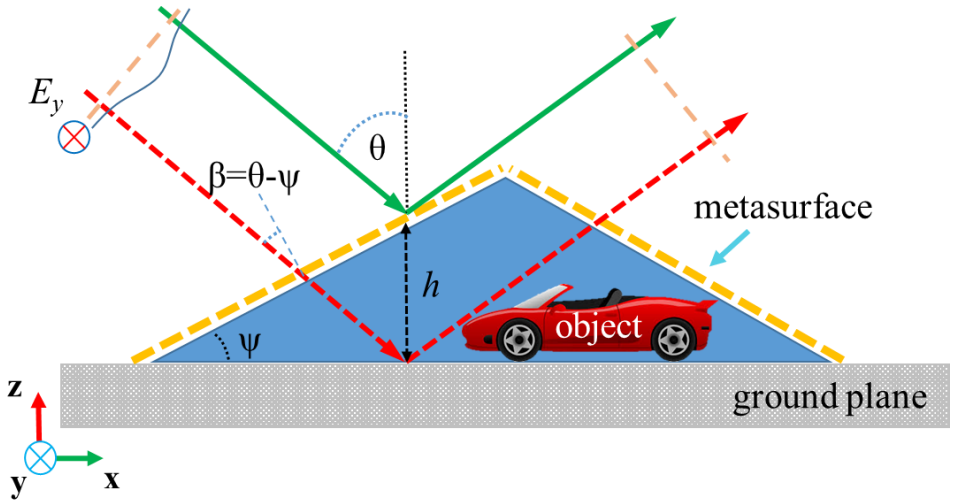

Fig. 3.10. Scheme of the carpet cloak with metasurface.

3.2.2. Numerical analysis of metasurface cloak for millimeter waves

Polarization independent cloaking metasurface

In order to obtain the required phase distribution, a metasurface based on pairs of closed ring resonators (CRR) is employed, whose unit cell is shown in the inset of Fig. 3.11(a). A clear advantage of such topology is its insensitivity to the polarization of the incident electromagnetic field. To realize the effect, we need to be able to control the phase response of the reflected wave from each block over the entire 2π phase range. To this purpose, we simulated the reflection from

infinite planar arrays of such closed rings using the commercial software CST Microwave Studio™ [184], using unit cell boundaries and frequency-domain solver. A fine tetrahedral mesh was chosen with maximum edge length 0.285 mm ($0.076\lambda_0$) and minimum edge length 0.0007 mm ($0.0002\lambda_0$). To create a high resolution surface with better control over the phase distribution of the reflected beam, the lateral dimension of the unit cell was fixed at 400 μm ≈ $\lambda_0/10$, for the working frequency f = 80 GHz (λ_0 = 3.75 mm). Each unit cell consists of two concentric metallic rings with a fixed width w = 10 um, separated by a gap g = 10 um. The radius of the outer ring is then found as $r_2 = r_1+w+g$, where r_1 is the radius of the inner ring. The rings are separated from the ground plane by a thin silicon layer of thickness h = 165 um (≈ $\lambda_0/22$) with dielectric permittivity ε_r = 11.2 and loss tangent $\tan\delta = 4.7\times10^{-6}$. The metal used for the rings is aluminum with a conductivity $\sigma_{Al} = 3.56\times10^7$ S/m.

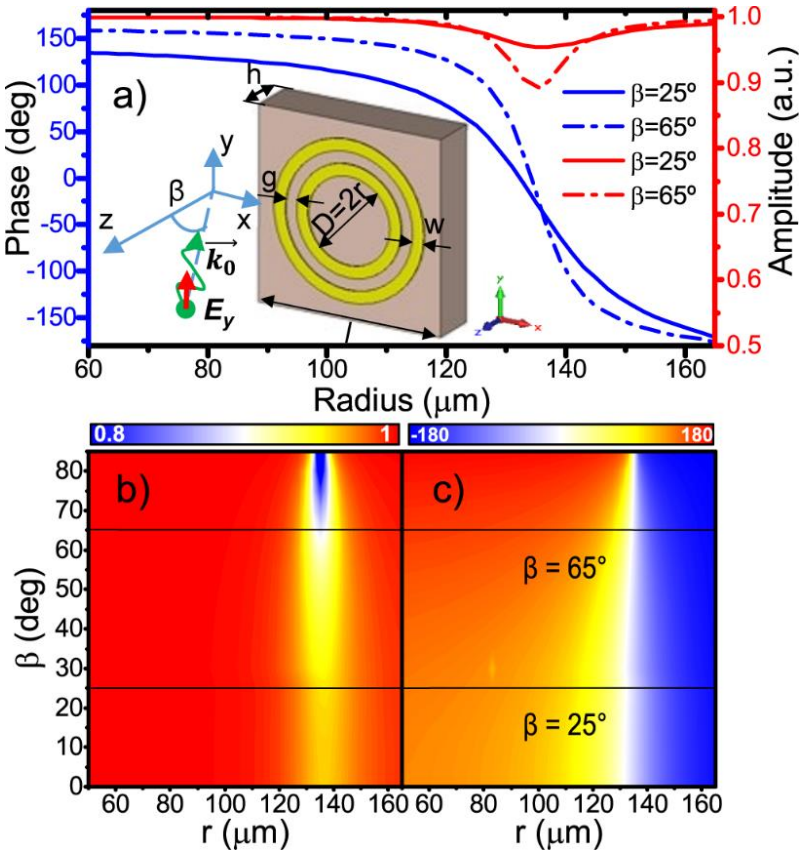

Fig. 3.11. (a) Phase response of the unit cell for different angles of incidence. (Inset indicates the unit cell geometry and its corresponding parameters.) Color-map for the amplitude (b) and phase (c) of the reflection coefficient as a function of the incidence angle and radius of the inner ring.

Due to the geometry of the carpet cloak, the incoming wave has two possible incidence angles (β) on each block of the metasurface, depending on which side of the bump the block is located. In our particular case for an obliquely incident wave with angle θ = 45° and tilt angle of the bump ψ = 20°, the incidence angles at the bump edges are $\beta_1 = \theta - \psi = 25°$ and $\beta_2 = \theta + \psi = 65°$ for the left and right side respectively. The amplitude and phase of the reflection coefficient was obtained as a function of the radius of the inner ring and the angle of incidence β, shown in Fig. 3.11(b-c). In order to increase the design precision, instead of the normal reflection

coefficients, here we design the cloaking layers on each side of the bump based on the data calculated for the corresponding incidence angles. As observed in Fig. 3.11(a-b), the amplitude of the reflected beam slightly drops around r_1 =135 um, due to the CRR resonance. Apart from the resonance, however, the metasurface operates almost as an ideal mirror with close to unitary efficiency. Fig. 3.11(a) also shows the phase response of the unit cell for two incidence angles β_1 (solid blue line) and β_2 (dash dotted blue line). The range of phase variation changing the fing radius spans almost 2π, confirming that this unit cell can adequately control the local phase response of the cloaking metasurface. It is also clearly seen that for a larger incidence angle the phase response has a steeper slope and, therefore, it is more sensitive to the radius variation of the rings, as it may be expected. This means that a bump with a larger tilt angle requires a metasurface with a smaller variation of radii, in the order of a few μm.

Numerical performance of carpet cloak

Once the phase response of the unit cell has been characterized, it is possible to put together the carpet cloak using the design equation (3.11), in order to hide a perfectly conducting bump with triangular shape laying in the *xz*-plane and infinite in the transverse *y* direction. For practical realizations, it is preferred to cloak electrically large objects with bigger tilt angles, which allows to utilize more efficiently the space under the cloak. Extreme shapes and large corner angles may require nonlocal and active surfaces [185], but for slowly varying configurations, including the current proposed design, surface phase engineering is adequate [111]. The ground cloak was designed for a bump with a tilt angle $\psi = 20°$, height of 4.09 mm ($1.09\lambda_0$), edge length of 12 mm ($3.2\lambda_0$) and base length 22.55 mm ($6.01\lambda_0$). Full-wave simulations of the structure were performed using the transient solver CST Microwave Studio™. The structure was illuminated by an obliquely incident ($\theta = 45°$) Gaussian beam with *TE* polarization. To this end, an array of electric dipoles was used with Gaussian distribution of amplitudes, providing a quasi-Gaussian beam excitation. The ground plane was emulated by using an electric boundary (perfect electric conductor) in the *xy*-plane ($z = 0$). Given the symmetry of the structure an electric symmetry was applied in the *xz*-plane ($y = l/2$) in order to reduce computational time. A fine hexahedral mesh was applied with minimum cell length of 0.1 mm ($0.026\lambda_0$) and maximum of 0.44 mm ($0.112\lambda_0$)

As explained above, the phase response of each block was obtained using unit cell boundaries, assuming that all cells in each simulation have the same parameters. On the contrary, to successfully mimic the ground plane, the radii of the rings must change according to the phase distribution determined by (3.11). The transverse inhomogeneities modify the mutual coupling between adjacent blocks, and therefore, its response to the incident wave. Hence, an optimization procedure is required to fine tune the design based on (3.11), imparting a local variation to the radii of surface blocks (60 blocks in the current design). Due to the reciprocity principle [186], we need to optimize only half of the bump, so only 30 unit cells need to be considered in the optimization process. Fig. 3.12(a-c) show the spatial distribution of electric field (E_y component) at the operation frequency f_0 = 80 GHz for three cases: (a) ground plane, (b) bare bump and (c) cloaked bump.

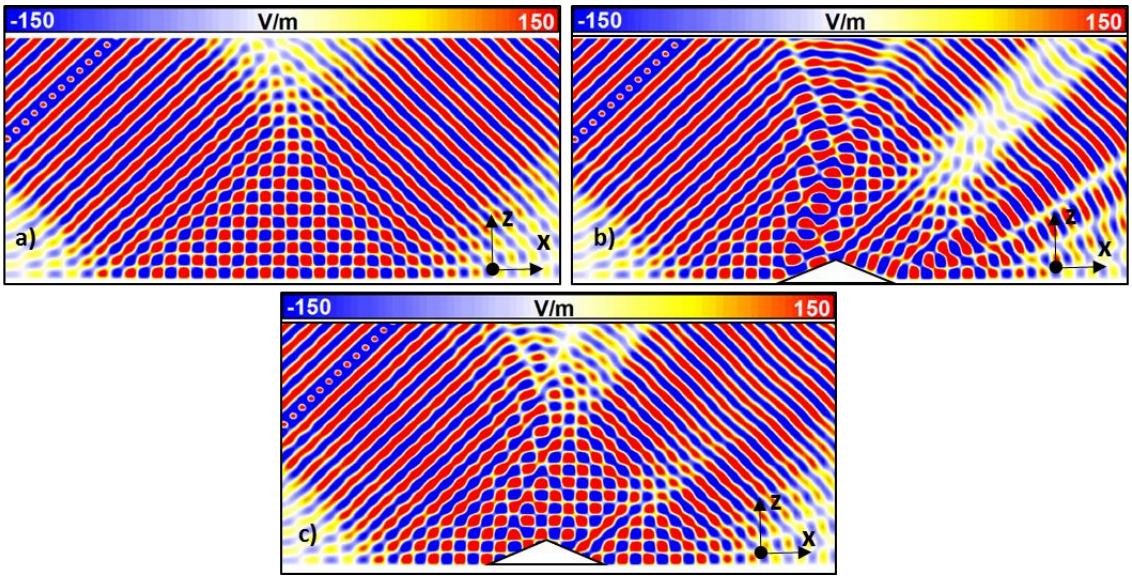

Fig. 3.12. Electric field distribution on *xz* plane for (a) ground plane, (b) bare bump, and (c) cloaked bump.

As it can be seen, when an irregularity is introduced on the ground plane the Gaussian beam is scattered over a wide a range of the angles. After the cloak is applied, the near-field distribution of the reflected wave is restored to the original Gaussian beam. The small disturbance of the reflected beam is caused by the finite discretization of the cloaking metasurface and high ($\beta = 65°$) incidence angle at the second edge of the bump, which may be mitigated with active cloaking surfaces [185]. As it was shown in Fig. 3.11(a) absorption losses are higher for high angles of incidence, provoking higher scattering level. Despite all these factors, Fig. 3.13 demonstrates that we are able to obtain a similar far-field radiation pattern from the cloaked beam as if a bare ground plane were interacting with the incident wave.

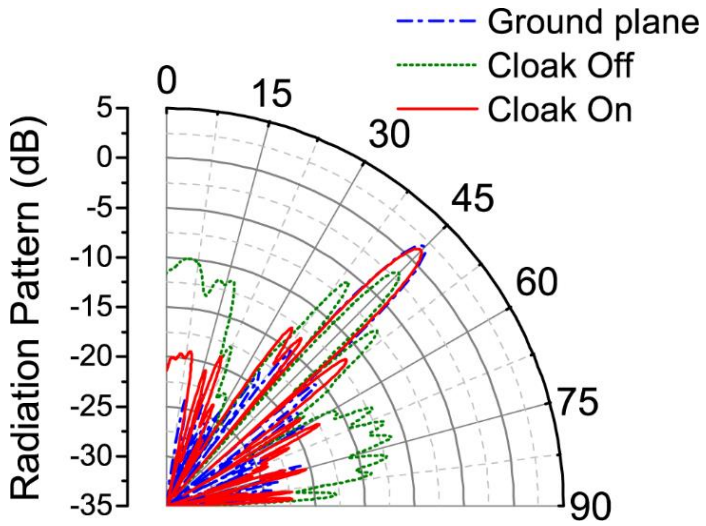

Fig. 3.13. Radiation pattern for the reflected Gaussian beam from the ground plane (dash-dotted blue line), the bump without cloak (dotted green line), and from the cloaked bump (solid red line).

Numerical bandwidth of carpet cloak

Next, the performance of the optimized cloak was analyzed in terms of the angle and frequency bandwidth. For this study, the numerical simulations were run within a frequency span from 75 to 85 GHz with a step of 0.2 GHz and steering the incidence angle from 25° to 60° with a step of 1°. The resulting color-maps for the far-field scattering electric field magnitude as a function of azimuth angle and frequency are shown in Fig. 3.14(a-c). Analogous color-maps for the far-field magnitude as a function of azimuth angle and incident angle θ of the incoming wave are shown in Fig. 3.14(d-f). The cloak works close to ideally at the designed frequency and angle of incidence, yet, and in spite of the original unidirectional design, it is able to significantly reduce the scattering level in the whole simulated range of frequencies and incidence angles. The multi-lobe pattern created in the presence of the bump is converted into a directive beam, as desired for an ideal ground plane.

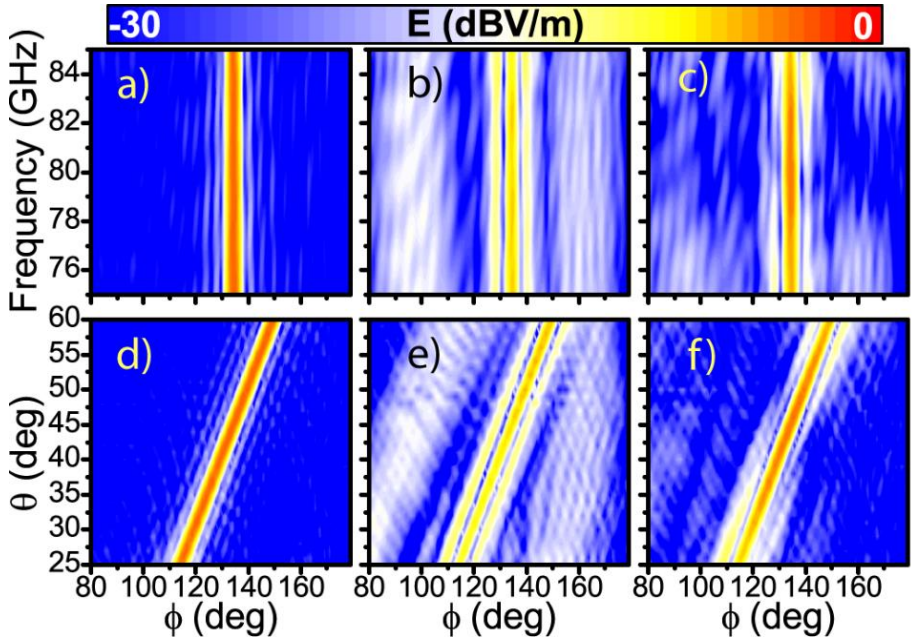

Fig. 3.14. Amplitude of the far-field component of the electric field as a function of azimuth angle ϕ and frequency (a)–(c) and as a function of the incidence angle θ and azimuth angle ϕ (d)–(f). Left column refers to the beam reflected from the ground plane, center from the bare bump, and right column from the bump covered with the cloak.

In order to quantitatively define the region over which the beam reconstruction is acceptable we use a root mean square error (RMSE), which determines the goodness of the fit, and can be defined as [187]:

$$RMSE(f,\theta)=\sqrt{\frac{1}{N}\sum_{i=1}^{N}\left[E_s(f,\theta,\phi_i)-E_b(f,\theta,\phi_i)\right]^2} \tag{3.12}$$

where N is the number of sample azimuth angles, $E_s(f, \theta, \varphi_i)$ and $E_b(f, \theta, \varphi_i)$ are the far-field magnitudes of the reflected wave from the bump and the ground plane at a given azimuth angle φ_i, frequency f, and incidence angle θ. The calculated $RMSE(f, \theta)$ for the scattered beam without

and with the cloak are shown in Fig. 3.15(a) and (b). A sufficiently accurate fit is considered when the *RMSE* is less than 10% [188]. Hence, our parametric study reveals that the ground cloak maintains a reasonable performance in a frequency span of about 8 GHz (fractional bandwidth *FBW* = 10%) and angular span of 35°. In addition, it is noticeable that the cloak has a wider bandwidth for lower incidence angles, which is in good agreement with our previous study for the phase response as a function of the incidence angle θ. For applications in which the accuracy of the recovered beam is important, for example for high precision measurements, an *RMSE* below 5% [dash contour line in Fig. 3.15(b)] would still provide a bandwidth of 2.2 GHz (*FBW* = 3%) and an angular span of 10°.

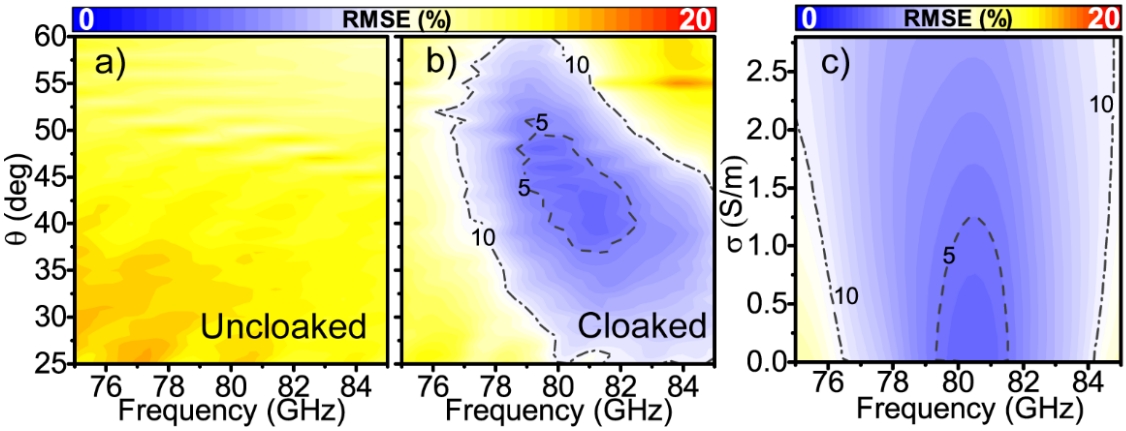

Fig. 3.15. *RMSE* distribution vs incident angle and frequency for (a) uncloaked and (b) cloaked bump. (c) *RMSE* distribution as a function of the conductivity σ of dielectric substrate and frequency.

These results have been obtained for relatively small substrate losses ($\tan\delta = 4.7\times10^{-6}$ or $\sigma = 2.5\times10^{-4}$ S/m). However, in practical realizations the losses can be several orders higher and may disrupt the cloak operation. Therefore, an analysis of the performance of the cloak was done for higher values of dielectric losses. The recovery of the Gaussian beam at the operational frequency of 80 GHz was estimated for different values of conductivity, using the same *RMSE* metric, and the corresponding results are plotted in Fig. 3.15(c). Interestingly, even for very low *RMSE* (<5%) the cloaking metasurface is able to recover the far-field pattern of the original reflected Gaussian beam for values of conductivity up to 1.2 S/m ($\tan\delta = 0.023$), as it may be expected due to the inherently nonresonant nature of the proposed cloaking technique. Silicon samples with an equivalent value of resistivity $\rho = 83\ \Omega\cdot$cm are relatively cheap and commercially available, making the proposed cloaking device appealing for low cost THz devices such as automotive radar systems, to reduce unwanted scattering from electrically large objects.

3.3. Experimental verification of metasurface based carpet cloak

Once we numerically demonstrated the good cloaking performance of the designed metasurface based carpet cloak, our goal is to experimentally verify the scattering reduction of the proposed design for both *TE* and *TM* polarizations. A similar metasurface based cloak has been already experimentally demonstrated in optics [113], showing good perspectives for such

cloaking technique. Moreover, a recent experimental work on the metasurface based cloak in the low band of the microwave range demonstrated the possibility of the restoring not only the amplitudes and phases, but also the initial polarization [189]. Although the fabrication at higher frequencies is more complicated, due to the smaller sizes of the metasurface elements, this method can also find appealing applications in other frequency ranges, such as the emergent millimeter-wave and THz bands. A polarization independent metasurface based cloaking device in these frequency ranges may be highly promising in a variety of sectors such as communication, security, military, space and biomedical applications [190,191]. Moreover, a response independent of polarization is critical for real-life applications given that the polarization of the incident wave is usually unknown. In this section we experimentally realize a cloaking prototype operating at 80 GHz, demonstrating scattering cross-section reduction from a metallic bump over a ground plane, within a relatively wide range of angles and frequencies for both *TE* and *TM* incident polarizations.

Design of polarization-independent metasurface carpet cloak

Fig. 3.16 shows the metasurface cloak considered in this thesis. The object to be concealed is a triangular bump with height 4.1 mm ($1.1\lambda_0$) and long side 40 mm ($10.7\lambda_0$). The restoration of the scattered wavefront is achieved by compensating the phase difference δ between the waves reflected from the ground plane and the edge of the concealed object, calculated by (3.11) at each point of the bump's edge following the method originally envisioned in [112] and used in previous numerical analysis.

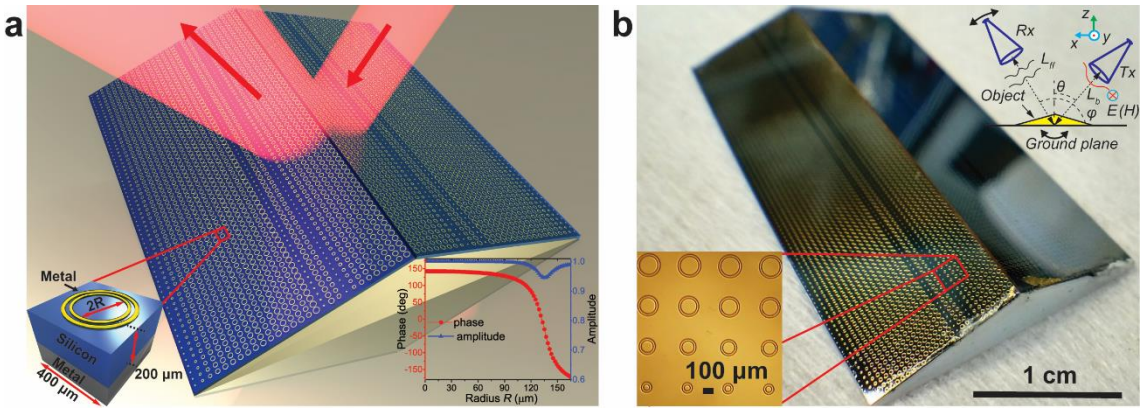

Fig. 3.16. Schematic illustration and photographs of the fabricated metasurface cloak. (a) 3D view of the cloak metasurface composed of an array of double coaxial metallic rings. Left inset: detail of a metasurface element with representative parameters. Right inset: amplitude and phase response of the unit cell as a function of the ring radius. (b) Photograph of the fabricated cloak. Left inset: microscope picture showing a detail of the fabricated rings. Right inset: scheme of experimental set-up.

As shown in the bottom left inset of Fig. 3.16(a), the metasurface is composed of double coaxial metallic rings with total metal thickness 0.8 μm, period 400 μm ($\lambda_0/9$) and gap between rings 10 μm placed on a high resistivity silicon substrate ($\rho > 10000\ \Omega\cdot$m) with thickness 200 μm ($\lambda_0/19$). This geometry was chosen to make the metasurface insensitive to the polarization of the

incident wave [112]. The response of each unit cell was tuned by changing the radii of the rings. The amplitude and phase curves of the reflection coefficient as a function of the ring radius are shown in the inset of Fig. 3.16(a).

Due to availability and mechanical restrictions, the silicon thickness is different from the one used in the numerical simulations described above (165 μm). Therefore, an additional optimization of the cloaking metasurface was performed for the new silicon thickness (200 μm), resulting in the new optimal cloaking metasurface configuration.

Fabrication of cloaking metasurface

The fabrication of the metasurfaces was made by photolithography followed by a lift-off procedure. The lift-off technique is a three-step process in which a photoresist film is first deposited and patterned, a metal layer is then grown and finally the resist sacrificial layer is stripped off in order to remove the undesired metal. In the first step, a double-side-polished (DSP), float-zone grown (FZ), high resistivity ($\rho > 10000\ \Omega\cdot m$) silicon wafer with diameter 50.8 mm and thickness of 200 μm was cleaned and dehydrated. A thick layer of negative resist was then spin-coated, soft baked and exposed with a Suss MJB4 mask aligner. The UV exposure dose was carefully chosen to adjust the angle of the vertical walls of the resist. A positive angle would cause a later deposition of metal in the side-walls of the resist resulting in metal fence formation after the resist striping, whereas a too negative angle would compromise the accuracy of the process. With this technique a resolution of 1 μm can be reached, ensuring a minimal gap between two coaxial rings of 10 μm. After developing the resist, a 500 nm thick layer of copper and a 300 nm gold layer were sputtered. Although at the working frequency (0.08 THz) the skin depth does not exceed 300 nm the metal the thickness was fixed to 1 μm to ensure low losses, as was also done in the numerical calculations. The sputtering technique uses ionized argon plasma to attack the target material and strike out metal atoms that are deposited onto the sample. Since for this process the chamber pressure is relatively high (around 1.3 Pa), the deposition pattern is not completely directive, which can cause step coverage unless a sufficient negative angle is achieved during the photolithography process. The sacrificial resist layer was removed with a striper based on a solution of tetra-methyl ammonium hydroxide (TMAH). A photograph of the fully cloaked structure with the fabricated metasurface covering the triangular bump is presented in Fig. 3.16, along with a microscope picture showing details of the metallic rings. The detailed microscopic images are shown in Fig. 3.17.

Simulation set-up

Full-wave simulations of the structure were performed using the transient solver of CST Microwave Studio™. The ground plane was emulated by using an electric boundary (perfect electric conductor) in the *xy* plane ($z = 0$). Given the symmetry of the structure, an electric (magnetic) symmetry for the *TE* (*TM*) polarization was applied in the *xz* plane in order to reduce computational time. A fine hexahedral mesh was applied with minimum cell length of 0.005 mm ($0.0021\lambda_0$) and maximum of 0.35 mm ($0.09\lambda_0$). A thin silicon layer was used for the substrate

with thickness h = 200 μm (≈ $\lambda_0/19$), dielectric permittivity ε_r = 11.2 and loss tangent tanδ = 4.7×10^{-6}. Metallic rings were modelled as aluminum with conductivity $\sigma_{Al} = 3.56\times10^7$ S/m.

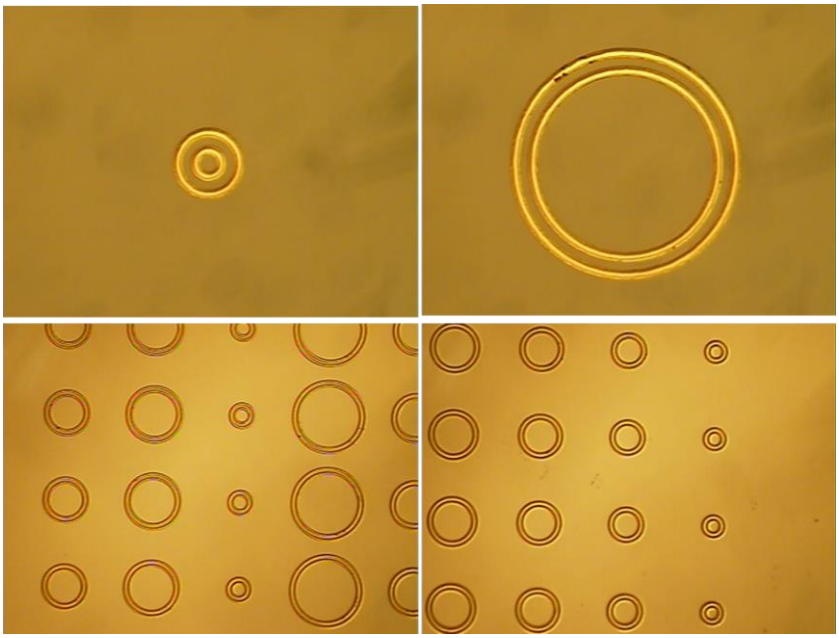

Fig. 3.17. Microscopic photos of fabricated metasurfaces.

The structure was illuminated by an obliquely incident Gaussian beam with both *TE* and *TM* polarizations. To this end, an array of electric dipoles perpendicular (in-plane) to the incident plane was used with Gaussian distribution of amplitudes and phases, emulating a quasi-Gaussian beam distribution of the corrugated horn antenna with *TE* (*TM*) polarization. The array was placed at 500 mm ($133\lambda_0$) from the sample, the same distance as in the experiment. The radiation patterns were directly calculated by the built-in far-field monitors of CST Microwave Studio™.

To obtain the radar cross section and scattering gain the structure was illuminated by a plane wave source and periodic boundaries were used in *y*-axis direction with period d = 400 μm. The total RCS was calculated by integrating the RCS in the azimuthal *xz* plane, obtained by the built-in far-field monitors of CST Microwave Studio™.

Experimental setup

To evaluate the cloaking performance, we used two different experimental setups: based on an ABmm vector network analyzer (VNA) (setup 1) and an Agilent E3861C VNA (setup 2). The scheme of the two experimental setups used in our work is shown in Fig. 3.18. In both setups corrugated high gain horn antennas were used as transmitter (*Tx*) and receiver (*Rx*) and placed at the distances L_b and L_{ff} respectively.

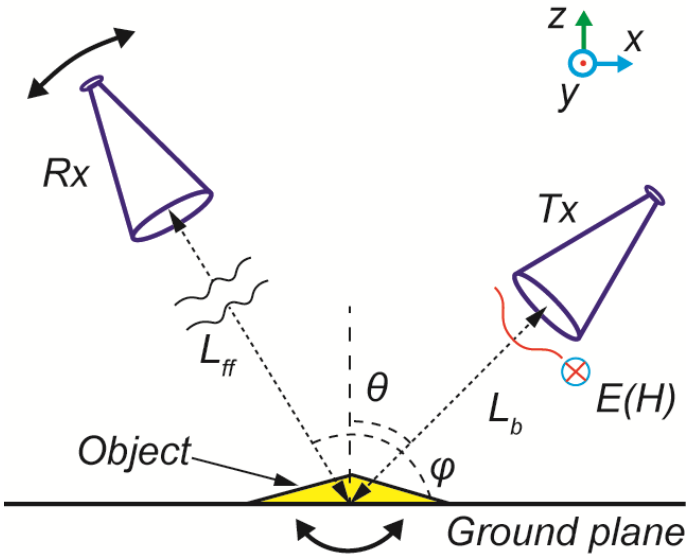

Fig. 3.18. Schematic view of the experimental set-ups.

In the first setup we used the AB millimeter vector network analyzer (ABmm VNA) to measure the scattered *E*-field by capturing the scattering parameter S_{21} in the range 75 - 95 GHz. The transmitter and the ground plane (a copper plate with dimensions 300×400 mm) with bump attached were both mounted on a rotational platform, and the whole structure was rotated in the range φ = 45° – 180° (maximum available range due to the setup configuration) keeping the incidence angle constant [see Fig. 3.19(a)].

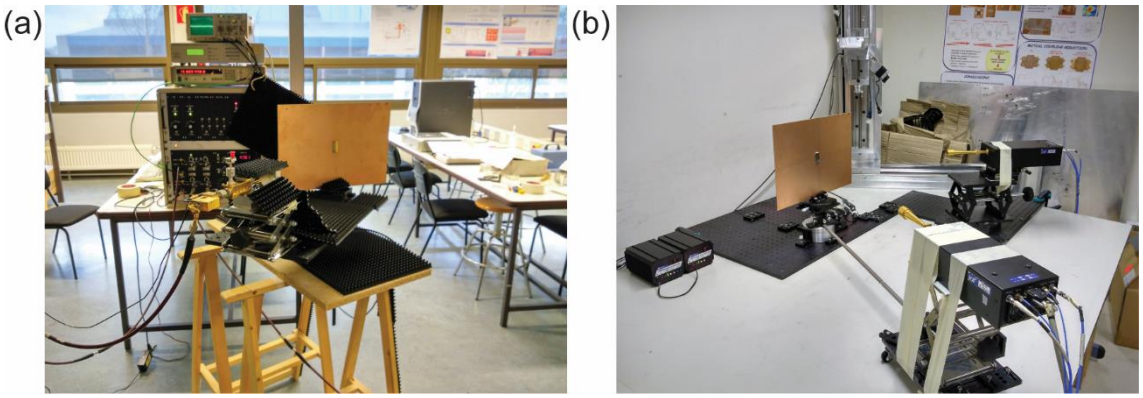

Fig. 3.19. Photographs of the experimental setup (a) based on ABmm VNA (setup 1) and (b) based on Agilent VNA (setup 2).

The transmitting antenna was placed at L_b = 460 mm to ensure both uniform illumination of the structure and a beam waist diameter (67 mm) smaller than the ground plane (300 mm × 400 mm) to avoid diffraction. The receiver was placed at L_{ff} = 3230 mm (860λ_0). With these distances we ensured that the measurements were done in the far-field region of the horn antennas (≈ 230 mm). The floor and walls were partially covered with absorbers in order to mimic anechoic chamber conditions. Furthermore, the setup was calibrated by recording the maximum reflected field from the ground plane when no object was presented. To this end, both transmitter and receiver were placed at the same angle 45°. This reflected field was subsequently subtracted from

the measured reflected fields for other scattering angles. In the first study, *TE* polarization with incidence angle θ = 45° was used. In this configuration, we measured three samples: bare ground plane, metallic bump on the ground plane, and bump cloaked with the gradient metasurface.

For RCS measurements we use another set-up based on an Agilent E3861C VNA to capture the scattering parameter S_{21} in the range 75-95 GHz and in the range φ = 60° – 180° [see Fig. 3.19(b)]. In this set-up, transmitter and receiver are placed at the distances L_b = 500 mm and L_{ff} = 630 mm respectively. In this configuration the beam waist diameter (71 mm) is also smaller than the ground plane. Analogously to the first setup, a calibration was performed. Moreover, a software-based time-gating was applied to eliminate spurious reflections.

Experimental cloaking performance

The colour-maps of the reflected electric field distribution as a function of frequency and azimuth angle φ obtained with setup 1 for all three cases are shown in Fig. 3.20(a-c).

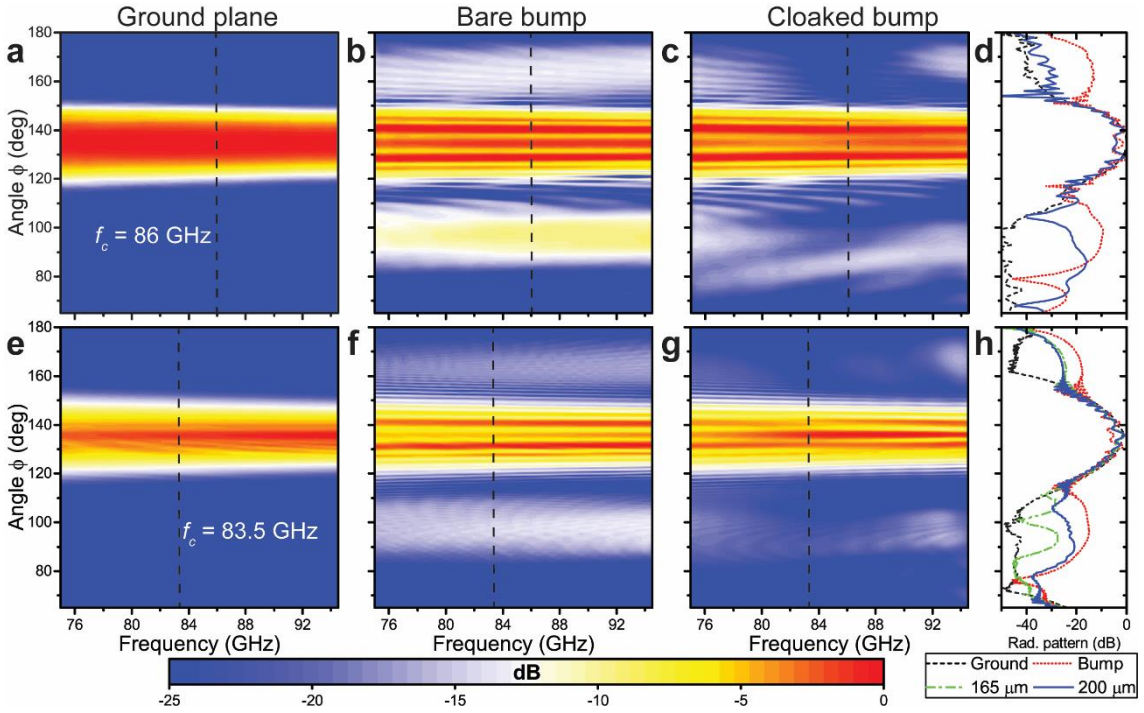

Fig. 3.20. Radiation pattern for ground plane, bare bump and cloaked bump at the optimum incidence angle θ = 45° and TE-polarization. (a-c) Experimental results. (d) Experimental radiation patterns for all three cases at f_c = 86 GHz. (e-g) Simulation results. (h) Numerical radiation patterns at frequency f_c = 83.5 GHz.

As expected, the electrically large bare bump strongly scatters the electric field, resulting in two additional high peaks on both sides of the main specular reflection for all measured frequencies. When the cloak is applied, these peaks are significantly suppressed (almost –20 dB for some angles, see Fig. 3.20(d, h), where the experimental and numerical radiation patterns are shown for f_c = 86 GHz and 83.5 GHz respectively), confirming the scattering reduction. These results are compared with numerical simulations done with CST Microwave Studio in Fig. 3.20(e-g). As observed, measurements and simulations are in good agreement. The experiment presents

a slight blue-shift ($f_c \approx 86$ GHz) with respect to the design ($f_c = 80$ GHz) and also simulation frequency ($f_c = 83.5$ GHz). We attribute this shift to multiple factors, such as deviations in the gap between the rings and the thickness of the fabricated metallic rings, due to the tolerances in the fabrication process. From additional simulations, shown in Fig. 3.21, it can be seen that the central frequency f_c blue-shifts as the metal thickness is increased.

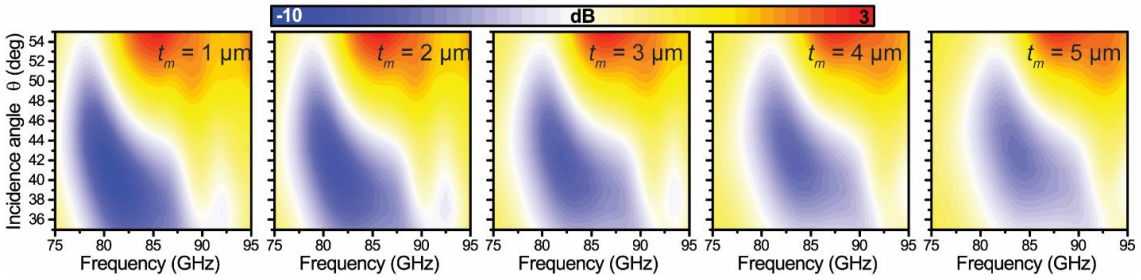

Fig. 3.21. Numerical scattering gain vs incidence angle and frequency for different thicknesses of the metal rings.

Comparing the simulation results with numerical results presented above (that correspond to a substrate height of 165 μm) it is clear that the present cloak is still able to significantly reduce the scattering in almost the same frequency range, even though the substrate thickness and therefore the optimal cloaking metasurface are not the same. The most important difference is that the main beam shape is not ideally recovered (see Fig. 3.22).

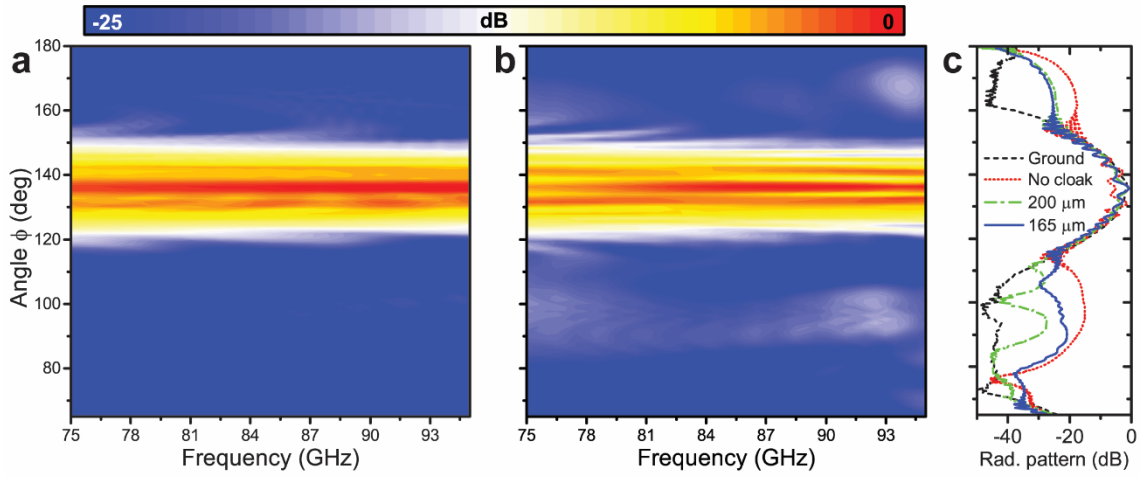

Fig. 3.22. Radiation pattern for a cloaked bump at the optimum incidence angle θ = 45°. (a) Numerical radiation pattern for a cloak with substrate thickness 165 μm. (b) Numerical radiation pattern for a cloak with substrate thickness 200 μm. (c) Numerical radiation patterns for substrate thickness 165 μm (green dash dotted curve) and 200 μm (blue solid curve) at frequency $f_c = 83.5$ GHz.

Next, we analyze the cloaking performance under *TM*-polarization. The numerical and measured radiation patterns for all three cases are shown in Fig. 3.23. In a similar way as for *TE* incidence, the cloak is able to reduce the scattering from the metallic triangular bump in the same frequency range. Moreover, the agreement of measurements and simulation results [Fig. 3.22(e-

g)] is again excellent. The cloaking performance is slightly degraded in comparison with the *TE* case, see Fig. 3.23(d, h).

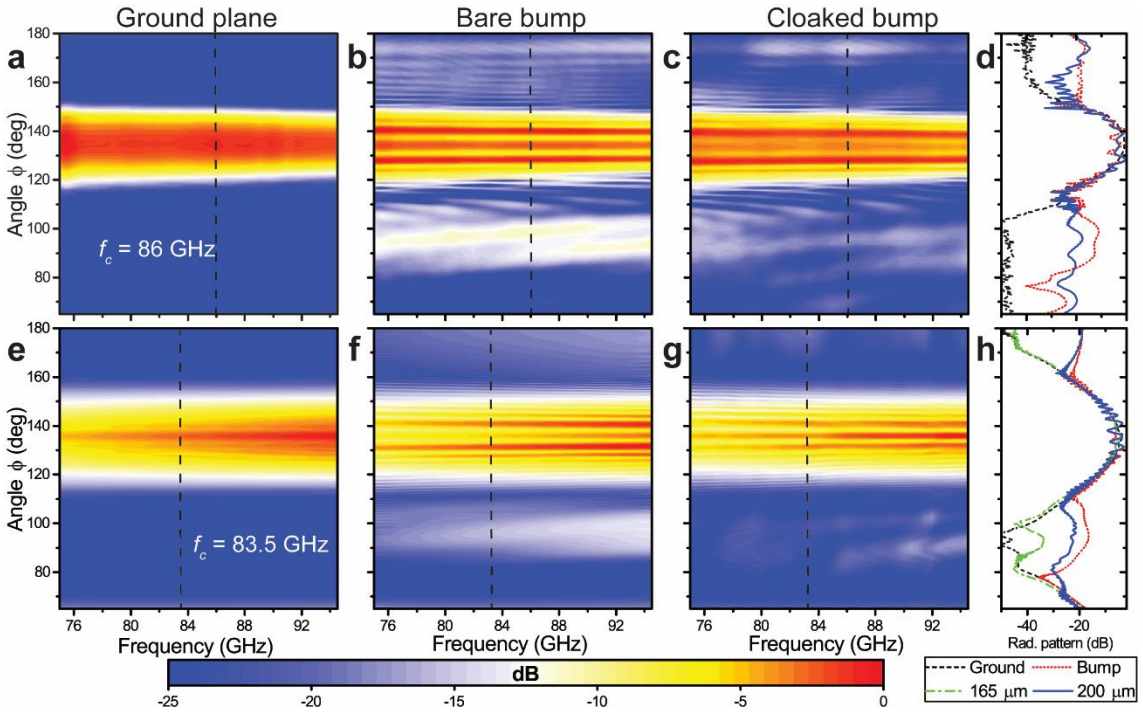

Fig. 3.23. Radiation pattern for ground plane, bare bump and a cloaked bump at the optimum incidence angle θ = 45° and TM-polarization. (a-c) Experimental results. (d) Experimental radiation patterns for all three cases at f_c = 86 GHz. (e-g) Simulation results. (h) Numerical radiation patterns at frequency f_c = 83.5 GHz.

In order to quantitatively assess this difference in performance we calculate the scattering gain for θ = 45º and both polarizations, defined as the ratio between the total RCS of the cloaked and bare bump. To this end, after the measurements were calibrated by subtracting the background contribution, the post-processed *S*-parameter values are converted to RCS (σ) values using the radar range equation [192]:

$$\sigma = \frac{(4\pi)^3 L_b^2 L_{ff}^2 \left|S_{21}\right|^2}{G_r G_t \lambda_0^2} \tag{3.13}$$

where *Gr* and *Gt* are gains of the receiver and transmitter respectively, and L_b and L_{ff} are the distances from the cloaked object to the receive and transmit antennas. The total RCS is found by integrating the RCS over measured angles (φ = 45°-180°).

The scattering gain (dBm^2) is calculated as the ratio between the RCS of the cloaked and bare bump:

$$G = 10\log\left(\frac{\sigma_{cloak}}{\sigma_{bump}}\right) \tag{3.14}$$

where σ_{cloak} and σ_{bump} are total scattering cross section for the cloaked and bare bump respectively. The results obtained with setup 2 are shown in Fig. 3.24(a). In both cases a scattering reduction

is clearly observed with a minimum scattering gain around 86 GHz for both *TE* and *TM* polarizations. In the *TE* case, it reaches −6.5 dB, whereas under *TM* incidence the minimum is less pronounced (around −4.5 dB), demonstrating slightly worse performance for this polarization. This degradation of performance can be due to the fact that in *TM*-polarization the design is more sensitive to the substrate thickness and the non-uniformity of the structure (which manifests itself at large incidence angles). Moreover, for a better performance in *TM* polarization one could use a more complicated structure, for instance, a pyramidal shape, which more accurately restores the phase distribution on the metasurface [185,189].

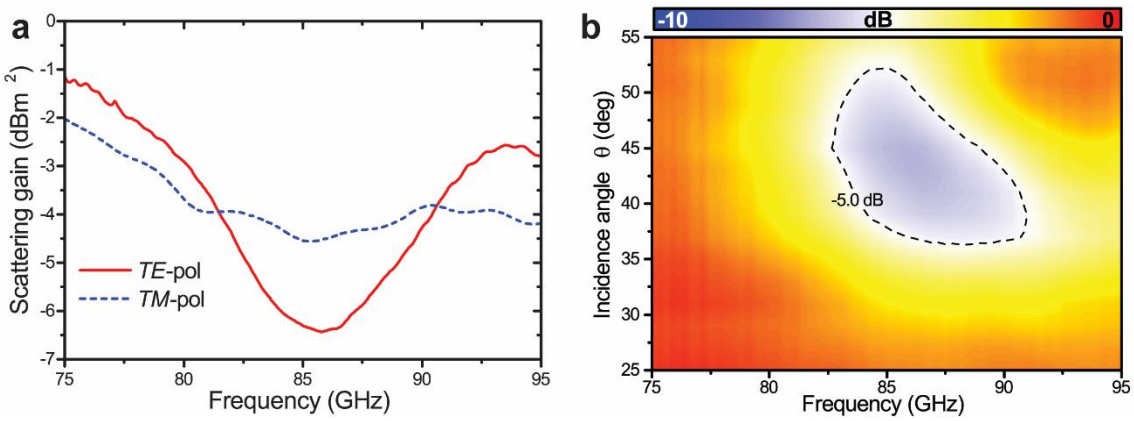

Fig. 3.24. Experimental scattering gain. (a) Experimentally measured scattering gain at the optimum incidence angle θ = 45° for the *TE*-polarization (solid red line) and for the *TM*-polarization (dashed blue line). (b) Experimental scattering gain vs incident angle and frequency for *TE*-polarization.

Experimental analysis of carpet cloak bandwidth

Finally, analogously to the previous numerical results of Section (3.2.2), we experimentally analyze the bandwidth and angular span of the fabricated cloak. In order to evaluate them quantitatively, we measured the RCS and from it we calculated the scattering gain $G(f, \theta)$ for incidence angles ranging from 25º to 55º, focusing in this case on *TE* polarization. For this purpose, we used setup 2 and obtained the azimuthal distribution of the reflection coefficient for all three cases mentioned above. This information was converted to RCS using (3.13). In Fig. 3.24(b) the experimental scattering gain is shown as a function of frequency and incidence angle θ. In good agreement with the results obtained with setup 1 the RCS of the cloaked bump is suppressed by over 6 dB around f_c = 86 GHz and θ = 45°. As shown in Fig. 3.24(b), the cloak demonstrates a 5 dB RCS suppression within a relatively large fractional bandwidth (~8%) and angular span (~15°).

The presented results show that an ultrathin metasurface cloak ($\lambda_0/19$) operating at millimeter-wave frequencies can suppress the scattering from a moderately large bump over a ground plane, independently of the incident polarization. The numerical results for the proposed cloak demonstrate an acceptable beam reconstruction over a good angular span of 35° and a moderately broad bandwidth *FBW* = 10% (for *RMSE* < 10%). The measured prototype demonstrates a relatively wide frequency range with fractional bandwidth of 8% and angular span

of 15° (for G < -5dB). Although the triangular shape of the bump makes the cloak more sensitive to imperfections of the metasurface (especially on top of the structure), it greatly facilitates the fabrication process, making it more feasible for a practical implementation. These results also highlight the possibility of building polarization-independent practical cloaks for macroscopic objects that may work for unknown polarizations and over a relatively wide angular and frequency ranges, and may be integrated in millimeter-wave applications, such as radar automotive systems or ultrahigh speed telecommunication systems. More broadly, since this metasurface cloak can be scaled up for THz band, our work shows how gradient metasurfaces may make a significant impact to control and tailor THz radiation and wave propagation, in a frequency range for which ultrathin components and devices are scarcely available and inefficient, and for which deeply subwavelength control may be routinely achieved with conventional fabrication processes.

3.4. Transformation optics for diffusive light cloaks

The invisibility cloaks previously discussed in this chapter are considered to work under the realm of Maxwell's equations. However, in many practical cases, the propagation of light cannot be described adequately by the macroscopic Maxwell's equations for continua, for example when it does not propagate ballistically. This kind of propagation can be found in natural substances, such as clouds, fog, milk, frosted glass, etc. In these systems containing many randomly distributed scattering centers, every photon of light performs a random walk. Therefore, the light propagation is slower with respect to vacuum and any incident polarization is lost. This latter feature makes diffusive cloaks very interesting for the real applications, since ideal cloaking (meaning operation under any arbitrary polarization) can be achieved. In this thesis, our aim is to develop a cloak device, which works in diffusive light with both static and transient illumination.

Multiple light scattering can be well described by the diffusion of photons [193], allowing the application of the traditional scattering cancellation and TO cloaking principles in the static regime [194,195]. However, as it was demonstrated in [195], the diffusive light cloak fails to conceal an object under truly transient conditions, whether it is based on a core-shell geometry or on typical coordinate transformations. In the first case, the disruption of the cloaking performance for transient illumination is attributed to the high diffusivity of the shell, which results in a faster light propagation in it than in the surrounding medium [195]. Thus, when the core-shell cloak is applied, a short illumination pulse will appear earlier for an external observer than in a medium with no object, with a subsequent fast drop of the intensity, making the cloaked object detectable. In turn, the TO-based cloak also fails, since, in diffusive light processes, the time-dependent diffusion equation is generally not form invariant under coordinate transformations (a basic requirement for this technique to work). In particular, the typical transformations that blow up a point to open a hole in space and achieve the cloaking effect change the form of this equation [195]. As a consequence, the TO method can only be partially implemented in this case, leading to a similar performance to that of a core-shell, again rendering the cloak detectable in the transient regime.

In this thesis, we show that there is a special type of coordinate transformations, namely, unimodular (compression-free) transformations, which preserve the form of the time-dependent diffusion equation. In addition, we propose a particular unimodular transformation able to reroute the flux of photons in a specific direction around a certain region, achieving a perfect unidirectional invisibility effect under truly transient conditions. Moreover, we demonstrate that an approximate multidirectional transient cloaking performance can be attained by applying (polygonal) linear coordinate transformations [196]. The proposed cloak has an additional advantage, as it only requires a homogeneous anisotropic medium for its implementation. We demonstrate numerically that such a medium can be replaced by a thin layered system of two isotropic materials, facilitating the practical realization.

3.4.1. TO-based unidirectional cloak for diffusive light in the transient regime

Using Fick's first law, the generic time-dependent diffusion equation reads [194]:

$$\nabla\cdot\left(D_0\nabla\varphi\right)-C_0\frac{\partial\varphi}{\partial t}=0 \tag{3.15}$$

where t denotes time and φ some diffusing quantity (possible physical meanings for the coefficients D_0 and C_0 will be discussed next) After applying a coordinate transformation (with the aim of molding the diffusion flux, see below), the previous equation becomes [195,197]:

$$\nabla'\cdot\left(\Lambda D_0\Lambda^T\frac{1}{\det\left(\Lambda\right)}\nabla'\varphi\right)-\frac{C_0}{\det\left(\Lambda\right)}\frac{\partial\varphi}{\partial t}=0 \tag{3.16}$$

where ∇' is the gradient with respect to the new coordinates and Λ is the Jacobian matrix of the coordinate transformation[8]. As it can be seen, the coefficient associated with the time derivative in (3.16) is different from unity. In the case of thermodynamics, φ represents the temperature T, D_0 the thermal conductivity tensor and C_0 the specific heat. Hence, (3.16) can be interpreted as that corresponding to a second medium characterized by a new set of parameters:

$$D=\frac{\Lambda D_0\Lambda^T}{\det\left(\Lambda\right)} \tag{3.17}$$

$$C=\frac{C_0}{\det\left(\Lambda\right)} \tag{3.18}$$

which induces the desired transformation [197]. However, in the case of light diffusion, for which φ represents the photon density n_p and D_0 the diffusivity, the coefficient of the time derivative (C_0) is always equal to 1 (since for the diffusion process there is only one material parameter – the diffusivity D_0). Therefore, the condition specified by (3.18) cannot be fulfilled in general. This is not important in the static (or quasi-static) regime, in which the time derivative term is negligible and the diffusivity is the only relevant parameter. However, this is no longer true in the

[8] The Jacobian matrix $\Lambda_i^{i'}=\partial x^{i'}/\partial x^i$ denotes the transformation matrix between the virtual space with coordinates $x_{i'}$ and the original space with coordinates x_i .

upna Universidad Pública de Navarra Nafarroako Unibertsitate Publikoa

transient regime, in which using a material with a diffusivity given by (3.17) will not be enough to mimic the transformed equation. This results in the imperfect invisibility performance discussed in [195].

However, one can see from (3.16) that, for a transformation with det(Λ) = 1, the transformed light diffusion equation preserves its original form. This means that the Jacobian matrix has to be unimodular (note that transformations with det(Λ) = −1 are also unimodular, although we will not consider them in this work), which requires a coordinate transformation without compression of space. In this case, the transformed equation can be exactly implemented only with a diffusivity given by (3.17). This fact has been overlooked so far.

Although the no-compression condition limits the achievable functionalities, it is still possible to obtain a cloaking effect in specific situations. As an example, we propose here a compression-free mapping that yields unidirectional invisibility under transient conditions. Fig. 3.25(a) shows how this transformation maps a rectangular grid in the original space, described by a Cartesian coordinate system (x, y, z), to physical space, described by a coordinate system (x', y', z').

Specifically, an affine mapping is applied to the region $-c < x < c$, $-a < y < a$, while the identity transformation is applied outside this region. For the first quadrant ($0 < x < c$, $0 < y < a$), the transformation equations can be written as:

$$x' = x, y' = y + k(c - x), z' = z \tag{3.19}$$

with symmetric expressions for the other quadrants. Note that this transformation is unimodular and continuous everywhere. As can be seen, the segment ($y = 0$, $-c < x < c$) is blown up to a rhombic region with side length b and angle α ($k = \tan\alpha$ and $c = b/\cos\alpha$), which will constitute the cloaked region.

Using (3.17) and taking advantage of the symmetries of the structure, the diffusivity tensor is obtained for the first and third (– sign) and second and forth (+ sign) quadrants as:

$$D = D_0 \begin{pmatrix} 1 & \mp k & 0 \\ \mp k & 1+k^2 & 0 \\ 0 & 0 & 1 \end{pmatrix} \tag{3.20}$$

where D_0 is the diffusivity of the surrounding medium. Clearly, (3.20) represents a homogeneous anisotropic medium.

From the schematic illustration in Fig. 3.25(a), it can be seen that the diffusive light flux is redirected by the transformed medium (blue) around the cloaked region without compressing space. Note that, in order to efficiently conceal an object, the aperture a of the cloak has to be larger than the incident beam waist. In addition, it is worth mentioning that a double carpet cloak transformation as the ones employed in [198,199] would not satisfy the unimodular condition, since its determinant is constant but different from unity.

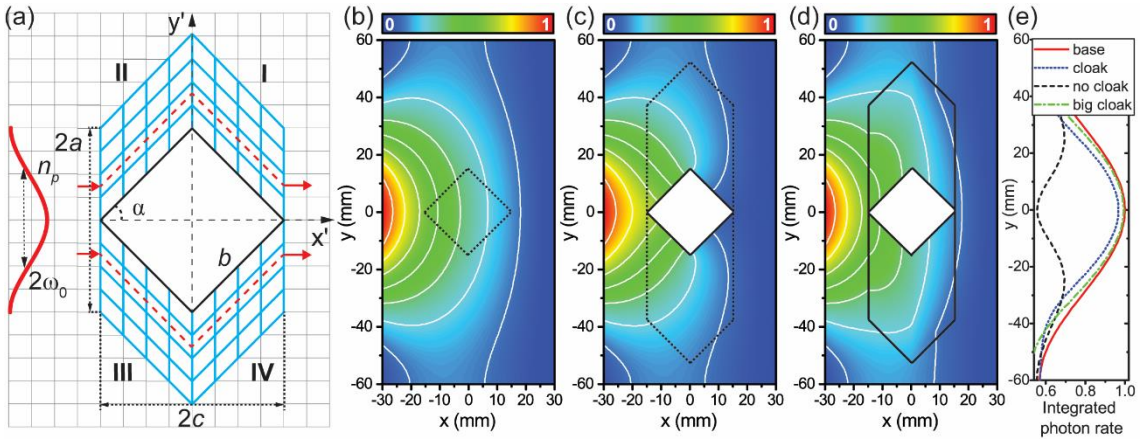

Fig. 3.25. (a) Transformation employed to build the proposed TO-based diffusive light cloak. (b-d) Normalized numerical photon density distribution for the cases: (b) no object, (c) only object and (d) object with cloak. (e) Transmitted photon rate, integrated over time at x = 30 mm for no object (solid red line), only object (dashed black line), object with cloak (dotted blue line) and object with cloak of aperture $2a$ = 90 mm (dash-dotted green line). The incident photon flux has a Gaussian shape with radius ω_0 = 32 mm.

To verify the proposed design, numerical simulations are performed using COMSOL Multiphysics™. In all simulations the diffusivity of the background medium is fixed to D_0 = 7.58×10^4 m^2/s (as in [195]), whilst losses are neglected for the sake of simplicity. The structures are illuminated by a Gaussian-shape beam with a diameter of $2\omega_0$ = 64 mm. A cloak with an aperture $2a$ = 70 mm is used to conceal a diffusively isolated (with $-\mathbf{n}\cdot\mathbf{j}=0$, $\mathbf{n}$ being the unit vector normal to the boundary of the cloaked region and $\mathbf{j}=D\nabla n_p$ the photon flux) square object (α = 45°) with side b = 15 mm [Fig. 3.25(a)]. Note that the aperture of the cloak is chosen to be close to the incident beam waist, in order to account for the effect of the beam size on the cloak behavior.

First, the performance of the unidirectional cloak is checked in the static case, when $\partial n_p / \partial t = 0$. The numerical results for normalized photon density distribution for the cases without object, bare object and cloaked object are shown in Fig. 3.25(b-d), respectively. From these figures it is obvious that, when the cloak is applied, the distribution of the photon density is restored to that in which no object is present. However, due to the similar size of the beam waist and the aperture of the cloak, the transmitted photon rate (photon flux going through the boundary at x = 30 mm) integrated over time is slightly smaller than in the ideal case (-3%), as seen in Fig. 3.25(e) (blue dotted line). This slight "shadow" can be further reduced by either increasing the cloak aperture or by decreasing the incident beam waist. For example, for the same incident flux and a cloak aperture $2a$ = 90 mm, the transmitted photon rate distribution is almost equal to the ideal one, see Fig. 3.25(e) (green dash dotted line).

Next, we verify the performance of the cloak in the transient regime. In order to be a truly transient illumination source, its temporal variations have to be shorter than the propagation time

in the medium. Therefore, the duration of the pulse is determined by a diffusion time constant[9], which depends on the diffusivity D and the dimensions of the structure. For the chosen parameters, the diffusion time constant is around 5 ns. Thus, to ensure the transient illumination conditions, a pulse with both Gaussian temporal (duration of 500 ps, similar to that employed in [195]) and Gaussian spatial (ω_0 = 32 mm) distribution was chosen as the source. The rest of employed parameters were the same as in the static case. The numerical results for the time evolution of the spatial distribution of the transmitted photon rate (at x = 30 mm) are shown in Fig. 3.26(a, d, g) for the medium without object, uncloaked, and cloaked object, respectively.

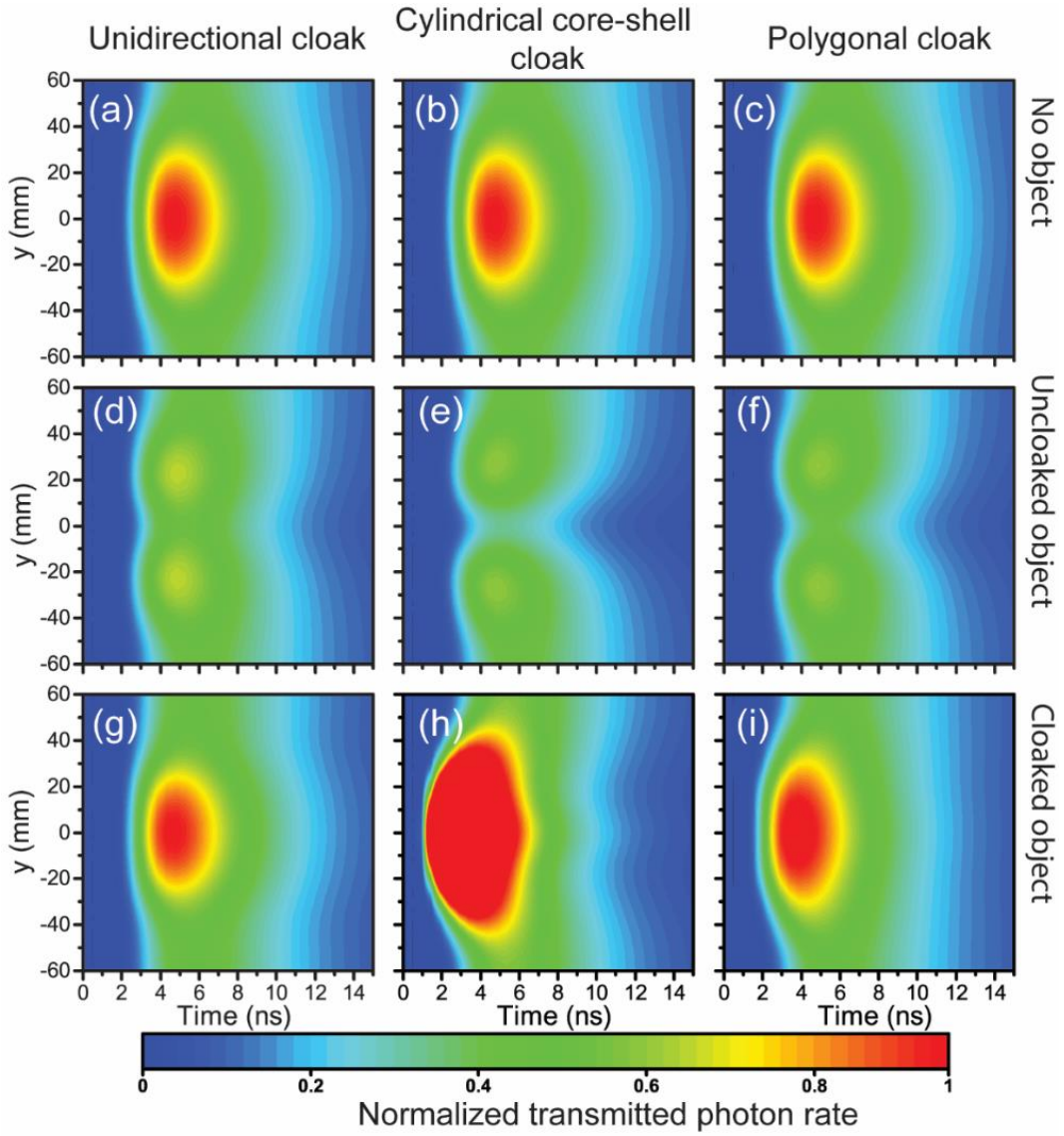

Fig. 3.26. Numerical results for the time evolution of the transmitted photon rate for the proposed unidirectional cloak (left column), the cylindrical core-shell cloak (center column) and the proposed polygonal cloak (right column). The photon rate distribution for the background medium (first row), uncloaked object (second row) and cloaked object (third row) is shown.

[9] The diffusion time constant generally can be defined as: $\tau_{diff} = L^2 / \left(\pi^2 D_0\right)$, where L is the length of path, which a photon has to cross, and D_0 is the diffusivity of the medium.

upna Universidad Pública de Navarra Nafarroako Unibertsitate Publikoa

As it can be seen, when the cloak is applied, the photon rate distribution is restored in space as well as in time. Note that, as in the static case, the mentioned "shadow" effect is present, resulting in a slightly smaller spot.

To explicitly demonstrate that this cloak works under transient illumination, we compare its performance with the cylindrical core-shell cloaks studied in [194,195]. For the core-shell simulations, we use the same background diffusion coefficient and dimensions as in the previous simulations. Since all media are assumed to be lossless, the diffusive coefficient of the shell is calculated using the formula derived in [194] for ideal cloaking. The ratio of the outer to inner radii of the cloak is fixed to $R_2/R_1 = 1.25$, giving a diffusivity coefficient for the shell of $D_2 = 3.58\times10^4$ m^2/s, where $R_1 = 16$ mm and $R_2 = 20$ mm are the inner and outer radii, respectively (same dimensions as in [195]). The illumination conditions and the rest of simulation parameters are kept the same. The results, shown in Fig. 3.26(b, e, h), are very similar to the numerical and experimental results obtained in [195], demonstrating that the core-shell geometry fails in the transient regime. On the contrary, the proposed unidirectional cloak recovers almost perfectly the distribution of the original transmitted diffusive wave. Analogously to the static case, the performance of this cloak can be further improved by increasing its aperture.

3.4.2. Polygonal multidirectional cloak

The cloak simplifications here performed (limitation of the incident beam size and restriction to a specific propagation direction), allowed us to apply the TO formalism not only for the static regime, but also for the transient one. However, in some applications the direction and size of the incident beam may not be known from the onset, in which case a multidirectional cloak is desirable. In such a type of cloak, the creation of a hidden region requires the compression of space and, consequently, a transformation that does not preserve the form of the light diffusion equation. For example, a cylindrical (in 2D geometry) TO-based cloak [65], despite its highly complex and hard-to-build design (due to the spatial anisotropy and inhomogeneity of the diffusivity), has a similar performance to that of the core-shell cloak, as demonstrated in [195].

We wondered, however, whether the suppression of the inhomogeneity of the transformation could improve the performance of a multidirectional cloak under transient illumination. The reason is that, in this case, $\det(\Lambda)$ would be constant inside the cloak (although not equal to 1) and could be taken out of the spatial derivative in (3.16), cancelling out the coefficient of the time derivative and yielding an effective coefficient $C = 1$, as desired. Unfortunately, $\det(\Lambda) = 1$ outside the cloak. This discontinuity in $\det(\Lambda)$ cannot be avoided (preventing us from taking it out from the spatial derivative) and is a possible source of degradation of the cloak performance in the transient regime. To analyze this possibility, we considered an N-sided polygonal cloak, which makes a large region appear as a much smaller one, rendering it virtually invisible [196]. Specifically, we studied a square cloak (N = 4) with side $a = 45$ mm [blue square in Fig. 3.27(a)]. To achieve the cloaking effect, the space between the blue square and a second small square of negligible area (black doted-line square in Fig. 3.27(a), with side $b_1 = 1$ mm and rotated by an angle of 45º with respect to the outer blue square), is divided into multiple regions. Finally, a linear coordinate transformation is performed in each

upna Universidad Pública de Navarra Nafarroako Unibertsitate Publikoa

region in order to expand the small square to a much larger one (black solid-line square in Fig. 3.27(a), with side b_2 = 25 mm), generating the cloaked region [196].

Taking advantage of the symmetries of the structure, only four different regions need to be considered, whose corresponding transformation equations can be written as:

$$\begin{aligned} &I: x' = \frac{x}{k_1}, y' = y, z' = z \\ &II: x' = k_2 x, y' = y - k_2 x, z' = z \\ &III: x' = x, y' = \frac{y}{k_1}, z' = z \\ &IV: x' = k_2 x, y' = y + k_2 x, z' = z \end{aligned} \tag{3.21}$$

where $k_1 = \left(a - \sqrt{2}b_1\right) / \left(a - \sqrt{2}b_2\right)$ and $k_2 = b_2 / b_1$. This transformation gives rise to a homogeneous anisotropic transformed medium.

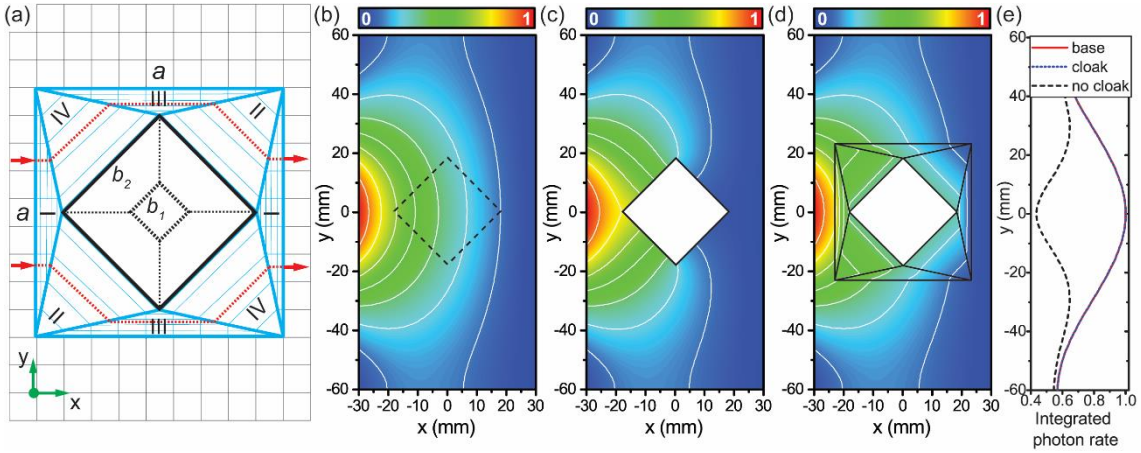

Fig. 3.27. (a) Scheme of the proposed multidirectional diffusive light cloak. (b-d) Normalized numerical photon density distribution in the static regime for the cases: (b) no object, (c) bare object and (d) object with cloak. (e) Transmitted photon rate, integrated over time at x = 30 mm, for no object (solid red line), only object (dashed black line), object with cloak (dotted blue line).

As in the previous cases, the performance of this device is analyzed through numerical simulations, considering that the cloaked region (delimited by the black solid-line square) is diffusively isolated. According to the results depicted in Figs. 3.27(b-d), in the static regime, the distribution of the photon density outside the device remains unperturbed, confirming the ideal cloaking of the object. Fig. 3.27(e) further demonstrates that the spatial distribution of the transmitted photon rate integrated over time in the case of the applied cloak (blue dotted line) is identical to that in which no object is present (red solid line).

Finally, we check the performance of the polygonal cloak in the transient regime. As in the previous designs, the spatial distribution of the transmitted photon rate is obtained as a function of time for three different cases (no object, uncloaked, and cloaked object) and the results are shown in Fig. 3.26(c, f, i). As expected, since the form of the diffusion equation cannot be completely preserved in this case, the cloaking effect is not perfect. However, it is much closer to

the ideal one than that achieved via scattering cancellation. For instance, unlike in the case of the core-shell cloak, the polygonal cloak hardly causes an over-shooting of intensity in the beginning (the spot occurs less than 1 ns earlier in time than in the reference case). In fact, the shape of the pulse is approximately the ideal one at all times, making the cloaked object much more difficult to detect.

3.4.3. Practical multilayer implementation of the transient diffusive cloak

Unlike the cylindrical TO cloak, the diffusive medium required to synthesize the cloak proposed in Section 3.3.1 is homogeneously anisotropic. In this section, we show that this fact can greatly simplify its implementation. We start by noticing that, thanks to its real symmetric character, the diffusivity tensor (3.20) becomes diagonal when expressed in a Cartesian system whose axes lie along its eigenvectors. This so-called principal coordinate system (u, v, z) can be obtained as a rotation of the original coordinate system (x ,y, z) by an angle θ around the z-axis [Fig. 3.28(a)].

For the cloak parameters used in this work (k = tanα = 1), the principal components (eigenvalues) of the diffusivity tensor in the first quadrant are determined as $D^u = 0.38D_0$ and $D^v = 2.62D_0$, with a corresponding rotation angle of θ = 32.72°. The diffusivity tensor principal components for the other quadrants can be easily obtained via symmetry considerations. From homogenization theory [200], we know that such an anisotropic medium can be replaced by a system of alternating thin layers of two different materials A and B [198,201], aligned with the mentioned principal axes and with isotropic diffusivities D_A and D_B and thicknesses t_A and t_B, respectively [see Fig. 3.28(a)].

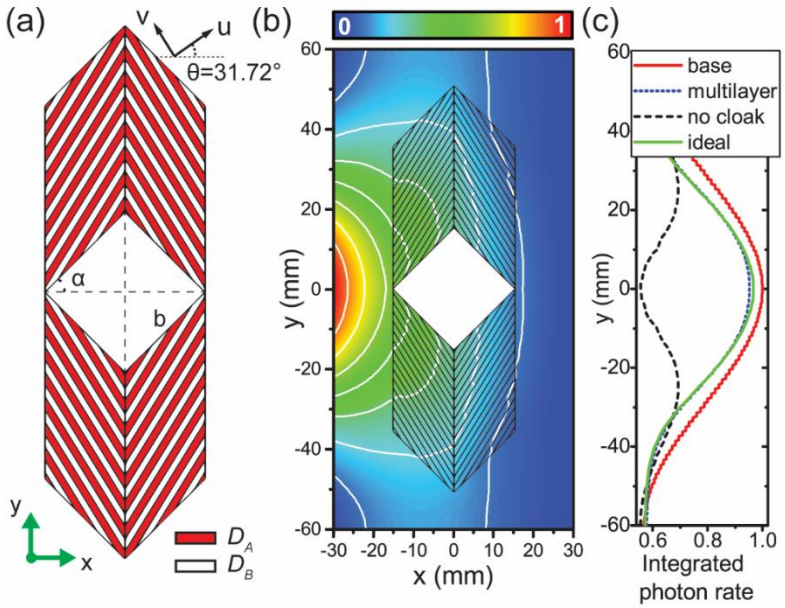

Fig. 3.28. (a) Scheme of the proposed multilayered diffusive light cloak. D_A = 38.2×10^4 m^2/s (5D_0), D_B = 1.5×10^4 m^2/s (0.2D_0). (b) Normalized photon density distribution in the presence of the cloaked object. (c) Transmitted photon rate at x = 30 mm and integrated over time for no object (solid red line), only object (dashed black line), object with multilayered cloak (dotted blue line) and object with ideal cloak (dash-dotted green line). The incident photon flux has a Gaussian shape with radius ω_0 = 32 mm.

Specifically, such a composite behaves as an effective anisotropic medium characterized by a diffusivity tensor with principal components given by [198]:

$$D^u = \frac{D_A D_B (1+f)}{D_A f + D_B}, D^v = \frac{D_A + D_B f}{f+1} \tag{3.22}$$

where $f = t_B/t_A$[10]. For simplicity, we assume here layers of equal thickness $t_A = t_B = t$ ($f = 1$). Using (3.22), we can calculate the values of the multilayer isotropic diffusivities that implement the anisotropic medium required by the cloak, which are found to be $D_A = 5D_0 = 38.2\times10^4$ m^2/s and $D_B = 0.2D_0 = 1.5\times10^4$ m^2/s. Note that the thickness t of the layers has to be small enough to have a correct effective medium diffusivity. In this example we used $t = 2$ mm. In order to verify that this value fulfils the mentioned requirement, the behavior of the multilayered diffusive cloak is numerically analyzed as well.

Analogously to the ideal homogeneous anisotropic cloak, Fig. 3.28(b) shows that the multilayered cloak restores the photon density distribution to the case in which no object is present. Furthermore, the spatial distribution of the integrated-over-time transmitted photon rate in the case of the multilayered cloak (blue dotted line) is almost identical to the distribution obtained when the ideal homogenous cloak is applied (green dash dotted line), see Fig. 3.28(c). Moreover, in the transient regime, the spatial distribution of the transmitted photon rate evolves in time identically to that obtained for the ideal cloak (see Fig. 3.29), proving the validity of the proposed structure.

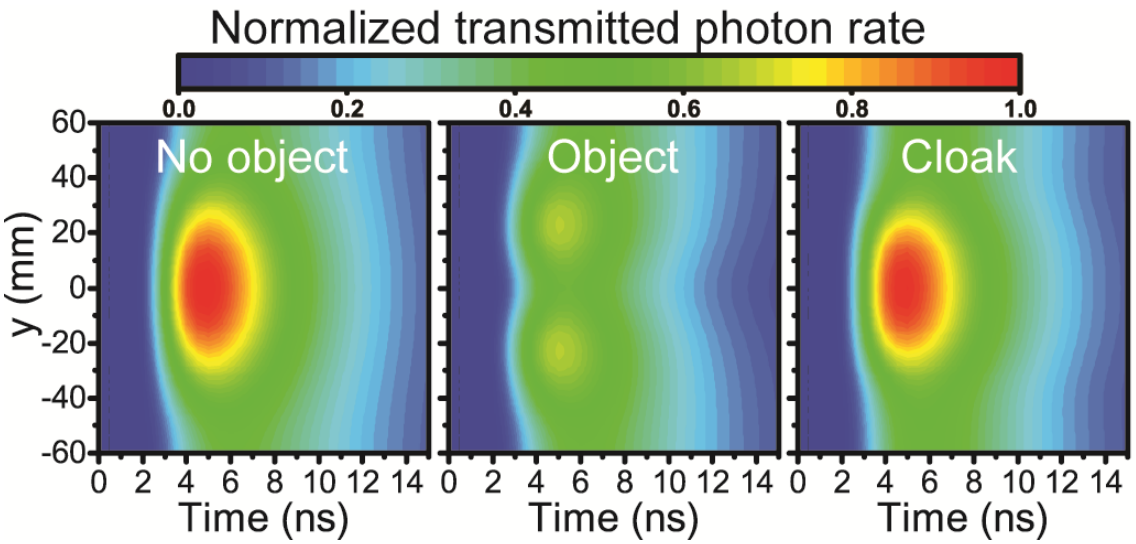

Fig. 3.29. Numerical results for the time evolution of the transmitted photon rate for the proposed multilayered unidirectional cloak. The photon rate distribution for the background medium (first column), uncloaked object (second column) and cloaked object (third column) is shown.

This multilayered system significantly facilitates the practical realization of the cloak, which becomes technologically comparable to that of the core-shell cloaks based on scattering

[10] The tensor components of effective medium can be derived using the Effective Medium Theory [236], which is based on a transfer-matrix method.

cancellation. For instance, the required thin layers with different diffusive coefficients D_a and D_b could be fabricated using solid state materials (for example, a transparent polymer poly-dimethylsiloxane doped with titania nanoparticles), as it was shown in [202], and attached together afterwards. Note that similar layered systems could be employed to implement the studied polygonal cloak.

In this thesis, we have proposed and numerically analyzed a unidirectional diffusive light cloak based on TO, which can provide an almost perfect invisibility effect in both the static and transient regimes. Additionally, we have demonstrated that it is possible to obtain multidirectional cloaking displaying a nearly-ideal performance in the transient regime by using a polygonal cloak. It is worth mentioning that this last technique could even be extended to the three-dimensional case [203]. From the fabrication standpoint, we have proposed a simple multilayered implementation of the studied cloak that facilitates its practical realization. Such a thin layered system could be fabricated using solid state diffusive materials.

Our results have several potential applications that cannot be addressed by the diffusive cloaks previously proposed. First, the studied cloaks offer a complete shielding strategy for advanced pulse-based detection techniques such as LIDAR. Second, this kind of cloak could be used to avoid interferences from scattering elements for high-speed communications in a diffusive environment. As a third example, in previous works it has been mentioned that any diffusive cloak could be detected by time-of-flight tomography. Although this seems to be true in the ideal case in which any number of directions can be analyzed in a very precise way, the cloaks proposed in this thesis could be very difficult to detect if only a limited (arbitrary, in principle) number of directions is considered, which may be the case in some real systems. This feature could be used to hide certain elements of an imaging system susceptible of introducing interferences, or to build even more sophisticated optical security elements than the ones based on static diffusive cloaks [195]. Moreover, the cloaking strategy here discussed could also be applied in the field of thermodynamics. Even though the heat equation is form invariant under general spatial coordinate transformations, a full implementation requires an independent control over the medium thermal conductivity and specific heat, which is challenging in practice [204]. Conversely, the thermal analogues of the considered diffusive cloaks would only demand an engineered diffusivity.

Chapter 4. Graphene based metamaterials for infrared applications

In this chapter we discuss in detail the properties of graphene, both in free standing layer configuration and as a multilayer graphene dielectric metamaterial. Due to its unique ability to dynamically tune the surface conductivity, the graphene and graphene-based metamaterial are promising for multiple applications in the THz and mid-infrared range (MIR). Among these applications are lenses [138], beam steerers [205], nanoantennas [206] to name a few. Here we design and analyze three different designs of a beam steerer (BS) based on multilayer graphene-dielectric metamaterial, which allows us to manipulate the direction of radiation in a wide range of angles.

4.1. Introduction to graphene based metamaterials

In Chapter I we already disscussed the history of graphene and mentioned some of its potential application fields, for instance telecommunication [118], imaging systems [119,120] and integrated optoelectronics [121,122]. However, thanks to its ultrathin nature, it can also be incorporated into other materials on a subwavelength scale opening the door to active metamaterials with exotic and tunable values of permittivity and permeability. These metamaterials can be advantageously used for the synthesis of ultra-compact devices operating in the THz regime, for a variety of applications such as super resolution imaging, cloaking, etc., overcoming the performance achievable with conventional, naturally available dielectrics [11,108,207,208].

Multilayer graphene-dielectric metamaterials have recently attracted the interest of the scientific community [115,130–132,209]. They consist of graphene sheets alternating with layers of a host dielectric [see inset in Fig. 4.1(a)]. In this configuration, the effective permittivity of the resulting metamaterial can be tuned by changing the surface conductivity of the graphene layers (it can be done, for example, by optical excitation or electric bias voltage [210]). Also, since the distribution of the chemical potential of graphene layers in the metamaterial can be arbitrary, it is possible to tailor an inhomogeneous medium for active control of light, e.g. beam steering, focusing, squeezing based on transformation optics, etc. [68,130,138]. Graphene-based devices offer a much higher modulation speed compared to conventional devices, whose design involves other mechanisms of light control: mechanical systems with movable mirrors, thermo-optic and acousto-optic phase tuning [211–215]. This makes graphene-based devices promising for future optical data processing [216,217], where high modulation speed is required.

As it was mentioned in Chapter I, graphene supports SPPs and, hence, leaky-wave antennas based on graphene mono-layers [118,205,206,218] have been proposed to date, which are feasible with the state-of-the-art technology and demonstrate good steering capabilities. However, their dimensions are limited by the attenuation of SPPs in graphene. The beam steering

devices enabled by multilayer graphene-dielectric metamaterials allow for bigger lateral dimensions and for a more efficient, directive beam steering. The physical aperture of these metamaterial-based devices is defined by the number of the layers of graphene and, consequently, by the cost and complexity of the constituent metamaterial fabrication. However, unlike the experimentally tested monolayer graphene technology, devices based on graphene multilayer structures or graphene metamaterials are beyond current fabrication capabilities and, for the moment, exist only as theoretical concepts. Nevertheless, recent advances in the fabrication and practical applications of multilayer graphene structures [219–221] can reduce the cost and complexity of the graphene metamaterial technology in the future.

4.1.1. Modelling graphene and its properties

In this thesis the graphene layer is modelled assuming a linear response[11] and in the absence of magnetic bias field[12]. Therefore, using the general Kubo formula [134], the graphene's conductivity σ_g can be modelled as:

$$\sigma_g = \sigma_{\text{intra}} + \sigma_{\text{inter}} = \frac{\mathrm{i}k_B T \log\left(2\cosh\left(\frac{\mu_c}{2k_B T}\right)\right)}{\pi h^2 (\omega + \mathrm{i}\gamma)} + \\ + \frac{e^2}{4h}\left(G\left(\frac{\omega}{2},\mu_c,T\right) + \frac{4\mathrm{i}\omega\int_0^\infty \frac{G(\Omega,\mu_c,T) - G\left(\frac{\omega}{2},\mu_c,T\right)}{\omega^2 - 4\Omega^2}\mathrm{d}\Omega}{\pi}\right) \tag{4.1}$$

$$G(\omega,\mu_c,T) = \frac{\sinh\left(\frac{h\omega}{k_B T}\right)}{\cosh\left(\frac{h\omega}{k_B T}\right) + \cosh\left(\frac{\mu_c}{k_B T}\right)}$$

where, σ_{intra}, σ_{intra} are the conductivities for the intraband and interband contributions respectively, k_B is the Boltzmann's constant, μ_c is the chemical potential, h is the Plank's constant, ω is the angular frequency, γ is the scattering rate and T is the temperature.

The graphene conductivity σ_g is calculated at ambient temperature T = 300 K and scattering rate of $\gamma = 10^{12}$ s^{-1}, which corresponds to the experimentally measured mobility of exfoliated suspended graphene [222]. This is a relatively small value which is chosen as a best case, since our aim is to provide a clear principle demonstration. Lower quality graphene, fabricated using chemical vapor deposition (CVD), can worsen the performance of the device. Nevertheless, constant improvements in graphene fabrication allow us to be optimistic and

[11] The linear response of graphene allows to apply the Kubo formalism. As it was shown in [237], graphene exhibits nonlinearity in the far-infrared to terahertz regime for electric fields higher than ~ (300 – 10^3) V/cm and for room temperature.

[12] In the absence of magnetic bias field, the off-diagonal (Hall) components of conductivity tensor disappear and the graphene's conductivity becomes isotropic.

upna Universidad Pública de Navarra Nafarroako Unibertsitate Publikoa

believe that high mobility may soon be reached in CVD samples, see [116,117]. For the chosen parameters, the calculated conductivity of graphene as a function of frequency and its chemical potential μ_c is shown in Fig. 4.1(a-b).

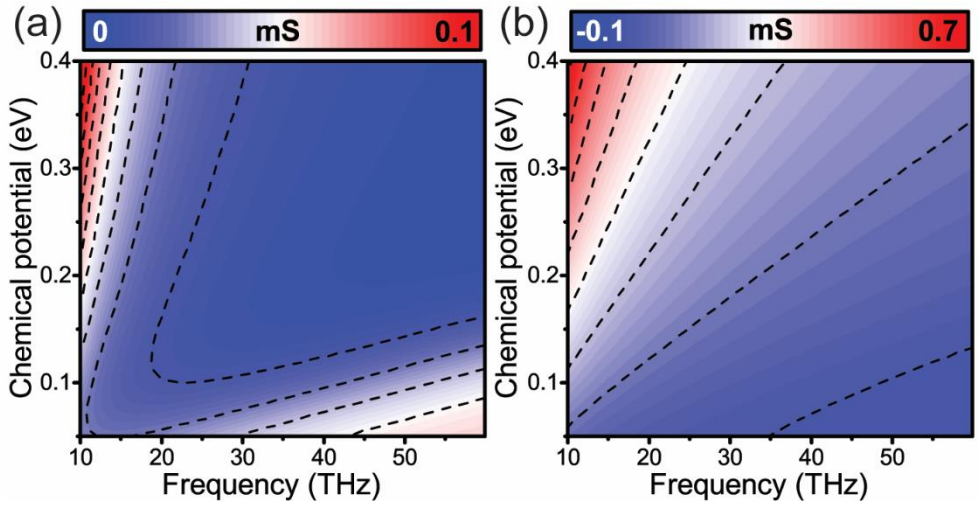

Fig. 4.1. Real (a) and imaginary (b) part of the conductivity as a function of the chemical potential and frequency (T = 300 K, $\gamma = 10^{12}$ s^{-1}), following the Kubo formula.

As it can be seen in Fig. 4.1, for low frequencies or low chemical potential the real part of conductivity has higher values, which results in big losses. In this thesis we set the operating frequency at f = 20 THz. At this frequency the real part of conductivity is relatively small and the imaginary part is positive for all values of chemical potential. This can be better seen in Fig. 4.2(a), where the real and imaginary part of conductivity are shown as a function of the chemical potential at f = 20 THz.

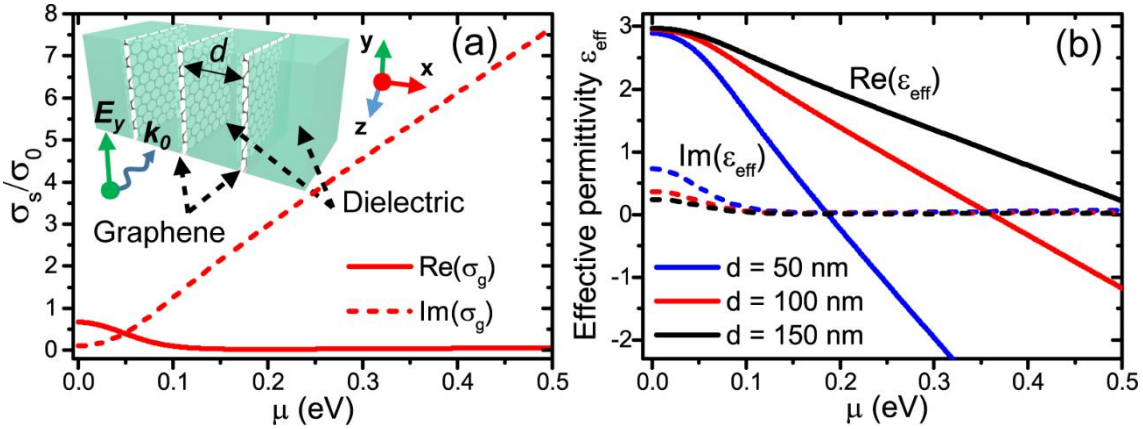

Fig. 4.2. (a) Graphene complex conductivity normalized to $\sigma_0 = e^2/4\hbar$ =0.061 mS for T = 300 K, $\gamma = 10^{-12}$ s^{-1} at f = 20 THz. (Inset) Geometry of the graphene-dielectric metamaterial. (b) Complex effective permittivity, ε_{eff}, for ε_m = 3, T = 300 K, f = 20 THz and different values of spacer thickness d. Solid and dashed lines stand for real and imaginary parts, respectively.

4.1.2. Multilayered graphene-dielectric system

The graphene-dielectric metamaterial used in this thesis, consists of an array of graphene layers with period *d* and embedded in a host dielectric with permittivity ε_m [115,136]. The structure is shown in the inset of Fig. 4.2(a). Its local permittivity can be tuned by changing the conductivity of graphene sheets. This can be done, for instance, by applying a bias voltage to each pair of the latter [115,210]. In this geometry, the electric field components parallel to graphene layers (E_y, E_z) see a metamaterial effective permittivity ε_{eff}, whereas the perpendicular component (E_x) sees the host dielectric permittivity ε_m. Thus, the metamaterial permittivity tensor is:

$$\varepsilon = \begin{pmatrix} \varepsilon_m & 0 & 0 \\ 0 & \varepsilon_{eff} & 0 \\ 0 & 0 & \varepsilon_{eff} \end{pmatrix} \tag{4.2}$$

where ε_{eff} is the relative effective permittivity described by the following expression [114,223]:

$$\varepsilon_{eff}\left(\omega, \mu_c, d\right) = \varepsilon_m + \frac{\mathrm{i}\sigma_g\left(\omega, \mu_c\right)}{d\omega\varepsilon_0} \tag{4.3}$$

where *d* is the thickness of the host dielectric, σ_g is the graphene surface conductivity, ε_0 is the free space permittivity and ω is the angular frequency. Cesium iodide (CsI, $\varepsilon_m = 3$) is chosen as a host dielectric since it has a good performance in terms of transparency and absorption losses in the infrared range [224]. The effective permittivity calculated as a function of the chemical potential μ and different values of the spacer *d* is shown in Fig. 4.2(b). For small values of *d*, the curve for $\mathrm{Re}(\varepsilon_{eff})$ is steeper, so that it can be tuned with small changes of graphene's Fermi energy. However, a small *d* increases $\mathrm{Im}(\varepsilon_{eff})$ [see Fig. 4.2(b)] as well as the total number of graphene layers, raising losses in the metamaterial, as well as the cost and complexity of fabrication. As a compromise, a period $d = 100$ nm is chosen, providing a broad tunability range ($0.1 < \mathrm{Re}(\varepsilon_{eff}) < 2.8$) for relatively low values and range of graphene's chemical potential ($350\ \mathrm{meV} > \mu_c > 50\ \mathrm{meV}$) and corresponding low values of the imaginary effective permittivity component ($0.02 < \mathrm{Im}(\varepsilon_{eff}) < 0.2$).

Numerical simulations were performed using the frequency domain solver of COMSOL Multiphysics™. The graphene-dielectric metamaterial was modelled using infinitesimally thin conductive layers for graphene sheets. Their dispersion was set using the Kubo formula. A fine hexahedral mesh was used with minimum and maximum mesh cell sizes of 0.75 μm ($0.05\lambda_0$) and 1.5 μm ($0.1\lambda_0$), respectively. A waveguide port with a vertically polarized electric field (E_y) mode, impinging normally on the beam steerer was used as a source. To reduce the computation time, all simulations were performed in a 2D geometry, imposing periodic boundary conditions along the *y*-axis. Perfectly matched layers were used for the rest of the boundaries to emulate open space.

4.2. Beam steering based on graphene-dielectric metamaterial

We propose a concept of a reconfigurable BS based on a multilayer graphene-dielectric metamaterial using three different approaches: (BS1) a GRIN metamaterial block, where the tunability of the graphene metamaterial is used to synthesize a prescribed phase change as a wave propagates through the structure; (BS2) a BS exploiting decoupled transmission channels (metallic parallel-plate waveguides filled with graphene-dielectric metamaterial) to create a phased array with high speed reconfiguration of each channel, enabling beam steering capability; and (BS3) a device that combines the previous designs by synthesizing an array of planar dielectric waveguides (transmission channels) in a graphene-dielectric metamaterial by defining a specific distribution of Fermi energy levels in graphene layers. The performance of all designs is investigated numerically, demonstrating their steering capability for a wide range of output angles. The results are compared against analytical calculations based on the Huygens-Fresnel principle.

4.2.1. GRIN medium for controlling waves

The first design, BS1, is based on a phase delay line, created in a GRIN structure [225]. A linear distribution of the local refractive index in a medium steers the beam in the required direction. The scheme of the proposed BS1 is shown in Fig. 4.3(a). The GRIN medium is achieved by creating a spatial distribution of chemical potential values $\mu_c(x)$ on the graphene-dielectric metamaterial.

Since the imaginary part of effective permittivity is small (see Sect.4.1) it is omitted in the analytical calculations for simplicity. Therefore the distribution of the refractive index $n(x)$ of the metamaterial along the x-axis, required for achieving a beam steering angle θ, can be calculated using the ray tracing method, as follows [6,79]:

$$n(x) = \frac{\sin(\theta)}{L_z}(x - L_x) + n_{\max} \tag{4.4}$$

where x is the coordinate along the x-axis, n_{max} is the maximum refractive index of the BS, L_x is the total width and L_z is the length of the BS1. The minimal length $L_{z(min)}$ depends on the maximum output angle and can be calculated as:

$$L_{z(\min)} = \frac{L_x \sin(\theta_{\max})}{\sqrt{\varepsilon_{\max}} - \sqrt{\varepsilon_{\min}}} \tag{4.5}$$

where θ_{max} is maximum output angle, and ε_{max}, ε_{min} are the extreme values of the real permittivity attainable in the considered graphene-dielectric metamaterial.

Since the material is a GRIN medium, the beam inside the structure is focused towards the side with a higher refractive index [226]. For high values of θ, the gradient of the refractive index becomes steeper, which results in a focusing of the transmitted beam (as it will be shown later). In the limit, this can even cause a reflection back to the input. To obtain the maximum

achievable angle, θ_{theor}, we analyse light propagation inside a GRIN medium using the Eikonal equation under the formalism of ray theory [226]:

$$\frac{d^2x}{dz^2} = \frac{1}{n(x)}\frac{dn(x)}{dx} \tag{4.6}$$

By inserting (4.4) into (4.6) and after solving the differential equation we obtain the ray trajectory $x(z)$ [226] [see dashed line in Fig. 4.5(a-c)]. The output angle θ' of the ray can be derived using the slope of the trajectory at the output $\theta_{sl} = dx/dz$ particulared at ($x = x_{out}$, $z = L_z$) and Snell's law: $\theta' = \sin^{-1}[n(x_{out})\sin(\theta_{sl})]$, where $n(x_{out})$ is the refractive index at the output ($x = x_{out}$). Note, that since the ray theory allows finding the actual ray slope at the output surface, the final output angle θ' can slightly deviate from the design output angle θ, which is derived using approximate equations, without taking into account ray propagation inside the GRIN medium.

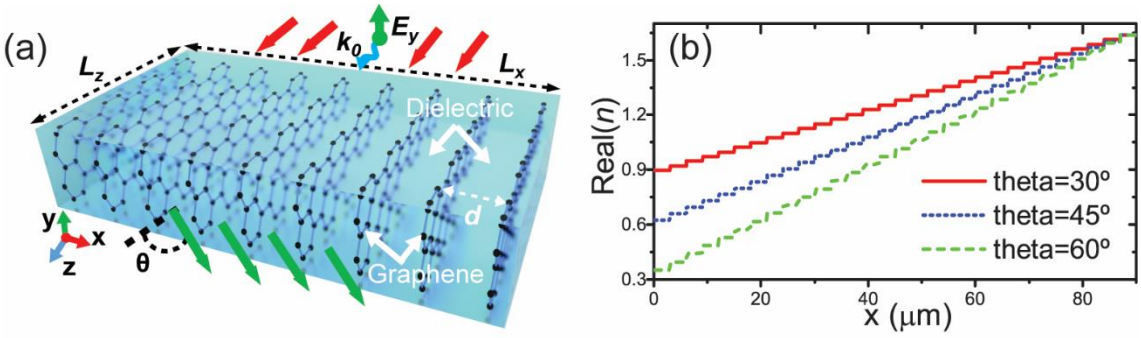

Fig. 4.3. (a) Illustrative scheme for the BS1. (b) Real part of the effective refractive index vs the x coordinate for the BS1.

Since the beam is refracted towards the side with higher refractive index, an analogy between a GRIN lens and the proposed GRIN BS (BS1) can be drawn. The focal length FL (distance from the output surface of the BS1 to the focal point) can be calculated as $FL = (L_x - x_{out})/\tan(\theta')$ (in this case we define the optical axis at $x = L_x$). Therefore, by numerically solving (4.6) and extracting the focal distance as a function of the design output angle θ, the maximum output angle $\theta_{theor} = 66°$ is found, which corresponds to the case when the beam is focused exactly at the output surface ($FL = 0$). In order to minimize the length L_z of the BS and therefore losses, in this work $\theta_{max} = 60°$ (with $\varepsilon_{max} = 2.7$, $\varepsilon_{min} = 0.1$ and corresponding $\mu_{min} = 0.06$eV, $\mu_{max} = 0.35$ eV, $L_z = 58$ μm) is chosen, slightly smaller than the theoretical maximum angle θ_{theor}.

Once the effective refractive index profile is obtained, the corresponding values of the chemical potential $\mu_c(x)$ of graphene layers can be interpolated using (4.3). To simplify the structure, the required ideally smooth spatial distribution of the metamaterial effective index of refraction is discretized in 30 steps [see Fig. 4.3(b)]. The final design of the BS1 is shown in Fig. 4.3(a) and has the following dimensions: $L_x = 6\lambda_0 = 90$ μm, $L_z = 3.8\lambda_0 = 58$ μm. The total number of graphene layers is $N = L_x/d = 900$. The tunability of the BS1 is numerically checked by means of full-wave simulations, performed in COMSOL Multiphysics™. The output angles are obtained as a function of the inclination of the chemical potential $inc = \Delta\mu_c/\Delta x$ in the BS1's profile, where

$\Delta\mu_c$ is the change of chemical potential induced by the gating voltage difference and Δx is the variation of the coordinate x. The result is plotted in the Fig. 4.4 (solid red line). The maximum output angle for the specified parameters is $\theta_{\max}^{(1)} = 63°$. Larger angles are impossible to achieve due to the reflection of the incident wave inside the structure. This is in good agreement with the previously calculated theoretical maximum angle θ_{theor}.

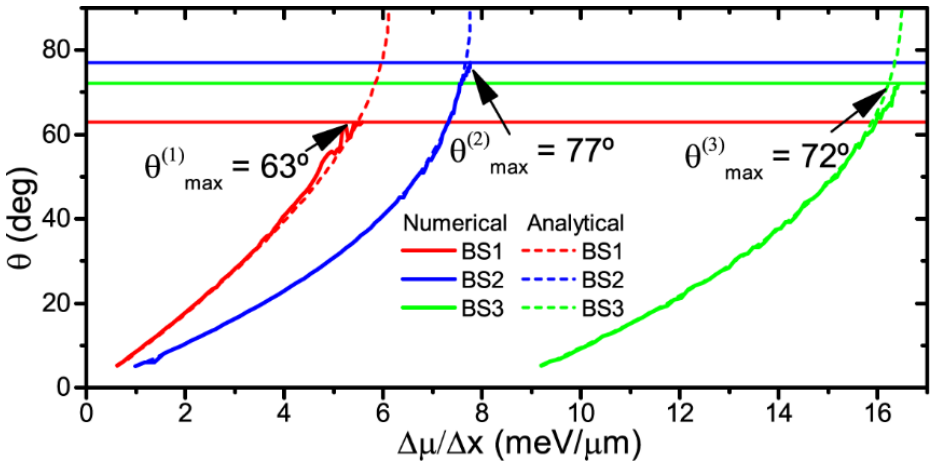

Fig. 4.4. Analytically (dashed lines) and numerically (solid lines) calculated output angles of the BSs vs the inclination of the graphene's chemical potential $\Delta\mu_c/\Delta x$ in the metamaterial for the BS1 (red), BS2 (blue) and BS3 (green). Horizontal solid lines represent the maximum output angles for the three BS designs.

For illustrative purposes, the performance of designed BS is analyzed at 3 different output angles: 30°, 45° and 60°. The E_y-field magnitude distribution obtained for these angles for the BS1 is presented in Fig. 4.5(a-c).

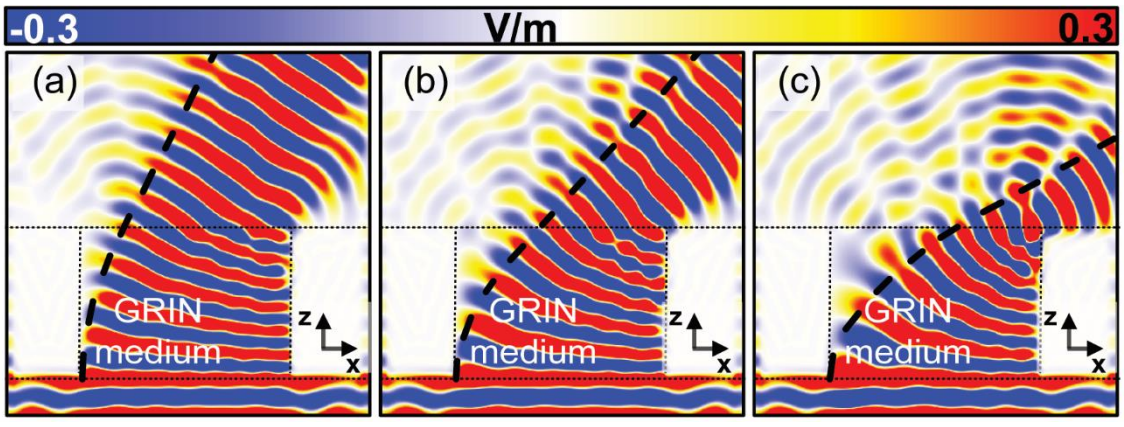

Fig. 4.5. Numerically calculated magnitude of the E_y-field for BS1 and output angles: (a) $\theta = 30°$, (b) $\theta = 45°$, (c) $\theta = 60°$. Black dashed lines represent the analytical solutions for the ray propagation inside the GRIN medium.

As can be seen from Fig. 4.5(c), due to the steep profile of the refractive index the beam is focused at the output. This leads to a significantly reduced effective aperture of the BS1, which broadens the beamwidth. For extreme angles (θ > 50°), this provokes higher side lobes due to reflection at the BS1 borders. This is demonstrated in Fig. 4.6, where the normalized radiation patterns for all three angles are plotted. One can see that the side lobe level for θ = 60° is higher than for θ = 30°, 45°. The radiation properties of all three analyzed BSs are summarized in Table IV.

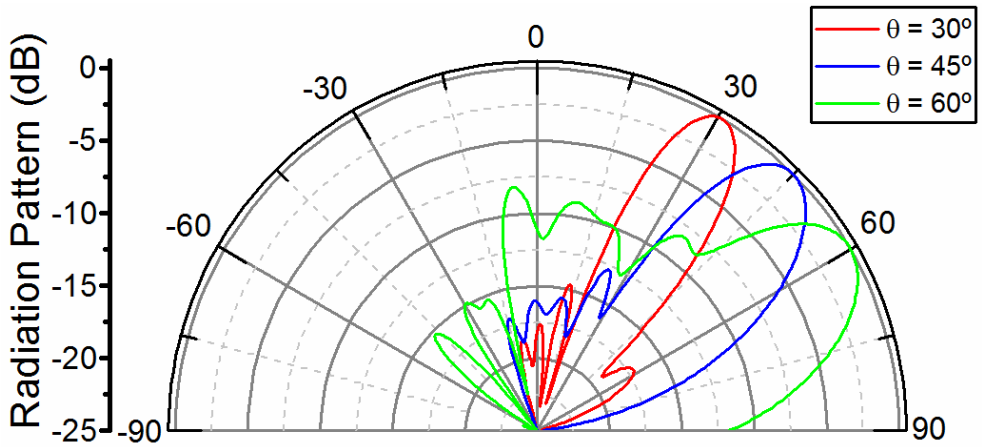

Fig. 4.6. Normalized numerical radiation patterns of the BS1 calculated for the output angles of 30° (red), 45° (blue), and 60° (green).

4.2.2. Phased array of graphene-enabled metallic waveguides

As it can be seen in Fig. 4.5(a-c), the BS1 design is relatively simple and provides good performance for small output angles, but it has a fundamental limitation on the maximum output angle due to the ray refraction inside the GRIN medium. One way to overcome this limitation is to recall the phased array principle, where each phase delay line is isolated from the adjacent lines, providing a more uniform phase and amplitude distribution at the output [6,227]. This idea is exploited in the BS2 design we describe in this Section.

The BS2 consists of an array of metallic parallel-plate waveguides of identical height a (working at single TEM mode regime with horizontal E_x component), filled with graphene-dielectric metamaterial [115,213] [see sketch in Fig. 4.7(a)]. Therefore, unlike the BS1, the BS2 structure is excited with a horizontally polarized (E_x) waveguide port in order to excite such TEM mode in each waveguide. To obtain the required local phase delay at the output of such structure, we tune the effective refractive index n_{eff} of the q^{th} parallel-plate waveguide core, thus, changing the propagation constant β^q of its TEM mode:

$$\beta^q = k_0 n_{eff}^q \tag{4.7}$$

where k_0 is the wave vector in free space and q is an integer denoting each waveguide. Here, analogously to the previous design, only the real part of refractive index is considered due to the small values of the imaginary part.

In order to reduce the length of the waveguides, and hence their weight and losses, the modulo of 2π is applied to the output phase. The required phase at the output of the q^{th} waveguide and its length are calculated as follows [6,227]:

$$\phi^q = \beta^0 L_z - \mathrm{mod}\left(k_0 x^q \sin(\theta), 2\pi\right) \tag{4.8}$$

$$L_z = \frac{2\pi}{\beta_{\max} - \beta_{\min}} \tag{4.9}$$

where $\beta^0 = \beta_{max}$ is the propagation constant of the guided mode in the reference waveguide, q = 1, 2, 3… is the number of waveguide, θ is the output angle, x^q is the x coordinate of the q^{th} waveguide, L_z is the length of the waveguides, $\beta_{\max} = k_0 n_{eff}^{(\max)}$ and $\beta_{\min} = k_0 n_{eff}^{(\min)}$ are maximal and minimal propagation constants respectively [$n_{eff}^{(\max)}, n_{eff}^{(\min)}$ are maximal and minimal effective refractive indices of the waveguide core, which are chosen to provide high and uniform transmission coefficient $S_{21}(n_{eff})$ for all values of refractive index ($n_{eff}^{(\min)} \le n_{eff} \le n_{eff}^{(\max)}$)]. Finally, the effective refractive index n_{eff}^q of the q^{th} waveguide core required to obtain a desired output phase delay ϕ^q can be defined as:

$$n_{eff}^q = \frac{\phi^q}{k_0 L_z} \tag{4.10}$$

The distribution of n_{eff}^q is shown in Fig. 4.7(b). The corresponding values of the chemical potential μ^q of graphene layers in the q^{th} waveguide can be interpolated using (4.3). The final BS design consists of a total q = 25 waveguides with height a = 1 μm, separated by metallic walls with thickness w = 4 μm, which gives a total period of p = 5 μm [see Fig. 4.7(a)]. From additional simulations for one waveguide $n_{eff}^{(\max)}$ = 1.05 and $n_{eff}^{(\min)}$ = 0.32 are found, which provide a flat response of $S_{21}(n_{eff})$ > -2dB. Thus the final dimensions are: total width $L_x = 25p$ = 125 μm ($8.3\lambda_0$), and length L_z = 20.5 μm ($1\lambda_0$).

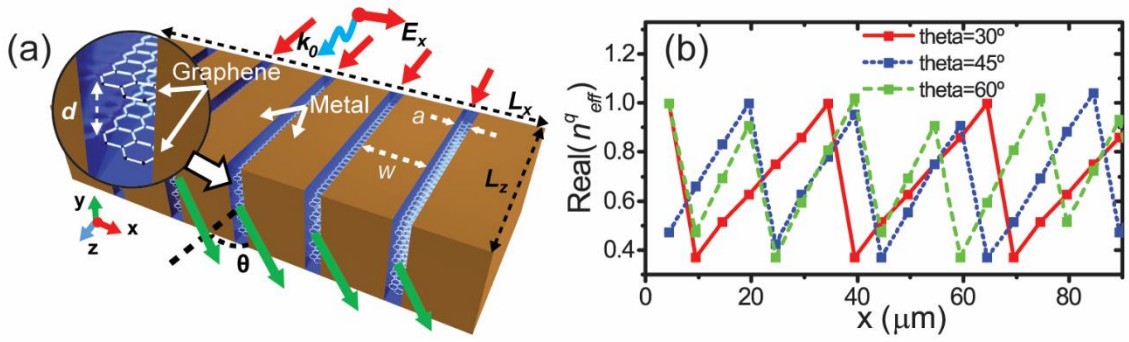

Fig. 4.7. (a) Illustrative scheme for the BS2. (b) Real part of the effective refractive index vs the x coordinate for the BS2.

The rest of the boundaries remain unchanged. In our numerical model, the metallic walls are made of copper. At the design frequency f = 20 THz, the analytical skin depth in the copper

is δ_{Cu} = 0.03 μm [228], which is much smaller than the thickness of the walls. To reduce the computation time, we use the tensorial effective medium approximation for the graphene-dielectric metamaterial, (4.2) and (4.3). To prove the validity of this approach we simulate a single waveguide filled with homogeneous dielectric and graphene-metamaterial. The refractive index of the effective medium can be extracted from the scattering parameters S_{11} and S_{21}, using a retrieval method [56]. Fig. 4.8 shows the refractive indices extracted from the *S*-parameters for the waveguide filled with graphene-dielectric metamaterial and an equivalent homogeneous dielectric. As it can be seen, the retrieved refractive indices perfectly match the analytical values, confirming the validity of the metamaterial homogenization.

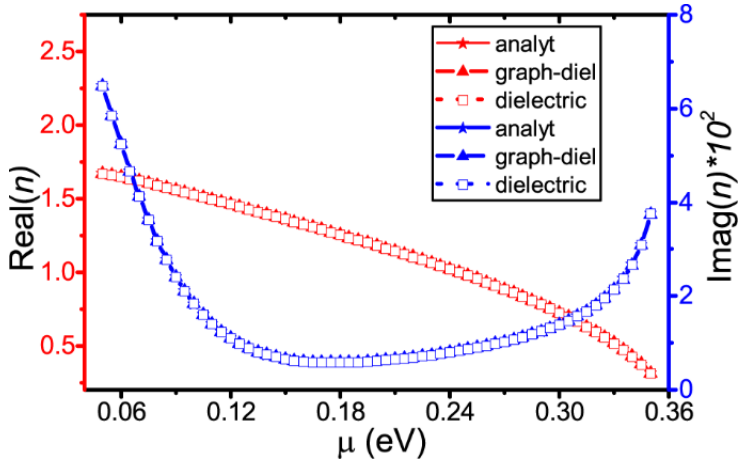

Fig. 4.8. Analytically (solid lines) and numerically calculated effective refractive index for a TEM mode of a parallel-plate waveguide filled with a dielectric medium (dotted lines) and with graphene-dielectric metamaterial (dashed lines). This shows the validity of tensorial effective medium approach for BS2 for faster calculations.

Analogously to the BS1, the steering capability of BS2 is studied using full-wave simulations. The output angle is tuned by changing the inclination of the chemical potential in the metamaterial $inc = \Delta\mu_c/\Delta x$. The numerically obtained output angles for the second BS design are shown in Fig. 4.4 (solid blue line). The maximum angle is $\theta_{\max}^{(2)}$ = 77°, which is larger than in the previous design. However, the designed maximum angle 90° (dashed blue line) is never reached, which can be explained by the non-isotropic radiation pattern of each phased array element (end of each waveguide). Therefore, an array of such elements cannot reach end-fire performance.

The numerically obtained E_x-field distributions in the *xz*-plane for the BS2 are shown in Fig. 4.9(a-c). The results demonstrate that the structure can bend the plane wave incident at 0º to output angles of 30°, 45° and 60°. Moreover, it can be seen that the wavefronts at the output for all angles are closer to a plane wavefront than the ones observed in BS1, Fig. 4.5(a-c).

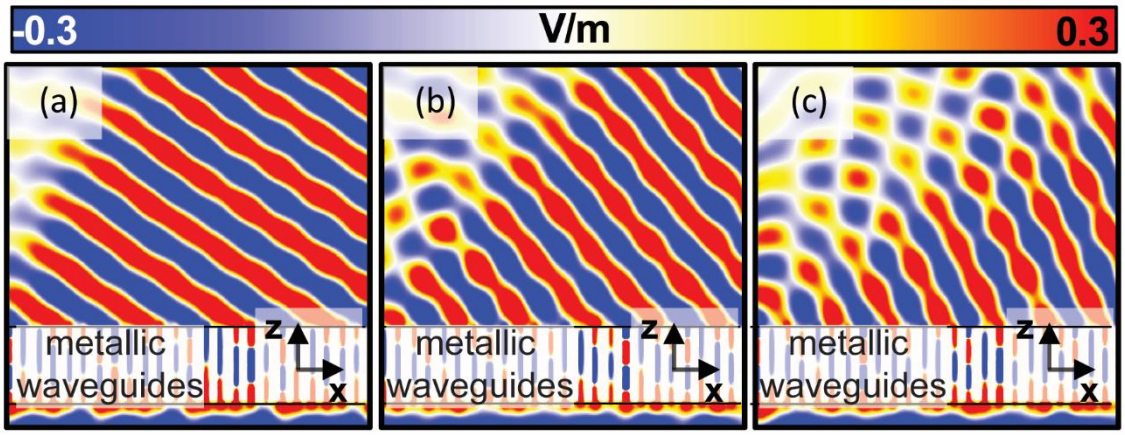

Fig. 4.9. Numerically calculated magnitude of the E_y-field for the first design for output angles: (a) θ = 30°, (b) θ = 45°, (c) θ = 60°.

This improved performance can be explained by a more uniform distribution of the amplitudes and phases at the output, since the beam in the BS2 is not focused at the output, thanks to the decoupled transmission channels. The numerically obtained normalized radiation patterns of the BS2 are plotted for the three angles considered in Fig. 4.10 and compared with analytical results, obtained with the Huygens-Fresnel method considering an array of isotropic sources with same amplitude (which has not been applied in the first design due to a more complicated amplitude and phase distribution at the output of the BS1) [79,145]. The analytical and simulated radiation patterns are almost identical for all angles and coincide with the design output angles. However, from Fig. 4.10, it is also clear that the grating lobes increase for large output angles due to the finite period p of the waveguide array. As shown in Table *IV*, the reflection coefficient Γ of the BS2 is below −5.2 dB in all cases. As expected, it is significantly higher than for the BS1, due to the higher impedance mismatch between free space and the array of metallic waveguides.

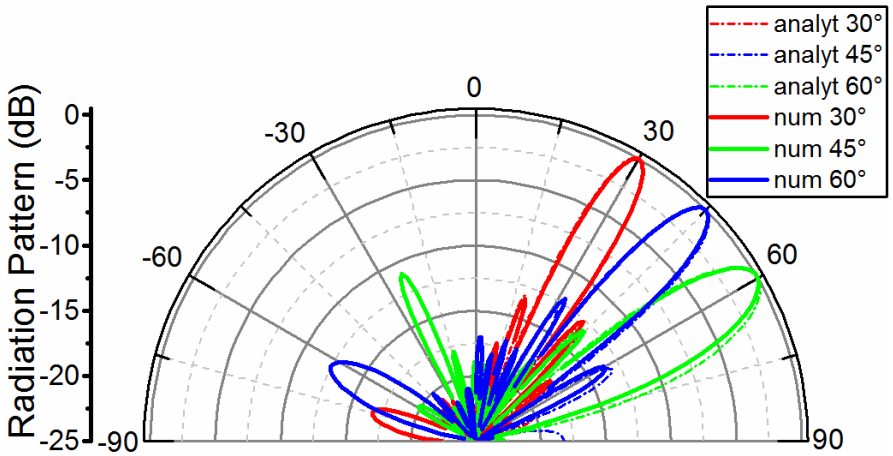

Fig. 4.10. Normalized numerical radiation patterns for the BS2, analytically (dashed) and numerically (solid) calculated for the output angles of 30° (red), 45° (blue), and 60° (green).

4.2.3. Phased array of graphene-dielectric waveguides

The array of metallic waveguides provides better performance in terms of beamwidth and maximum output angle. However, the BS2 requires complex fabrication due to the small distance between waveguides, *w*. It is possible to increase the period *p* of the array at the cost of higher grating lobes. However, thicker metallic walls also increase the impedance mismatch of the BS2 with free space, resulting in a higher reflection loss of the device.

These limitations are overcome in the design BS3 [see Fig. 4.11(a)]. It is a combination of the previous concepts of BS1 and BS2 and consists of a phased array of planar waveguides, created in the graphene-dielectric metamaterial by alternating the regions (waveguide core and cladding) with high contrast of refractive indices ($n_c >> n_{cl}$). This can be obtained through non-uniform doping of graphene layers in the metamaterial, resulting in a totally reconfigurable system.

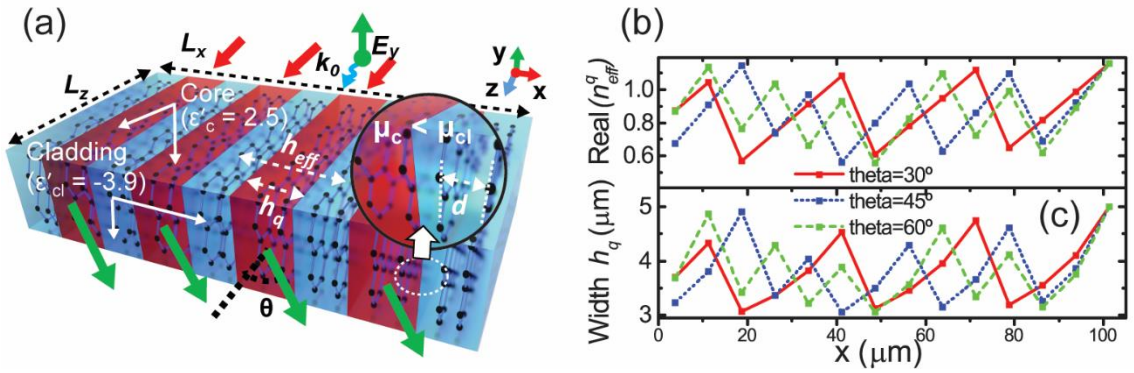

Fig. 4.11. (a) Illustrative scheme for the BS3. (b) Real part of the effective refractive index vs the *x* coordinate for the BS2. (c) Spatial distribution of the widths h_q in BS3.

The propagation constant $k_0 n^q_{eff}$ of the mode *m* in each waveguide *q* can be found using the dispersion equation of a planar waveguide [229]:

$$h_q k_0 \sqrt{\varepsilon'_c - (n^q_{eff})^2} = 2\tan^{-1}\left(\frac{\sqrt{(n^q_{eff})^2 - \varepsilon'_{cl}}}{\sqrt{\varepsilon'_c - (n^q_{eff})^2}}\right) + \pi(m-1) \tag{4.11}$$

where h_q is the waveguide width, k_0 is the wave vector in free-space, ε'_c, ε'_{cl} are the real values of the effective permittivity of the core and cladding respectively, n^q_{eff} is the effective refractive index of the mode in each *q* waveguide, and $m = 1, 2, 3\ldots$ is the mode number. For the sake of simplicity and in order to minimize the width h_q, a single-mode waveguide configuration is chosen ($m = 1$).

The length of each waveguide and the output phase at its end are calculated using (4.8) and (4.9), similarly to the previous designs considering only the real part of the effective index of refraction. To minimize mutual coupling between adjacent waveguides, a certain minimal distance between them is required. This increases the period of the array and therefore can lead

to higher grating lobes. To reduce the effective width of each waveguide or the distance between waveguides, it is necessary to minimize the mutual coupling effect or, in other words, provide strong guiding in each element. The effective width of the waveguides can be found as [229]:

$$h_{eff} = h_q + \frac{2}{k_0(\varepsilon'_c - \varepsilon'_{cl})} \tag{4.12}$$

Therefore, our aim is to increase the difference between the effective permittivity of the core ε'_c and the cladding ε'_{cl} so that the effective width h_{eff} is reduced.

In our particular case layers with real values of effective permittivity $\varepsilon'_c = \varepsilon_{max} = 2.5$ ($\varepsilon''_c = 0.1$) and $\varepsilon'_{cl} = \varepsilon_{min} = -3.9$ ($\varepsilon''_{cl} = 0.05$) are used which correspond to values of chemical potential $\mu_{min} = 0.08$ eV and $\mu_{max} = 0.82$ eV, respectively. The cladding with negative effective permittivity acts as a weakly metallic wall, which results in a smaller field penetration [132] into the cladding (analytical skin depth $\delta_w = \lambda[2\pi(-\varepsilon'_{cl})^{1/2}]^{-1} = 1.2$ μm) and therefore smaller period of waveguides, s. However, since at MIR frequencies and for the considered doping levels, the real part of the conductivity of graphene layer is noticeably smaller than in metals (e.g. copper or silver) such "metallic" medium provides lower losses [131]. Thus, for the chosen values of permittivity the minimal period of waveguides $s_{min} = 7.5$ μm ($>h_q$) is achieved. Analogously to the previous BS design, the modulo of 2π is applied to the output phase in order to reduce the length of the waveguides and therefore the losses. Moreover, the shorter length of the waveguides also reduces the coupling between adjacent waveguides, which is proportional to their length.

From (4.11), the propagation constant (or effective refractive index) in each planar waveguide can be tuned by changing either the core permittivity or the width of the waveguide. However, a small core permittivity ε'_c is not desired, since it increases the effective width of the core. Thus, the effective refractive index of each planar waveguide is tuned from $n_{eff}^{(min)} = 0.52$ to $n_{eff}^{(max)} = 1.56$ by varying the waveguide width from $h_q = 3$μm to 5μm. After calculating the phase profile at the output, using (4.8), the corresponding effective refractive indices n_{eff}^q are obtained. The final distributions of n_{eff}^q for the chosen parameters are shown in Fig. 4.11(b). The corresponding values of the waveguide widths h_q can be found from (4.11) and they are shown in Fig. 4.11(c). The final geometry is similar to the first BS design shown in Fig. 4.3(a). It has the following dimensions: $L_x = 14h_q = 105$ μm, $L_z = 23.5$ μm ($1.2\lambda_0$) [Fig. 4.11 (a)]. The total number of graphene layers is $N = L_x/d = 1050$.

The performance of the BS3 is evaluated by changing the inclination of the refractive index $inc = \Delta\mu_c/\Delta x$. The numerically obtained output angles of the BS3 are shown in Fig. 4.4 (solid green line) and compared with design pre-set values (dashed green line). Similar to the BS2, the beam steering angle of 90° is never reached. This is also due to the finite directivity of each phased array element, i.e. non-isotropic radiation of an open waveguide. Moreover, the maximum angle of the BS3 is $\theta_{max}^{(3)} = 72°$, which is slightly smaller than in the BS2 design. This is due to the fact that the

aperture of each waveguide in the array is larger than in the previous design ($h_q > a$), resulting in a more directive radiation.

Finally, as for the previously discussed BS1 and BS2 designs, the performance of the BS3 is investigated at three demonstrative output angles: 30°, 45° and 60°. The obtained E_y-field distributions in *xz*-plane are shown in Fig. 4.12(a-c).

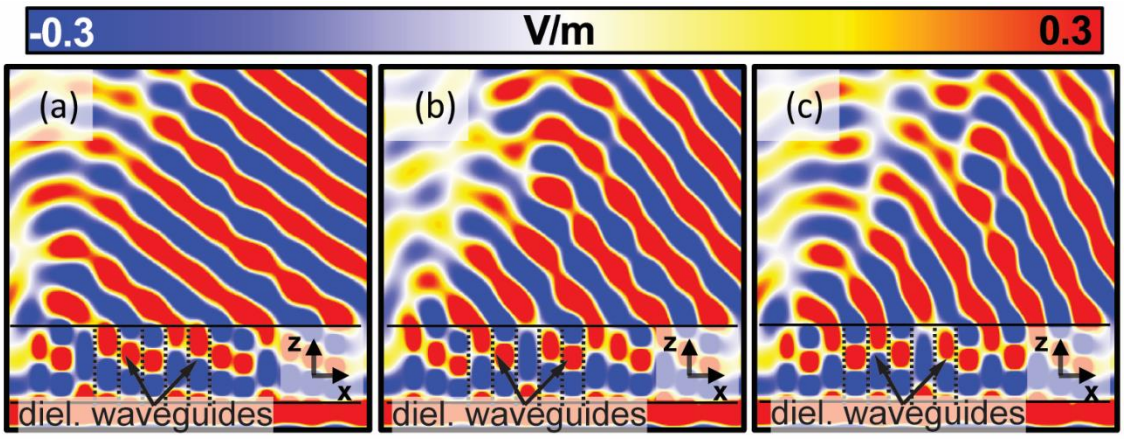

Fig. 4.12. Numerically calculated magnitude of the E_y-field for the first design for output angles: (a) θ = 30°, (b) θ = 45°, (c) θ = 60°.

There are some perturbations of the field, which can be related to the numerically obtained effective refractive indices n_{eff}^{q} slightly differing from their analytical values, and the mutual coupling between adjacent waveguides. The normalized numerical and analytical *E*-field patterns are plotted in Fig. 4.13.

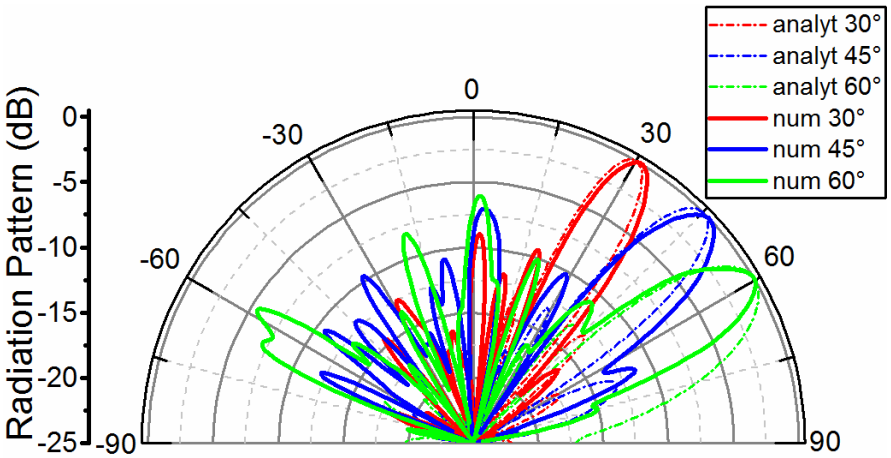

Fig. 4.13. Normalized numerical radiation patterns for BS3, analytically (dashed) and numerically (solid) calculated for the output angles of 30° (red), 45° (blue), and 60° (green).

The grating lobes in BS3 are higher than in BS2. This can be explained by the larger period of the waveguide array, $s = 7.5\ \mu m \geq \lambda_0/2$, and a less uniform distribution of the amplitude at the output due to the factors described above. The reflection coefficient Γ of the BS3 is below -14 dB

for all angles, which is much lower than in the BS2. This can be attributed to a better coupling between the incident field and waveguide modes due to bigger apertures of the waveguides (h_q). To facilitate the comparison of the three BS designs, all numerical results are summarized in Table IV.

Table IV. Numerical analysis of the three proposed BSs.

	Output angle, °			***Γ*[a], dB**			**HPBW[b], °**			**SLL[c], dB**		
Steering angle θ, °	*30*	*45*	*60*	*30*	*45*	*60*	*30*	*45*	*60*	*30*	*45*	*60*
BS1[d]	30.8 (29.3)	44.9 (43.4)	59.9 (-)	-7.8 (-6.8)	-8 (-6.8)	-8.1 (-6.9)	12.8 (13.7)	18.3 (21.9)	22.5 (-)	-14.7 (-10.1)	-12.9 (-5.5)	-8.1 (-)
BS2[e]	30 (30)	45 (45)	60 (60)	-6.1 (-2.4)	-5.2 (-2.4)	-5.5 (-2.4)	6.8 (6)	8.4 (7.3)	11.4 (10.4)	-12.7 (-12.5)	-12.1 (-11.7)	-11 (-11.8)
BS3[f]	30.8 (29.8)	46.4 (44.9)	59.4 (59.4)	-15.1 (-14.3)	-14.7 (-14)	-15.3 (-14.1)	8.4 (7.8)	10 (10)	13.8 (13.2)	-11.9 (-7.6)	-8.9 (-6.4)	-7.3 (-4.4)

[a] *Γ* is the reflection coefficient.
[b] HPBW is the half-power beam width.
[c] SLL is the side-lobe level.
[d] BS based on metamaterial block.
[e] BS based on array of parallel plate waveguides.
[f] BS based on array of waveguides implemented in a graphene metamaterial block with no additional materials.
In the parentheses are given parameters for $\gamma = 10^{13}$ s^{-1}.

As mentioned in Sect. 4.2, all the calculations were done assuming low values of the scattering rate of the graphene ($\gamma = 10^{12}$ s^{-1}). To demonstrate the impact of losses in graphene on the performance of the designed BSs, we ran additional simulations with higher scattering rate, $\gamma = 10^{13}$ s^{-1}. The corresponding numerical results are presented in Table *IV* (values in parentheses). Poorer quality of graphene deteriorates the performance in all BS designs, which is noticed in the increased side lobe and reflection levels.

An open question that remains to be answered is the practical realization of the structures we propose here. Fortunately, recent advances in the fabrication of multilayer graphene [219–221] let us be optimistic about the feasibility of such structures in the near future. Additionally, biasing multilayer graphene seems difficult in practice. One can use self-biased graphene layers [210] connected to opposite poles of a voltage source. Finally, if bias voltage should be avoided, graphene layers can be excited optically [127,230,231].

4.2.3. Conclusions

We propose and numerically analyze three different designs of mid-infrared beam steering devices based on graphene-dielectric metamaterial: (1) GRIN graphene-based metamaterial block, (2) an array of metallic waveguides filled with graphene-dielectric metamaterial and (3) an array of planar waveguides created in a graphene-dielectric metamaterial block with a specific spatial profile of graphene sheets doping. All designs demonstrate an

effective beam control over a wide range of output angles: from 0° to 70° for the considered metamaterial parameters. The numerical results are in a good agreement with analytical results based on Huygens Fresnel method. The calculated radiation patterns demonstrate low side lobe levels of – 11.9 dB for small output angles (≤ 30°). The BS1 provides good side lobe levels with low reflection losses. However, it is limited by the maximum output angle. The BS2 has large range of output angles along with a low side lobe levels and a more robust design. As a penalty, it presents higher reflection losses, reducing the overall efficiency. The BS3 is phased array of planar graphene-dielectric waveguides, which provides a totally reconfigurable mechanism of beam control. It demonstrates an acceptable side lobe level, while maintaining a low reflection coefficient of -14 dB for all sample output angles. These graphene-dielectric metamaterial BSs are promising ultrafast electro-optical and all-optical tunable devices for imaging, sensing and communication applications, which require a small level of reflection losses.

Chapter 5. Conclusions and future lines

The research work presented in this thesis comprises the design and experimental realization of wide variety of applications based on metamaterials: from lenses and beam steerers to cloaking devices. The idea behind this thesis is to demonstrate how broad the field of metamaterials is and the almost unlimited opportunities they offer to design novel devices, rather than focusing on a single application or device. Here we provide a summary of the obtained results and the possible future lines.

5.1. Conclusions

In the field of the metamaterial lenses we have proposed three different designs, with a common building medium – the fishnet metamaterial.

- We proposed to exploit the strong dispersion of the fishnet, which is usually considered as a drawback, turning it into an advantage and designing broadband diffractive optical devices. An optimization procedure based on root-mean-square-error was developed and used to design a broadband zoned fishnet metalens. We showed that the designed prototype broadens the operating frequency range up to three times (with numerical fractional bandwidth $FBW = 8.5\%$), compared with a single mode zoned fishnet metalens. We experimentally demonstrated at two different frequencies of the V-band of the millimeter-waves the focusing performance with transverse resolution less than a wavelength (0.6λ).

- We proposed to apply the fishnet metamaterial to a classical Soret lens, a member of Fresnel zone plate lenses family, with the aim to reduce the reflections from the lens, by improving the coupling between the lens and the incident field; and to increase a directivity of the hybrid Soret fishnet metalens antenna, by forcing the fishnet metamaterial into a near zero refractive index regime. The fabricated Soret fishnet metalens was experimentally analyzed at the W-band of the millimeter-waves, exhibiting a good agreement with the numerical results. A subwavelength transverse resolution (0.6λ) of the focal spot has been confirmed. Consequently, the analysis of the hybrid Soret fishnet metalens antenna has demonstrated that the application of the metamaterial with a refractive index near zero could improve the radiation characteristics. We showed that, due to the inhomogeneity of the fishnet metamaterial, an optimum number of three stacked fishnet plates is required.

- We extended our study on fishnet metalenses by proposing an advanced design of a Wood zone plate fishnet metalens, which eliminates the main drawback of the Fresnel zone plate lenses – the reflections from the opaque zones. We presented the numerical analysis of

the metalens with enhanced matching with free space and experimentally confirmed the focusing performance of the fabricated prototype.

In the field of the cloaking devices we proposed two different cloaking designs based on different cloaking mechanisms: an ultrathin metasurface based carpet cloak and a transformation based diffusive light cloak.

- We presented a design of a carpet cloak based on a cloaking metasurface with array of closed ring resonators. The cloaking metasurface has an ultrathin and simpler than 3D metamaterials design, which allows building more practical cloaking solutions, unlike the transformation optics based solutions. Moreover, due to the symmetry of the used unit cell, the cloaking metasurface is polarization independent and brings a step closer the possibility of ideal cloaking: a cloak able to work under any arbitrary polarization. We numerically analyzed and experimentally demonstrated the cloaking performance of the proposed design. The fabricated cloak could successfully reduce the scattering from an electrically large object (1.1λ) in a relatively large frequency range (*FBW* ~8%) and wide angular span (~15°).

- We theoretically proposed and numerically demonstrated a design of a transformation based cloak, which can work in diffusive light with both static and transient illumination. The cloaking performance of the transformation based diffusive light cloak under a transient illumination (which normally is disrupted due to the non-form invariance of the time-dependent diffusion equation) is possible thanks to a special type of coordinate transformations – unimodular (compression-free) transformations, which preserve the form of the time-dependent diffusion equation. Moreover, we proposed a multidirectional diffusive light cloak, which provides an approximate transient cloaking performance. This cloak requires a homogeneous anisotropic medium for its implementation and can be replaced by a thin layered system of two isotropic materials, facilitating the practical realization.

Finally, in the field of the graphene based metamaterials we proposed three different designs for ultrafast beam steering.

- We proposed a multilayer graphene-dielectric metamaterial beam steerer based on a GRIN medium to control a propagation of transmitted wave. We numerically demonstrated that such design can efficiently bend the beam while maintaining low side lobe level.
- We proposed to extend the range of output angles by introducing phased array systems based on metallic waveguides filled with multilayer graphene-dielectric metamaterial. We demonstrated that such system can steer the beam in wide range of angles at ultrahigh speed.

❖ We theoretically proposed and numerically demonstrated a totally configurable system of a planar dielectric waveguides created in multilayer graphene-dielectric metamaterial. Such system demonstrates good steering capabilities and reduced reflection losses.

Conclusiones

En el campo de las lentes de metamateriales hemos propuesto tres diseños diferentes, con un medio de construcción común - el metamaterial fishnet.

- Hemos propuesto explotar la fuerte dispersión del metamaterial fishnet, que generalmente se considera como un inconveniente, convirtiéndola en una ventaja para el diseño de dispositivos ópticos de difracción de banda ancha. Se ha desarrollado un procedimiento de optimización basado en la raíz cuadrada de la media de errores y se ha utilizado para diseñar una metalente fishnet zonada de banda ancha. Hemos demostrado que el prototipo diseñado amplía el rango de frecuencia de operación hasta tres veces (con ancho de banda fraccional numérica FBW = 8.5%), en comparación con una metalens fishnet zonada monomodo. Hemos demostrado experimentalmente en dos frecuencias diferentes de la banda V de las ondas milimétricas el rendimiento del enfoque con la resolución transversal inferior a una longitud de onda (0.6λ).
- Hemos propuesto aplicar el metamaterial fishnet a una lente de Soret clásica, un miembro de la familia de lentes zonadas de Fresnel, con el objetivo de reducir los reflejos de la lente, mejorando el acoplamiento entre la lente y el campo incidente; y para aumentar la directividad de una antena híbrida de Soret-fishnet, forzando el metamaterial fishnet en un régimen con el índice de refracción cercano a cero. La metalente Soret-fishnet fabricada se ha analizado experimentalmente en la banda W de las ondas milimétricas, con un buen acuerdo con los resultados numéricos. Se ha confirmado una resolución sublongitud de onda transversal (0.6λ) del punto focal. En consecuencia, el análisis de la metalente híbrida Soret-fishnet ha demostrado que la aplicación de un metamaterial con un índice de refracción cercano a cero puede mejorar las características de radiación. Hemos demostrado que, debido a la falta de homogeneidad del metamaterial fishnet, se requiere un número óptimo de tres placas apiladas de fishnet.
- Hemos ampliado nuestro estudio sobre metalentes tipo fishnet mediante la propuesta de un diseño avanzado de una metalente de placas zonadas de Wood, lo que elimina la principal desventaja de las lentes zonadas de Fresnel - las reflexiones de las zonas opacas. Se ha presentado el análisis numérico de una metalente con mejora de adaptación de impedancias al espacio libre, además de la confirmación experimental del rendimiento del enfoque del prototipo fabricado.

En el campo de los dispositivos de invisibilidad propusimos dos diseños diferentes basados en diferentes mecanismos de ocultación: un "carpet cloak" basado en una metasuperficie ultrafina y una capa de transformación para luz difusa.

- Se ha presentado el diseño de un carpet cloak basado en una metasuperficie de consistente en una matriz de resonadores de anillos cerrados. La metasuperficie tiene un diseño ultrafino y más simple que el diseño de los metamateriales 3D, permitiendo la creación de estructuras de más prácticas, a diferencia de las soluciones basadas en la óptica de transformación. Por otra parte, debido a la simetría de la celda unidad, la metasuperficie es independiente de polarización y lleva un paso más cerca de la posibilidad de invisibilidad ideal: una capa de invisibilidad capaz de trabajar bajo cualquier polarización arbitraria. Hemos analizado numéricamente y demostrado experimentalmente el diseño propuesto. La capa de invisibilidad fabricada podría reducir con éxito el scattering de un objeto eléctricamente grande (1.1λ) en un rango de frecuencias relativamente grande (FBW ~8%) y el intervalo angular ancho (~15 °).

- Hemos propuesto teóricamente y demostrado numéricamente un diseño de una capa de invisibilidad basada en transformación óptica, que puede trabajar con luz difusa e iluminación tanto estática como en régimen transitorio. Este tipo de operación de capa de invisibilidad con luz difusa basada en transformación bajo una iluminación transitoria (que normalmente está prohibido debido a la no invariancia de la forma de la ecuación de difusión dependiente del tiempo) es posible gracias a un tipo especial de transformación de coordenadas: transformación unimodular (libre de compresión), que conserva la forma de la ecuación de difusión dependiente del tiempo. Por otra parte, hemos propuesto una capa de luz difusa multidireccional, que proporciona un comportamiento no ideal pero suficientemente robusto para ocultación en régimen transitorio. Esta capa requiere un medio anisotrópico homogéneo para su aplicación y puede ser sustituida por un sistema de capas delgadas formadas por dos materiales isotrópicos, lo cual facilita la realización práctica.

Por último, en el campo de los metamateriales basados en grafeno hemos propuesto tres diseños diferentes para la orientación del haz ultrarrápida.

- Hemos propuesto un director de haz de metamaterial con multicapas de grafeno-dieléctrico basado en un medio de índice gradual (GRIN) para controlar la propagación de la onda transmitida. Hemos demostramos numéricamente que el diseño puede doblar de manera eficiente el haz manteniendo un bajo nivel de lóbulos laterales.

- Se propone ampliar la gama de ángulos de salida mediante la introducción de una agrupación de guías de ondas metálicas rellenas de múltiples capas de

grafeno-dieléctrico, operando en régimen "phased array". Se ha demostrado que dicho sistema puede dirigir el haz en una amplia gama de ángulos a velocidad ultra alta.

- Hemos propuesto teóricamente y numéricamente un sistema totalmente configurable de guías de onda dieléctricos planas creados en un metamaterial de múltiples capas de grafeno-dieléctrico. Tal sistema demuestra una buena capacidad de dirección y pérdidas de reflexión reducidas.

5.2. Future lines

❖ Given the multiple possible applications of the diffusive light cloak with ideal cloaking performance in transient regime, a fabrication of the proposed cloak and its experimental demonstration is being now analyzed.

❖ Study of carpet cloak based on metasurface with subwavelength grating. In this case, the metasurface with subwavelength grating can create a required phase variation of reflected circular polarization, using a Pancharatnam-Berry phase principle. This phase is based on the anisotropic effective permittivity of the subwavelength grating and depends on the direction of the grating vector.

❖ The graphene is a one-atom thick carbon layer with many interesting features. Despite the numerous published works to date, the graphene still has a huge number of potential novel devices and structures. For example, it could be studied the application of using a graphene or a graphene-dielectric metamaterial as a cloaking metasurface in carpet cloaking. Or the application of the multilayer graphene-dielectric metamaterial in integrated optical devices, such as modulators, couplers etc.

Líneas futuras

- En vista de las múltiples posibilidades de aplicación de la capa de difusión de luz con un rendimiento de camuflaje ideal en el régimen transitorio, ahora se está analizando la fabricación de la capa de invisibilidad propuesta y su demostración experimental.

- Estudio de la capa de invisibilidad basada en una metasuperficie tipo grating de dimensión sublambda. La metasuperficie puede crear una variación de fase requerida de la polarización circular reflejada, utilizando el principio de fase de Pancharatnam-Berry. Esta fase se basa en la permitividad efectiva anisotrópica del grating y depende de la dirección del vector de grating.

- El grafeno es una capa de carbono de espesor de un átomo con muchas características interesantes. A pesar de los numerosos trabajos publicados hasta la fecha, el grafeno ofrece numerosas posibilidades en el diseño de dispositivos y estructuras novedosas. Por ejemplo, se podría estudiar la aplicación de la utilización de un grafeno o un metamaterial de grafeno-dieléctrico como una metasuperficie para el diseño de una capa de invisibilidad. O la aplicación de un metamaterial de múltiples capas de grafeno-dieléctrico en dispositivos ópticos integrados, tales como moduladores, acopladores, etc.

Appendix A

Huygens-Fresnel principle

In his paper, published more than 300 years ago, Huygens proposed a new mechanism for light propagation [232]. He supposed that in analogy with sound, each point of a wavefront acts as a secondary wave source, see Fig. A.1.

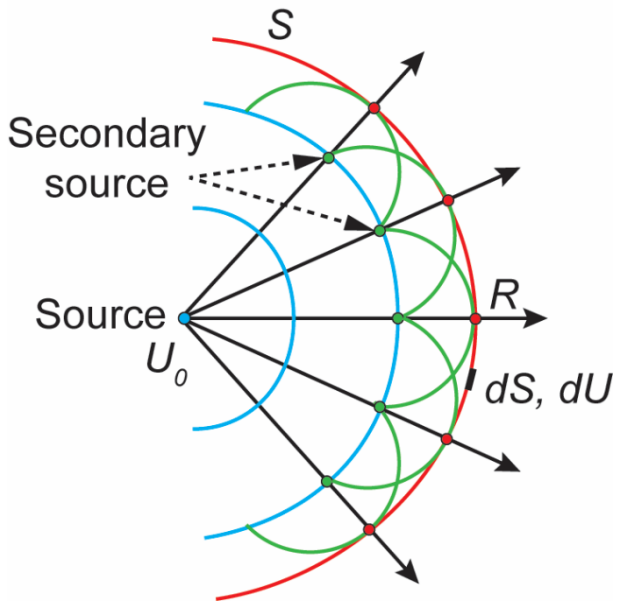

Fig. A.1. Classical illustration of Huygens' principle.

Later Fresnel completed this assumption by adding time periodicity, mutual interference and polarization effects into this principle. The resulting Huygens-Fresnel principle became one of the fundamental methods to solve wave diffraction problems.

If we write a spherical wave as:

$$U = U_0 \exp(\mathrm{j}\omega \mathrm{t}) \frac{\exp(-j\,\mathrm{k}_0 \mathrm{R})}{R}, \tag{A.1}$$

where R is distance from the source to the evaluation point, k_0 is the wavenumber in free space, ω the angular frequency and U_0 the complex amplitude at the source point, the Huygens-Fresnel principle can be written mathematically as [79]:

$$dU = U_0 K \frac{\exp(-j\,\mathrm{k}_0 \mathrm{R})}{R} dS, \tag{A.2}$$

where K is the Kirchhoff diffraction coefficient, S is a closed surface, dU and dS are elementary electric field amplitude and surface area respectively.

In order to find the total field, it is necessary to integrate over the entire surface *S*. In this thesis we simplify this method by discretizing the radiating surface into an array with a finite number of point sources with coordinates (x_i, y_i, z_i). In this case the integral becomes an arithmetic series of all components – point sources. Also we neglect all reflections and absorptions. Furthermore, we assume that all sources have the same amplitude and radiate vertically/horizontally polarized spherical waves .

In case of the zoned fishnet metamaterial lens (Section 3.1), it is assumed to be made from isotropic dispersive material with refractive index *n(f)* corresponding to the effective bulk refractive index $n_z(f)$ of the fishnet metamaterial (Fig. 3.1). Moreover, the discretization is based on the holey nature of the fishnet, i.e. each hole the fishnet is assumed to be a point source. The phase of each source is calculated as a sum of an incident wave phase and a phase shift in the lens. Then the resulting field in each point of space (x, y, z) is calculated by adding the fields of all sources. Mathematically, this can be written as:

$$A(x,y,z) = \sum_{i=1}^{N} \frac{A_i}{\sqrt{l_i(x,y,z)}} e^{j(k_0 l_i(x,y,z) + k_0 n(f) d_i + \varphi_0)} \tag{A.3}$$

$$l_i(x,y,z) = \sqrt{(x-x_i)^2 + (y-y_i)^2 + (z-z_i)^2} \tag{A.4}$$

where A_i is amplitude of point source i; $l_i(x,y)$ is the distance between the point source i and point in the space (x,y,z); k_0 is the wave vector in free space; x_i, y_i, z_i are the position coordinates of the holes; *n(f)* is the effective bulk refractive index of the lens; f is the operation frequency; d_i is the path inside the lens; φ_0 is the phase of incident plane wave.

In the case of the Soret and Wood zone plate fishnet metalens (Sections 2.3, 2.4) we use the same method and apply the same equations. The only difference is that now all holes at the output of the fishnet metamaterial have not only the same amplitude but also the same phase. For the case of the beam steerers based on graphene based (Section 4.2) again we use Huygens-Fresnel method. However, now instead of the holes there are outputs of the waveguides, which have different phases but same amplitudes.

Despite all assumptions done in the model, such analytical tool demonstrates adequately precise results, which agree well with numerical and experimental results. This allows us to estimate the performance of the designed device in fast and efficient way.

Appendix B

Methods and techniques

B.1. Simulation tool

The analytical tool based on Huygens-Fresnel principle has many advantages and is very helpful for estimation of the performance. However, due to its limitations and many simplifications, this tool cannot provide precise and detailed solution for electromagnetic wave propagation. Such problems can be easily solved by numerical solvers, based on the Finite Integration Technique (FIT) [233] and Finite Element Method (FEM). In this work we use both CST Microwave Studio™ (FIT) [184] and COMSOL™ (FEM), which are fully featured software packages for 3D electromagnetic analysis and design in the high frequency range.

CST Microwave Studio™ contains several different simulation techniques (transient solver, frequency domain solver, integral equation solver, multilayer solver, asymptotic solver, and eigenmode solver) to best suit various applications. Each method in turn supports meshing types best suited for each simulation technique. In this thesis we used transient, frequency domain and eigenmode solvers. The numerical method (FIT) provides a universal spatial discretization scheme applicable to various electromagnetic problems ranging from static field calculations to high frequency applications in time or frequency domain. In order to solve Maxwell's equations in integral form numerically, a finite calculation domain must be defined enclosing the application problem to simulate. The structure is subdivided applying a mesh generation algorithm with the purpose to discretize the structures to be simulated by many small elements (grid cells), which means that the mesh system used is very important. CST has three available mesh types: *hexahedral*, *tetrahedral* and *superficial mesh*. Depending on the solver type used, some of the mesh types will be available:

- Transient Solver (Time domain solver) → hexahedral mesh.
- Frequency domain solver → hexahedral and tetrahedral mesh.
- Eigenmode solver→ hexahedral and tetrahedral mesh.

In order to save time and computer resources we used symmetry planes for the design and simulation processes of those structures which had electromagnetic symmetries.

COMSOL Multiphysics™ also contains several add-on modules to best suit various applications in various branches of physics (acoustics, mechanics, chemical processes etc.). In this thesis we used a RF module, exploiting the transient and frequency domain solvers. The numerical method (FEM) subdivides a large problem into smaller, simpler, parts, called finite elements. The simple equations that model these finite elements are then assembled into a larger

system of equations that models the entire problem. FEM then uses variational methods from the calculus of variations to approximate a solution by minimizing an associated error function.

Moreover, both simulation softwares can be driven by a third-party application MATLAB™, through compiled object oriented code. This allows to realize a full control over the model and simulation results (save and export the results to different file formats), and perform different operations, such as parameter sweep, optimization of the structure etc. Here are some examples of the controlling the solvers by means of MATLAB™:

COMSOL™:

```
model = ModelUtil.create('beamsteerer'); %% create model
rf = model.physics('emw');
f=15;l=300/f; %% Parameters
model.param.set('l', [num2str(l) '[um]'], 'Wavelength');
geom1 = model.geom.create('beamsteerer', 2); %% Create geometry
r1 = geom1.feature.create('ground', 'Rectangle');
model.physics.create('emw2','RF','beamsteerer') %% Define Physics
model.sol('sol1').runAll; %% Run
pg = model.result.create('pg', 'PlotGroup2D'); %% Create plots
surf.set('expr', 'sqrt((emw.Poavx)^2+(emw.Poavy)^2+(emw.Poavz)^2)');
mphplot(model,'pg','rangenum',1) %% Plot results
Etot                                                                    =
mphinterp(model,'sqrt((emw.Poavx)^2+(emw.Poavy)^2+(emw.Poavz)^2)','coo
rd',xx); %% Extract data
Etot = reshape(Etot,length(y0),length(x0));
%% Save project
mphsave(model, 'first')
```

CST Microwave Studio™:

```
cst = actxserver('CSTStudio.application') % open COM port
mws = invoke(cst, 'NewMWS') % create new project
% Open the MWS model
invoke(mws,                                                    'OpenFile',
'C:\Users\Baha\Documents\CST\Pruebas\matlab\prueba_matlab.cst');
for iii = 1:1:2 % Parameter sweep
% Set value of parameter
invoke(mws, 'StoreParameter','a', iii);
invoke(mws, 'Rebuild');
% Start solver
solver = invoke(mws, 'FDSolver');
invoke(solver, 'Start');
invoke(mws,'SelectTreeItem', '1D Results\S-Parameters\S11');
res=invoke(mws,'Plot1D');
invoke(res,'PlotView','magnitude');
invoke(res,'Plot');
export=invoke(mws, 'ASCIIExport');
invoke(export,'FileName','C:\Users\Documents\CST\prueba21.txt');
invoke(export,'Execute');
invoke(mws, 'Save');
invoke(mws, 'Quit');
release(mws);
release(cst);
```

B.2. Equipment

For experimental verification of the fabricated prototypes we used a Vector Network Analyzer (VNA) MVNA-8-350-4 (Fig. B.1), which measures the complex, or vector, transmission and reflection parameters in the millimeter and sub-millimeter frequency domain. It covers the frequency range from 40 GHz up to 1 THz [234].

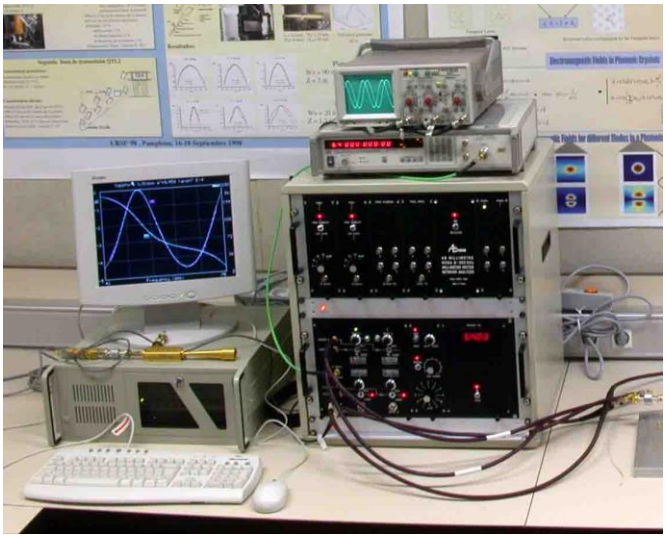

Fig B.1. MVNA-8-350-4.

The VNA allows to obtain both the amplitude and phase of transmitted and reflected signal. In other words, it is possible to obtain the complete response of the tested device, which is located in the signal path of the VNA. As sources for different bands it has different MVNA heads – active multiplier chains composed of frequency multipliers cascaded with an equivalent medium power waveguide amplifiers delivering 40-1000 GHz. Each millimeter head contains a high-efficiency broadband Schottky device, which is electronically tuned over the full frequency range provide the availability of Full Broadband sources for the bands V (50-75 GHz), W (75-110 GHz), D (110-130 GHz), G (140-220 GHz, WR-5.1), WR-3.4 (220-330 GHz), WR-1.2 (660-1000 GHz) . In the MVNA's signal path, the measured millimeter wave signal, which reaches the detector head, is converted by a Schottky diode harmonic mixer to much lower frequency. Then, the converted signal is further processed in the heterodyne vector receiver which uses an internal reference channel. The receiver frequency tuning is achieved with an internal synthesizer.

Also we used an Agilent E3861C VNA (Fig. B.2), which measures the complex, or vector, transmission and reflection parameters in the millimeter and sub-millimeter frequency domain. Analogously to ABmm VNA it has multiple extensions for different bands and covers the frequency range from 0.1 GHz up to 550 GHz [235].

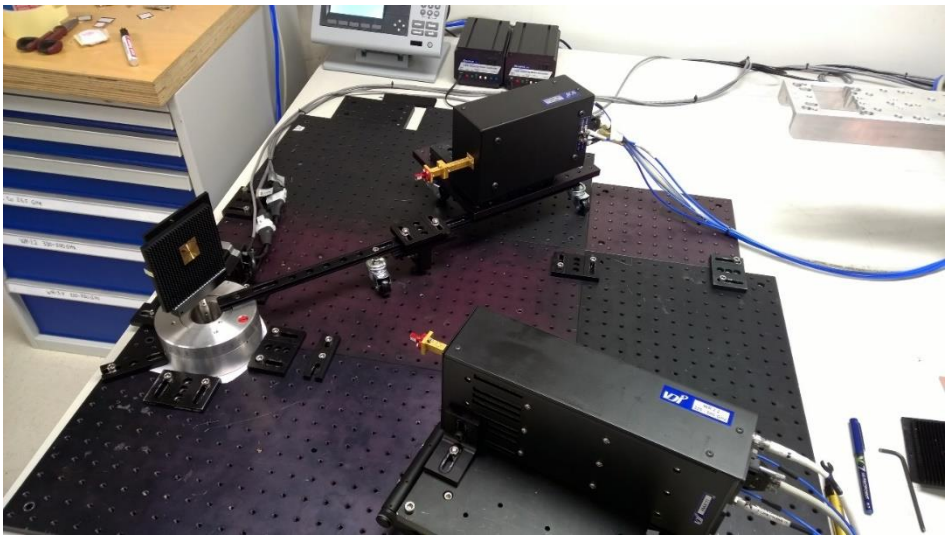

Fig B.2. Experimental setup with millimeter wave extensions of Agilent E3861C VNA for G band (140-220 GHz).

Appendix C

Author's merits

C.1. Journal publications

1. B. Orazbayev, M. Beruete, A. Martínez, and C. García-Meca, "Diffusive-light invisibility cloak for transient illumination," *submitted*, 2016.
2. B. Orazbayev, N. Mohammadi Estakhri, A. Alù, and M. Beruete, "Experimental demonstration of metasurface-based ultrathin carpet cloak for millimetre waves," *Adv. Opt. Mater., in revision*, 2016.
3. B. Orazbayev, M. Beruete, and I. Khromova, "Tunable beam steering enabled by graphene metamaterials," *Opt. Express*, vol. 24, no. 8, pp. 8848–8861, Apr. 2016.
4. B. Orazbayev, M. Beruete, and M. Navarro-Cía, "Wood zone plate fishnet metalens," *EPJ Appl. Metamaterials*, vol. 2, p. 8, 2015.
5. U. Beaskoetxea, V. Pacheco-Pena, B. Orazbayev, T. Akalin, S. Maci, M. Navarro-Cia, and M. Beruete, "77-GHz High-Gain Bull's-Eye Antenna With Sinusoidal Profile," *IEEE Antennas Wirel. Propag. Lett.*, vol. 14, no. 99, pp. 205–208, 2015.
6. B. Orazbayev, N. Mohammadi Estakhri, M. Beruete, and A. Alù, "Terahertz carpet cloak based on a ring resonator metasurface," *Phys. Rev. B*, vol. 91, no. 19, p. 195444, 2015.
7. B. Orazbayev, M. Beruete, V. Pacheco-Peña, G. Crespo, J. Teniente, and M. Navarro-Cía, "Soret Fishnet Metalens Antenna," *Sci. Rep.*, vol. 4, p. 9988, Jan. 2015.
8. B. Orazbayev, V. Pacheco-Peña, M. Beruete, and M. Navarro-Cía, "Exploiting the dispersion of the double-negative-index fishnet metamaterial to create a broadband low-profile metallic lens," *Opt. Express*, vol. 23, no. 7, pp. 8555–8564, Apr. 2015.
9. V. Pacheco-Pena, M. Navarro-Cia, B. Orazbayev, I. V. Minin, O. V. Minin, and M. Beruete, "Zoned Fishnet Lens Antenna With Reference Phase for Side-Lobe Reduction," *IEEE Trans. Antennas Propag.*, vol. 63, no. 8, pp. 3710–3714, Aug. 2015.
10. V. Torres, B. Orazbayev, V. Pacheco-Pena, J. Teniente, M. Beruete, M. Navarro-Cia, M. S. Ayza, and N. Engheta, "Experimental Demonstration of a Millimeter-Wave Metallic ENZ Lens Based on the Energy Squeezing Principle," *IEEE Trans. Antennas Propag.*, vol. 63, no. 1, pp. 231–239, Jan. 2015.
11. V. Pacheco-Peña, V. Torres, B. Orazbayev, M. Beruete, M. Navarro-Cía, M. Sorolla Ayza, and N. Engheta, "Mechanical 144 GHz beam steering with all-metallic epsilon-near-zero lens antenna," *Appl. Phys. Lett.*, vol. 105, no. 24, p. 243503, Dec. 2014.
12. V. Pacheco-Peña, B. Orazbayev, U. Beaskoetxea, M. Beruete, and M. Navarro-Cía, "Zoned near-zero refractive index fishnet lens antenna: Steering millimeter waves," *J. Appl. Phys.*, vol. 115, no. 12, p. 124902, Mar. 2014.
13. V. Pacheco-Peña, B. Orazbayev, V. Torres, M. Beruete, and M. Navarro-Cía, "Ultra-compact planoconcave zoned metallic lens based on the fishnet metamaterial," *Appl. Phys. Lett.*, vol. 103, no. 18, p. 183507, 2013.

upna Universidad Pública de Navarra Nafarroako Unibertsitate Publikoa

C.2. Conference publications

International Conferences

1. B. Orazbayev, N. Mohammadi Estakhri, M. Beruete, A. Alù, "Ultrathin Carpet Cloak Based on Ring Resonators", 10th International Congress on Advanced Electromagnetic Materials in Microwaves and Optics (Metamaterials 2016), (2016)
2. B. Orazbayev, M. Navarro-Cía, M. Beruete, "W-band Hybrid Wood Zone Plate Fishnet Metalens", 10th International Congress on Advanced Electromagnetic Materials in Microwaves and Optics (Metamaterials 2016), (2016)
3. B. Orazbayev, M. Beruete, I. Khromova, "Graphene-Dielectric Metamaterial for Beam Steering", 10th International Congress on Advanced Electromagnetic Materials in Microwaves and Optics (Metamaterials 2016), (2016)
4. B. Orazbayev, M. Navarro-Cía, M. Beruete, "Wood zone plate lens based on fishnet metamaterial", The 7th International Conference on Metamaterials, Photonic Crystals and Plasmonics (META'16), (2016)
5. B. Orazbayev, N. Mohammadi Estakhri, M. Beruete, A. Alù, "Ultrathin metasurface carpet cloak", The 7th International Conference on Metamaterials, Photonic Crystals and Plasmonics (META'16), (2016)
6. V. Pacheco-Peña, M. Navarro-Cía, B. Orazbayev, I.V. Minin, O.V. Minin, M. Beruete, "V-Band Reference-Phase-Based Zoned Fishnet Metalens", IEEE International Symposium on Antennas and Propagation/USNC-URSI National Radio Science meeting (APS/URSI 2016), (2016)
7. A. E. Torres-Garcia, B. Orazbayev, R. Gonzalo, I. Ederra, "Dual-Band Integrated Detector for THz and IR based on Quasi-Spiral Antenna coupled to Schottky Diode", IEEE International Symposium on Antennas and Propagation/USNC-URSI National Radio Science meeting (APS/URSI 2016), (2016)
8. V. Pacheco-Peña, M. Beruete, V. Torres, B. Orazbayev, M. Navarro-Cía, N. Engheta, "Permittivity-Near-Zero (ENZ) Meta-devices at THz Frequencies", EMN meeting on THz Energy Materials Nanotechnology, (2016)
9. B. Orazbayev, N. Mohammadi Estakhri, M. Beruete, A. Alù, "Metasurface-based Ultrathin Carpet Cloak", The 10th European Conference on Antennas and Propagation (EuCAP 2016), (2016)
10. B. Orazbayev, M. Beruete, V. Pacheco-Peña, G. Crespo, J. Teniente, M. Navarro-Cía, "Soret Lens-Antenna based on the Fishnet Metamaterial", The 10th European Conference on Antennas and Propagation (EuCAP 2016), (2016)
11. V. Pacheco-Peña, M. Navarro-Cia, B. Orazbayev, I.V. Minin, O.V. Minin, M. Beruete, "Improving the performance of the zoned fishnet metalens using the reference phase technique", The 10th European Conference on Antennas and Propagation (EuCAP 2016), (2016)

12. B. Orazbayev, V. Pacheco-Peña, M. Beruete, M. Navarro-Cía, "A self-supporting broadband zoned fishnet metamaterial lens operating at the millimeter-wave V-band", 9th International Congress on Advanced Electromagnetic Materials in Microwaves and Optics (Metamaterials 2015), (2015)
13. B. Orazbayev, V. Pacheco-Peña, V. Torres, M. Beruete, M. Navarro-Cía, "Zoning Technique for a Broadband Fishnet Metamaterial Lens", 40th International Conference on Infrared, Millimeter and Terahertz Waves (IRMMW-THz 2015), (2015)
14. V. Torres, B. Orazbayev, V. Pacheco-Peña, J. Teniente, M. Beruete, Miguel Navarro- Cía, Mario Sorolla Ayza, Nader Engheta, "144 GHz Epsilon-Near-Zero Metamaterial Lens", The 9th European Conference on Antennas and Propagation (EuCAP 2015), (2015)
15. B. Orazbayev, V. Pacheco-Peña, V. Torres, M. Beruete, M. Navarro-Cía, "Zoned fishnet metamaterial lens with millimetre wave dual-band response", The 9th European Conference on Antennas and Propagation (EuCAP 2015), (2015)
16. U. Beaskoetxea, V. Pacheco-Peña, B. Orazbayev, T. Akalin, S. Maci, M. Navarro-Cía, M. Beruete, "High Gain Flat 77GHz Sinusoidal Bull's Eye", The 9th European Conference on Antennas and Propagation (EuCAP 2015), (2015)
17. V. Pacheco-Peña, B. Orazbayev, P. Rodríguez-Ulibarri, M. Beruete, M. Navarro-Cía, "Focusing Millimeter Waves Using a Zoned Fishnet Metalens", 14th Mediterranean Microwave Symposium (MMS 2014), (2014)
18. B. Orazbayev, V. Torres, V. Pacheco-Peña, P. Rodríguez-Ulibarri, J. Teniente, M. Beruete, M. Sorolla, M. Navarro-Cía, N. Engheta, "All-Metallic ε-Near-Zero (ENZ) Lens Based On Ultra-Narrow Hollow Rectangular Waveguides: Experimental Results", 14th Mediterranean Microwave Symposium (MMS 2014), (2014)
19. V. Pacheco-Peña, V. Torres, B. Orazbayev, M. Beruete, M. Navarro-Cía, N. Engheta, "Focusing Millimetre Waves by Means of a Permittivity-Near Zero Narrow-Waveguide Lens", 8th International Congress on Advanced Electromagnetic Materials in Microwaves and Optics (Metamaterials 2014), (2014)
20. V. Pacheco-Peña, B. Orazbayev, U. Beaskoetxea, V. Torres, M. Beruete, M. Navarro-Cía, "All-metallic Zoned Fishnet Metamaterial Lens for the Unlicensed Millimetre-wave V-band", 8th International Congress on Advanced Electromagnetic Materials in Microwaves and Optics (Metamaterials 2014), (2014)
21. M. Sorolla, M. Beruete, F. Falcone, V. Torres, V. Pacheco-Peña, B. Orazbayev, P. Rodríguez-Ulibarri, M. Navarro-Cía, "From the Extraordinary Transmission to the Zoned Fishnet Metamaterial Lens", 2014 IEEE International Symposium on Antennas and Propagation and USNC-URSI National Radio Science Meeting (APS/URSI 2014), (2014)
22. V. Pacheco-Peña, B. Orazbayev, V. Torres, M. Beruete, M. Navarro-Cía, "Slimming the Fishnet Metamaterial Lens", 8th European Conference on Antennas and Propagation (EuCAP 2014), (2014)
23. P. Rodríguez-Ulibarri, B. Orazbayev, V. Torres, M. Beruete, M. Navarro-Cía, "Controlling Extraordinary Transmission by Means of Hedgehog Subwavelength Hole Arrays" (Metamaterials 2013), (2013)

National Conferences

1. B. Orazbayev, M. Beruete, I. Khromova, "Graphene-based tunable beam steerer", XXXI Simposium Nacional de la Unión Científica Internacional de Radio, URSI 2016, (2016)
2. A. E. Torres García, I. Ederra, R. Gonzalo, B. Orazbayev, "An Integrated Detector for Submillimeter and Infrared ranges based on a modified Planar Fresnel Zone Lens Antenna", XXXI Simposium Nacional de la Unión Científica Internacional de Radio (URSI 2016), (2016)
3. U. Beaskoetxea, V. Pacheco-Peña, B. Orazbayev, T. Akalin, S. Maci, M. Navarro-Cía, M. Beruete, "Antena Bull's Eye de Ondas de Fuga de Perfil Senoidal para Aplicaciones Radar", XXX Simposium Nacional de la Unión Científica Internacional de Radio (URSI 2015), (2016)
4. M. Navarro-Cía, M. Beruete, V. Torres, V. Pacheco-Peña, B. Orazbayev, M. A. Astafev, S. A. Kuznetsov, "Dispositivos de ondas milimétricas y terahercio basados en medios y superficies artificiales", XXX Simposium Nacional de la Unión Científica Internacional de Radio (URSI 2015), (2015)
5. B. Orazbayev, M. Beruete, V. Pacheco-Peña, G. Crespo, J. Teniente, M. Navarro-Cía, "Lente de Soret Basada en el Metamaterial Fishnet", XXX Simposium Nacional de la Unión Científica Internacional de Radio (URSI 2015), (2015)
6. V. Pacheco-Peña, M. Navarro-Cía, B. Orazbayev, I.V. Minin, O.V. Minin, M. Beruete, "Lentes Zonadas con Referencia de Fase Basadas en el Metamaterial Tipo Fishnet", XXX Simposium Nacional de la Unión Científica Internacional de Radio (URSI 2015), (2015)
7. V. Pacheco-Peña, V. Torres, B. Orazbayev, M. Beruete, M. Navarro-Cía, N. Engheta, "Plano-concave lens based on ultra-narrow hollow rectangular waveguides mimicking an effective ENZ medium", XXIX Simposium Nacional de la Unión Científica Internacional de Radio (URSI 2015), (2014)
8. B. Orazbayev, V. Pacheco-Peña, V. Torres, M. Beruete, M. Navarro-Cía, "Zoning technique application for the fishnet metamaterial lens", XXIX Simposium Nacional de la Unión Científica Internacional de Radio (URSI 2015), (2014)
9. V. Torres, B. Orazbayev, P. Rodríguez-Ulibarri, M. Beruete, M. Navarro-Cía, "Control de la Transmisión Extraordinaria mediante pines metálicos ortogonales al Plano de los Agujeros Sublambda", XXVIII Simposium Nacional de la Unión Científica Internacional de Radio, URSI 2013 (URSI 2015), (2013)

References

1. J. B. Pendry, "Negative Refraction Makes a Perfect Lens," Phys. Rev. Lett. **85**, 3966–3969 (2000).

2. V. V. Shevchenko, "The geometric-optics theory of a plane chiral-metamaterial lens," J. Commun. Technol. Electron. **54**, 662–666 (2009).

3. N. Fang, "Sub-Diffraction-Limited Optical Imaging with a Silver Superlens," Science **308**, 534–537 (2005).

4. D. Lu and Z. Liu, "Hyperlenses and metalenses for far-field super-resolution imaging.," Nat. Commun. **3**, 1205 (2012).

5. D. Schurig, J. J. Mock, B. J. Justice, S. A. Cummer, J. B. Pendry, A. F. Starr, and D. R. Smith, "Metamaterial Electromagnetic Cloak at Microwave Frequencies," Science **314**, 977–980 (2006).

6. V. Pacheco-Peña, V. Torres, B. Orazbayev, M. Beruete, M. Navarro-Cía, M. Sorolla Ayza, and N. Engheta, "Mechanical 144 GHz beam steering with all-metallic epsilon-near-zero lens antenna," Appl. Phys. Lett. **105**, 243503 (2014).

7. N. Yu and F. Capasso, "Flat optics with designer metasurfaces," Nat. Mater. **13**, 139–150 (2014).

8. P. Genevet, F. Aieta, M. a. Kats, R. Blanchard, G. Aoust, J.-P. Tetienne, Z. Gaburro, and F. Capasso, "Flat Optics: Controlling Wavefronts With Optical Antenna Metasurfaces," IEEE J. Sel. Top. Quantum Electron. **19**, 4700423–4700423 (2013).

9. P. R. West, J. L. Stewart, A. V Kildishev, V. M. Shalaev, V. V Shkunov, F. Strohkendl, Y. a Zakharenkov, K. Robert, and R. Byren, "All-dielectric subwavelength metasurface focusing lens," Opt. Express **22**, 1593–1595 (2014).

10. C. Argyropoulos, F. Monticone, N. Mohammadi Estakhri, and A. Alù, "Tunable Plasmonic and Hyperbolic Metamaterials Based on Enhanced Nonlinear Response," Int. J. Antennas Propag. **2014**, 1–11 (2014).

11. R. Marqués, F. Martín, and M. Sorolla, *Metamaterials with Negative Parameters : Theory, Design, and Microwave Applications* (John Wiley & Sons, 2008).

12. L. Solymar and E. Shamonina, *Waves in Metamaterials* (Oxford University Press, 2009).

13. J. Brown, "Artificial dielectrics having refractive indices less than unity," Proc. Inst. Electr. Eng. London **100**, 51–62 (1953).

14. W. Rotman, "Plasma simulation by artificial dielectrics and parallel-plate media," IRE Trans. Antennas Propag. **10**, 17–19 (1962).

15. J. C. Bose, "On the Rotation of Plane of Polarisation of Electric Waves by a Twisted Structure," Proc. R. Soc. London **63**, 146–152 (1898).

16. W. E. Kock, "Metal-Lens Antennas," Proc. IRE **34**, 828–836 (1946).

17. J. D. Jackson, *Classical Electrodynamics* (Wiley, 1998).

18. A. Alù, N. Engheta, A. Erentok, and R. W. Ziolkowski, "Single-negative, double-negative, and low-index metamaterials and their electromagnetic applications," IEEE Antennas Propag. Mag. **49**, 23–36 (2007).

19. A. Sihvola, S. Tretyakov, and A. Baas, "Metamaterials with extreme material parameters," J. Commun. Technol. Electron. **52**, 986–990 (2007).

20. V. G. Veselago, "The electrodynamics of substances with simultaneously negative values of ε and μ," Sov. Phys. Uspekhi **10**, 509–514 (1968).

21. J. B. Pendry, a. J. Holden, D. J. Robbins, and W. J. Stewart, "Magnetism from conductors and enhanced nonlinear phenomena," IEEE Trans. Microw. Theory Tech. **47**, 2075–2084 (1999).

22. D. R. Smith and N. Kroll, "Negative Refractive Index in Left-Handed Materials," Phys. Rev. Lett. **85**, 2933–2936 (2000).

23. D. R. Smith, W. J. Padilla, D. C. Vier, S. C. Nemat-Nasser, and S. Schultz, "Composite Medium with Simultaneously Negative Permeability and Permittivity," Phys. Rev. Lett. **84**, 4184–4187 (2000).

24. R. A. Shelby, "Experimental Verification of a Negative Index of Refraction," Science **292**, 77–79 (2001).

25. S. Zhang, W. Fan, N. C. Panoiu, K. J. Malloy, R. M. Osgood, and S. R. J. Brueck, "Experimental Demonstration of Near-Infrared Negative-Index Metamaterials," Phys. Rev. Lett. **95**, 137404 (2005).

26. M. Beruete, M. Sorolla, and I. Campillo, "Left-handed extraordinary optical transmission through a photonic crystal of subwavelength hole arrays," Opt. Express **14**, 5445–5455 (2006).

27. A. Alù, M. M. Silveirinha, A. Salandrino, and N. Engheta, "Epsilon-near-zero metamaterials and electromagnetic sources: Tailoring the radiation phase pattern," Phys. Rev. B **75**, 155410 (2007).

28. N. Engheta and R. W. Ziolkowski, *Metamaterials: Physics and Engineering Explorations* (John Wiley & Sons, Inc., 2006).

29. M. Navarro-Cía, M. Beruete, M. Sorolla Ayza, N. Engheta, and M. Sorolla, "Lensing system and Fourier transformation using epsilon-near-zero metamaterials," Phys. Rev. B **86**, 165130 (2012).

30. V. Torres, B. Orazbayev, V. Pacheco-Pena, J. Teniente, M. Beruete, M. Navarro-Cia, M. S. Ayza, and N. Engheta, "Experimental Demonstration of a Millimeter-Wave Metallic ENZ Lens Based on the Energy Squeezing Principle," IEEE Trans. Antennas Propag. **63**, 231–239 (2015).

31. M. Beruete, M. Sorolla, M. Navarro-Cía, F. Falcone, I. Campillo, and V. Lomakin, "Extraordinary transmission and left-handed propagation in miniaturized stacks of doubly periodic subwavelength hole arrays," Opt. Express **15**, 1107–1114 (2007).

32. T. W. Ebbesen, H. J. Lezec, H. F. Ghaemi, T. Thio, and P. A. Wolff, "Extraordinary optical transmission through sub-wavelength hole arrays," Nature **391**, 667–669 (1998).

33. R. W. Wood, "On a Remarkable Case of Uneven Distribution of Light in a Diffraction Grating Spectrum," Proc. Phys. Soc. London **18**, 269–275 (1902).

34. L. Rayleigh, "On the Dynamical Theory of Gratings," Proc. R. Soc. A Math. Phys. Eng. Sci. **79**, 399–416 (1907).

35. S. S. Akarca-Biyikli, I. Bulu, and E. Ozbay, "Enhanced transmission of microwave radiation in one-dimensional metallic gratings with subwavelength aperture," Appl. Phys. Lett. **85**, 1098–1100 (2004).

36. M. Beruete, M. Sorolla Ayza, I. Campillo, J. S. Dolado, L. Martín-Moreno, J. Bravo-Abad, and F. J. García-Vidal, "Enhanced millimeter-wave transmission through subwavelength hole arrays," Opt. Lett. **29**, 2500–2502 (2004).

37. Beruete, Campillo, Dolado, Rodriguez-Seco, Perea, and Sorolla, "Enhanced microwave transmission and beaming using a subwavelength slot in corrugated plate," IEEE Antennas Wirel. Propag. Lett. **3**, 328–331 (2004).

38. M. Beruete, M. Sorolla, I. Campillo, and J. S. Dolado, "Increase of the transmission in cut-off metallic hole arrays," IEEE Microw. Wirel. Components Lett. **15**, 116–118 (2005).

39. M. Beruete, M. Sorolla, I. Campillo, and J. S. Dolado, "Subwavelength slotted corrugated plate with enhanced quasioptical millimeter wave transmission," IEEE Microw. Wirel. Components Lett. **15**, 286–288 (2005).

40. T. J. Kim, T. Thio, T. W. Ebbesen, D. E. Grupp, and H. J. Lezec, "Control of optical transmission through metals perforated with subwavelength hole arrays," Opt. Lett. **24**, 256–258 (1999).

41. D. E. Grupp, H. J. Lezec, T. W. Ebbesen, K. M. Pellerin, and T. Thio, "Crucial role of metal surface in enhanced transmission through subwavelength apertures," Appl. Phys. Lett. **77**, 1569–1571 (2000).

42. V. Lomakin and E. Michielssen, "Enhanced transmission through metallic plates perforated by arrays of subwavelength holes and sandwiched between dielectric slabs," Phys. Rev. B **71**, 235117 (2005).

43. E. Popov, M. Nevière, S. Enoch, and R. Reinisch, "Theory of light transmission through subwavelength periodic hole arrays," Phys. Rev. B **62**, 16100–16108 (2000).

44. J. B. Pendry, "Mimicking Surface Plasmons with Structured Surfaces," Science **305**, 847–848 (2004).

45. M. Sarrazin and J.-P. Vigneron, "Optical properties of tungsten thin films perforated with a bidimensional array of subwavelength holes," Phys. Rev. E **68**, 16603 (2003).

46. H. F. Ghaemi, T. Thio, D. Grupp, T. W. Ebbesen, and H. J. Lezec, "Surface plasmons enhance optical transmission through subwavelength holes," Phys. Rev. B **58**, 6779–6782 (1998).

47. F. Medina, F. Mesa, and R. Marques, "Extraordinary Transmission Through Arrays of Electrically Small Holes From a Circuit Theory Perspective," IEEE Trans. Microw. Theory Tech. **56**, 3108–3120 (2008).

48. M. Beruete, I. Campillo, M. Navarro-Cía, F. Falcone, and M. Sorolla Ayza, "Molding left- or right-handed metamaterials by stacked cutoff metallic hole arrays," IEEE Trans. Antennas Propag. **55**, 1514–1521 (2007).

49. H. Liu and P. Lalanne, "Microscopic theory of the extraordinary optical transmission," Nature **452**, 728–731 (2008).

50. C. García-Meca, R. Ortuño, F. J. Rodríguez-Fortuño, J. Martí, and A. Martínez, "Double-negative polarization-independent fishnet metamaterial in the visible spectrum," Opt. Lett. **34**, 1603–1605 (2009).

51. C. García-Meca, J. Hurtado, J. Martí, A. Martínez, W. Dickson, and A. V. Zayats, "Low-Loss Multilayered Metamaterial Exhibiting a Negative Index of Refraction at Visible Wavelengths," Phys. Rev. Lett. **106**, 67402 (2011).

52. M. Beruete, M. Navarro-Cía, M. Sorolla Ayza, and I. Campillo, "Planoconcave lens by negative refraction of stacked subwavelength hole arrays," Opt. Express **16**, 9677–9683

(2008).

53. M. Navarro-Cía, M. Beruete, I. Campillo, and M. Sorolla, "Enhanced lens by ε and μ near-zero metamaterial boosted by extraordinary optical transmission," Phys. Rev. B **83**, 115112 (2011).

54. V. Pacheco-Peña, B. Orazbayev, V. Torres, M. Beruete, and M. Navarro-Cía, "Ultra-compact planoconcave zoned metallic lens based on the fishnet metamaterial," Appl. Phys. Lett. **103**, 183507 (2013).

55. D. R. Smith, S. Schultz, P. Markoš, and C. M. Soukoulis, "Determination of effective permittivity and permeability of metamaterials from reflection and transmission coefficients," Phys. Rev. B **65**, 195104 (2002).

56. X. Chen, T. Grzegorczyk, B.-I. Wu, J. Pacheco, and J. Kong, "Robust method to retrieve the constitutive effective parameters of metamaterials," Phys. Rev. E **70**, 16608 (2004).

57. D. R. Smith, D. C. Vier, T. Koschny, and C. M. Soukoulis, "Electromagnetic parameter retrieval from inhomogeneous metamaterials," Phys. Rev. E **71**, 36617 (2005).

58. C. R. Simovski, "On electromagnetic characterization and homogenization of nanostructured metamaterials," J. Opt. **13**, 13001 (2010).

59. C. S. R. Kaipa, A. B. Yakovlev, F. Medina, F. Mesa, C. A. M. Butler, and A. P. Hibbins, "Circuit modeling of the transmissivity of stacked two-dimensional metallic meshes.," Opt. Express **18**, 13309–13320 (2010).

60. R. Marqués, F. Mesa, L. Jelinek, and F. Medina, "Analytical theory of extraordinary transmission through metallic diffraction screens perforated by small holes.," Opt. Express **17**, 5571–5579 (2009).

61. J. Carbonell, C. Croënne, F. Garet, E. Lheurette, J. L. Coutaz, and D. Lippens, "Lumped elements circuit of terahertz fishnet-like arrays with composite dispersion," J. Appl. Phys. **108**, 14907 (2010).

62. M. Kafesaki, I. Tsiapa, N. Katsarakis, T. Koschny, C. M. Soukoulis, and E. N. Economou, "Left-handed metamaterials: The fishnet structure and its variations," Phys. Rev. B **75**, 235114 (2007).

63. M. Beruete, P. Rodriguez-Ulibarri, V. Pacheco-Peña, M. Navarro-Cía, and A. E. Serebryannikov, "Frozen mode from hybridized extraordinary transmission and Fabry-Perot resonances," Phys. Rev. B **87**, 205128 (2013).

64. M. Navarro-Cia, V. Torres Landivar, M. Beruete, and M. Sorolla Ayza, "A slow light fishnet-like absorber in the millimeter-wave range," Prog. Electromagn. Res. **118**, 287–301 (2011).

65. J. B. Pendry, "Controlling Electromagnetic Fields," Science **312**, 1780–1782 (2006).

66. U. Leonhardt, "Optical Conformal Mapping," Science **312**, 1777–1780 (2006).

67. H. Chen, C. T. Chan, and P. Sheng, "Transformation optics and metamaterials," Nat. Mater. **9**, 387–396 (2010).

68. C. García-Meca, M. M. Tung, J. V Galán, R. Ortuño, F. J. Rodríguez-Fortuño, J. Martí, and A. Martínez, "Squeezing and expanding light without reflections via transformation optics," Opt. Express **19**, 3562–3575 (2011).

69. J. Valentine, J. Li, T. Zentgraf, G. Bartal, and X. Zhang, "An optical cloak made of dielectrics," Nat. Mater. **8**, 568–571 (2009).

70. Y. Zhao and A. Alù, "Tailoring the dispersion of plasmonic nanorods to realize broadband optical meta-waveplates," Nano Lett. **13**, 1086–1091 (2013).

71. N. Yu, F. Aieta, P. Genevet, M. A. Kats, Z. Gaburro, and F. Capasso, "A broadband, background-free quarter-wave plate based on plasmonic metasurfaces," Nano Lett. **12**, 6328–6333 (2012).

72. N. Yu, P. Genevet, M. A. Kats, F. Aieta, J.-P. Tetienne, F. Capasso, and Z. Gaburro, "Light Propagation with Phase Discontinuities: Generalized Laws of Reflection and Refraction," Science **334**, 333–337 (2011).

73. Y. Ra'di, V. S. Asadchy, and S. A. Tretyakov, "Tailoring Reflections From Thin Composite Metamirrors," IEEE Trans. Antennas Propag. **62**, 3749–3760 (2014).

74. F. Monticone, N. Mohammadi Estakhri, and A. Alù, "Full Control of Nanoscale Optical Transmission with a Composite Metascreen," Phys. Rev. Lett. **110**, 203903 (2013).

75. V. S. Asadchy, Y. Ra'di, J. Vehmas, and S. A. Tretyakov, "Functional Metamirrors Using Bianisotropic Elements," Phys. Rev. Lett. **114**, 95503 (2015).

76. C. Pfeiffer and A. Grbic, "Metamaterial Huygens' Surfaces: Tailoring Wave Fronts with Reflectionless Sheets," Phys. Rev. Lett. **110**, 197401 (2013).

77. C. Pfeiffer, N. K. Emani, A. M. Shaltout, A. Boltasseva, V. M. Shalaev, and A. Grbic, "Efficient Light Bending with Isotropic Metamaterial Huygens' Surfaces," Nano Lett. **14**, 2491–2497 (2014).

78. J. Huang and J. A. Encinar, *Reflectarray Antennas* (John Wiley & Sons, Inc., 2007).

79. I. V Minin and O. Minin, *Diffractional Optics of Millimetre Waves* (CRC, 2004).

80. D. R. Smith, J. Mock, A. F. Starr, and D. Schurig, "Gradient index metamaterials," Phys. Rev. E **71**, 36609 (2005).

81. A. Greenleaf, Y. Kurylev, M. Lassas, and G. Uhlmann, "Electromagnetic Wormholes and Virtual Magnetic Monopoles from Metamaterials," Phys. Rev. Lett. **99**, 183901 (2007).

82. X. Luo, T. Yang, Y. Gu, H. Chen, and H. Ma, "Conceal an entrance by means of superscatterer," Appl. Phys. Lett. **94**, 223513 (2009).

83. H. Chen, C. T. Chan, S. Liu, and Z. Lin, "A simple route to a tunable electromagnetic gateway," New J. Phys. **11**, 83012 (2009).

84. U. Leonhardt and P. Piwnicki, "Optics of Nonuniformly Moving Media," Phys. Rev. A **60**, 4301–4312 (1999).

85. D. A. Genov, S. Zhang, and X. Zhang, "Mimicking celestial mechanics in metamaterials," Nat. Phys. **5**, 687–692 (2009).

86. E. E. Narimanov and A. V. Kildishev, "Optical black hole: Broadband omnidirectional light absorber," Appl. Phys. Lett. **95**, 1–4 (2009).

87. W. Lu, J. Jin, Z. Lin, and H. Chen, "A simple design of an artificial electromagnetic black hole," J. Appl. Phys. **108**, 64517 (2010).

88. M. Tsang and D. Psaltis, "Magnifying perfect lens and superlens design by coordinate transformation," Phys. Rev. B **77**, 35122 (2008).

89. M. Yan, W. Yan, and M. Qiu, "Cylindrical superlens by a coordinate transformation," Phys. Rev. B **78**, 125113 (2008).

90. W. X. Jiang, T. J. Cui, H. F. Ma, X. M. Yang, and Q. Cheng, "Layered high-gain lens

antennas via discrete optical transformation," Appl. Phys. Lett. **93**, 221906 (2008).

91. D.-H. Kwon and D. H. Werner, "Flat focusing lens designs having minimized reflection based on coordinate transformation techniques.," Opt. Express **17**, 7807–7817 (2009).

92. D. a Roberts, N. Kundtz, and D. R. Smith, "Optical lens compression via transformation optics.," Opt. Express **17**, 16535–16542 (2009).

93. J. Li, S. Han, S. Zhang, G. Bartal, and X. Zhang, "Designing the Fourier space with transformation optics.," Opt. Lett. **34**, 3128–3130 (2009).

94. M. Rahm, D. Schurig, D. A. Roberts, S. A. Cummer, D. R. Smith, and J. B. Pendry, "Design of electromagnetic cloaks and concentrators using form-invariant coordinate transformations of Maxwell's equations," Photonics Nanostructures - Fundam. Appl. **6**, 87–95 (2008).

95. H. Chen and C. T. Chan, "Transformation media that rotate electromagnetic fields," Appl. Phys. Lett. **90**, 241105 (2007).

96. H. Chen, B. Hou, S. Chen, X. Ao, W. Wen, and C. T. Chan, "Design and Experimental Realization of a Broadband Transformation Media Field Rotator at Microwave Frequencies," Phys. Rev. Lett. **102**, 183903 (2009).

97. H. Chen and C. T. Chan, "Electromagnetic wave manipulation by layered systems using the transformation media concept," Phys. Rev. B **78**, 54204 (2008).

98. J. Huangfu, S. Xi, F. Kong, J. Zhang, H. Chen, D. Wang, B.-I. Wu, L. Ran, and J. A. Kong, "Application of coordinate transformation in bent waveguides," J. Appl. Phys. **104**, 14502 (2008).

99. D. A. Roberts, M. Rahm, J. B. Pendry, and D. R. Smith, "Transformation-optical design of sharp waveguide bends and corners," Appl. Phys. Lett. **93**, 2006–2009 (2008).

100. Z. L. Mei and T. J. Cui, "Arbitrary bending of electromagnetic waves using isotropic materials," J. Appl. Phys. **105**, 104913 (2009).

101. D.-H. Kwon and D. H. Werner, "Polarization splitter and polarization rotator designs based on transformation optics.," Opt. Express **16**, 18731–18738 (2008).

102. W. X. Jiang, T. J. Cui, H. F. Ma, X. Y. Zhou, and Q. Cheng, "Cylindrical-to-plane-wave conversion via embedded optical transformation," Appl. Phys. Lett. **92**, 261903 (2008).

103. J. Li and J. B. Pendry, "Hiding under the Carpet: A New Strategy for Cloaking," Phys. Rev. Lett. **101**, 203901 (2008).

104. X. Xu, Y. Feng, S. Xiong, J. Fan, J.-M. Zhao, and T. Jiang, "Broad band invisibility cloak made of normal dielectric multilayer," Appl. Phys. Lett. **99**, 154104 (2011).

105. M. Gharghi, C. Gladden, T. Zentgraf, Y. Liu, X. Yin, J. Valentine, and X. Zhang, "A Carpet Cloak for Visible Light," Nano Lett. **11**, 2825–2828 (2011).

106. A. Alù and N. Engheta, "Achieving transparency with plasmonic and metamaterial coatings," Phys. Rev. E **72**, 16623 (2005).

107. A. Alù and N. Engheta, "Multifrequency Optical Invisibility Cloak with Layered Plasmonic Shells," Phys. Rev. Lett. **100**, 113901 (2008).

108. D. Rainwater, A. Kerkhoff, K. Melin, J. C. Soric, G. Moreno, and A. Alù, "Experimental verification of three-dimensional plasmonic cloaking in free-space," New J. Phys. **14**, 13054 (2012).

109. P.-Y. Chen and A. Alù, "Mantle cloaking using thin patterned metasurfaces," Phys. Rev.

B **84**, 205110 (2011).

110. F. Monticone and A. Alù, "Do cloaked objects really scatter less?," Phys. Rev. X **3**, 41005 (2013).

111. J. Zhang, Z. Lei Mei, W. Ru Zhang, F. Yang, and T. Jun Cui, "An ultrathin directional carpet cloak based on generalized Snell's law," Appl. Phys. Lett. **103**, 151115 (2013).

112. N. Mohammadi Estakhri and A. Alù, "Ultra-Thin Unidirectional Carpet Cloak and Wavefront Reconstruction With Graded Metasurfaces," IEEE Antennas Wirel. Propag. Lett. **13**, 1775–1778 (2014).

113. X. Ni, Z. J. Wong, M. Mrejen, Y. Wang, and X. Zhang, "An ultrathin invisibility skin cloak for visible light," Science **349**, 1310–1314 (2015).

114. M. A. K. Othman, C. Guclu, and F. Capolino, "Graphene-based tunable hyperbolic metamaterials and enhanced near-field absorption," Opt. Express **21**, 7614–7632 (2013).

115. I. Khromova, A. Andryieuski, and A. Lavrinenko, "Ultrasensitive terahertz/infrared waveguide modulators based on multilayer graphene metamaterials," Laser Photon. Rev. **8**, 916–923 (2014).

116. D. A. Boyd, W.-H. Lin, C.-C. Hsu, M. L. Teague, C.-C. Chen, Y.-Y. Lo, W.-Y. Chan, W.-B. Su, T.-C. Cheng, C.-S. Chang, C.-I. Wu, and N.-C. Yeh, "Single-step deposition of high-mobility graphene at reduced temperatures," Nat. Commun. **6**, 6620 (2015).

117. L. Banszerus, M. Schmitz, S. Engels, J. Dauber, M. Oellers, F. Haupt, K. Watanabe, T. Taniguchi, B. Beschoten, and C. Stampfer, "Ultrahigh-mobility graphene devices from chemical vapor deposition on reusable copper," Sci. Adv. **1**, 1–6 (2015).

118. M. Esquius-Morote, J. S. Gomez-Diaz, and J. Perruisseau-Carrier, "Sinusoidally modulated graphene leaky-wave antenna for electronic beamscanning at THz," IEEE Trans. Terahertz Sci. Technol. **4**, 116–122 (2014).

119. G. Wang, X. Liu, H. Lu, and C. Zeng, "Graphene plasmonic lens for manipulating energy flow," Sci. Rep. **4**, 1–7 (2014).

120. C.-H. Liu, Y.-C. Chang, T. B. Norris, and Z. Zhong, "Graphene photodetectors with ultra-broadband and high responsivity at room temperature," Nat. Nanotechnol. **9**, 273–278 (2014).

121. B. Sensale-Rodriguez, "Graphene-Based Optoelectronics," Light. Technol. J. **33**, 1100–1108 (2015).

122. F. Bonaccorso, Z. Sun, T. Hasan, and a. C. Ferrari, "Graphene Photonics and Optoelectronics," Nat. Photonics **4**, 611–622 (2010).

123. P.-Y. Chen and A. Alù, "Atomically thin surface cloak using graphene monolayers," ACS Nano **5**, 5855–5863 (2011).

124. K. S. N. A. N. Grigorenko , M. Polini, "Graphene plasmonics," Nat. Photonics **6**, 749 – 758 (2012).

125. M. Jablan, H. Buljan, and M. Soljačić, "Plasmonics in graphene at infrared frequencies," Phys. Rev. B **80**, 245435 (2009).

126. Z. Fei, G. O. Andreev, W. Bao, L. M. Zhang, A. S. McLeod, C. Wang, M. K. Stewart, Z. Zhao, G. Dominguez, M. Thiemens, M. M. Fogler, M. J. Tauber, A. H. Castro-Neto, C. N. Lau, F. Keilmann, and D. N. Basov, "Infrared nanoscopy of dirac plasmons at the graphene-SiO2 interface," Nano Lett. **11**, 4701–4705 (2011).

127. J. Chen, M. Badioli, P. Alonso-González, S. Thongrattanasiri, F. Huth, J. Osmond, M. Spasenović, A. Centeno, A. Pesquera, P. Godignon, A. Zurutuza Elorza, N. Camara, F. J. G. de Abajo, R. Hillenbrand, and F. H. L. Koppens, "Optical nano-imaging of gate-tunable graphene plasmons," Nature **487**, 77–81 (2012).

128. A. Vakil and N. Engheta, "Transformation Optics Using Graphene," Science **332**, 1291–1294 (2011).

129. A. Alù and N. Engheta, "Optical nanotransmission lines: synthesis of planar left-handed metamaterials in the infrared and visible regimes," J. Opt. Soc. Am. B **23**, 571 (2006).

130. I. V. Iorsh, I. S. Mukhin, I. V. Shadrivov, P. A. Belov, and Y. S. Kivshar, "Hyperbolic metamaterials based on multilayer graphene structures," Phys. Rev. B **87**, 75416 (2013).

131. B. Zhu, G. Ren, S. Zheng, Z. Lin, and S. Jian, "Nanoscale dielectric-graphene-dielectric tunable infrared waveguide with ultrahigh refractive indices," Opt. Express **21**, 17089–17096 (2013).

132. R. Z. Zhang and Z. M. Zhang, "Tunable positive and negative refraction of infrared radiation in graphene-dielectric multilayers," Appl. Phys. Lett. **107**, 191112 (2015).

133. Y. Chang, C. Liu, C. Liu, S. Zhang, and S. R. Marder, "Realization of mid-infrared graphene hyperbolic metamaterials," Nat. Commun. **7**, 1–12 (2016).

134. B. Wunsch, T. Stauber, F. Sols, and F. Guinea, "Dynamical polarization of graphene at finite doping," New J. Phys. **8**, 318 (2006).

135. K. Ziegler, "Minimal conductivity of graphene: Nonuniversal values from the Kubo formula," Phys. Rev. B **75**, 233407 (2007).

136. M. A. K. Othman, C. Guclu, and F. Capolino, "Graphene–dielectric composite metamaterials: evolution from elliptic to hyperbolic wavevector dispersion and the transverse epsilon-near-zero condition," J. Nanophotonics **7**, 73089 (2013).

137. C. Argyropoulos, N. M. Estakhri, F. Monticone, and A. Alù, "Negative refraction, gain and nonlinear effects in hyperbolic metamaterials," Opt. Express **21**, 15037 (2013).

138. A. Andryieuski, A. V. Lavrinenko, and D. N. Chigrin, "Graphene hyperlens for terahertz radiation," Phys. Rev. B **86**, 121108 (2012).

139. S. A. Ramakrishna, J. B. Pendry, M. C. K. Wiltshire, and W. J. Stewart, "Imaging the near field," J. Mod. Opt. **50**, 1419–1430 (2003).

140. C. L. Cortes, W. Newman, S. Molesky, and Z. Jacob, "Quantum nanophotonics using hyperbolic metamaterials," J. Opt. **14**, 63001 (2012).

141. R. S. Penciu, M. Kafesaki, T. Koschny, E. N. Economou, and C. M. Soukoulis, "Magnetic response of nanoscale left-handed metamaterials," Phys. Rev. B **81**, 235111 (2010).

142. M. Navarro-Cía, M. Beruete, M. Sorolla Ayza, I. Campillo, and M. Sorolla, "Converging biconcave metallic lens by double-negative extraordinary transmission metamaterial," Appl. Phys. Lett. **94**, 144107 (2009).

143. M. Navarro-Cía, M. Beruete, I. Campillo, M. Sorolla, and M. Sorolla Ayza, "Fresh metamaterials ideas for metallic lenses," Metamaterials **4**, 119–126 (2010).

144. P. F. Goldsmith, "Zone plate lens antennas for millimeter and submillimeter wavelengths," in *The Third International Symposium on Space Terahertz Technology: Symposium Proceedings* (1992), pp. 345–361.

145. H. D. Hristov, *Fresnel Zones in Wireless Links, Zone Plate Lenses, and Antennas* (Artech

House, 2000).

146. V. Pacheco-Peña, B. Orazbayev, U. Beaskoetxea, M. Beruete, and M. Navarro-Cía, "Zoned near-zero refractive index fishnet lens antenna: Steering millimeter waves," J. Appl. Phys. **115**, 124902 (2014).

147. M. Navarro-Cía, M. Beruete, I. Campillo, and M. Sorolla Ayza, "Beamforming by Left-Handed Extraordinary Transmission Metamaterial Bi- and Plano-Concave Lens at Millimeter-Waves," IEEE Trans. Antennas Propag. **59**, 2141–2151 (2011).

148. D. F. Filipovic and G. M. Rebeiz, "Double-slot antennas on extended hemispherical and elliptical quartz dielectric lenses," Int. J. Infrared Millimeter Waves **14**, 1905–1924 (1993).

149. N. Llombart, G. Chattopadhyay, A. Skalare, and I. Mehdi, "Novel Terahertz Antenna Based on a Silicon Lens Fed by a Leaky Wave Enhanced Waveguide," IEEE Trans. Antennas Propag. **59**, 2160–2168 (2011).

150. D. L. Runyon, "Optimum directivity coverage of fan-beam antennas," IEEE Antennas Propag. Mag. **44**, 66–70 (2002).

151. J. L. Soret, "Ueber die durch Kreisgitter erzeugten Diffractionsphänomene," Ann. der Phys. und Chemie **232**, 99–113 (1875).

152. H. Hristov and M. Herben, "Millimeter-wave Fresnel-zone plate lens and antenna," IEEE Trans. Microw. Theory Tech. **43**, 2779–2785 (1995).

153. T. Matsui, A. Agrawal, A. Nahata, and Z. V. Vardeny, "Transmission resonances through aperiodic arrays of subwavelength apertures.," Nature **446**, 517–21 (2007).

154. S. Enoch, G. Tayeb, P. Sabouroux, N. Guérin, and P. Vincent, "A Metamaterial for Directive Emission," Phys. Rev. Lett. **89**, 213902 (2002).

155. R. Ziolkowski, "Propagation in and scattering from a matched metamaterial having a zero index of refraction," Phys. Rev. E **70**, 46608 (2004).

156. M. Beruete, I. Campillo, J. S. Dolado, J. E. Rodriguez-Seco, E. Perea, F. Falcone, and M. Sorolla Ayza, "Very Low-Profile "Bull's Eye" Feeder Antenna," Antennas Wirel. Propag. Lett. **4**, 365–368 (2005).

157. M. Beruete, M. Navarro-Cía, F. Falcone, M. Sorolla, I. Campillo, J. E. Rodriguez-Seco, E. Perea, and I. J. Nunez-Manrique, "Extraordinary Transmission surfaces as superstrate," in *2009 Mediterrannean Microwave Symposium (MMS)* (IEEE, 2009), pp. 1–4.

158. G. A. Hurd, "IEEE Standard Test Procedures for Antennas," Electron. Power **26**, 749 (1980).

159. L. Rayleigh, *Lord Rayleigh Scientific Papers* (1902), Vol. 111.

160. R. W. Wood, "Phase-reversal zone-plates, and diffraction-telescopes," Philos. Mag. Ser. 5 **45**, 511 (1898).

161. B. Orazbayev, M. Beruete, V. Pacheco-Peña, G. Crespo, J. Teniente, and M. Navarro-Cía, "Soret Fishnet Metalens Antenna," Sci. Rep. **4**, 9988 (2015).

162. B. Orazbayev, V. Pacheco-Peña, M. Beruete, and M. Navarro-Cía, "Exploiting the dispersion of the double-negative-index fishnet metamaterial to create a broadband low-profile metallic lens," Opt. Express **23**, 8555–8564 (2015).

163. V. Pacheco-Pena, M. Navarro-Cia, B. Orazbayev, I. V. Minin, O. V. Minin, and M. Beruete, "Zoned Fishnet Lens Antenna With Reference Phase for Side-Lobe Reduction,"

IEEE Trans. Antennas Propag. **63**, 3710–3714 (2015).

164. J. Zhou, T. Koschny, M. Kafesaki, and C. M. Soukoulis, "Negative refractive index response of weakly and strongly coupled optical metamaterials," Phys. Rev. B **80**, 35109 (2009).

165. M. Navarro-Cía, M. Beruete, M. Sorolla, and I. Campillo, "Viability of focusing effect by left-handed stacked subwavelength hole arrays," Phys. B Condens. Matter **405**, 2950–2954 (2010).

166. A. Alù, "Mantle cloak: Invisibility induced by a surface," Phys. Rev. B **80**, 245115 (2009).

167. B. A. Munk, *Finite Antenna Arrays and FSS* (John Wiley & Sons, Inc., 2003).

168. A. Alù, M. Silveirinha, and N. Engheta, "Transmission-line analysis of ε-near-zero–filled narrow channels," Phys. Rev. E **78**, 16604 (2008).

169. A. Alù and N. Engheta, "Cloaking a Sensor," Phys. Rev. Lett. **102**, 233901 (2009).

170. J. Stratton, *Electromagnetic Theory* (Mcgraw-Hill College, 1941).

171. C. Papas, *Theory of Electromagnetic Wave Propagation* (McGraw-Hill, 1965).

172. C. F. Bohren and D. R. Huffman, *Absorption and Scattering of Light by Small Particles* (Wiley-VCH Verlag GmbH, 1998).

173. N. G. Alexopoulos and N. K. Uzunoglu, "Electromagnetic scattering from active objects: invisible scatterers," Appl. Opt. **17**, 235–239 (1978).

174. A. Alù and N. Engheta, "Polarizabilities and effective parameters for collections of spherical nanoparticles formed by pairs of concentric double-negative, single-negative, and/or double-positive metamaterial layers," J. Appl. Phys. **97**, 94310 (2005).

175. P.-Y. Y. Chen, J. Soric, Y. R. Padooru, H. M. Bernety, A. B. Yakovlev, and A. Alù, "Nanostructured graphene metasurface for tunable terahertz cloaking," New J. Phys. **15**, 123029 (2013).

176. A. Alù and N. Engheta, "Plasmonic materials in transparency and cloaking problems: mechanism, robustness, and physical insights.," Opt. Express **15**, 3318–3332 (2007).

177. R. Fleury, J. Soric, and A. Alù, "Physical bounds on absorption and scattering for cloaked sensors," Phys. Rev. B **89**, 45122 (2014).

178. P.-Y. Chen, J. Soric, and A. Alù, "Invisibility and Cloaking Based on Scattering Cancellation," Adv. Mater. **24**, OP281-OP304 (2012).

179. B. Edwards, A. Alù, M. Silveirinha, and N. Engheta, "Experimental Verification of Plasmonic Cloaking at Microwave Frequencies with Metamaterials," Phys. Rev. Lett. **103**, 153901 (2009).

180. R. Liu, C. Ji, J. J. Mock, J. Y. Chin, T. J. Cui, and D. R. Smith, "Broadband Ground-Plane Cloak," Science **323**, 366–369 (2009).

181. P. Zhang, M. Lobet, and S. He, "Carpet cloaking on a dielectric half-space," Opt. Express **18**, 18158–18163 (2010).

182. H. F. Ma, W. X. Jiang, X. M. Yang, X. Y. Zhou, and T. J. Cui, "Compact-sized and broadband carpet cloak and free-space cloak," Opt. Express **17**, 19947–19959 (2009).

183. B. Zhang, T. Chan, and B.-I. Wu, "Lateral Shift Makes a Ground-Plane Cloak Detectable," Phys. Rev. Lett. **104**, 233903 (2010).

184. CST, "CST MICROWAVE STUDIO," (2016).

185. N. Mohammadi Estakhri, C. Argyropoulos, and A. Alù, "Graded metascreens to enable a new degree of nanoscale light management," Philos. Trans. R. Soc. A Math. Phys. Eng. Sci. **373**, 20140351 (2015).

186. D. L. Sounas and A. Alù, "Extinction symmetry for reciprocal objects and its implications on cloaking and scattering manipulation," Opt. Lett. **39**, 4053–4056 (2014).

187. I. Moreno and C.-C. Sun, "Modeling the radiation pattern of LEDs," Opt. Express **16**, 1808–1819 (2008).

188. C. Daniel and F. S. Wood, *Fitting Equations to Data: Computer Analysis of Multifactor Data for Scientists and Engineers* (John Wiley & Sons Canada, 1971).

189. Y. Yang, L. Jing, B. Zheng, R. Hao, W. Yin, E. Li, C. M. Soukoulis, and H. Chen, "Full-Polarization 3D Metasurface Cloak with Preserved Amplitude and Phase," Adv. Mater. (2016).

190. P. H. Siegel, "Terahertz technology," IEEE Trans. Microw. Theory Tech. **50**, 910–928 (2002).

191. M. Tonouchi, "Cutting-edge terahertz technology," Nat. Photonics **1**, 97–105 (2007).

192. C. A. Balanis, *Antenna Theory: Analysis and Design* (Wiley, 2015).

193. C. M. Soukoulis, *Photonic Crystals and Light Localization in the 21st Century* (Springer Netherlands, 2001).

194. R. Schittny, M. Kadic, T. Buckmann, and M. Wegener, "Invisibility cloaking in a diffusive light scattering medium," Science **345**, 427–429 (2014).

195. R. Schittny, A. Niemeyer, M. Kadic, T. Bückmann, A. Naber, and M. Wegener, "Transient behavior of invisibility cloaks for diffusive light propagation," Optica **2**, 84–87 (2015).

196. H. Chen and B. Zheng, "Broadband polygonal invisibility cloak for visible light," Sci. Rep. **2**, 255 (2012).

197. S. Guenneau, C. Amra, and D. Veynante, "Transformation thermodynamics: cloaking and concentrating heat flux," Opt. Express **20**, 8207–8218 (2012).

198. S. Xi, H. Chen, B. I. Wu, and J. a. Kong, "One-directional perfect cloak created with homogeneous material," IEEE Microw. Wirel. Components Lett. **19**, 131–133 (2009).

199. N. Landy and D. R. Smith, "A full-parameter unidirectional metamaterial cloak for microwaves," Nat. Mater. **12**, 25–28 (2012).

200. A. Bensoussan, G. Papanicolau, and J.-L. Lions, *Asymptotic Analysis for Periodic Structures* (North-Holland, 1978).

201. Y. Huang, Y. Feng, and T. Jiang, "Electromagnetic cloaking by layered structure of homogeneous isotropic materials.," Opt. Express **15**, 11133–11141 (2007).

202. R. Schittny, A. Niemeyer, M. Kadic, T. Bückmann, A. Naber, and M. Wegener, "Diffuse-light all-solid-state invisibility cloak," Opt. Lett. **40**, 4202–4205 (2015).

203. Y. H. Yang, S. S. Lin, Z. J. Wang, H. Chen, H. Wang, and E. Li, "Three-dimensional polyhedral invisible cloak consisting of homogeneous materials," Prog. Electromagn. Res. **142**, 31–40 (2013).

204. R. Schittny, M. Kadic, S. Guenneau, and M. Wegener, "Experiments on Transformation Thermodynamics: Molding the Flow of Heat," Phys. Rev. Lett. **110**, 195901 (2013).

205. P.-Y. Chen, M. Farhat, A. N. Askarpour, M. Tymchenko, and A. Alù, "Infrared beam-steering using acoustically modulated surface plasmons over a graphene monolayer," J. Opt. **16**, 94008 (2014).

206. M. Tamagnone, J. S. Gómez-Díaz, J. R. Mosig, and J. Perruisseau-Carrier, "Reconfigurable terahertz plasmonic antenna concept using a graphene stack," Appl. Phys. Lett. **101**, 214102 (2012).

207. O. Sydoruk, E. Tatartschuk, E. Shamonina, and L. Solymar, "Analytical formulation for the resonant frequency of split rings," J. Appl. Phys. **105**, 14903 (2009).

208. B. Orazbayev, N. Mohammadi Estakhri, M. Beruete, and A. Alù, "Terahertz carpet cloak based on a ring resonator metasurface," Phys. Rev. B **91**, 195444 (2015).

209. T. Chen and S. He, "Frequency-tunable circular polarization beam splitter using a graphene-dielectric sub-wavelength film," Opt. Express **22**, 19748–19757 (2014).

210. J. S. Gomez-Diaz, C. Moldovan, S. Capdevila, J. Romeu, L. S. Bernard, A. Magrez, A. M. Ionescu, and J. Perruisseau-Carrier, "Self-biased reconfigurable graphene stacks for terahertz plasmonics," Nat. Commun. **6**, 6334 (2015).

211. Q. Sun, Y. V. Rostovtsev, and M. S. Zubairy, "Optical beam steering based on electromagnetically induced transparency," Phys. Rev. A **74**, 33819 (2006).

212. T. P. Steinbusch, H. K. Tyagi, M. C. Schaafsma, G. Georgiou, and J. G. Rivas, "Active terahertz beam steering by photo-generated graded index gratings in thin semiconductor films," Opt. Express **22**, 26559–26571 (2014).

213. C. T. DeRose, R. D. Kekatpure, D. C. Trotter, A. Starbuck, J. R. Wendt, A. Yaacobi, M. R. Watts, U. Chettiar, N. Engheta, and P. S. Davids, "Electronically controlled optical beam-steering by an active phased array of metallic nanoantennas," Opt. Express **21**, 5198–5208 (2013).

214. D. Kwong, A. Hosseini, Y. Zhang, and R. T. Chen, "1×12 Unequally spaced waveguide array for actively tuned optical phased array on a silicon nanomembrane," Appl. Phys. Lett. **99**, 1–4 (2011).

215. K. Van Acoleyen, H. Rogier, and R. Baets, "Two-dimensional optical phased array antenna on silicon-on-insulator," Opt. Express **18**, 13655–13660 (2010).

216. W. Li, B. Chen, C. Meng, W. Fang, Y. Xiao, X. Li, Z. Hu, Y. Xu, L. Tong, H. Wang, W. Liu, J. Bao, and Y. R. Shen, "Ultrafast all-optical graphene modulator," Nano Lett. **14**, 955–959 (2014).

217. S. H. Lee, J. Choi, H.-D. Kim, H. Choi, and B. Min, "Ultrafast refractive index control of a terahertz graphene metamaterial," Sci. Rep. **3**, 2135 (2013).

218. J. S. Gómez-Díaz, M. Esquius-Morote, and J. Perruisseau-Carrier, "Plane wave excitation-detection of non-resonant plasmons along finite-width graphene strips," Opt. Express **21**, 24856–24872 (2013).

219. J. Cong, Y. Chen, J. Luo, and X. Liu, "Fabrication of graphene/polyaniline composite multilayer films by electrostatic layer-by-layer assembly," J. Solid State Chem. **218**, 171–177 (2014).

220. X. Liu, N. Wen, X. Wang, and Y. Zheng, "Layer-by-layer self-assembled graphene multilayer films via covalent bonds for supercapacitor electrodes," Nanomater. Nanotechnol. **5**, 1–7 (2015).

221. D. Qiu and E. K. Kim, "Electrically tunable and negative Schottky barriers in multi-layered graphene/MoS2 heterostructured transistors," Sci. Rep. **5**, 13743 (2015).

222. K. I. Bolotin, K. J. Sikes, Z. Jiang, M. Klima, G. Fudenberg, J. Hone, P. Kim, and H. L. Stormer, "Ultrahigh electron mobility in suspended graphene," Solid State Commun. **146**, 351–355 (2008).

223. S. A. Maier, *Plasmonics: Fundamentals and Applications* (Springer US, 2007).

224. M. Wakaki, T. Shibuya, and K. Kudodeceased, *Physical Properties and Data of Optical Materials* (CRC, 2007).

225. J. Neu, R. Beigang, and M. Rahm, "Metamaterial-based gradient index beam steerers for terahertz radiation," Appl. Phys. Lett. **103**, 1–5 (2013).

226. B. E. A. Saleh and M. C. Teich, *Fundamentals of Photonics*, Wiley Series in Pure and Applied Optics (John Wiley & Sons, Inc., 1991).

227. V. Pacheco-Peña, V. Torres, M. Beruete, M. Navarro-Cía, and N. Engheta, "ϵ -near-zero (ENZ) graded index quasi-optical devices: steering and splitting millimeter waves," J. Opt. **16**, 94009 (2014).

228. S. Roberts, "Optical Properties of Copper," Phys. Rev. **118**, 1509–1518 (1960).

229. H. Kogelnik, "Theory of dielectric waveguides," in *Integrated Optics*, Topics in Applied Physics (Springer, 1975), Vol. 7.

230. Z. Fei, A. S. Rodin, G. O. Andreev, W. Bao, A. S. McLeod, M. Wagner, L. M. Zhang, Z. Zhao, M. Thiemens, G. Dominguez, M. M. Fogler, A. H. C. Neto, C. N. Lau, F. Keilmann, and D. N. Basov, "Gate-tuning of graphene plasmons revealed by infrared nano-imaging," Nature **487**, 82–85 (2012).

231. L. Yang, C. Pei, A. Shen, C. Zhao, Y. Li, X. Li, H. Yu, Y. Li, X. Jiang, and J. Yang, "An all-optical modulation method in sub-micron scale," Sci. Rep. **5**, 9206 (2015).

232. C. Huygens, "Traite de la Lumiere," Soc. Hollandaise des Sci. **19**, (1967).

233. T. Weiland, "A discretization method for the solution of Maxwell's equations for six-component Field," Int. J. Electron. Commun. **31**, 116–120 (1977).

234. "AB Millimetre," http://www.abmillimetre.com/.

235. Agilent Technologies, "Agilent E3861C," http://www.agilent.com/home/.

236. B. Wood, J. B. Pendry, and D. P. Tsai, "Directed subwavelength imaging using a layered metal-dielectric system," Phys. Rev. B **74**, 115116 (2006).

237. S. A. Mikhailov and K. Ziegler, "Nonlinear electromagnetic response of graphene: frequency multiplication and the self-consistent-field effects," J. Phys. Condens. Matter **20**, 384204 (2008).